




Article

Formation of Nickel Oxide Nanocuboids in Ferromagnetic $\text{La}_2\text{Ni}_{1-x}\text{Mn}_{1+x}\text{O}_6$

Monica Bernal-Salamanca ^{1,*}, Zorica Konstantinović ^{2,*} , Carlos Frontera ¹, Víctor Fuentes ¹, Alberto Pomar ¹, Lluís Balcells ^{1,*} and Benjamín Martínez ¹

¹ Institut de Ciència de Materials de Barcelona-Consejo Superior de Investigaciones Científicas (ICMAB-CSIC), Campus de Universitat Autònoma de Barcelona, 08193 Bellaterra, Spain; frontera@icmab.es (C.F.); vfuentes@icmab.es (V.F.); apomar@icmab.es (A.P.); benjamin@icmab.es (B.M.)

² Center for Solid State Physics and New Materials, Institute of Physics Belgrade, University of Belgrade, Pregrevica 118, 11080 Belgrade, Serbia

* Correspondence: mbernal@icmab.es (M.B.-S.); zorica@ipb.ac.rs (Z.K.); balcells@icmab.es (L.B.)

Abstract: The control of the spontaneous formation of nanostructures at the surface of thin films is of strong interest in many different fields, from catalysts to microelectronics, because surface and interfacial properties may be substantially enhanced. Here, we analyze the formation of nickel oxide nanocuboids on top of $\text{La}_2\text{Ni}_{1-x}\text{Mn}_{1+x}\text{O}_6$ double perovskite ferromagnetic thin films, epitaxially grown on SrTiO_3 (001) substrates by radio-frequency (RF) magnetron sputtering. We show that, by annealing the films at high temperature under high oxygen partial pressure, the spontaneous segregation of nanocuboids is enhanced. The evolution of the structural and magnetic properties of the films is studied as a function of the annealing treatments at different temperatures. It is shown that the formation of NiOx nanocuboids leads to a nanostructured film surface with regions of locally different electrical transport characteristics.

Keywords: ferromagnetic double perovskite; spontaneous formation of NiO_x nanocuboids; local transport properties



Citation: Bernal-Salamanca, M.; Konstantinović, Z.; Frontera, C.; Fuentes, V.; Pomar, A.; Balcells, L.; Martínez, B. Formation of Nickel Oxide Nanocuboids in Ferromagnetic $\text{La}_2\text{Ni}_{1-x}\text{Mn}_{1+x}\text{O}_6$. *Nanomaterials* **2021**, *11*, 804. <https://doi.org/10.3390/nano11030804>

Academic Editor: João Pedro Araujo

Received: 24 February 2021

Accepted: 18 March 2021

Published: 21 March 2021

Publisher's Note: MDPI stays neutral with regard to jurisdictional claims in published maps and institutional affiliations.



Copyright: © 2021 by the authors. Licensee MDPI, Basel, Switzerland. This article is an open access article distributed under the terms and conditions of the Creative Commons Attribution (CC BY) license (<https://creativecommons.org/licenses/by/4.0/>).

1. Introduction

Magnetic insulators have gained renewed interest due to their promising properties as material platforms with efficient magnetization dynamics [1,2]. In this regard, double perovskite $\text{La}_2\text{NiMnO}_6$ (LNMO) is one of the most widely studied materials due to its large magnetodielectric properties and high Curie temperature $T_c \sim 280$ K [3–5]. For these reasons, LNMO has been considered as a promising candidate for the development of magneto-electronic and spintronic devices and thus, has attracted much attention lately [6,7]. LNMO has a double perovskite structure ($A_2BB'O_6$), where Ni and Mn ions ideally occupy alternatively the B site positions giving place to a rocksalt-type lattice [5]. However, in thin film form, as occurs in other double perovskite systems, full B-site Ni-Mn cationic ordering is difficult to achieve [8–11]. In particular, in LNMO system, phase segregation often occurs and the coexistence of two structural phases is detected at room temperature [12,13], leading to the observation of two Curie temperatures [14].

To improve the magnetic properties of LNMO samples post-growth annealing processes are commonly employed [15–17]. Nonetheless, recent studies report the formation of the NiO phase impurities in LNMO thin films grown by MBE technique with the post-growth annealing, with apparently defect-free growth [18,19]. Detailed cross-sectional high-angle annular dark-field studies revealed an inverted “pyramid-like” shape morphology of the NiO precipitate, which progresses from a 2–3 nm base to a ~ 10 nm wide mouth at the film surface [19]. The coexistence of double perovskite and NiO secondary phase is supported by first principles modeling of growth in oxygen deficient conditions with

expected dissolution of inclusions during annealing [18]. Nanometer size nickel-oxide precipitates were also detected during the growth of LaNiO_3 - LaAlO_3 superlattices on SrTiO_3 substrate, changing their electronic properties [20]. Similar phase segregation processes are also observed in other manganite systems with cationic deficiency, strongly affecting magnetic and transport properties of the materials [21].

In this work, we report on the spontaneous formation of nickel-oxide nanocuboids at the surface of $\text{La}_2\text{Ni}_{1-x}\text{Mn}_{1+x}\text{O}_6$ thin films, deposited by RF magnetron sputtering technique. Annealing treatments in oxygen at high temperature (in-situ or ex-situ) after thin film growth promote the spontaneous formation of NiO nanocuboids giving place to the formation of a nanostructured surface. The evolution of the structural and magnetic properties of the films as a function of the annealing temperatures has also been studied. As expected, the post-annealing processes improve magnetic properties as well as structural properties, while modifying significantly the local transport properties at the film surface.

2. Materials and Methods

$\text{La}_2\text{Ni}_{1-x}\text{Mn}_{1+x}\text{O}_6$ (LNMO) thin films were fabricated by RF magnetron sputtering under a total oxygen pressure of 19 Pa at high temperatures (900 °C) on top of SrTiO_3 (001) substrates using a stoichiometric $\text{La}_2\text{NiMnO}_6$ target. The mini-MAK from US-INC magnetron was 33 mm (1.3 inch) in diameter. The RF power used during thin film deposition was 40 W. The background pressure of the home-made sputtering chamber is in order of $\sim 10^{-5}$ Pa. Electron probe microanalysis revealed Ni-deficiency ($x \sim 0.47$) in the films [11]. Before deposition, substrates were cleaned in an ultrasonic bath with Milli-Q water and then annealed at 1000 °C in air for 2 h to obtain a clean and smooth TiO_2 terminated surface [22]. Samples with thicknesses, t , of $40 \text{ nm} < t < 50 \text{ nm}$, as determined by X-ray reflectivity, were prepared. After film deposition, as-grown samples were annealed (in-situ or ex-situ) for 1 h under high oxygen partial pressure ($\text{PO}_2 \sim 5 \times 10^4 \text{ Pa}$) to optimize the magnetic properties and oxygen stoichiometry. The evolution of the physical and structural properties was studied after successive annealing processes at 800 °C (Annealed-800 °C) and 900 °C (Annealed-900 °C) for 1 h of the same LNMO thin film.

The surface morphology of the LNMO film was characterized by scanning electron microscopy (SEM, QUANTA FEI 200 FEG-ESEM) and atomic force microscopy (AFM, MFP-3D AFM Asylum Research, Gole, CA, USA) in tapping mode. Structural characterization was made by means of X-ray diffraction (XRD) and reflectivity techniques (X'Pert MRD-Panalytical and a Siemens D5000, Malvern Panalytical, Malvern, UK). Reciprocal space mappings (RSM) were recorded using a Bruker-AXS General Detector Diffraction System (GADDS) model D8 Advance with a 2D detector. Energy dispersive X-ray analysis (EDX) has been performed on a FEI Magellan 400 L XHR SEM using an X-Max Ultim Extreme EDX detector (Oxford Instruments, Abingdon, UK). Transmission electron microscope (TEM) measurements were made by means of a field emission gun FEI Tecnai F20 microscope at 200 kV with a point-to-point resolution of 0.19 nm. Magnetization measurements were done using a superconducting quantum interference device (SQUID, Quantum Design, San Diego, CA, USA). The local electrical response of the films surface was explored by conductive atomic force microscopy (C-AFM), measurements were performed employing a MFP-3D microscope from Asylum Research with an Optimized Resistance Conductance Amplifier (ORCA) module. Diamond doped coated probes (DDESP-FM-V2 from Bruker, Billerica, MA, USA) were used in both the current maps and the I-V curves to ensure the stability of the tip during data acquisition. Moreover, these measures were carried out in a closed chamber with nitrogen atmosphere with the aim of reducing the ambient humidity and, therefore, avoid possible anodic oxidation effects.

3. Results and Discussion

As evidenced in Figure 1, the surface morphology of a LNMO film, after usual annealing in-situ process at 900 °C, reveals the existence of a nanostructured surface. The SEM image (Figure 1a) detects uniformly distributed nanocuboids throughout the film

surface, with nearly square-based, sub-100 nm in size. AFM topography in Figure 1b confirms the presence of nanocuboids, distributed on top of a flat LNMO surface with low roughness (rms~0.3 nm). The estimated occupation of the surface is below 15%. The distribution of nanocuboids size is well described by the log-normal function with the most probable size of around $S_0 \sim 58$ nm and the distribution width of $\sigma \sim 0.23$ (see Figure A4 in Appendix B). The inset of Figure 1b reveals a nanocuboid height of ~ 12 nm. An interesting observation is that nanocuboids' edges are mainly oriented along the [100] direction of the substrate (note that SEM and AFM images are rotated around 45° respect to the substrate edge during observation).

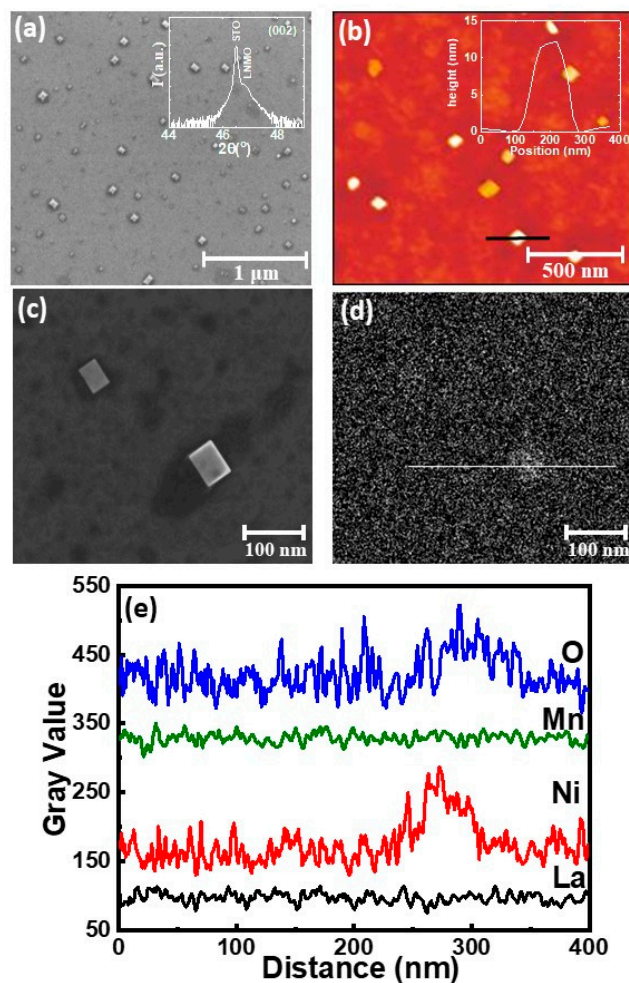


Figure 1. (a) SEM micrographs of LNMO-900 °C with in-situ annealing (thickness, $t = 42$ nm). Inset shows the $\theta/2\theta$ XRD pattern around 002 bragg peak of the substrate. (b) AFM image of LNMO-900 °C film with the height profile of one nanocuboid in the inset. (c,d) Small area SEM and EDX map at energy of $E = 15$ eV with the corresponding profile spectra of different elements by X-ray spectroscopy analysis in (e).

A deeper insight in the films' structure was obtained by X-ray diffraction and reflectivity techniques. For simplicity and comparison between the film and the substrate, the LNMO lattice parameter is considered in pseudocubic notation ($a_{\text{bulk}} = 3.876$ Å) [23,24]. LNMO films on top of STO ($a_{\text{STO}} = 3.905$ Å) substrates grow under small tensile strain $(a_{\text{LNMO}} - a_{\text{STO}}) / a_{\text{STO}} \times 100\% = -0.74\%$. The in-plane lattice parameter of the film determined from the reciprocal space maps, around $(103)_{\text{STO}}$ reflection, perfectly matches with that of the STO substrate (see Figure A1a in Appendix A). The high resolution $\theta/2\theta$ X-ray diffraction allows identifying the LNMO peak in the proximity of the intense substrate one (see inset of Figure 1a) with an out-of-plane lattice parameter of $a_{\perp} = 3.877 \pm 0.003$ Å.

The estimated LNMO unit cell volume ($\sim 59.12 \text{ \AA}^3$) is very similar to the unit cell volume of Ni-deficient bulk counterpart ($\text{LaNi}_{0.25}\text{Mn}_{0.75}\text{O}_{3+\delta}$) [12]. A planar view high resolution TEM (HRTEM) images supports XRD measurements, with a coexistence of domains with different orientations (Figure A2 in Appendix A).

Information regarding the chemical composition of the nanometric cuboids was obtained from energy dispersive x-ray (EDX) analysis. A small area SEM image of a single nanocuboid and the corresponding EDX map obtained at 15 KeV are shown in Figure 1c,d. The profile spectra of constituent elements (La $L_{\alpha 1}$, Ni, Mn and O $K_{\alpha 1}$) in a single nanocuboid are shown in Figure 1e, indicating the presence of nickel and oxygen. The presence of La and Mn have been excluded due to the very low detection percentage (no difference observed along the baseline in Figure 1d). Therefore, semi-quantitative EDX analysis indicate that the nanometric cuboids formed on top of the LNMO films surface are Ni-rich phase, most probably NiOx phases, in agreement with recent reports of the formation of NiOx segregates in LNMO double perovskites [18,19]. In those works, it is proposed that oxygen deficiency in LNMO films could favors the formation of antisite defects [23] and NiOx phase segregations [18,19].

To gain a deeper insight into the formation of NiOx nanocuboids, successive annealing processes at different temperatures are applied ex-situ to a non-annealed as-grown film. The evolution of the physical and structural properties was followed on the same LNMO thin film after each annealing process and the changes on the morphology are presented in Figure 2a–c. SEM (left-hand image) and AFM (right-hand image) micrographs in Figure 2a of the as-grown LNMO film without annealing process show a flat surface with an average roughness of $\text{rms} \sim 0.3 \text{ nm}$. In this case, no signals of segregation were detected.

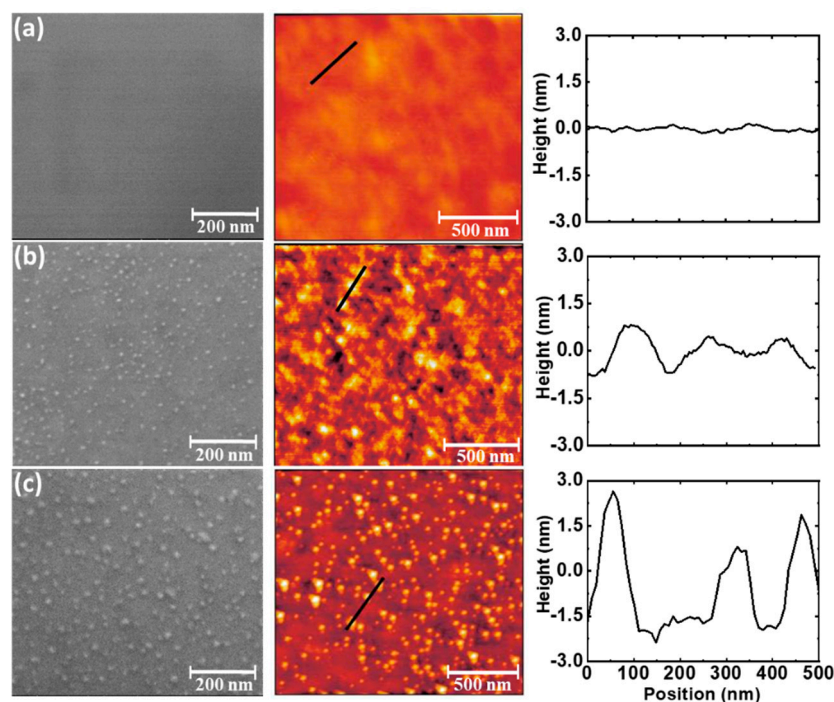


Figure 2. SEM micrographs (left-hand image) and AFM images (right-hand image) with the typical line profile of the same LNMO thin film (thickness, $t = 48 \text{ nm}$) after different annealing processes: (a) as-grown film (no-annealing process), (b) annealing at $800 \text{ }^\circ\text{C}$ and (c) annealing at $900 \text{ }^\circ\text{C}$.

However, after an ex-situ annealing at $800 \text{ }^\circ\text{C}$, segregated nanostructures appears distributed through the whole surface as shown in Figure 2b. SEM micrographs revealed the presence of uniformly distributed small nanoparticles. The corresponding AFM confirms the presence of these nanoparticles, reflected in a higher value of global surface roughness ($\text{rms} \sim 0.45 \text{ nm}$). Log-normal distribution indicates the most probable nanoparticle size of

around $S_0 \sim 13.5$ nm with the distribution width of $\sigma \sim 0.13$ (see Figure A5a in Appendix B). However, the mean-size of nanostructures remains rather small and with a height of few nanometers ~ 2 nm (see the line profile in Figure 2b).

Performing further ex-situ annealing process at higher temperatures (900 °C) on the very same LNMO film resulted in an enhancement of the growth of the nanoparticles. Nanoparticles became larger in-size as shown in Figure 2c). Log-normal distribution reveals the most probable nanoparticle size of $S_0 \sim 18.5$ nm with the distribution width of $\sigma \sim 0.17$ (see Figure A5b in Appendix B). The average nanoparticle height increases to around ~ 5 nm which is also reflected in an increase of the roughness (rms ~ 0.7 nm). Although the density of nanoparticles appears to decrease by increasing the annealing temperature (from 5.34×10^{-4} nanoparticles/nm² for Annealed-800 °C, to 3.70×10^{-4} nanoparticles/nm² for Annealed-900 °C) the average volume of NiO_x at the surface has been estimated to increase around three times (see Table A2 in Appendix B), thus confirming that annealing process enhances the segregation.

The effect of different annealing processes on the structural properties of the same LNMO thin film has been also followed by high resolution XRD scan of the (002) reflection and the asymmetric RSM around (103) reflection (Figure 3). In Figure 3a, a shoulder could be distinguished in the proximity of the prominent substrate (0 0 2) peak, which can be associated to the LNMO peak with an out-of-plane parameter of $a_{\perp} = 3.939 \pm 0.002$ Å. At the same time, RSM around (103) reflection of the same film, indicates the position of the LNMO film just below the substrate peak (right-hand image in Figure 3a), confirming that the as-grown film is fully strained with the in-plane parameter that mimics the lattice parameter of underlying substrate ($a_{\text{STO}} = 3.905$ Å).

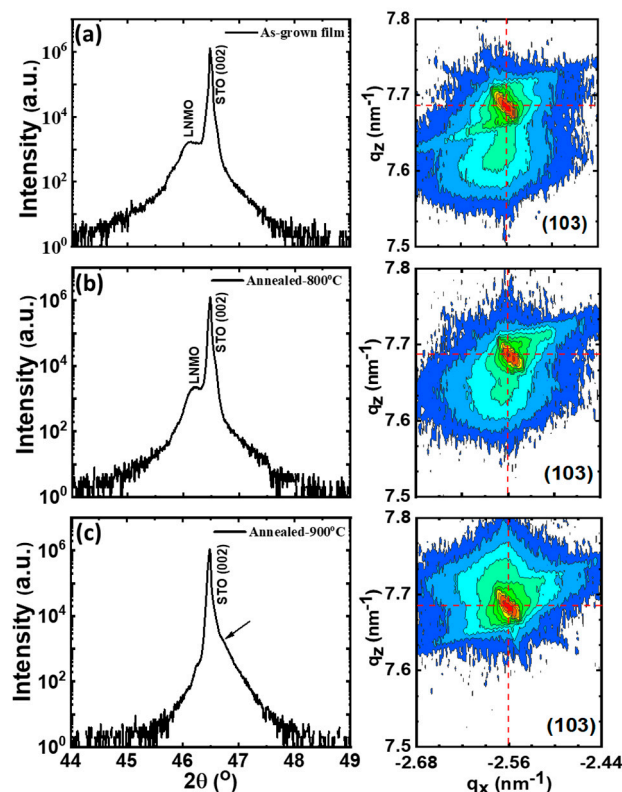


Figure 3. High-resolution $\theta/2\theta$ XRD scans of the (002) reflections (**left**) and RSM around (103) reflection (**right**) of the same LNMO thin film (thickness, $t = 48$ nm) after different annealing processes: (a) as-grown film, (b) annealing at 800 °C and (c) annealing at 900 °C. The arrow indicates position of LNMO peak and the red dotted line indicates the position of the STO peak.

The first annealing process at 800 °C (Figure 3b) does not significantly change the structural parameters. From $\theta/2\theta$ XRD scans (left-hand image in Figure 3b), the out-of-

plane lattice parameter is found to decrease to $a_{\perp} = 3.929 \pm 0.002 \text{ \AA}$, remaining elongated respect to the corresponding pseudocubic perovskite lattice parameter of bulk LNMO ($a_{\text{bulk}} = 3.876 \text{ \AA}$) [23]. However, under annealing process at $900 \text{ }^{\circ}\text{C}$ in Figure 3c, the shoulder in $\theta/2\theta$ XRD scan disappears completely and only the substrate peak can be clearly observed. Nevertheless, the RSM around (103) reflection indicates that the LNMO film peak is just above the substrate peak corresponding to a slight asymmetry detected in $\theta/2\theta$ XRD scan (see arrow in left-hand Figure 3c). While the in-plane lattice parameter still remains constant ($a_{\parallel} = 3.905 \pm 0.005 \text{ \AA}$), the out-of-plane lattice parameter further decreases to $a_{\perp} = 3.883 \pm 0.001 \text{ \AA}$. The variation of the in-plane and the out-of-plane cell parameters in pseudo-cubic notation after different annealing processes are depicted in Figure 4a. The in-plane lattice parameters (red dashed line in Figure 4a) match the SrTiO_3 lattice parameter indicating that the film remains strained even after various annealing processes. On the other hand, the out-of-plane lattice parameter (black dashed line in Figure 4a) decreases progressively towards the LNMO bulk value (blue dashed line).

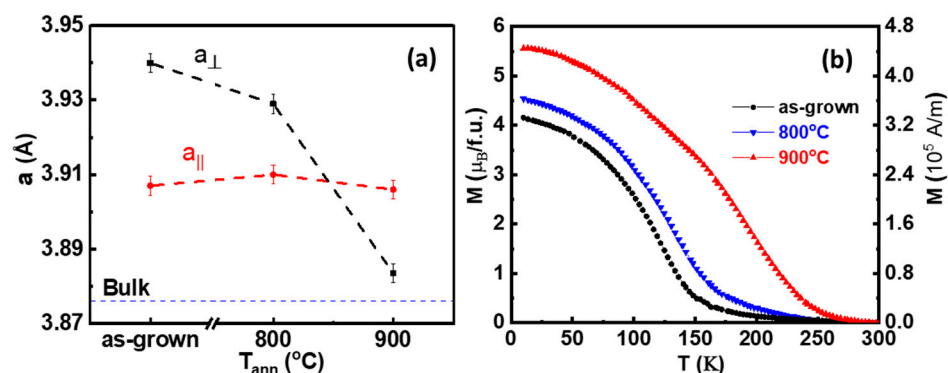


Figure 4. (a) Variation of in-plane (red dashed line) and out-of-plane (black dashed line) lattice parameters of LNMO film after different ex-situ annealing processes. The blue dashed line represents the bulk counterpart value [23] and (b) corresponding temperature dependence of in-plane magnetization at $\mu_0H = 0.5 \text{ T}$.

It is worth to note that non-annealed as-grown film has a larger out-of-plane lattice parameter than expected and consequentially larger unit cell volume ($\sim 60.06 \text{ \AA}^3$). This larger unit cell usually denotes some oxygen deficiency and the presence of Mn^{3+} [25]. In fact, as can be deduced from Figure 4a, the shrinkage of the out-of-plane lattice parameter while in-plane parameters remain unchanged results in a reduction of the unit cell volume after successive annealing, which is consistent with oxygen incorporation during the annealing processes and the formation of Mn^{4+} , as previously observed in similar manganite systems [25–27]. Indeed, as-grown non-annealed film exhibit clearly depressed values of Curie temperature (black curve in Figure 4b while T_c is enhanced in annealed films (blue and red curves), in agreement with previous observations in the LNMO system [15]. It should be noted that we cannot exclude the presence of NiOx segregations inside the film matrix and that the presence of NiO secondary phase may also contribute to the increment of the out-of-plane lattice parameter in as-grown samples, besides oxygen deficiency. These results agree with previous studies showing that annealing processes in oxygen rich atmosphere promote an increase of the Curie temperature in $\text{La}_2\text{NiMnO}_6$ films and other double perovskites [15,16]. Furthermore, it has been shown that post-growth annealing treatments are also effective to reduce the number of antisite defects [17] and to dissolve NiO segregations, thus contributing to increase the saturation magnetization [18]. However, in our case, in spite of a clear improvement of the ferromagnetic properties after post-growth annealing (ex-situ or in-situ, see also Figure A1 in Appendix A), nanometric nickel-oxide segregations are still present at the LNMO surface.

It is worth mentioning that Curie temperatures found in our samples although significantly improved, are still lower than that found in the bulk counterpart even after

oxygen annealing at the highest temperature (900 °C). This could be attributed to the non-homogeneity of the sample detected by HRTEM (see Figure A2 in Appendix A), that causes the formation of NiO secondary phases (as detected from EDX measurements) and cationic vacancies, giving rise to octahedral distortions in the film, and thus affecting their ferromagnetic properties [28,29]. Moreover, as Ni agglomeration at the surface is larger after annealing process it is sound to assume that the Ni deficiency inside the film increases that, as a consequence, could further affect the ferromagnetic transition, as T_c is known to decrease when reducing the Ni content [3,12]. In conclusion, the strong structural strain exerted by the substrate on thin layers clamped to it allows only the contraction of the out-of-plane cell parameter. Thus, high-temperature annealing in oxygen atmosphere promotes a vertical cationic migration (the entry of oxygen ions as well as nickel migration towards surface), allowing the formation of nickel-oxide nanoparticles at film surface.

Additionally, the presence of nickel-oxide nanoparticles at the surface of LNMO films may strongly influence local electrical properties. To analyze the electronic properties of the different phases present at the LNMO film surface, conductive atomic force microscopy measurements were performed in films prepared after an in-situ annealing at 900 °C. Figure 5a shows topographic image in a $2 \times 2 \mu\text{m}^2$ area of a LNMO film with NiO_x nanoparticles formed on its surface, while Figure 5b depict its simultaneous acquired current map (applying 1.5 V).

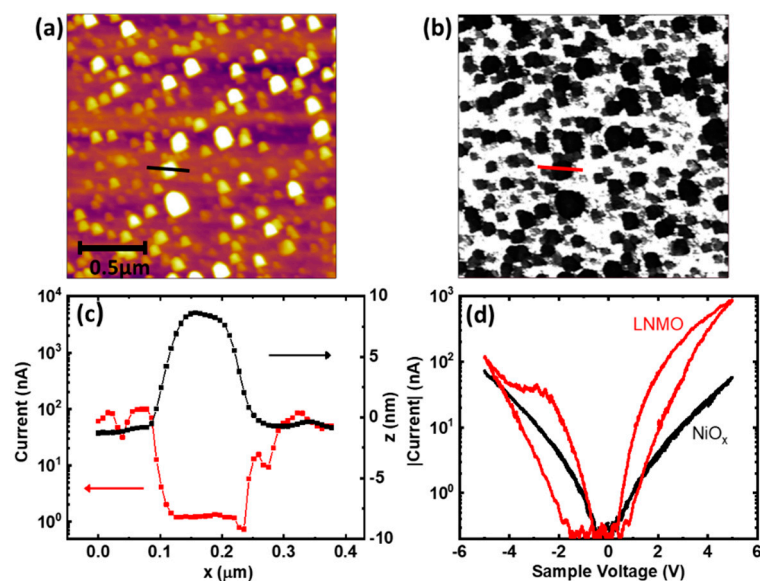


Figure 5. Local electric properties of the LNMO films with NiO_x nanoparticles at the surface measured by C-AFM. (a) Topography image of a $2 \times 2 \mu\text{m}^2$ area of the film. (b) Simultaneous current map of the same area taken (applying 1.5 V), where the less conductive parts can be related with the particles observed in the topography. (c) Current (red) and height (black) profiles of a NiO_x nanoparticle and the surrounding LNMO film marked in (a,b). (d) I-V curves on the LNMO film (red) and on a particle (black), respectively.

In the topography image, NiO_x nanoparticles can be identified as the parts of the surface with higher height (bright circles) while in the current map a conductive matrix (white background) is disrupted by less conductive circles (black). Comparing both images allows identifying NiO_x nanoparticles as the less conductive parts of the current map, i.e., NiO_x particles are more resistive than the LNMO film. This correlation can be better appreciated in Figure 5c, where the profiles of the topography (black) and the current (red) of the lines (see Figure 5a,b) are depicted. In Figure 5c, it can be clearly observed that, in the higher height (z) region, which corresponds to a NiO_x particle, the current drops to ≈ 1 nA, while in the flat surrounding regions, where the LNMO film is directly measured, the current is almost two orders of magnitude higher (≈ 100 nA).

Furthermore, the response of the LNMO film and the NiO_x particles to voltage cycling is clearly different, as evidenced in Figure 5d. Voltage cycles taken directly on the LNMO surface (red curve) show a hysteretic behavior pinned at 0 V characteristic of a resistive switching behavior. At the same time, it is also observed that the application of a negative voltage (−5 V) locally increases the resistance of the film, switching the affected area to the so-called high resistance state (HRS). This HRS can be reverted back by the application of a positive voltage (+5 V) which returns the affected area of the film back into a more conductive state, i.e., the low resistance state (LRS).

It is important to mention that both HRS and LRS are of a non-volatile nature and can be switched between them multiple times, stating the base for a bipolar resistive switching behavior suitable for the implementation of memory devices. A totally different behavior is observed sweeping the voltage on the top of a particle (black line). In this case, a non-hysteretic symmetrical curve is obtained, where the application of positive or negative voltage does not have any influence in the resistivity properties of the particles. The absence of resistive switching in the particles can be also visualized in Figure A3 (Appendix A). After switching an area to the HRS, the LNMO current is heavily reduced while the particles included in the area maintain their initial current, thus showing more conductivity than the high resistive state. Thus, our results show that nanostructured LNMO films may be switched from a system of poor conductive particles onto a conductive matrix to the opposite case, with conductive particles onto an insulating matrix, thus behaving as a model to study interfacial local transport.

4. Conclusions

In conclusion, we report on the controlled formation of nickel-oxide nanocuboids at the surface of La₂Ni_{1−x}Mn_{1+x}O₆ (x~0.47) thin films deposited by the RF magnetron sputtering technique. It is shown that the LNMO functional properties are highly influenced by the post-growth annealing process. Even LNMO films remains strained after various consecutive annealing processes, annealing treatments in oxygen atmosphere at high temperature allow a partial structural relaxation reflected in a reduction of the unit cell volume towards the LNMO bulk value. This structural relaxation, detected through a reduction of the out-of-plane cell parameter, allows some kind of vertical cationic migration and promotes an improvement of the ferromagnetic properties that affects both the Curie temperature and the saturation magnetization of the films. On the other hand, oxygen annealing processes promote Ni segregation towards the surface of the films where the formation of NiO_x nanoparticles is detected. The presence of NiO_x nanocuboids significantly changes the local surface transport properties, allowing one to obtain a composite surface in which areas exhibiting a resistive switching behavior alternate with other insulating behaviors.

Author Contributions: Thin film preparation and characterization, M.B.-S.; supervision, Z.K. and L.B.; structural properties, C.F.; local transport properties, V.F.; writing—original draft preparation, M.B.-S., Z.K., L.B., and C.F.; writing—review and editing, C.F., A.P., and B.M. All authors have read and agreed to the published version of the manuscript.

Funding: We acknowledge financial support from the Spanish Ministry of Science, Innovation and Universities through Severo Ochoa Program (CEX2019-000917-S) and RTI2018-099960-B-I00 (SPINCURIOX) and funding from the European Union's Horizon 2020 research and innovation program under the Marie-Sklodowska-Curie grant agreement No. 645658 (DAFNEOX Project) and FEDER Program. Z.K. acknowledge the support of the Serbian Ministry of Education, Science and Technological Development (III45018). This work has been performed in the framework of the PhD program of the Universitat Autònoma de Barcelona (UAB).

Data Availability Statement: The data that support the findings of this study are available on request from the corresponding authors.

Acknowledgments: We acknowledge Jordi Arbiol and Jeremy David for electronic microscopy assistance and ICMAB technical services.

Conflicts of Interest: The authors declare no conflict of interest.

Appendix A

Figure A1 shows structural and magnetic properties of $\text{La}_2\text{Ni}_{0.53}\text{Mn}_{1.47}\text{O}_6$ thin film (thickness, $t = 42$ nm) with in-situ annealing temperature at 900°C for 1 h under 5×10^4 Pa O_2 (growth at 900°C under $\text{PO}_2 \sim 19$ Pa). The reciprocal space map, around $(103)_{\text{STO}}$ reflection, indicates strained film as discussed above (Figure A1a). The T_c value found in our samples is slightly lower compared to the bulk value, as expected for nickel deficient samples [3,12] (Figure A1b). In-plane and out-of-plane hysteresis loops $M(H)$ at 10 K (Figure A1c) exhibit the expected hysteretic behavior with similar coercive field, $H_c \sim 400$ Oe (see corresponding inset). On the other side, a saturation magnetization of ($M_s \approx 5.8 \mu\text{B}/\text{f.u.}$) is found to be somewhat larger than the expected theoretical value ($\sim 5 \mu\text{B}/\text{f.u.}$) for fully ordered stoichiometric LNMO, as discussed previously [11]. More details about the ferromagnetic nature in LNMO films with similar magnetic behavior, including X-ray magnetic circular dichroism, can be found in [11].

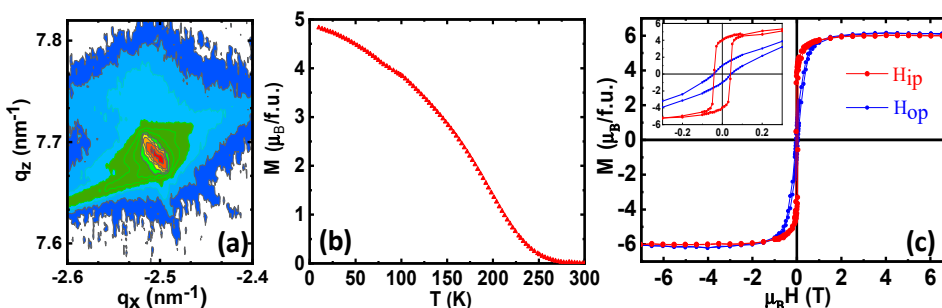


Figure A1. (a) RSM around (103) reflection of LNMO 900°C thin film (thickness, $t = 42$ nm) with in-situ annealing temperature at 900°C (b) In-plane magnetization as a function of temperature under an applied field of $\mu_0H = 0.5$ T. (c) In-plane and out-of-plane hysteresis loops $M(H)$ at 10. Inset shows the low field region in detail.

Figure A2 shows a plan-view in high resolution TEM (HRTEM) images, acquired in order to obtain information about the microstructure and crystallographic features of a LNMO film with in-situ annealed- 900°C process. The sample was cut parallel to the sample surface (perpendicular to the (001) planes). HRTEM images show a non-homogeneous surface with the coexistence of domains with different orientations. The Fourier transform (FT) of selected areas of the image were computed in order to assess the periodicity of the crystal lattice. The FT of a large area was marked by squares, which shows different spots corresponding to the enlargement of the LNMO lattice with respect to STO (LNMO cell parameters are of the type $a \approx b \approx \sqrt{2}a_p$, $c \approx 2a_p$ where a_p is the primitive perovskite cell parameter). These spots can be indexed as $(0\ k/2\ 1/2)$ (k and l odd), $(0\ k/2\ 1/)$ (k odd), and $(0\ k\ 1/2)$ (l odd) and indicate different orientations of the LNMO cell in the film.

The Resistive switching characteristics (or their absence), depicted in Figure 5d of the main text, has also been probed on large surface areas to assess its reproducibility. Figure A3a,b depicts the topography and current images of a $5 \times 5 \mu\text{m}^2$ area. In the center of this area a $3 \times 3 \mu\text{m}^2$ square has been previously scanned at -4 V. As a consequence of this initial scan, the area has been switched into the HRS without harming the surface, as can be noticed in the topography image. Figure A3c,d show a detail picture ($2 \times 2 \mu\text{m}^2$) of the previous image. Adjusting the scale of the current map it can be observed that, inside the switched area, the particles are more conductive than the LNMO film in the HRS, while in the pristine state the particles are more resistive. The lack of resistance change after the biased scan supports the I-V curves presented in the main text and confirms the absence of RS behavior in the NiO_x particles.

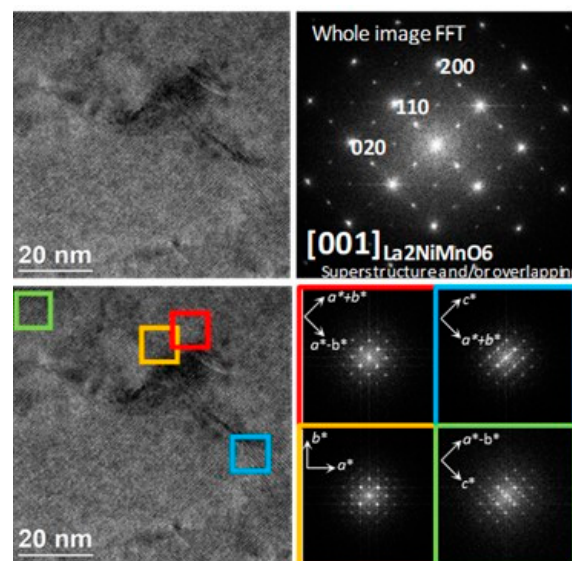


Figure A2. A plan-view HRTEM image of LNMO900 °C thin film. Fourier transform (FT) shows the coexistence of nanodomains with different orientations.

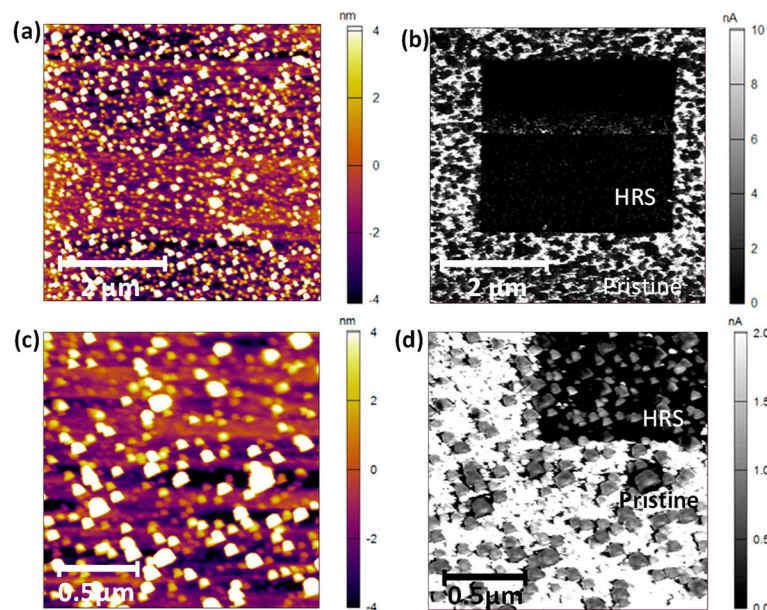


Figure A3. Switching of a $3 \times 3 \mu\text{m}^2$ area of a LNMO film into the HRS. (a) Topography and (b) current map images of a $5 \times 5 \mu\text{m}^2$ area, where the central $3 \times 3 \mu\text{m}^2$ has been previously scanned at -4 V of sample Voltage. The current map shows a switching to the HRS of the LNMO film in the scanned area, which does not induce any changes in the topography. (c) Topography and (d) Current map images of a detailed area ($2 \times 2 \mu\text{m}^2$) showing the lack of switching of NiOx particles that are more resistive than the film in the pristine state but more conductive than the film in the HRS.

Appendix B

The size of nanocuboids was determined from SEM micrographs using image analysis (ImageJ software [30]) averaging measurements of a large number of particles at different regions of the film surface. The distribution of nanoparticle size is well described by the log-normal function $f(S) = \frac{1}{\sqrt{2\pi}\sigma S} \exp\left[-\frac{\ln^2\left(\frac{S}{S_0}\right)}{2\sigma^2}\right]$, where the fitting parameters S_0 and σ are the most probable nanoparticle size and the width of the distribution, respectively. The average nanoparticle size S_M is determined from the most probable nanoparticle size

($S_M = S_0 \exp(\sigma^2/2)$). Examples of the analysis performed for different thin films are shown in Figure A4 (in-situ annealed film) and Figure A5 (ex-situ annealed film). A summary of the obtained values for the surface density and average nanoparticle volume is presented in Tables A1 and A2.

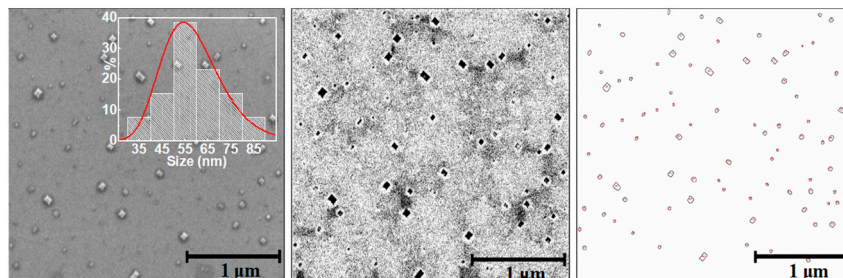


Figure A4. SEM micrograph with a magnification of $50,000\times$ of LNMO-900 °C thin film (thickness, $t = 42$ nm, in-situ annealing at 900 °C). Filtered image of its corresponding SEM image (**medium**) and automated grains counting with Image J software (**right**).

Table A1. Surface density, average nanoparticle volume, total volume of the nanoparticles (NiO_x) per unit surface ($1 \mu\text{m}^2$) and nanoparticle fraction volume of LNMO-900 °C thin film (determined from Figure A4).

Annealing T (In-Situ)	Density ($\text{NP}/\mu\text{m}^2$)	NP Volume (nm^3)	NPs Volume ($\text{nm}^3/\mu\text{m}^2$)	NP Fraction Volume
900 °C	$\sim 1.04 \times 10^{-1}$	$\sim 4.2 \times 10^4$	$\sim 4.4 \times 10^5$	~ 0.011

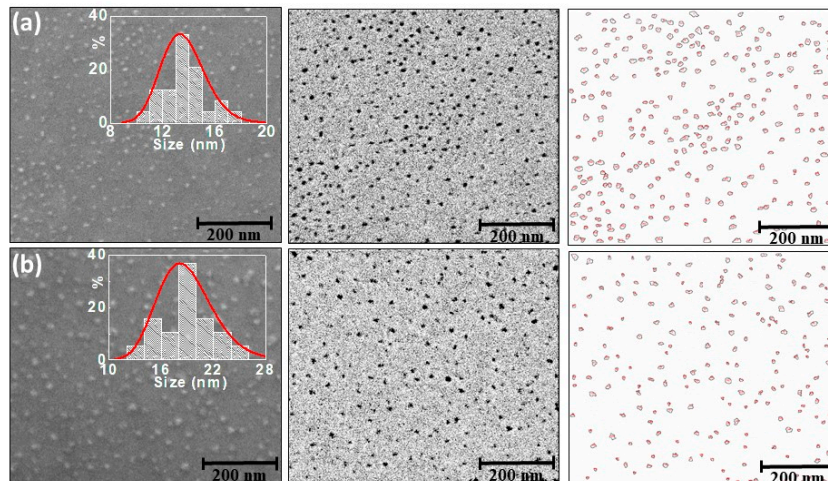


Figure A5. SEM micrographs with a magnification of $200,000\times$ of the same LNMO thin film (thickness, $t = 48$ nm) after different ex-situ annealing temperatures: (a) Anneal-800 °C and (b) Anneal-900 °C. Filtered image of its corresponding SEM image (**medium**) and automated grains counting with Image J software (**right**).

Table A2. Surface density, average nanoparticle volume, total volume of the nanoparticles (NiO_x) per unit surface ($1 \mu\text{m}^2$) and nanoparticle fraction volume of the same LNMO thin film after different ex-situ annealing temperatures, determined from Figure A5.

Annealing T (Ex-Situ)	Density ($\text{NP}/\mu\text{m}^2$)	NP Volume (nm^3)	NPs Volume ($\text{nm}^3/\mu\text{m}^2$)	NP Fraction Volume
800 °C	$\sim 5.34 \times 10^2$	$\sim 3.7 \times 10^2$	$\sim 2.0 \times 10^5$	~ 0.004
900 °C	$\sim 3.70 \times 10^2$	$\sim 1.8 \times 10^3$	$\sim 6.5 \times 10^5$	~ 0.014

References

1. Chumak, A.V.; Vasyuchka, V.I.; Serga, A.A.; Hillebrands, B. Magnon spintronics. *Nat. Phys.* **2015**, *11*, 453–461. [[CrossRef](#)]
2. Hoffmann, A.; Bader, S.B. Opportunities at the Frontiers of Spintronics. *Phys. Rev. Appl.* **2015**, *4*, 047001. [[CrossRef](#)]
3. Goodenough, J.B.; Wold, A.; Arnett, R.J.; Menyuk, N. Relationship between crystal symmetry and magnetic properties of ionic compounds containing Mn^{3+} . *Phys. Rev.* **1961**, *124*, 373–384. [[CrossRef](#)]
4. Dass, R.I.; Yan, J.-Q.; Goodenough, J.B. Oxygen stoichiometry, ferromagnetism, and transport properties of $La_{2-x}NiMnO_{6-\delta}$. *Phys. Rev. B* **2003**, *68*, 064415. [[CrossRef](#)]
5. Rogado, N.S.; Li, J.; Sleight, A.W.; Subramanian, M.A. Magnetocapacitance and Magnetoresistance Near Room Temperature in a Ferromagnetic Semiconductor: La_2NiMnO_6 . *Adv. Mater.* **2005**, *17*, 2225–2227. [[CrossRef](#)]
6. Choudhury, D.; Mandal, P.; Mathieu, R.; Hazarika, A.; Rajan, S.; Sundaresan, A.; Waghmare, U.V.; Knut, R.; Karis, O.; Nordblad, P.; et al. Near-room-temperature colossal magnetodielectricity and multiglass properties in partially disordered La_2NiMnO_6 . *Phys. Rev. Lett.* **2012**, *108*, 127201. [[CrossRef](#)] [[PubMed](#)]
7. Padhan, P.; Guo, H.Z.; LeClair, P.; Gupta, A. Dielectric relaxation and magnetodielectric response in epitaxial thin films of La_2NiMnO_6 . *Appl. Phys. Lett.* **2008**, *92*, 022909. [[CrossRef](#)]
8. Singh, M.P.; Truong, K.D.; Jandl, S.; Fournier, P. Long-range Ni/Mn structural order in epitaxial double perovskite La_2NiMnO_6 thin films. *Phys. Rev. B* **2009**, *79*, 224421. [[CrossRef](#)]
9. Kitamura, M.; Ohkubo, I.; Kubota, M.; Matsumoto, Y.; Koinuma, H.; Oshima, M. Ferromagnetic properties of epitaxial thin films grown by pulsed laser deposition. *Appl. Phys. Lett.* **2009**, *94*, 132506. [[CrossRef](#)]
10. Jin, X.-W.; Lu, L.; Mi, S.-B.; Liu, M.; Jia, C.-L. Phase stability and B-site ordering in La_2NiMnO_6 thin films. *Appl. Phys. Lett.* **2016**, *109*, 031904. [[CrossRef](#)]
11. Bernal-Salamanca, M.; Konstantinovic, Z.; Balcells, L.; Pannunzio-Miner, E.; Sandiumenge, F.; Lopez, L.; Bozzo, B.; Herrero-Martin, J.; Pomar, A.; Frontera, C.; et al. Nonstoichiometry driven ferromagnetism in double perovskite $La_2Ni_{1-x}Mn_{1+x}O_6$ insulating thin films. *Cryst. Growth Des.* **2019**, *19*, 2765–2771. [[CrossRef](#)]
12. Blasco, J.; Sanches, M.C.; Perez-Cacho, J.; Garcia, J.; Subias, J.; Campo, J. Synthesis and structural study of $LaNi_{1-x}Mn_xO_{3+\delta}$ perovskites. *J. Phys. Chem. Solids* **2002**, *63*, 781–792. [[CrossRef](#)]
13. Yang, D.; Wang, W.; Yang, T.; Lampronti, G.I.; Ye, H.; Wu, L.; Yu, Q.; Lu, S. Role of spontaneous strains on the biphasic nature of partial B-site disorder double perovskite La_2NiMnO_6 . *APL Mater.* **2018**, *6*, 066102. [[CrossRef](#)]
14. Zhang, Z.; Jian, H.; Tang, X.; Dai, J.; Zhu, X.; Sun, Y. Structural, magnetic and dielectric properties of La_2NiMnO_6 thin film by chemical solution deposition method. *J. Sol-Gel Sci. Technol.* **2012**, *61*, 224. [[CrossRef](#)]
15. Sayed, F.N.; Achary, S.N.; Jayakumar, O.D.; Deshpande, S.K.; Krishna, P.S.R.; Chatterjee, S.; Ayyub, P.; Tyagi, A.K. Role of annealing conditions on the ferromagnetic and dielectric properties of La_2NiMnO_6 . *J. Mater. Res.* **2011**, *26*, 567–577. [[CrossRef](#)]
16. Kim, M.K.; Moon, J.Y.; Choi, H.Y.; Oh, S.H.; Lee, N.; Choi, Y.J. Effects of different annealing atmospheres on magnetic properties in La_2CoMnO_6 single crystals. *Curr. Appl. Phys.* **2015**, *15*, 776–779. [[CrossRef](#)]
17. Nasir, M.; Khan, M.; Kumar, S.; Bhatt, S.; Patra, N.; Bhattacharya, D.; Jha, S.N.; Biring, S.; Sen, S. The effect of high temperature annealing on the antisite defects in ferromagnetic La_2NiMnO_6 double perovskite. *J. Magn. Magn. Mat.* **2019**, *483*, 114–123. [[CrossRef](#)]
18. Spurgeon, S.R.; Du, Y.; Droubay, T.; Devaraj, A.; Sang, X.; Longo, P.; Yan, P.; Kotula, P.G.; Shutthanandan, V.; Mark, E.; et al. Competing Pathways for Nucleation of the Double Perovskite Structure in the Epitaxial Synthesis of La_2MnNiO_6 . *Chem. Mater.* **2016**, *28*, 3814–3822. [[CrossRef](#)]
19. Spurgeon, S.R.; Sushko, P.V.; Devaraj, A.; Du, Y.; Droubay, T.; Chambers, S.A. Onset of phase separation in the double perovskite oxide La_2MnNiO_6 . *Phys. Rev. B* **2018**, *97*, 134110. [[CrossRef](#)]
20. Detemple, E.; Ramasse, Q.M.; Sigle, W.; Cristiani, G.; Habermeier, H.-U.; Benckiser, E.; Boris, V.; Frano, A.; Wochner, P.; Wu, M.; et al. Polarity-driven nickel oxide precipitation in $LaNiO_3$ -LSaAlO₃ superlattices. *Appl. Phys. Lett.* **2011**, *99*, 211903. [[CrossRef](#)]
21. Pomar, A.; Konstantinovic, Z.; Bagués, N.; Roqueta, J.; López-Mir, L.; Balcells, L.; Frontera, C.; Mestres, N.; Gutiérrez-Llorente, A.; Šćepanovic, M.; et al. Formation of Self-Organized Mn_3O_4 Nanoinclusions in $LaMnO_3$ Films. *Front. Phys.* **2016**, *4*, 41. [[CrossRef](#)]
22. Iwahori, K.; Watanabe, S.; Kawaia, M.; Mizuno, K.; Sasaki, K.; Yoshimoto, M. Nanoscale composition analysis of atomically flat $SrTiO_3$ (001) by friction force microscopy. *J. Appl. Phys.* **2000**, *88*, 7099–7103. [[CrossRef](#)]
23. Guo, H.Z.; Burgess, J.; Ada, E.; Street, S.; Gupta, A.; Iliev, M.N.; Kellock, A.J.; Magen, C.; Varela, M.; Pennycook, S.J. Influence of defects on structural and magnetic properties of multifunctional La_2NiMnO_6 thin films. *Phys. Rev. B* **2008**, *77*, 174423. [[CrossRef](#)]
24. Bull, C.L.; Gleeson, D.; Knight, K.S. Determination of B-site ordering and structural transformations in the mixed transition metal perovskites La_2CoMnO_6 and La_2NiMnO_6 . *J. Phys.* **2003**, *15*, 4927–4936.
25. Prellier, W.; Rajeswari, M.; Venkatesan, T.; Greene, R.L. Effects of annealing and strain on $La_{1-x}Ca_xMnO_3$ thin films: A phase diagram in the ferromagnetic region. *Appl. Phys. Lett.* **1999**, *75*, 1446. [[CrossRef](#)]
26. Coey, J.M.D.; Viret, M. and von Molnar, S. Mixed-valence manganites. *Adv. Phys.* **1999**, *48*, 167. [[CrossRef](#)]
27. Konstantinovic, Z.; Santiso, J.; Balcells, L.; Martinez, B. Driven self-assembled network of antidots in complex oxide thin films. *Small* **2009**, *5*, 265–271. [[CrossRef](#)]

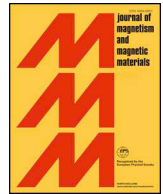
28. Orayech, B.; Urcelay-Olabarria, I.; Lopez, G.A.; Fabelo, O.; Faik, A.; Igartua, J.M. Synthesis, structural, magnetic and phase transition studies of the ferromagnetic $\text{La}_2\text{CoMnO}_6$ double perovskite by symmetry-adapted modes. *Dalton Trans.* **2015**, *44*, 13867. [[CrossRef](#)] [[PubMed](#)]
29. Wu, S.-Q.; Cheng, S.; Lu, L.; Liu, M.; Jin, X.-W.; Cheng, S.-D.; Mi, S.-B. B-site ordering and strain-induced phase transition in double perovskite $\text{La}_2\text{NiMnO}_6$ films. *Sci. Rep.* **2018**, *8*, 2516. [[CrossRef](#)] [[PubMed](#)]
30. Schneider, C.A.; Rasband, W.S.; Eliceiri, K.W. NIH Image to Image J: 25 years of image analysis. *Nat. Methods* **2012**, *9*, 671–675. [[CrossRef](#)]



ELSEVIER

Contents lists available at ScienceDirect

Journal of Magnetism and Magnetic Materials

journal homepage: www.elsevier.com/locate/jmmmSelf-assembled line network in BiFeO₃ thin filmsB. Colson^a, V. Fuentes^a, Z. Konstantinović^{b,*}, D. Colson^c, A. Forget^c, N. Lazarević^b, M. Šćepanović^b, Z.V. Popović^b, C. Frontera^a, Ll. Balcells^a, B. Martínez^a, A. Pomar^a^a Institut de Ciència de Materials de Barcelona, ICMA-B-CSIC, Campus UAB, 08193 Bellaterra, Spain^b Center for Solid State Physics and New Materials, Institute of Physics Belgrade, Pregrevica 118, University of Belgrade, Serbia^c SPEC, CEA, CNRS UMR 3680, Université Paris-Saclay, 91191 Gif sur Yvette Cedex, France

ARTICLE INFO

Keywords:

Multiferroic thin films
 Long-range ordered nanostructures
 Growth kinetic
 Mixed phase nanodomains

ABSTRACT

In this work we report on the controlled fabrication of a self-assembled line network in highly epitaxial BiFeO₃ thin films on top of LaAlO₃ in the kinetically limited grown region by RF sputtering. As previously shown in the case of manganite thin films, the remarkable degree of ordering is achieved using vicinal substrates with well-defined step-terrace morphology. Nanostructured BiFeO₃ thin films show mixed-phase morphology. Besides typical formation following (100) and (010) axes, some mixed phase nanodomains are detected also in-between the regular line network. These particular microstructures open a playground for future applications in multi-ferroic nanomaterials.

1. Introduction

Bismuth ferrite BiFeO₃ (BFO) is a very active research domain due to environment friendly room-temperature multiferroic character with wide range of potential applications, from the low-power spintronic to optical devices [1,2]. The very large electrical polarization [3,4], coupling between the polarization and magnetic easy plane [5–7] and its strong sensitivity on the epitaxial strain are crucial parameters for applications and for understanding their fundamental properties in general [8,9]. The control over the ferroelectric polarization through the structural strain and the miscut angle of underlying substrates rapidly gain interest [10], additionally enhanced with the discovery of mixed phase nanodomains [9,11–13]. In addition, it has been recently shown that the kinetic growth conditions allow synthesizing high quality films with selective ferroelectric domains [14].

Self-organization of long-range ordered nanostructures of transition metal oxide thin films is of major relevance for both, the study of enhanced or novel physical properties at the nanoscale (from enhanced magneto-resistive properties to unexpected interfacial effects) and for developing a new generation of devices [15,16]. This bottom-up nanostructural approach presents an alternative to the more conventional top-down lithography-based methods with numerous advantages ranging from rapid preparation of low-cost and large surface oxide nanotemplates to the formation of nanoobjects with size and densities beyond actual possibilities [17]. Finally, ferroelectric BFO thin films crystallize in the very similar rhombohedral structure as previously

studied LSMO thin films [15,17] and open a huge playground for the formation of nanostructured networks at the surface.

In this paper, we report on the formation of regular nanostructures in ferroelectric BFO thin films grown on top of LaAlO₃ (LAO) substrates by RF sputtering. The nanostructuring of BFO thin films is directly induced by structural and morphological features of the underlying substrate (lattice parameter inducing strain conditions on the one side and step-terrace morphology and chemical affinity on the other side). In addition to regular network, stripe-like features are detected and analyzed by X-ray, Raman and AFM spectroscopy.

2. Experimental

BFO thin films were grown by RF magnetron sputtering on top of LaAlO₃ (0 0 1) substrates under an oxygen partial pressure of 0.19 Pa using commercial stoichiometric target (Kurt J. Lesker Company). Growth conditions (growth rate of F ~ 0.03 ML/s and high growth temperature) were adjusted to promote self-organized surface nanostructures in the kinetic growth regime, i.e. far away from thermodynamic relaxation mechanisms, that have been previously studied in detail in GeSi semiconductors [18]. By a fine tuning of the growth kinetic pathway, the surface diffusion was reduced (but not completely suppressed), taking advantage of the unusual misfit strain relaxation in presence of stepped substrate [17]. Substrates were previously washed in milliQ water and thermally treated at 1000 °C to assure the presence of terrace-step morphology with unit cell height. The thickness value, *t*,

* Corresponding author.

E-mail address: zorica.konstantinovic@ipb.ac.rs (Z. Konstantinović).<https://doi.org/10.1016/j.jmmm.2020.166898>

Received 16 October 2019; Received in revised form 6 April 2020; Accepted 14 April 2020

Available online 15 April 2020

0304-8853/ © 2020 Elsevier B.V. All rights reserved.

of the different BFO/LAO films presented in this study is in the range of $40 \text{ nm} < t < 50 \text{ nm}$.

The surface morphology of the films was studied using Atomic Force Microscopy (AFM) and Scanning Electron Microscopy (SEM). AFM images were obtained in a MFP3D Asylum AFM while SEM images were obtained with a QUANTA FEI 200 FEG-ESEM. The crystal structure was characterized by X-ray diffraction (XRD) and reflectivity techniques (XRR) using a Siemens D5000 diffractometers with $K\alpha$ -Cu radiation.

Magnetic characterization was performed at room temperature (in-plane configuration H \parallel (100) and out-of-plane configuration H \perp (100)) with a superconducting quantum interference device magnetometer (Quantum Design). In order to estimate the magnetization of the film, the diamagnetic background of substrates was subtracted (estimated from negative slope of M(H) at high magnetic field, $10000 < H < 50000 \text{ Oe}$).

Raman scattering measurements were performed using a Jobin Yvon T64000 Raman system in μ -Raman configuration. A Coherent VerdiG solid state laser with 532 nm line was used as an excitation source. Laser beam focusing was accomplished by a microscope objective with $\times 50$ magnification.

3. Results and discussion

BiFeO $_3$ presents, at room temperature, a rhombohedral structure in bulk form (lattice constant $a_{\text{bulk}} = 3.964 \text{ \AA}$) [3,5]. In thin films, structural and functional properties of this multiferroic compound can be drastically modified due to presence of the structural strain induced by the selected substrate [19]. Particularly, the epitaxial growth of BFO on top of LAO substrate induces huge compressive in-plane strain, which allows stabilizing the tetragonal phase, correlated with theoretically predicted giant ferroelectric polarization [20]. In this study, the films were grown under large compressive strain of $\varepsilon = (a_{\text{LAO}} - a_{\text{BFO}}) / a_{\text{BFO}} = -4.62\%$, giving rise to a significantly larger perpendicular cell parameter compared to bulk counterpart (see below).

Fig. 1 shows the formation of the long range ordered line network on top of the BFO surface during crystal growth. Fast Fourier Transform (FFT) (Fig. 1(b)) of topographic AFM image (Fig. 1(a)) indicate long-range order of grooves along one specific direction (see two high intensity dots in circles) with a separation around $1/k_{\perp} \sim 150 \text{ nm}$. Two

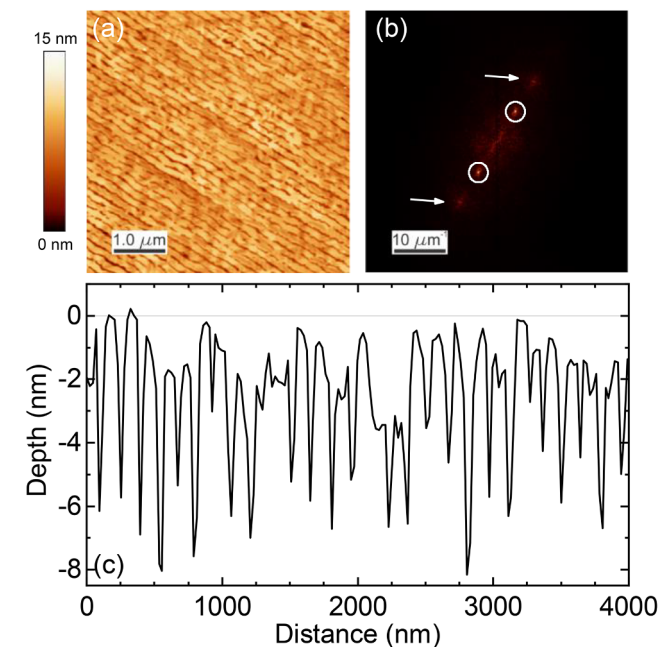


Fig. 1. (a) Topographic AFM image ($4 \times 4 \mu\text{m}^2$) of BiFeO $_3$ film (thickness, $t = 45 \text{ nm}$) grown on top of LAO and (b) corresponding Fast Fourier Transform (c) Typical line profile of regular grooves.

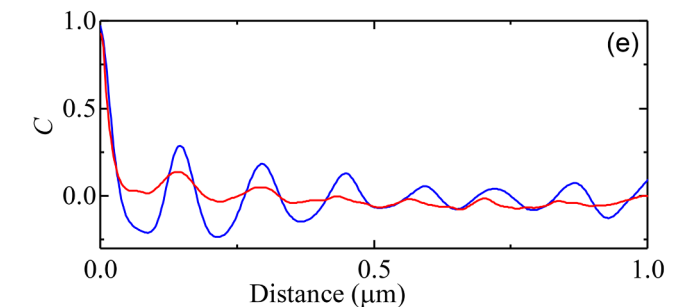
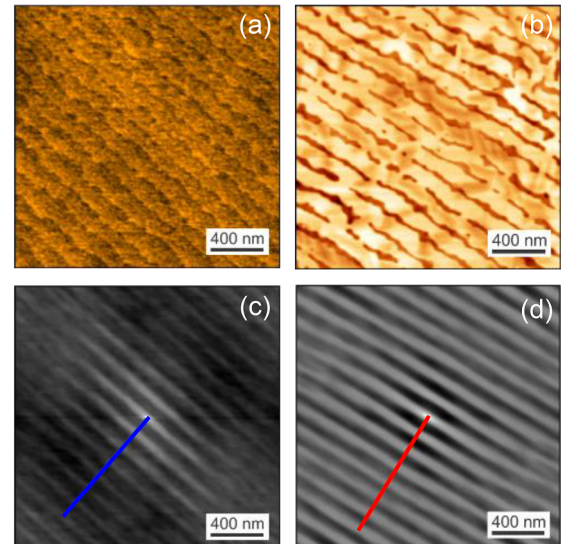


Fig. 2. (a) Topographic AFM images ($2 \times 2 \mu\text{m}^2$) of (a) LaAlO $_3$ substrates ($\alpha \sim 0.155^\circ$) and (b) BiFeO $_3$ film (thickness, $t = 45 \text{ nm}$) grown on top of it. The corresponding height-height correlation functions of the topographic surfaces are shown in (c) and (d) respectively. (e) Corresponding profile lines of LAO (blue) and of BFO (red).

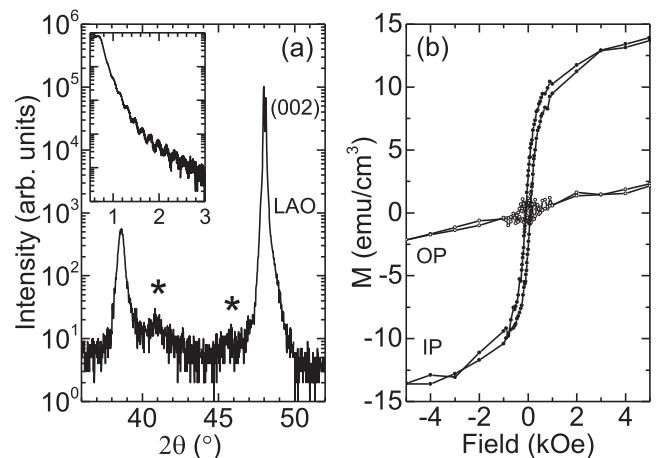


Fig. 3. (a) θ - 2θ XRD scans of the (0 0 2) reflections for BFO/LAO thin film. In the inset, corresponding XRR data with thickness values of 45 nm. (b) Magnetization versus field corrected with the diamagnetic slope for the in-plane (IP) and out-of-plane field (OP) at room temperature.

additional dots (see arrows) are also visible (doubled distance in k space) in possible correlation with the formation of the polarization nano-domains (see below). The regular lines, i.e. grooves have typical depth of around $6 \pm 2 \text{ nm}$ (Fig. 1(c)).

In order to further clarify the structural arrangement of the regular lines the topography of BFO thin films (Fig. 2(b)) is compared directly

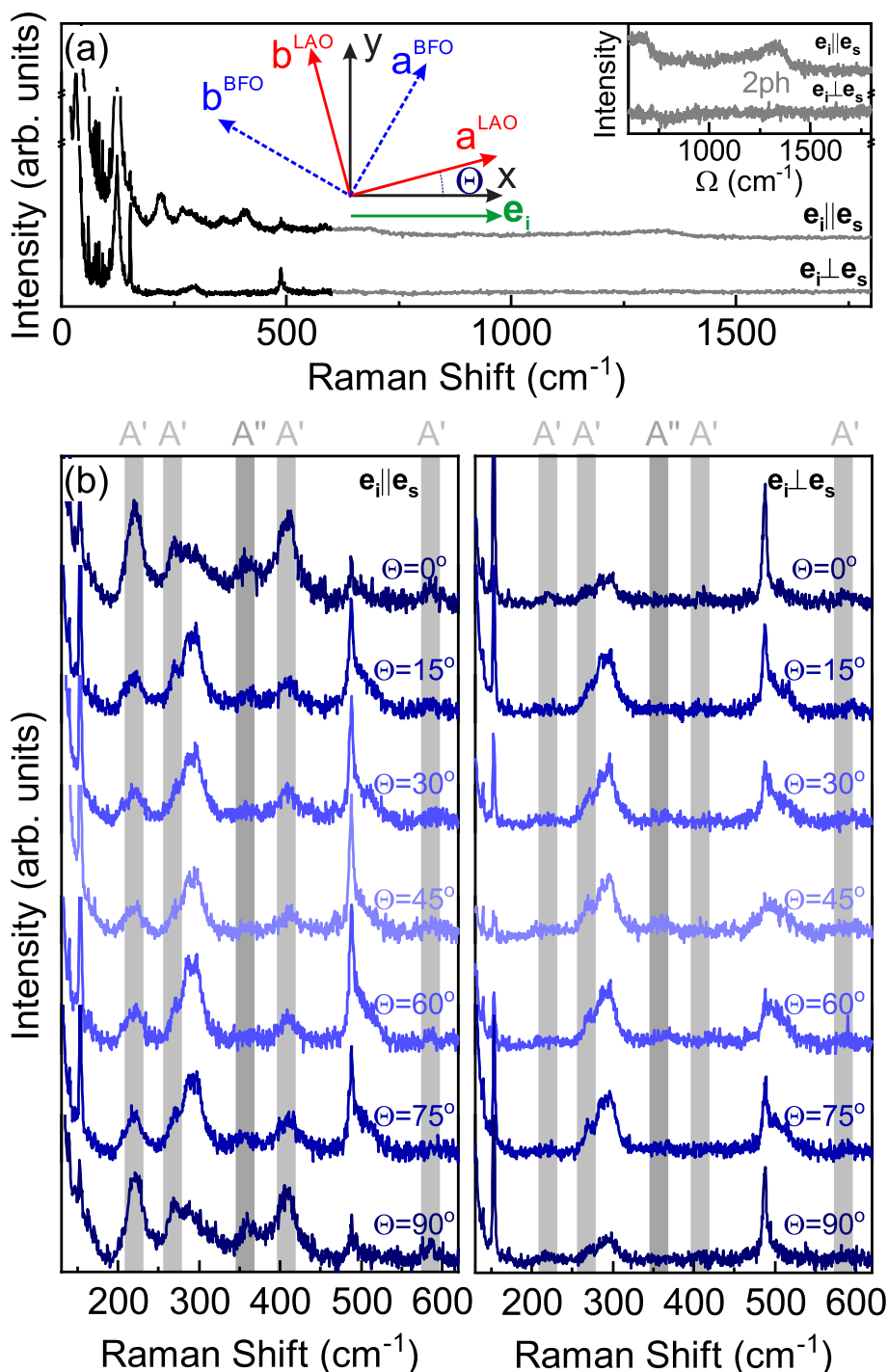


Fig. 4. (a) Raman spectra measured in parallel and cross polarization configurations for $\Theta = 0$. xy is the laboratory system at room temperature. Black and grey lines represent spectra obtained with binning 1 and 2 respectively. Inset: High energy region of the BFO/LAO Raman spectra. (b) BFO/LAO Raman spectra measured in parallel and cross polarization configurations for various sample orientations.

with the topography of the underlying LAO substrate (Fig. 2(a)). The corresponding height-height autocorrelation functions are shown in Fig. 2(c) for LAO and (d) for BFO topography. The regular line pattern is visible at the overall surface in both cases, also as non-vanishing oscillations in the corresponding profile perpendicular to lines. A clear correlation between the two patterns is evident from the corresponding profile lines in Fig. 2(e), demonstrating a typical separation between ordered nanostructured lines of $l \sim 140$ nm, in agreement with the underlying terrace-step morphology of the LAO substrate with a miscut angle of $\alpha \sim 0.155^\circ$.

The structural properties have been investigated by θ -2 θ X-ray diffraction (XRD), Fig. 3(a) shows scans around (0 0 2) LAO reflection. The strongest peak in Fig. 3(a) corresponds to the LAO substrate ($2\theta = 48.05^\circ$ with lattice parameter of $c = 3.787 \text{ \AA}$). Besides this, a dominant peak ($2\theta = 38.62^\circ$) and two small intensity peaks are also detected ($2\theta = 40.87^\circ$ and $2\theta = 45.74^\circ$, see stars in Fig. 3(a)). Dominant peak corresponds to an out-of-plane parameter of $c_{\text{perp}} = 4.66(2) \text{ \AA}$, much larger than the pseudocubic cell parameter of bulk BFO and it is associated with hyper strained tetragonal phase.

The position of the two small peaks suggests the presence of two

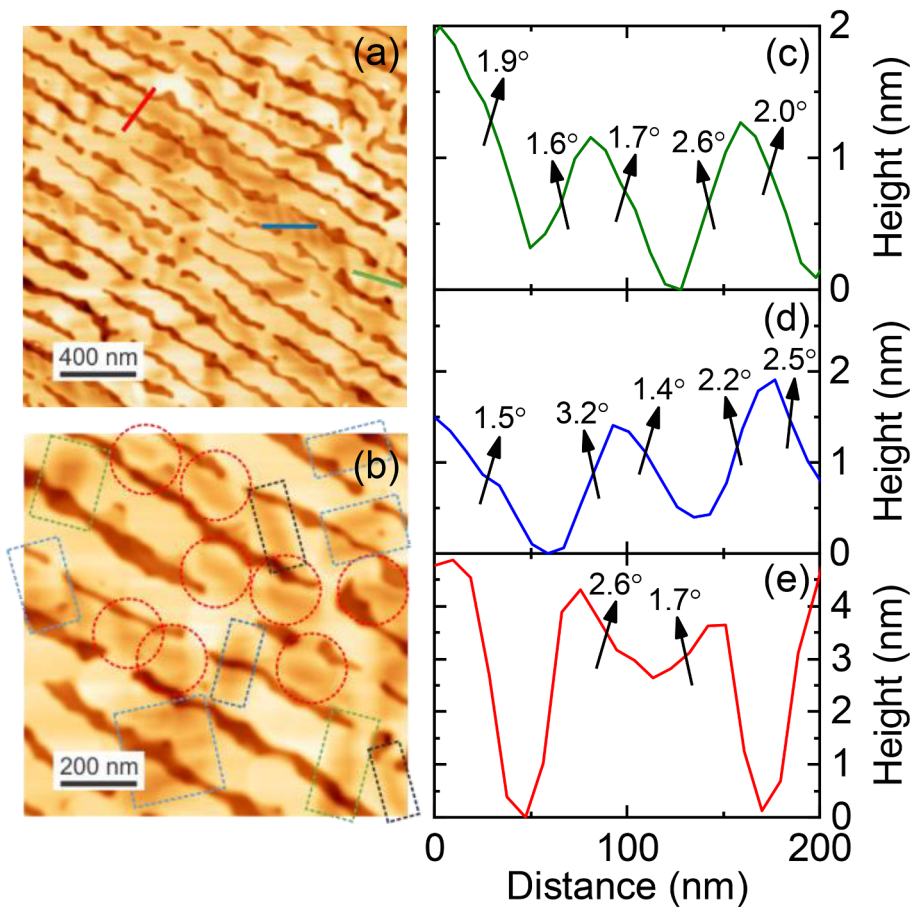


Fig. 5. The formation of nanodomains in the presence of regular line network. (a) AFM topography ($2 \times 2 \mu\text{m}^2$) with profile lines. (b) Small area AFM topography ($1 \times 1 \mu\text{m}^2$) with different orientation of detected nanodomains (expected orientation in blue and green rectangles and new nanodomains induced by line network in red circles). (c)-(e) Profile lines of nanodomains from (a).

additional phases with out-of-plane parameters in the order of $c_{\text{perp1}} = 4.41(6) \text{ \AA}$ and $c_{\text{perp2}} = 3.96(7) \text{ \AA}$, which are ascribed to the intermediate monoclinic structure and the rhombohedral phase respectively. While the intermediate monoclinic phase is associated to the formation of nanodomains [9,12] the rhombohedral phase is the residue of the bulk counterpart phase [3]. Thickness value of the BFO/LAO film ($t \sim 45 \text{ nm}$) is determined from XRR curve (inset of Fig. 3(a)). No magnetic impurity phases are detected, in agreement with the weak ferromagnetic moment measured at room-temperature (Fig. 3(b)).

Raman spectra of BFO film with ordered connected pits morphology are shown in Fig. 4. Due to the fact that the film thickness is much smaller than the penetration depth of the beam, significant contribution from the LAO substrate is clearly observable in the BFO/LAO Raman spectra (Fig. 4(a)). For the purpose of probing the crystal structure of the BFO film, Raman spectra were collected for different sample orientation (as presented in Fig. 4) in two polarization configurations.

Detailed analysis of the Raman intensity angular dependence [21] taking into account the twinning effects, indicates that Raman features observed at about 227, 273, 417 and 587 cm^{-1} correspond to the A' symmetry modes, whereas peak at 368 cm^{-1} correspond to A'' symmetry mode of the monoclinic Cc crystal structure. These findings are in accordance with the density-functional calculations predicting that BFO structure under strain values higher than 4% become tetragonal-like with larger c/a ratio [22]. According to the first principles calculations, this structure has Cc symmetry with the base centered unit cell containing four formula units, for which the factor group analysis predicts the existence of $13A' + 14A''$ Raman-active phonon modes [22]. Note that, a large number of modes ascribed to the Cc structure have been experimentally observed in the low-temperature Raman spectra of BiFeO_3 films commensurately grown on LaAlO_3 substrates and subjected to $\sim 4.4\%$ compressive strain, wherein it was indicated that 13

most intense modes (including those at 237, 282, 415, and 605 cm^{-1}) could be referred to the A' symmetry [23]. However, Himcinschi et al. [23] suggested that the modes at 225, 263 and 367 cm^{-1} in the Raman spectrum of highly strained BiFeO_3 epitaxial films deposited on LaAlO_3 may correspond to A'' symmetry mode of the Cc monoclinic structure [23]. Therefore, there is no doubt that BFO/LAO film whose Raman spectra are shown in Fig. 4 has Cc structure, but small differences in the positions of the identified modes in comparison with those referred in the literature [23] indicate that the structure of the film investigated here is monoclinically distorted in a specific way.

More details of the formation of the mixed-phase structures in the middle of the regular network line can be obtained from AFM topography shown in Fig. 5. The thin strip-line patterns could be visualized in Fig. 5(a), known in literature as asymmetric “saw-tooth” surface structure and identified as intimated mixture between highly distorted monoclinic phase (monoclinic version of highly tetragonal phase with $c/a = 1.23$), detected by Raman scattering in Fig. 4 and an intermediate monoclinic phase ($c/a = 1.17$), detected as small peak by XRD in Fig. 3(a). The profile line of these strip-like patterns can be found in Fig. 5(c)-(e). Typical strip-like patterns, disoriented around $\sim 1^\circ$ from the in-plane (100) and (010) axes, could be seen in green and blue squares in Fig. 5(b). Corresponding AFM profile line indicate that they are tilted away from the surface normal for about $2.5\text{--}3^\circ$ (intermediate monoclinic phase) and $1.5\text{--}2^\circ$ (highly distorted monoclinic phase), in agreement with previous reports [9,12]. The typical height difference between different phases (around 3 nm) [9,24] is not always observed, as strongly perturbed with formation of regular grooved (for more details see Fig. S1 in supplementary material). In addition, the stripe-like formation could be observed also in our case between regular line-network and disoriented around $\sim 15^\circ$ from the in-plane (100) axes (red circles in Fig. 5(b)) with very similar profile line (Fig. 5(e)).

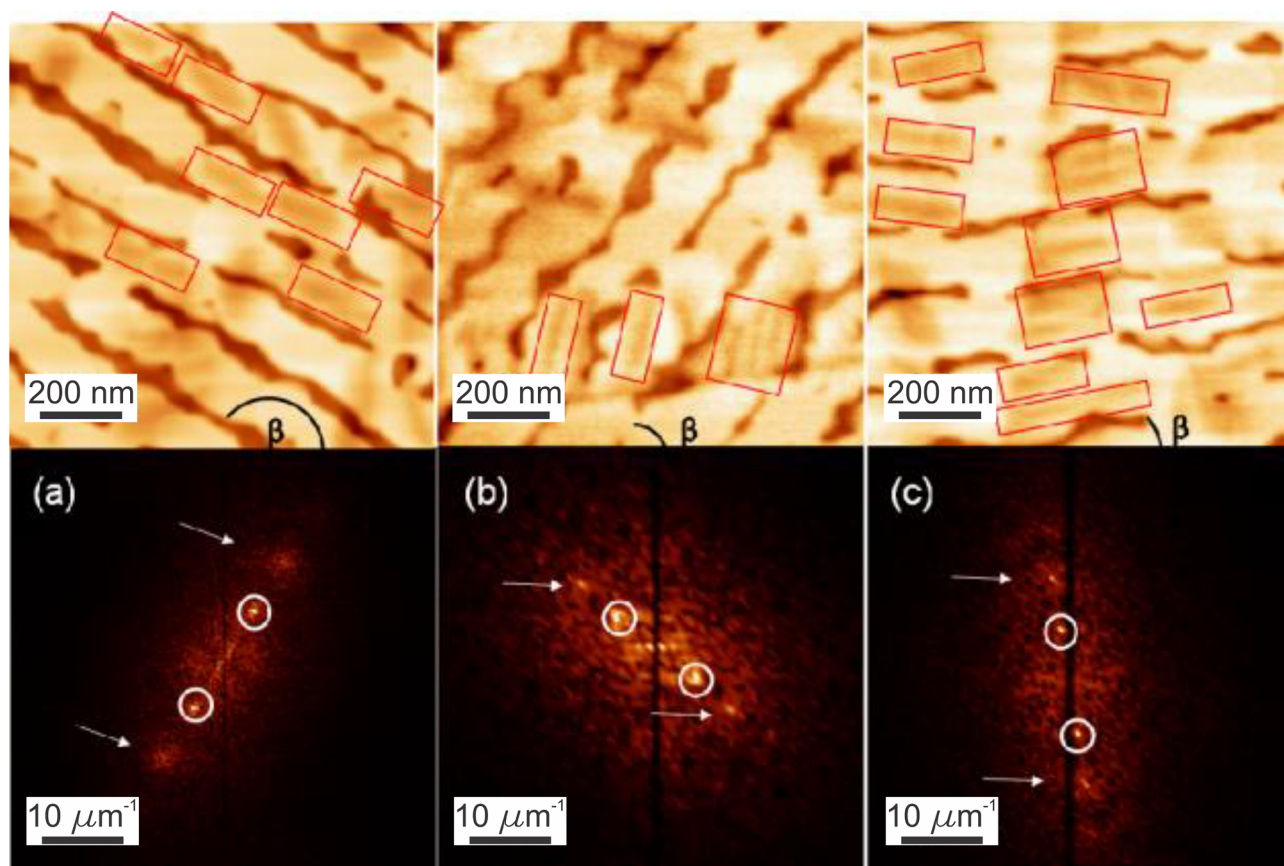


Fig. 6. AFM of BFO films grown on the top of LAO with similar miscut angle ($0.12^\circ < \alpha < 0.16^\circ$) with different orientation of nanostructured lines respected to $[1\ 0\ 0]$ direction (a) $\beta \sim 150^\circ$, (b) 52° and (c) 6° . The corresponding FFT images are given below.

Finally, the formation of the mixed-phase structures in the middle of the regular network is followed for different network orientations respected to $[100]$ direction. In Fig. 6, AFM topography with corresponding Fast Fourier Transform is shown for BFO thin films grown on LAO with similar terrace width but with different orientation respected to substrate edges ($6^\circ < \beta < 150^\circ$). FFT of topographic images indicate the long-range order coming from formation of groove network (two high intensity dots in circles in all cases). In addition, as mentioned before, two additional points (see arrows) are visible at doubled distance in k space, suggesting the presence of additional structures in-between the regular line network. In all cases, the presence of “saw-tooth” surface structures in between the grooves could be identified in the corresponding AFM topography (see red rectangles and Fig. S1 in supplementary). Noticeably, in the case of network line slightly disoriented from the in-plane (100) axes ($\beta \sim 6^\circ$), the nanodomains form more easily in-between the grooves (see Fig. 6(c)) as it is closer to their spontaneous configuration [9,12,24].

4. Conclusion

In summary, a regular nanostructured network is grown on the surface of BFO films, in close correlation with the step-terraces morphology of the underlying LAO substrate (miscut angle $0.12^\circ < \alpha < 0.16^\circ$). Raman scattering detected the dominant contribution from the monoclinic version of highly strained tetragonal phase. XRD spectra also indicate the presence of additional polymorphs, rhombohedral and intermediate monoclinic phases. The stripe-like patterns, formed by intimate mixture between two monoclinic polymorphs, are visualized by AFM topography. Beside typical formation following (100) and (010) axes, some stripe-like patterns are also detected in-between the regular line network. Finally, the observed self-nanostructuring of the BFO surface

opens a playground for tailoring structural polymorphs with strong potential interest for future applications in multiferroic nanomaterials.

5. Author statement

B. Colson: thin film preparation and characterization, Z. Konstantinović: design and leading the research, manuscript preparation, D. Colson, A. Forget: ferroelectric properties, N. Lazarević, M. Šćepanović, Z. V. Popović: Raman measurements, V. Fuentes, C. Frontera: X-ray diffraction characterization, D. Colson, Ll. Balcells, B. Martinez, A. Pomar: Reviewing and editing manuscript.

Declaration of Competing Interest

The authors declare that they have no known competing financial interests or personal relationships that could have appeared to influence the work reported in this paper.

Acknowledgements

This work has received funding from the European Union’s Horizon 2020 research and innovation under the Marie Skłodowska-Curie grant agreement No. 645658 (DAFNEOX Project). A.P., V. F. and Z.K. thank Sensor-INFIZ (Serbia) for the cooperation provided during their respective secondments. E. P.-M. acknowledge financial support from the Spanish Ministry of Economy and Competitiveness through the “Severo Ochoa” Programme for Centres of Excellence in R&D (SEV-2015- 0496), and project MAT2015-71664 and SPINCURIOX (RTI2018-099960-B-I00). N. L., M. S., Z. K. and Z.V.P. acknowledge the support of the Serbian Ministry of Education, Science and Technological Development (Projects No III45018).

Appendix A. Supplementary data

Supplementary data to this article can be found online at <https://doi.org/10.1016/j.jmmm.2020.166898>.

References

- [1] G. Catalan, J.F. Scott, Physics and applications of bismuth ferrite, *Adv. Mater.* 21 (2009) 2463.
- [2] D. Sando, A. Barthelemy, M. Bibes, BiFeO₃ epitaxial thin films and devices: past, present and future, *J. Phys.: Condens. Matter* 26 (2014) 473201.
- [3] D. Lebeugle, D. Colson, A. Forget, M. Viret, P. Bonville, J.F. Marucco, S. Fusil, Room temperature coexistence of large electric polarization and magnetic order in BiFeO₃ single crystals, *Phys. Rev. B* 76 (2007) 024116.
- [4] D. Lebeugle, D. Colson, A. Forget, M. Viret, Very large spontaneous electric polarization in BiFeO₃ single crystals at room temperature and its evolution under cycling fields, *Appl. Phys. Lett.* 91 (2007) 022907.
- [5] D. Lebeugle, D. Colson, A. Forget, M. Viret, A.M. Bataille, A. Gukasov, Electric Field-Induced Spin Flop in BiFeO₃ single crystals at room temperature, *Phys. Rev. Lett.* 100 (2008) 227602.
- [6] T. Zhao, A. Scholl, F. Zavaliche, K. Lee, M. Barry, A. Doran, M.P. Cruz, Y.H. Chu, C. Ederer, N.A. Spaldin, R.R. Das, D.M. Kim, S.H. Baek, C.B. Eom, R. Ramesh, Electrical control of antiferromagnetic domains in multiferroic BiFeO₃ films at room temperature, *Nature Mater.* 5 (2006) 823.
- [7] S. Lee, W. Ratcliff, S.W. Cheong, V. Kiryukhin, Electric field control of the magnetic state in BiFeO₃ single crystals, *Appl. Phys. Lett.* 92 (2006) 192906.
- [8] C. Ederer, N.A. Spaldin, Effect of epitaxial strain on the spontaneous polarization of thin film ferroelectrics, *Phys. Rev. Lett.* 95 (2005) 257601.
- [9] A.R. Damodaran, J.C. Agar, S. Pandya, Z. Chen, L. Dedon, R. Xu, B. Apgar, S. Saremi, L.W. Martin, New modalities of strain-control of ferroelectric thin films, *J. Phys.: Condens. Matter* 28 (2016) 263001.
- [10] Y.-H. Chu, M.P. Cruz, C.-H. Yang, L.W. Martin, P.-L. Yang, J.-X. Zhang, K. Lee, P. Yu, L.-Q. Chen, R. Ramesh, Domain control in multiferroic BiFeO₃ through substrate vicinality, *Adv. Mater.* 19 (2007) 2662.
- [11] J.X. Zhang, Q. He, M. Trassin, W. Luo, D. Yi, M.D. Rossell, P. Yu, L. You, C.H. Wang, C.Y. Kuo, J.T. Heron, Z. Hu, R.J. Zeches, H.J. Lin, A. Tanaka, C.T. Chen, L.H. Tjeng, Y.-H. Chu, R. Ramesh, Microscopic origin of the giant ferroelectric polarization in tetragonal-like BiFeO₃, *Phys. Rev. Lett.* 107 (2011) 147602.
- [12] L. You, Z. Chen, X. Zou, H. Ding, W. Chen, L. Chen, G. Yuan, J. Wang, Characterization and manipulation of mixed phase nanodomains in highly strained BiFeO₃ thin films, *ACS Nano* 6 (2012) 5388.
- [13] A. Kumar, S. Denev, R.J. Zeches, E. Vlahos, N.J. Podraza, A. Melville, D.G. Schlom, R. Ramesh, V. Gopalan, Probing mixed tetragonal/rhombohedral-like monoclinic phases in strained, bismuth ferrite films by optical second harmonic generation, *Appl. Phys. Lett.* 97 (2010) 112903; J. Seidel, M. Trassin, Y. Zhang, P. Maksymovych, T. Uhlig, P. Milde, D. Köhler, A.P. Baddorf, S.V. Kalinin, L.M. Eng, X. Pan, R. Ramesh, Electronic properties of isosymmetric phase boundaries in highly strained Ca-doped BiFeO₃, *Adv. Mater.* 26 (2014) 4376.
- [14] A. Solmaz, M. Huijben, G. Koster, R. Egoavil, N. Gauquelin, G. Van Tendeloo, J. Verbeeck, B. Noheda, G. Rijnders, Domain selectivity in BiFeO₃ thin films by modified substrate termination, *Adv. Funct. Mater.* 26 (2016) 2882.
- [15] Z. Konstantinovic, J. Santiso, Ll. Balcells, B. Martinez, Strain-driven self-assembled network of antidots in complex oxide thin films, *Small* 5 (2009) 265.
- [16] Y. Zhao, Z. Yin, X. Zhang, Z. Fu, J. Wu, Formation and local conduction of nanospots in BiFeO₃ epitaxial films, *J. Mater. Chem. C* 3 (2015) 11250.
- [17] Z. Konstantinovic, F. Sandiumenge, J. Santiso, Ll. Balcells, B. Martinez, Self-assembled pit arrays as templates for the integration of Au nanocrystals in oxide surfaces, *Nanoscale* 5 (2013) 1001.
- [18] J.L. Grey, R. Hull, C.-H. Lam, P. Sutter, J. Means, J.A. Floro, Beyond the hetero-epitaxial quantum dot: self-assembling complex nanostructures controlled by strain and growth kinetics, *Phys. Rev. B* 72 (2005) 155323.
- [19] H. Bea, B. Dupe, S. Fusil, R. Mattana, E. Jacquet, B. Warot-Fonrose, F. Wilhelm, A. Rogalev, S. Petit, V. Cros, A. Anane, F. Petroff, K. Bouzehouane, G. Geneste, B. Dkhil, S. Lisenkov, I. Ponomareva, L. Bellaiche, M. Bibes, A. Barthelemy, Evidence for room-temperature multiferroicity in a compound with a giant axial ratio, *Phys. Rev. Lett.* 102 (2009) 217603.
- [20] B. Colson, «Elaboration et caractérisation de films minces de BiFeO₃ nanostructurés», DUT Mesures Physiques, IUT d'Orsay, Université Paris-Sud, 2016.
- [21] D.R. Palai, H. Schmid, J.F. Scott, R.S. Katiyar, Raman spectroscopy of single-domain multiferroic BiFeO₃, *Phys. Rev. B – Condens. Matter Mater. Phys.* 81 (2010) 064110.
- [22] J. Hatt, N.A. Spaldin, C. Ederer, Strain-induced isosymmetric phase transition in BiFeO₃, *Phys. Rev. B – Condens. Matter Mater. Phys.* 81 (2010) 054109.
- [23] C. Himcinschi, A. Bhatnagar, A. Talkenberger, M. Barchuk, D.R.T. Zahn, D. Rafaja, J. Kortus, M. Alexe, Optical properties of epitaxial BiFeO₃ thin films grown on LaAlO₃, *Appl. Phys. Lett.* 106 (2015) 012908.
- [24] R.J. Zeches, M.D. Rossell, J.X. Zhang, A.J. Hatt, Q. He, C.-H. Yang, A. Kumar, C.H. Wang, A. Melville, C. Adamo, G. Sheng, Y.-H. Chu, J.F. Ihlefeld, R. Erni, C. Ederer, V. Gopalan, L.Q. Chen, D.G. Schlom, N.A. Spaldin, L.W. Martin, R. Ramesh, A strain-driven morphotropic phase boundary in BiFeO₃, *Science* 326 (2009) 977.



Research articles

Resistive switching in Strontium iridate based thin films

Víctor Fuentes^a, Borislav Vasić^b, Zorica Konstantinović^b, Benjamín Martínez^a, Lluís Balcells^a, Alberto Pomar^{a,*}

^a Institut de Ciència de Materials de Barcelona, ICMA-B-CSIC, Campus de la UAB Bellaterra 08193, Spain

^b Center for Solid State Physics and New Materials, Institute of Physics Belgrade, University of Belgrade, Pregrevica 118, 11080 Belgrade, Serbia



ARTICLE INFO

Keywords:

Resistive switching
Metal-insulator transition
SrIrO₃
Sr₂IrO₄
Conductive atomic force microscopy
Iridate thin films

ABSTRACT

We report on the local electrical properties, measured by conductive atomic force microscopy, of the Iridate-based Sr_{n+1}Ir_nO_{3n+1} family of thin films, in particular by comparing the n = 1, Sr₂IrO₄, and the n = ∞, SrIrO₃, phases. We analyze the different resistive switching behavior as a function of the pristine electronic properties of the films. We will show that, for films exhibiting insulating behavior, i.e., films of the n = 1 phase or films below 3 nm of thickness for the n = ∞ phase, hysteretic I–V curves with a sharp transition into a low resistance state (LRS), i.e. an abrupt increase of the current intensity, is detected above a well-defined threshold voltage. This suggests a resistive switching behavior associated to the jump between two resistance states that may be correlated to the activation energy, Δ, obtained by fitting the temperature dependence of the resistivity to a thermal activated Arrhenius law, ρ(T) ∼ ρ₀exp(−Δ/k_BT). On the other hand, thicker samples of the n = ∞ phase exhibit a semimetallic character and I–V curves show progressive changes of the local resistance without a clearly defined threshold voltage. Kelvin Probe Force Microscopy based measurements confirmed that, concomitantly to the resistive switching, an evolution of the electronic states at the surface takes place that may be associated to the migration of oxygen vacancies promoted by the electrical fields under the AFM tip.

1. Introduction

Reversible resistive switching (RS), i.e., the change of resistance in a reversible manner between two stable states of well-defined resistance by applying voltages pulses, is considered as one of the most promising solutions for the development of non-volatile memory devices [1,2]. A large variety of materials are known to exhibit RS behavior, including transition metal oxides (TMOs) [3,4]. Although several physical mechanisms have been invoked to account for the observed RS behavior [5–9], modifications of the doping rate by valence change due to the migration of oxygen vacancies is the most common case for TMOs. A broad interest is devoted to RS behavior where the active material is a Mott insulator or a correlated system as the occurrence of a metal-to-insulator transition (MIT) allows generating well defined low and high resistance states [2,5,10–12]. Moreover, various types of MIT may appear in response to variety of external stimuli, such as temperature, doping rate or structural strain [13]. In the case of TMOs, the close similarity between electronic correlations and crystal field splitting energies provides different mechanism for tuning their electronic properties and thus the MIT and, as a consequence, the RS phenomena [13]. Furthermore, in TMOs based on 5d elements, as Ir, spin-orbit

coupling (SOC) reaches values of about 0.5 eV [14–16], and becomes comparable to crystal field and electronic correlations, giving place to novel physics and exotic properties [17–19]. This has been recently manifested in the Ruddlesden-Popper series of 5d Strontium Iridates (Sr_{n+1}Ir_nO_{3n+1}) where subtle structural or chemical changes may trigger different electronic states. For example, in the n = 1 phase (Sr₂IrO₄), a gap is opened at the Fermi level, leading the system into a Mott insulator state [20] while the perovskite-like n = ∞ phase (SrIrO₃) presents a semimetallic ground state [21]. Nevertheless, in this latter case, a MIT can be also triggered by tuning the compressive strain induced by the substrate or by reducing the film thickness [22–26], although recent studies indicate the coexistence of disorder effects and electronic correlations leading to either disorder driven Anderson MIT or unconventional Mott-Anderson transition [23,27].

In this work we present a study of RS behavior in Sr_{n+1}Ir_nO_{3n+1} thin films of the n = 1 phase (hereafter SIO-214) and of the n = ∞ phase (SIO-113) by means of local I–V curve measurements and current mapping, by using conductive atomic force microscopy (C-AFM). While SIO-214 films are insulating, SIO-113 films present semimetallic behavior but, for film thickness below ∼3 nm an Anderson-type MIT i.e., induced by disorder, is triggered. We will show that a sharp RS process,

* Corresponding author.

E-mail address: apomar@icmab.es (A. Pomar).

with an abrupt increase of current at a defined threshold voltage is only attained in the presence of a MIT behavior where two well-defined resistance states separated by an energy jump exist. However, differences in the threshold voltage are observed in the case of both phases due to the different energy barrier to overcome. On the other hand, for thin films in a semimetallic state, I–V curves present a smooth variation of resistance, without a clear threshold voltage. By performing Kelvin Probe Force Microscopy (KPFM), we will show that the RS behavior may be attributed to the variation of charge carriers' density, usually associated to the migration of oxygen vacancies promoted by the electric field pulses. Current maps performed with voltage values above the threshold value and of different polarity allow demonstrating the writing/erasing processes making evident the feasibility of the system for the implementation of Re-RAMs.

2. Experimental details

Sr_2IrO_4 thin films were grown by Pulsed Laser Deposition on (0 0 1) SrTiO_3 (STO) substrates. The growth was carried out in an oxygen atmosphere of 70 mTorr and at a temperature of 850 °C. For the deposition, a KrF excimer laser (248 nm of wavelength) was employed at a frequency of 1 Hz and a laser fluence of 1.25 J/cm². On the other hand, SrIrO_3 thin films were grown by rf sputtering at 900 °C in 140 mTorr oxygen atmosphere as described elsewhere [27]. In order to achieve single Ti-terminated substrates with well-defined atomic steps, all STO substrates in this work were treated before the film deposition. The treatment consisted of a 10 min bath of ultrasounds in deionized water and a post-annealing of 2 h at 1000 °C [28].

Structural properties of both SrIrO_3 and Sr_2IrO_4 thin films were evaluated by means of X-Ray diffraction. A Bruker D8-Discover diffractometer was employed to measure the Reciprocal Space Map while the High Resolution θ - 2θ scan was measured with a PANalytical X'PERT PRO MRD system. The thickness of the films was determined by X-Ray Reflectometry using a D-5000 diffractometer from Siemens.

Resistivity curves of SIO-214 and SIO-113 films were measured in a standard 4 probe configuration by using a Physical Properties Measurement System by Quantum Design. Electrical electrodes were fabricated by depositing a thin layer (~40 nm) of Pt on the surface at room temperature.

RS properties were evaluated by employing an atomic force microscopy (AFM) system in the electrical modes of conducting (C-AFM) and Kelvin Probe (KPFM). The probes used to measure in these modes were DDESP-FM-V2 from Bruker. An AFM MFP3D from Asylum was used to obtain the Current maps (in nitrogen atmosphere) and the I–V curves while an NTEGRA Prima AFM system from NT-MDT was employed to obtain the KPFM data. I–V curves were performed without current compliance. Although it is known that current limitation could prevent sample degradation [29,30], we should note that the current values attained in this work were below typical current compliances used in the literature [31–33]. The KPFM images were recorded by a standard two-pass measurement. In the first step, AFM tapping mode was employed to measure the topography of the film. Then the probe was lifted at a certain height (10–20 nm) and replicated the topography while measuring the Contact Potential Difference (CPD) between the AFM tip and the sample. To obtain the CPD at each point, an AC Voltage was applied to the conducting probe to excite it at its resonance frequency. At the same time, a second DC voltage source was applied in order to nullify the electrical interaction between the tip and the sample. The surface distribution of the CPD can be then mapped by recording the DC voltage which nullifies the electrical tip-sample interaction during scanning [34].

It has been observed that thin films of iridates, such as Sr_2IrO_4 or SrIrO_3 possess a very sensitive surface [26,27,35]. The poor surface stability turns the C-AFM measurements more challenging since high electric fields should be applied between the tip and the iridate surface to obtain the desired switching. With the aim of protecting the films and

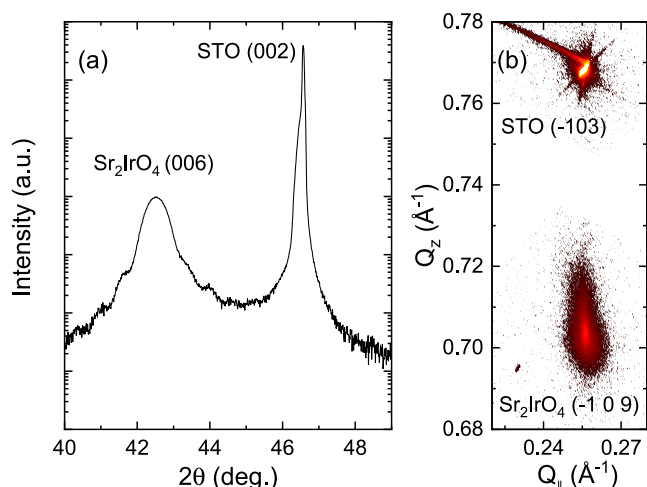


Fig. 1. X-Ray diffraction measurements of SIO-214 films on STO. (a) High-resolution θ - 2θ scan around (0 0 6) diffraction peaks. (b) Reciprocal space map of the $(-103)_{\text{STO}}$ and $(-109)_{\text{SIO}}$ peaks showing full strained state of the SIO-214 films.

stabilize the current, Pt nanoparticles were deposited *in situ* on some of the films after their growth. In the case of SIO-214 films, this deposition was performed with a laser fluence of 2.17 J/cm² with pulses at 1 Hz. Details for SIO-113 films may be found elsewhere [27].

3. Results

High resolution θ - 2θ x-ray diffraction scans in thin films of both phases confirmed epitaxial growth and high crystallinity evidenced by satellites fringes. Fig. 1(a) shows the result for a SIO-214 sample around the (0 0 6) diffraction peak. In this case, peak position leads to an out-of-plane lattice parameter of $c_{\text{SIO-214}} \sim 12.78$ Å, i.e. SIO-214 unit cell is slightly shortened with respect to the reported bulk value ($a_0 = 12.92$ Å) [36] in agreement with a small tensile strain [37]. Fig. 1(b) displays a reciprocal space map around (-109) reflection. It can be appreciated from the figure that SIO-214 film is fully strained with the underlying substrate. Similar results were obtained for SIO-113 films grown on STO with $c_{\text{SIO-113}} \sim 3.943$ Å, i.e., corresponding to compressive strain as it was previously reported [27,38].

As previously mentioned in the Introduction, in the iridate series, strength of spin-orbit coupling competes with crystal field and electronic correlations leading to a rich landscape of electrical properties. This is exemplified by the temperature dependence of electrical resistivity shown in Fig. 2(a). This Figure shows that electrical properties of SIO-113 films are clearly thickness-dependent. Robust metallic behavior is observed for the 26 nm thick film and the resistivity may be well described by the expression $\rho(T) = \rho_0 + CT^{4/5}$ in agreement with previous results [22–26,39]. However, as thickness decreases a progressive upturn of the resistivity at low temperatures is detected and the system exhibits fully insulating behavior for the 2 nm thick SIO-113 sample. The nature of the MIT induced by reducing the film thickness has been previously elucidated by analyzing the temperature dependence of the resistivity of the fully insulating 2 nm thick sample [27,40]. The low temperature regime, up to about 40–45 K, is well described by using the Mott's variable range hopping (VRH) model: $\text{Ln}\sigma \propto 1/T^{1/3}$, σ being the conductivity [41], while the high temperature range is properly described by using the Arrhenius equation for thermal activation conduction $\rho(T) = \rho_0 e^{(\Delta/k_B T)}$, Δ being an activation energy (a value of $\Delta_{123} \sim 6$ meV was obtained from the fit) and k_B the Boltzmann's constant. Fig. 2(b) shows, in typical Arrhenius plot, the quality of this fitting. Therefore, from the analysis of the $\rho(T)$ curves we can conclude that, while for thick SIO-113 films the system behaves as a three dimensional correlated metal, for the thinnest films the MIT is of

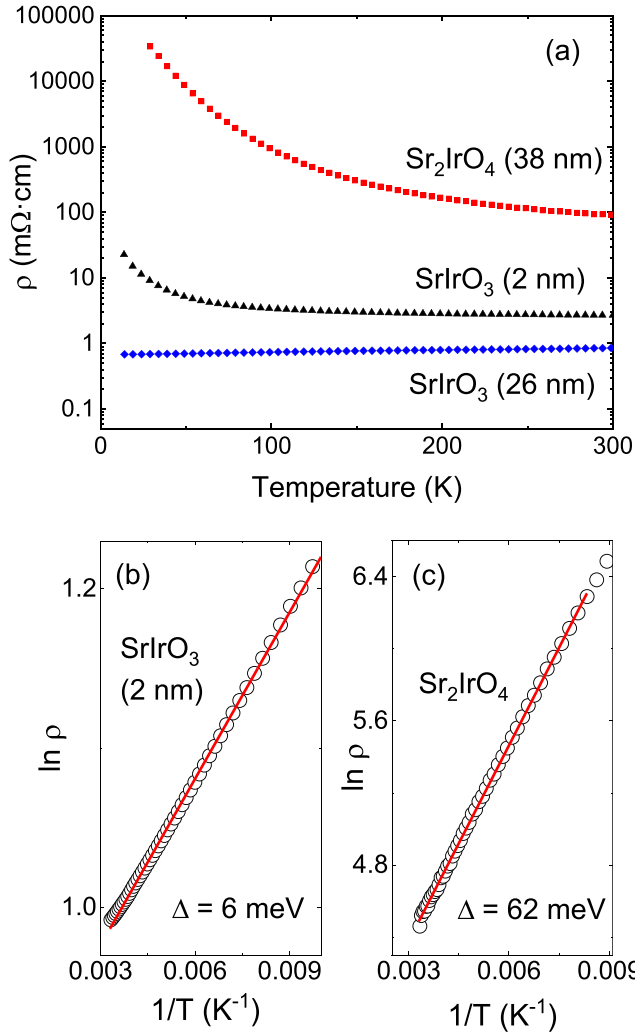


Fig. 2. (a) Temperature dependence of the electrical resistivity of an insulating SIO-214 film (38 nm) an insulating SIO-113 film (2 nm) and a semimetallic SIO-113 film (26 nm). (b) and (c) Arrhenius plot of the high temperature part of the $\rho(T)$ curve for the insulating films shown in (a). The activation energy Δ in each case has been obtained by the fit (solid lines) to the thermal activation law $\rho(T) = \rho_0 e^{(\Delta/k_B T)}$.

Anderson localization type due to disorder, in good agreement with previous reports [23,25,27]. On the other hand, SIO-214 film exhibit a robust insulating behavior with $d\rho/dT < 0$ in the whole temperature range independent of film thickness. Typical results for a 38 nm SIO-214 sample are plotted in Fig. 2(a). This behavior has been usually attributed to the opening of a band-gap in the electronic structure as a result of interplay between strong SOC and electronic correlations [37,42]. Temperature dependence of resistivity is again well described by a thermal activation law, see Fig. 2(c), but, in this case, the fitting leads to an activation energy of $\Delta_{214} \sim 62$ meV, i.e., around one order of magnitude higher than in the precedent case. Both activation energies are in agreement with the expected values reported from numerical simulations [20,43–45].

As resistivity of SIO thin films may be sensitive to different stimuli, iridate films become a promising alternative for obtaining a strong RS response and thus, of interest for the implementation of RS devices. For this purpose, we have studied local I-V curves measured at room temperature by C-AFM of SIO thin films. In Fig. 3 we present the I-V curves on samples with different electronic behavior, i.e., SIO-113 samples at both extremes of the thickness series (i.e. 26 nm and 2 nm), Fig. 3(a) and (b), respectively, and an insulating SIO-214 sample,

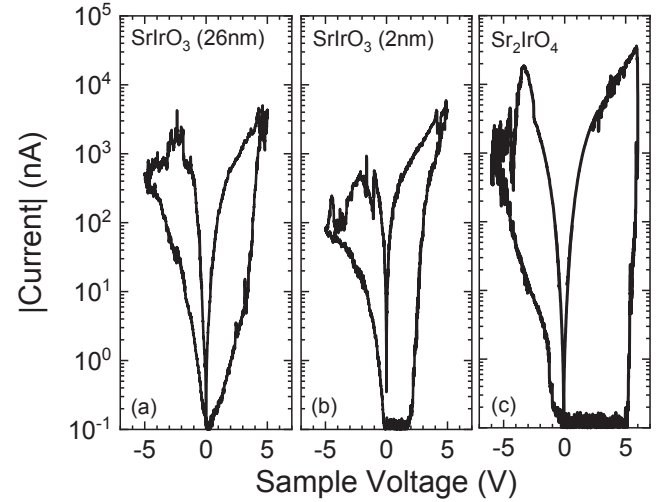


Fig. 3. C-AFM I-V curves measured on (a) 26 nm thick SIO-113 film; (b) 2 nm thick SIO-113 film and (c) SIO-214 film.

Fig. 3(c). In all cases hysteretic I-V curves are observed indicative of RS behavior. These curves are reproducible in the whole sample surface (see current maps below) and identical results were obtained when cycling IV curves over sample surface until sample-tip contact degrades (~ 10 cycles). An anti-clockwise behavior, where positive sample voltage induces the Low Resistance State (LRS) and negative sample voltage induces the High Resistance State (HRS) is found. From the results in Fig. 3 we observe two clear different RS behaviors if sample is initially in a metallic or in an insulating state. For the samples in an insulating state, SIO-113 (2 nm) and SIO-214, Fig. 3 (b) and (c), the current intensity remains constant and near to zero until a given threshold voltage value is reached after which a sudden increase of the current takes place. This voltage depends on the system and it was found to be around 2 V for the SIO-113 (2 nm) and 4.5 V for SIO-214. These threshold values may be correlated to the activation energy, Δ , obtained above from $\rho(T)$ measurements if we assume that Δ corresponds to the energy barrier needed to bring the system into a conducting state. Thus, the higher threshold voltage observed for the SIO-214 system is just reflecting a higher barrier between insulating and conducting states (remember that $\Delta_{\text{SIO-113}} = 6$ meV and $\Delta_{\text{SIO-214}} = 62$ meV) as previously observed for other compounds [46,47]. After reaching the maximum voltage, the sample remains in the LRS returning to 0 V through the superior limit of the graph. In the negative voltage range, the I-V curve starts at the LRS and the current is continuously increasing for voltages up to the maximum negative voltage. Once reached this voltage, the I-V curve returns to the LRS along the lower path. On the contrary, for the sample initially in the semimetallic state, SIO-113 (26 nm) shown in Fig. 3(b), the resistance changes in a continuous way and no well-defined resistance states separated by a clear voltage threshold are observed. The similarity of the measured I-V curves in all samples suggests that the mechanism behind the observed variations of resistance is the same in all cases. However, the absence of a clear voltage threshold in the case of the thick sample suggests the absence of a well defined energy transition separating the LRS and HRS.

Although all the films seem to follow the same mechanism for the changes of resistance, the set of I-V curves present notable differences. Fig. 3(a), corresponding to the SIO-113 26 nm thick sample, shows smoothly rising I-V curves for the positive voltage range from 0 V to the maximum of current. On the other hand, Fig. 3(b), corresponding to the SIO-113, 2 nm film and Fig. 3(c), corresponding to the SIO-214 film, show an almost zero current up to a clear voltage threshold value, when an abrupt increase of the current intensity occurs. This different behavior is closely related to the differences in the band structures of the films that are induced by the MIT. On one hand, it is reported that thick

SIO-113 films (such as the employed 26 nm thick one) behave as a semimetal [20,21,26,27] while an Anderson-type MIT transition with strong carriers' localization may be triggered by thickness reduction [23,25,27]. Even more, the aperture of a Mott gap in ultrathin SIO-113 films have been recently documented [44]. In the case of SIO-214, a band gap is expected to appear due to electron-electron correlations [37,42,48,49]. With this picture in mind, the behavior of thick SIO-113 film (26 nm) reflects changes of resistance in a system with continuous energy levels having thus a smooth increase of the current. Moreover, the shift of the Fermi level would bring the system into a state with higher Density of States, finally giving higher conductivity and setting it into the LRS. On the other hand, as long as Fermi energy lies inside localized states or belongs to the energy gap, charge carrier's mobility is seriously hampered or even suppressed and the current would be almost zero. Nevertheless, when the Fermi level crosses the mobility edge for the 2 nm thick SIO-113 or overcome band gap for SIO-214, an energy transition between localized and extended states takes place for high enough positive voltage, an abrupt increase of the current would be observed and obviously the system would be switched in the LRS with a higher conductivity.

Current maps over extended areas in both HRS and LRS states allowed us to obtain a deeper insight into the RS process in SIO samples. Performing a C-AFM map implies to move the AFM tip back and forth several times in the same area of the sample and the continuous scanning deteriorates the electrical tip-sample contact after a few cycles. This well-known drawback in C-AFM analysis of RS phenomena is usually attributed to tip contamination [30,34]. In our experience, current maps cannot be performed in bare iridate thin films due to surface degradation. However, we have found that capping of the SIO film surface with a non-continuous layer of metallic (Pt) nanoparticles (NPs) is useful to perform the C-AFM maps. In this way, quality of the tip-sample electrical contact is improved, while degradation of the electrical contact is avoided thanks to the enhanced tip life time since brushing with Pt nanoparticles removes tip-contaminations. Results for a SIO-214 film are shown in Fig. 4. Fig. 4(a) presents a 50x50 μm^2 current map measured at low voltage (1 V) after the scanning of the central 35x35 μm^2 area at the positive bias voltage (+4.5 V) applied to the sample and a further scan of 20x20 μm^2 area at -5 V applied to the sample. The dark outer part corresponds to the pristine state with a low conductivity. Inside, a bright squared ring represents the established LRS with high conductivity, or, as it is usually named, the written area. Finally, the central dark square exhibits again low conductivity and represents the switching back into the HRS, i.e., the erased region. The associated topography measurement is shown in Fig. 4(b). Some minor topography changes are detected in the central area switched into HRS that may be caused by a dragging of the Pt NPs during the scan.

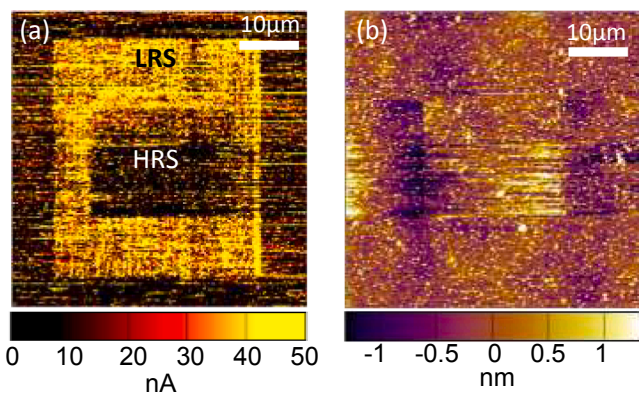


Fig. 4. C-AFM current map (a) and topography image (b) of a SIO-214 film. Current map shows a 35 \times 35 μm^2 area set into the LRS state and an inner 20 \times 20 μm^2 square reset to the HRS state. Minor changes in the topography associated with the writing-erasing process are noticed in (b).

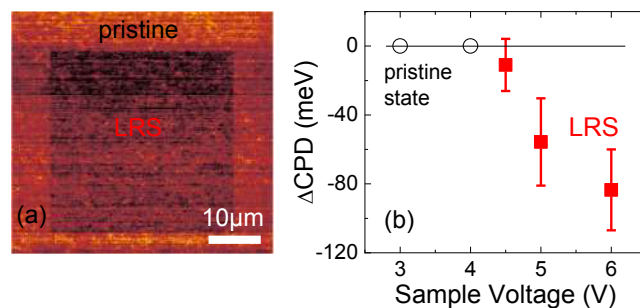


Fig. 5. (a) 50 \times 50 μm^2 CPD map measured in the SIO-214 thin film after applying a voltage of 4.5 V to an inner square of 35 \times 35 μm^2 (i.e., writing into LRS state). (b) Evolution of ΔCPD defined as the difference of the CPD measured in the inner written area and the CPD measured at the pristine area, $\Delta\text{CPD} = \text{CPD}_{\text{written}} - \text{CPD}_{\text{pristine}}$ as a function of applied voltage.

Nevertheless, as threshold voltage values observed in current maps are identical to those measured from IV curves, influence of Pt nanoparticles in RS may be considered negligible.

Redox based mechanisms, typically driven by the motion of oxygen vacancies, are usually invoked to explain RS phenomena in TMOs [5–9]. In correlated metals such as SIO, the variation of the concentration of oxygen vacancies can modify the valence of the surrounding metal cations. Since the oxygen vacancies substitute an oxygen position, the surrounding cations must adapt their valence to compensate the charge variation. Therefore, new electrons would fill Ir orbitals changing the Fermi level and electric properties [13]. To visualize this modification of Fermi level associated with the RS behavior, KPFM measurements were performed in SIO-214 samples. Fig. 5(a) depicts the CPD map measured by KPFM on a 50x50 μm^2 area after applying a sample voltage of +4.5 V on an inner 35x35 μm^2 region, i.e., the same procedure used to perform the above current maps. As can be seen, written region exhibits a decreased CPD. We have performed similar experiments by varying the maximum applied voltage. Fig. 5(b) shows the variation of CPD, ΔCPD , between the one measured in the outer region (i.e., corresponding to the pristine state) and the CPD measured in the square area (i.e., the written region), $\Delta\text{CPD} = \text{CPD}_{\text{written}} - \text{CPD}_{\text{pristine}}$, as a function of maximum applied voltage. We may observe that no modification of CPD is observed until the applied voltage attain the threshold value to switch the sample into a LRS state, around 4.5 V, i.e., the same value as in I–V curves, see Fig. 3(c). Once a LRS is achieved, a reduction of CPD can be measured. As CPD corresponds to the difference between the work function of the AFM tip and the sample, a decrease in CPD implies a higher work function on the LRS state when compared to the pristine sample and thus, the RS may be associated to a change in the electronic properties at the sample surface. Finally, the write-erase cycling was completed by applying a negative voltage of -6 V to a square region of 20 \times 20 μm^2 . Fig. 6(a) presents the CPD results of the complete cycle. We may see

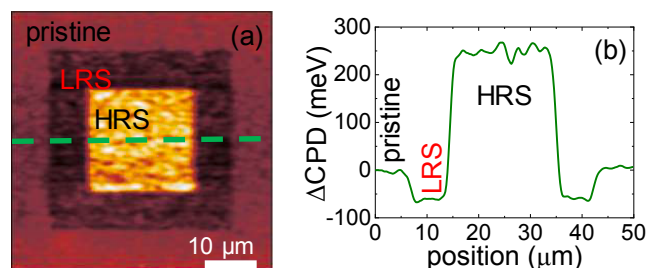
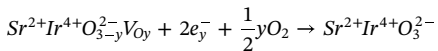


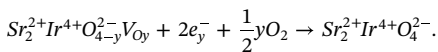
Fig. 6. (a) 50 \times 50 μm^2 CPD map measured in the SIO-214 thin film after applying a voltage of 6 V to an inner square of 20 \times 20 μm^2 (i.e., erasing into HRS state) in a previously written sample as in Fig. 5. (b) CPD profile showing the difference between pristine (taken as reference), LRS and HRS states.

that the inner square is much brighter than any of the surroundings areas, i.e., CPD is much higher in this HRS region. A quantification of the values may be followed by the CPD profile presented in Fig. 6(b). This result evidences that the erasing process bring the sample into a HRS state that it is not electronically equivalent to the pristine one.

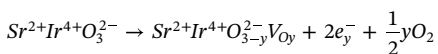
Combining the I–V curves and the KPFM results we may now elaborate a scenario for the RS behavior observed in SIO films. In general, an external applied electric field will promote a redox reaction at the film surface and, as a consequence, oxygen vacancies could be incorporated or removed from the film [50]. In hole-like systems as SIO-214 [51,52], vacancies are considered as acceptors scavengers and they decrease conductivity. The incorporation of oxygen anions into the oxide matrix, removing the vacancies occurs then under positive voltage (applied to sample) according to the following formula for SrIrO₃:



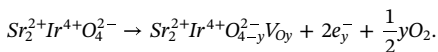
and, for Sr₂IrO₄



Then, the Fermi level would decrease, as observed in CPD maps, while the hole density and the conductivity would increase and transform the sample surface beneath the AFM tip into the LRS. By applying negative voltage to the sample the system can be reversed into the HRS with the following reaction taking place, for SrIrO₃



and, for Sr₂IrO₄



With these reactions, oxygen anions would be removed from the matrix leaving vacancies behind that would reduce drastically the number of holes and raise up the Fermi level, reducing this way the conductivity, in agreement with I–V curves and CPD measurements.

4. Conclusions

The local transport properties of iridate based thin films of the $n = 1$ phase, Sr₂IrO₄ and $n = \infty$ phase, SrIrO₃ have been analyzed. Macroscopic measurements of the film's resistivity as a function of temperature allow demonstrating that Sr₂IrO₄ films are insulating due to the opening of a gap while SrIrO₃ films are either semimetallic (for thickness above 3 nm) or insulating (for thickness below 3 nm), being in this case an Anderson type MIT, i.e., driven by disorder. On the other hand, all the SIO films exhibit hysteretic I–V curves indicative of RS behavior irrespective to their phase or thickness. Due to the particular experimental setup used, the observed RS takes place at the interface between the metal electrode (AFM tip) and the SIO film. Electric field pulses promote oxygen vacancies migration through the interface then, to maintain electrical neutrality, a valence change of the cations nearby takes place and therefore, a modification of the charge carriers' density and of the position of the Fermi level. However, the features of the RS process are clearly different as a function of their initial conducting state. In the case of Sr₂IrO₄ samples and for very thin samples of SrIrO₃ (below 3 nm), where carriers' localization occurs, it is observed the existence of a well-defined voltage threshold value separating the low and high resistance states. This threshold voltage is correlated with the activation energy needed to bring the system into a conducting state. In contrast, in thick SrIrO₃ films with semimetallic behavior, (i.e., for thickness above 3 nm) I–V curves present a continuous smooth variation of resistance, without a clear threshold voltage, making evident the absence of an energy sharp transition separating high and low resistance states. In this case, changes of resistance by applying voltage pulses are simply associated to the variation of charge carriers' density

due to the migration of oxygen vacancies. The electronic changes associated with the migration of oxygen vacancies during the electric field pulses were monitored by KPFM and suggested that majority carriers are holes. Current maps performed with voltage values above the threshold value and of different polarity allow demonstrating the writing/erasing processes in a large area of the sample surface.

Authors statement

V.F. and B.V. were responsible for the C-AFM and KPFM measurements and data analysis. V.F, Z.K. and Ll. B. were responsible for film and nanoparticles preparation. V.F., B.M. and A.P. were involved in transport measurements and data analysis.

All authors contributed to discussion, interpretation and manuscript preparation.

Declaration of Competing Interest

The authors declare that they have no known competing financial interests or personal relationships that could have appeared to influence the work reported in this paper.

Acknowledgments

We acknowledge financial support from the Spanish Ministry of Science, Innovation and Universities through Severo Ochoa Program (SEV-2015-04969), MAT2015-71664-R (HETEROCS) and RTI2018-099960-B-I00 (SPINCURIQX) and funding from the European Union's Horizon 2020 research and innovation program under the Marie Skłodowska-Curie grant agreement No. 645658 (DAFNEOX Project) and FEDER Program. B.V. and Z.K. acknowledge the support of the Serbian Ministry of Education, Science and Technological Development (Projects No. OI171005 and III45018). A.P., V.F. and Z.K. thank Sensor-INFIZ (Serbia) for the cooperation provided during their respective secondments.

Appendix A. Supplementary data

Supplementary data to this article can be found online at <https://doi.org/10.1016/j.jmmm.2020.166419>.

References

- [1] R. Waser, M. Aono, Nanoionics-based resistive switching memories, *Nat. Mater.* 6 (2007) 833–840.
- [2] A. Sawa, Resistive switching in transition metal oxides, *Mater. Today* 11 (2008) 28–36.
- [3] M.A. Villena, J.B. Roldán, F. Jiménez-Molinos, E. Miranda, J. Suñé, M. Lanza, SIM²RRAM: a physical model for RRAM devices simulation, *J. Comput. Electron.* 16 (2017) 1095–1120.
- [4] M. Lanza, H.S.P. Wong, E. Pop, D. Jelmini, D. Strukov, B.C. Regan, L. Larcher, M.A. Villena, J.J. Yang, L. Goux, A. Belmonte, Y. Yang, Y. Shi, et al., Recommended methods to study resistive switching devices, *Adv. Electron. Mater.* 5 (2019) 1800143.
- [5] R. Waser, R. Dittmann, C. Staikov, K. Szot, Redox-based resistive switching memories nanoionic mechanisms, prospects, and challenges, *Adv. Mater.* 21 (2009) 2632–2663.
- [6] T. Lee, Y. Chen, Organic resistive nonvolatile memory materials, *MRS Bull.* 37 (2012) 144–149.
- [7] D.S. Jeong, R. Thomas, R.S. Katiyar, J.F. Scott, H. Kohlstedt, A. Petraru, C.S. Hwang, Emerging memories: resistive switching mechanisms and current status, *Reports Prog. Phys.* 75 (2012) 076502.
- [8] J.J. Yang, D.B. Strukov, D.R. Stewart, Memristive devices for computing, *Nat. Nanotechnol.* 8 (2013) 13–24.
- [9] J.C. Scott, L.D. Bozano, Nonvolatile memory elements based on organic materials, *Adv. Mater.* 19 (2007) 1452–1463.
- [10] S. Bagdzevicius, K. Maas, M. Boudard, M. Burriel, Interface-type resistive switching in perovskite materials, *J. Electroceramics* 39 (2017) 157–184.
- [11] A. Mehonic, A.J. Kenyon, Resistive Switching in Oxides, in: J. Jupille, G. Thornton (Eds.), *Springer Series in Surface Sciences*, vol. 58, Springer International Publishing, Cham, 2015, pp. 401–428.
- [12] L. Peña, L. Garzón, R. Galceran, A. Pomar, B. Bozzo, Z. Konstantinovic,

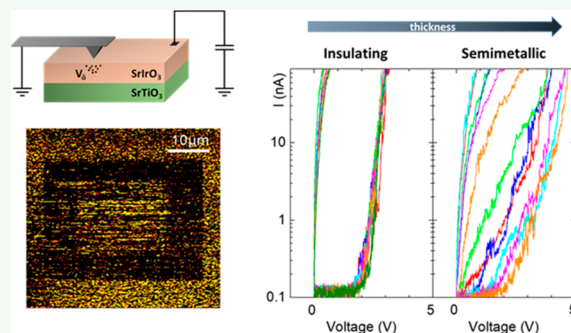
- F. Sandiumenge, L. Balcells, C. Ocal, B. Martínez, Macroscopic evidence of nanoscale resistive switching in $\text{La}_{2/3}\text{Sr}_{1/3}\text{MnO}_3$ micro-fabricated bridges, *J. Phys. Condens. Matter* 26 (2014) 395010.
- [13] E. Janod, J. Tranchant, B. Corraze, M. Querré, P. Stoliar, M. Rozenberg, T. Cren, D. Roditchev, V.T. Phuoc, M.P. Besland, L. Cario, Resistive switching in mott insulators and correlated systems, *Adv. Funct. Mater.* 25 (2015) 6287–6305.
- [14] L. Zhang, B. Pang, Y.B. Chen, Y. Chen, Review of spin-orbit coupled semimetal SrIrO_3 in thin film form, *Crit. Rev. Solid State Mater. Sci.* 43 (2018) 367–391.
- [15] G. Cao, P. Schlottmann, The challenge of spin-orbit-tuned ground states in iridates: a key issues review, *Reports Prog. Phys.* 81 (2018) 042502.
- [16] A. Biswas, Y.H. Jeong, Growth and engineering of perovskite SrIrO_3 thin films, *Curr. Appl. Phys.* 17 (2017) 605–614.
- [17] J. Kim, D. Casa, M.H. Upton, T. Gog, Y.J. Kim, J.F. Mitchell, M. Van Veenendaal, M. Daghofer, J. Van Den Brink, G. Khaliullin, B.J. Kim, Magnetic excitation spectra of Sr_2IrO_4 probed by resonant inelastic X-ray scattering: establishing links to cuprate superconductors, *Phys. Rev. Lett.* 108 (2012) 177003.
- [18] X. Wan, A.M. Turner, A. Vishwanath, S.Y. Savrasov, Topological semimetal and fermi-arc surface states in the electronic structure of pyrochlore iridates, *Phys. Rev. B* 83 (2011) 205101.
- [19] A. Shitade, H. Katsura, J. Kuneš, X.L. Qi, S.C. Zhang, N. Nagaosa, Quantum spin hall effect in a transition metal oxide Na_2IrO_3 , *Phys. Rev. Lett.* 102 (2009) 256403.
- [20] S.J. Moon, H. Jin, K.W. Kim, W.S. Choi, Y.S. Lee, J. Yu, G. Cao, A. Sumi, H. Funakubo, C. Bernhard, T.W. Noh, Dimensionality-controlled insulator-metal transition and correlated metallic state in 5 d transition metal oxides $\text{Sr}_{n+1}\text{Ir}_n\text{O}_{3n+1}$ ($n = 1, 2, \text{ and } \infty$), *Phys. Rev. Lett.* 101 (2008) 226402.
- [21] Z.T. Liu, M.Y. Li, Q.F. Li, J.S. Liu, W. Li, H.F. Yang, Q. Yao, C.C. Fan, X.G. Wan, Z. Wang, D.W. Shen, Direct observation of the Dirac nodes lifting in semimetallic perovskite SrIrO_3 thin films, *Sci. Rep.* 6 (2016) 30309.
- [22] L. Zhang, Q. Liang, Y. Xiong, B. Zhang, L. Gao, H. Li, Y.B. Chen, J. Zhou, S.T. Zhang, Z. Gu Bin, S.H. Yao, Z. Wang, Y. Lin, Y.F. Chen, Tunable semimetallic state in compressive-strained SrIrO_3 films revealed by transport behavior, *Phys. Rev. B* 91 (2015) 035110.
- [23] A. Biswas, K.-S. Kim, Y.H. Jeong, Metal insulator transitions in perovskite SrIrO_3 thin films, *J. Appl. Phys.* 116 (2014) 213704.
- [24] J.H. Gruenewald, J. Nichols, J. Terzic, G. Cao, J.W. Brill, S.S.A.A. Seo, Compressive strain-induced metal-insulator transition in orthorhombic SrIrO_3 thin films, *J. Mater. Res.* 29 (2014) 2491–2496.
- [25] F.X. Wu, J. Zhou, L.Y. Zhang, Y.B. Chen, S.T. Zhang, Z. Gu Bin, S.H. Yao, Y.F. Chen, Metal-insulator transition in SrIrO_3 with strong spin-orbit interaction, *J. Phys. Condens. Matter* 25 (2013) 125604.
- [26] N. Manca, D.J. Groenendijk, I. Pallechchi, C. Autieri, L.M.K. Tang, F. Telesio, G. Mattoni, A. McCollam, S. Picozzi, A.D. Caviglia, Balanced electron-hole transport in spin-orbit semimetal SrIrO_3 heterostructures, *Phys. Rev. B* 97 (2018) 081105(R).
- [27] V. Fuentes, B. Vasić, Z. Konstantinović, B. Martínez, L. Balcells, A. Pomar, Resistive switching in semimetallic SrIrO_3 thin films, *ACS Appl. Electron. Mater.* 1 (2019) 1981–1988.
- [28] J.G. Connell, B.J. Isaac, G.B. Ekanayake, D.R. Strachan, S.S.A. Seo, Preparation of atomically flat SrTiO_3 surfaces using a deionized-water leaching and thermal annealing procedure, *Appl. Phys. Lett.* 101 (2012) 98–101.
- [29] M. Lanza, A review on resistive switching in high-k dielectrics: a nanoscale point of view using conductive atomic force microscope, *Mater.* 7 (2014) 2155–2182.
- [30] M. Lanza, U. Celano, F. Miao, Nanoscale characterization of resistive switching using advanced conductive atomic force microscopy based setups, *J. Electroceramics* 39 (2017) 94–108.
- [31] M. Lanza, A. Bayerl, T. Gao, M. Porti, M. Nafria, G.Y. Jing, Y.F. Zhang, Z.F. Liu, H.L. Duan, Graphene-coated atomic force microscope tips for reliable nanoscale electrical characterization, *Adv. Mater.* 25 (2013) 1440–1444.
- [32] M.A. Villena, F. Jiménez-Molinos, J.B. Roldán, J. Suñé, S. Long, X. Lian, F. Gámiz, M. Liu, An in-depth simulation study of thermal reset transitions in resistive switching memories, *J. Appl. Phys.* 114 (2013) 144505.
- [33] K.C. Chang, J. Huang Wei, T.C. Chang, T.M. Tsai, K.H. Chen, T.F. Young, J.H. Chen, R. Zhang, J.C. Lou, S.Y. Huang, Y.C. Pan, H.C. Huang, Y.E. Syu, D.S. Gan, S.M. Sze, Space, Electric field concentrated effect for Zr:SiO_2 RRAM devices using porous SiO_2 buffer layer, *Nanoscale Res. Lett.* 8 (2013) 523.
- [34] S. Brivio, J. Frascaroli, M.H. Lee, Electrical AFM for the analysis of resistive switching, *Electrical Atomic Force Microscopy for Electronics*, Springer Nature, Switzerland, 2019, pp. 205–229.
- [35] D.J. Groenendijk, N. Manca, G. Mattoni, L. Kootstra, S. Gariglio, Y. Huang, E. Van Heumen, A.D. Caviglia, Epitaxial growth and thermodynamic stability of $\text{SrIrO}_3/\text{SrTiO}_3$ heterostructures, *Appl. Phys. Lett.* 109 (2016) 041906.
- [36] J.J. Randall, L. Katz, R. Ward, The preparation of a strontium-iridium oxide Sr_2IrO_4 , *J. Am. Chem. Soc.* 79 (1957) 266–267.
- [37] C. Lu, A. Quindeau, H. Deniz, D. Preziosi, D. Hesse, M. Alexe, Crossover of conduction mechanism in Sr_2IrO_4 epitaxial thin films, *Appl. Phys. Lett.* 105 (2014) 082407.
- [38] J.G. Zhao, L.X. Yang, Y. Yu, F.Y. Li, R.C. Yu, Z. Fang, L.C. Chen, C.Q. Jin, High-pressure synthesis of orthorhombic SrIrO_3 perovskite and its positive magnetoresistance, *J. Appl. Phys.* 103 (2008) 103706.
- [39] L. Fruchter, O. Schneegans, Z.Z. Li, Anisotropy and interaction effects of strongly strained SrIrO_3 thin films, *J. Appl. Phys.* 120 (2016) 075307.
- [40] K.W. Kim, J.S. Lee, T.W. Noh, S.R. Lee, K. Char, Metal-insulator transition in a disordered and correlated $\text{SrTi}_{1-x}\text{Ru}_x\text{O}_3$ system: changes in transport properties, optical spectra, and electronic structure, *Phys. Rev. B* 71 (2005) 125104.
- [41] N. Mott, *Metal-Insulator Transitions*, second ed., Taylor & Francis, London, 1998 Vol. 70.
- [42] B.J. Kim, H. Ohsumi, T. Komesu, S. Sakai, T. Morita, H. Takagi, T. Arima, Phase-sensitive observation of a spin-orbital mott state in Sr_2IrO_4 , *Science* 323 (2009) 1329–1332.
- [43] M.A. Villena, B. Magyari-Köpe, Y. Nishi, P.C. McIntyre, M. Lanza, Effect of IrO_2 spatial distribution on the stability and charge distribution of $\text{Ti}_{1-x}\text{Ir}_x\text{O}_2$ alloys, *Chem. Mater.* 31 (2019) 8742–8751.
- [44] D.J. Groenendijk, C. Autieri, J. Girovsky, M.C. Martínez-Velarte, N. Manca, G. Mattoni, A.M.R.V.L. Monteiro, N. Gauquelin, J. Verbeeck, A.F. Otte, M. Gabay, S. Picozzi, A.D. Caviglia, Spin-orbit semimetal SrIrO_3 in the two-dimensional limit, *Phys. Rev. Lett.* 119 (2017) 256403.
- [45] B.J. Kim, H. Jin, S.J. Moon, J.Y. Kim, B.G. Park, C.S. Leem, J. Yu, T.W. Noh, C. Kim, S.J. Oh, J.H. Park, V. Durairaj, G. Cao, E. Rotenberg, Novel $\text{Jeff} = 1/2$ Mott state induced by relativistic spin-orbit coupling in Sr_2IrO_4 , *Phys. Rev. Lett.* 101 (2008) 076402.
- [46] M.-H. Lin, M.-C. Wu, C.-H. Lin, T.-Y. Tseng, Effects of vanadium doping on resistive switching characteristics and mechanisms of SrZrO_3 -based memory films, *IEEE Trans. Electron Devices* 57 (2010) 1801–1808.
- [47] M.A. Affi, M.M. Abdel-Aziz, H.H. Labib, M. Fadel, E.G. El-Metwally, Electrical and switching properties of amorphous films based on the Ge-Se-Tl system, *Vacuum* 61 (2001) 45–53.
- [48] A. Biswas, Y.W. Lee, S.W. Kim, Y.H. Jeong, Metal insulator transition and magnetotransport anomalies in perovskite $\text{SrIr}_{0.5}\text{Ru}_{0.5}\text{O}_3$ thin films, *J. Appl. Phys.* 117 (2015) 115304.
- [49] C. Rayan Serrao, J. Liu, J.T. Heron, G. Singh-Bhalla, A. Yadav, S.J. Suresha, R.J. Paull, D. Yi, J.H. Chu, M. Trassin, A. Vishwanath, E. Arenholz, C. Frontera, J. Železný, T. Jungwirth, X. Marti, R. Ramesh, Epitaxy-distorted spin-orbit mott insulator in Sr_2IrO_4 thin films, *Phys. Rev. B* 87 (2013) 085121.
- [50] H.S. Lee, S.G. Choi, H.H. Park, M.J. Rozenberg, A new route to the Mott-Hubbard metal-insulator transition: strong correlations effects in $\text{Pr}_{0.7}\text{Ca}_{0.3}\text{MnO}_3$, *Sci. Rep.* 3 (2013) 1704.
- [51] Y. Klein, I. Terasaki, Transport properties and cationic substitutions in Sr_2IrO_4 , *J. Electron. Mater.* 38 (2009) 1331–1336.
- [52] M. Ito, M. Uchida, Y. Kozuka, K.S. Takahashi, M. Kawasaki, Effective carrier doping and metallization in $\text{La}_x\text{Sr}_{2-x}\text{Ba}_y\text{IrO}_{4-\delta}$ thin films, *Phys. Rev. B* 93 (2016) 045139.

Resistive Switching in Semimetallic SrIrO₃ Thin FilmsV́ctor Fuentes,[†] Borislav Vasić,[‡] Zorica Konstantinović,[‡] Benjamín Martínez,[†] Lluís Balcells,[†] and Alberto Pomar^{*,†}[†]Institut de Ciència de Materials de Barcelona (ICMAB-CSIC), Campus de la UAB, Bellaterra 08193, Spain[‡]Center for Solid State Physics and New Materials, Institute of Physics Belgrade, University of Belgrade, Pregrevica 118, 11080 Belgrade, Serbia

Supporting Information

ABSTRACT: Local electrical properties, measured by conductive atomic force microscopy, of semimetallic SrIrO₃ thin films are reported. The appearance of an Anderson-type metal–insulator transition (MIT) triggered by disorder and spatial localization due to film thickness reduction is analyzed as well as their influence on the resistive switching behavior. For thin enough films (below ~3 nm) samples are insulating with hysteretic *I*–*V* curves indicative of reversible resistive switching behavior between two states of clearly different resistance at room temperature. A sharp transition into a low resistance state (LRS), i.e., an abrupt increase of the current intensity, is detected above a well-defined threshold voltage indicative of localization of charge carriers. On the other hand, thicker samples exhibit a semimetallic character, and *I*–*V* curves show progressive changes of the local resistance without a clearly defined threshold voltage, thus evidencing the absence of a MIT transition with a well-defined resistance jump between the different resistance states.

KEYWORDS: resistive switching, metal–insulator transition, SrIrO₃, conductive atomic force microscopy, iridate thin films



INTRODUCTION

In the search for a new generation of faster and more energy efficient electronic devices, the use of reversible resistive switching (RS) phenomena has been proposed as a very appealing solution for the development of nonvolatile memory devices.^{1,2} RS is the change of resistance in a reversible manner between two stable states of well-defined resistance by applying voltage pulses. This bistable behavior between high- and low-resistance states can be used as the core of a memory cell to implement a resistive random access memory (Re-RAM). RS behavior, typically observed in metal–insulator–metal (MIM) structures, has been found in a variety of materials, including transition metal oxides (TMOs), chalcogenides, and even organic compounds, and diverse physical mechanisms, mostly based on thermochemical or electrochemical effects, have been invoked to account for the observed experimental behavior.^{3–7}

In the case of TMOs one of the most common mechanisms to induce RS is based on modifications of the doping rate by valence change. The migration of oxygen vacancies, or metal cations, under an electric field along defects, grain boundaries, dislocations, and so on induces a valence change of the cations nearby, and therefore a change of the doping rate that may promote strong changes of the resistivity or even to trigger the appearance of a metal-to-insulator transition (MIT).^{2,3,8–10}

This process of ionic migration can also occur at the interface between the metallic electrode and the active insulating oxide.⁸ Among TMOs exhibiting RS behavior, Mott insulators and

strongly correlated systems are of particular interest because they can exhibit different types of MIT transitions, i.e., huge changes of the electrical resistance, in response to a variety of external stimuli, such as temperature, doping rate, or structural strain.¹¹ The close similarity between electronic correlations and crystal field splitting energies in TMOs provides different mechanism for tuning their electronic properties, and these mechanisms can even be widened by making use of spin–orbit coupling (SOC). In 3d TMOs SOC is not very relevant because being proportional to Z^4 , where Z is the atomic number of the element under consideration, is much smaller than crystal field splitting and electronic correlations. However, in the case of 5d elements, such as Ir, SOC reaches values of about 0.5 eV.^{12–14} Thus, SOC becomes comparable to crystal field and electronic correlations, giving place to novel physics and exotic properties.^{15–17} In particular, the Ruddlesden–Popper series of 5d strontium iridates (Sr_{*n*+1}Ir_{*n*}O_{3*n*+1}) have been investigated in the past years because of the strong interplay between these three contributions. This interplay may trigger different electronic states just by subtle structural or chemical changes. For example, the perovskite-like $n = \infty$ phase (SrIrO₃) presents a semimetallic ground state¹⁸ while on the other extreme of the series, in the $n = 1$ phase (Sr₂IrO₄), a

Received: August 14, 2019

Accepted: August 20, 2019

Published: August 21, 2019

gap is opened at the Fermi level, leading the system into a Mott insulator state.¹⁹

As mentioned above, the MIT can be modified by applying different external perturbations, such as pressure²⁰ or electric field pulses as demonstrated for the $n = 1$ phase²¹ and in the $n = 2$ phase.²² In the case of the perovskite $n = \infty$ phase (SrIrO₃, hereafter denoted as SIO) thin films, it was reported that a MIT can be triggered by tuning the compressive strain induced by the substrate or by reducing the film thickness.^{23–27} Different studies indicate that the MIT induced in these cases can be either of disorder driven Anderson type or unconventional Mott–Anderson type in which disorder effects and electronic correlations coexist.²⁴ However, recent results in high quality epitaxial thin films also show a concomitant divergence of the magnetic susceptibility in very thin films (four unit cells) that clearly points to the opening of a Mott gap.^{28,29} Besides their fundamental relevance, the ability to modify at will the material resistivity by inducing a MIT is of strong interest from the application point of view. Even though the appearance of a MIT in SIO has been reported by different groups^{23–27} and some results regarding RS effects in the $n = 1$ phase^{21,22} have been reported, reports regarding RS in the interesting semimetallic $n = \infty$ phase are very scarce.

In this work we present a systematic study of RS behavior in high quality SIO thin films prepared by RF sputtering on top of (001)-STO substrates, through local I – V curve measurements and current mapping, by using conductive atomic force microscopy (C-AFM). Epitaxial SIO films show semimetallic character, and the appearance of a MIT is triggered by the reduction of film thickness. For film thickness below ~ 3 nm an Anderson-type MIT, i.e., induced by disorder, appears, and resistance increases notoriously on lowering temperature. I – V characteristic curves in thin samples exhibiting the MIT show the typical hysteretic behavior associated with RS processes with two well-defined resistance states. I – V curves show directional RS depending on the polarity of the applied voltage; thus, it can be classified as bipolar RS, with an abrupt increase of the current for voltages above a threshold value of around 2 V. Additionally, because of the particular features of the experimental setup, the observed RS is of interface type in which RS takes place at the interface between the metal electrode and the SIO film. Electric field pulses promote oxygen vacancies migration through the interface; then, to maintain electrical neutrality, a valence change of the cations nearby takes place and therefore a modification of the charge carriers' density and of the position of the Fermi level. A redox mechanism based on the band structure of SIO is proposed to account for the observed RS behavior. Current maps performed with voltage values above the threshold value and of different polarity allow demonstrating the writing/erasing processes, making evident the feasibility of the system for the implementation of Re-RAMs. On the other hand, in the case of thicker films, initially in a semimetallic state, I – V curves present a smooth variation of resistance, without a clear threshold voltage, suggesting the absence of two well-defined resistance states separated by an energy jump. In this case, changes of resistance by applying voltage pulses are simply associated with the variation of charge carriers' density due to the migration of oxygen vacancies.

EXPERIMENTAL DETAILS

SIO films were grown by RF magnetron sputtering on top of single crystalline (001)-SrTiO₃ (STO) substrates at 900 °C in an oxygen

atmosphere at 140 mTorr. STO substrates were treated before deposition to obtain atomically flat surfaces of TiO₂ terraces. The treatment consisted in an ultrasound leaching in deionized water for 10 min followed by an annealing for 2 h at 1000 °C.³⁰ SIO samples with different thickness ranging between 2 and 26 nm were prepared. X-ray reflectometry (Siemens D-5000 diffractometer) was used to determine the thickness of SIO thick samples and to calibrate the growth rate; then the thickness of the thinnest films was determined by adjusting the deposition time.

X-ray measurements were also used to check phase purity and epitaxial growth quality. For this purpose a high-resolution X-ray θ – 2θ scan of the (002) peak was performed by using a PANalytical X'PERT PRO MRD system. Additionally, reciprocal space maps (RSM) around the (–103) diffraction peak (pseudocubic notation) were also recorded by using a Bruker D8-Discover diffractometer.

The temperature dependence of the resistivity was measured by using a standard four-probe configuration in a PPMS system from Quantum Design. Measurements were performed in 400 μm long \times 100 μm wide tracks patterned by UV lithography and physical etching. The surface quality of the samples was studied by using scanning electron microscopy (SEM) (QUANTA FEI 200 FEG-ESEM). An MFP3D system from Asylum was used for the acquisition of topographic images, I – V curves, and current maps. Atomic force microscope (AFM) topography images were recorded in tapping mode by using Sb-doped Si probes (NCHV-A from Bruker). The surface roughness of the topographic images was calculated as a root mean square (rms) of the height distribution of the sample surface. I – V curves and current maps were measured at room temperature by Conductive-AFM (C-AFM) by using doped diamond-coated probes (DDESP-FM-V2 from Bruker), applying voltage to the sample while the tip was grounded. I – V curves were taken on random positions of the bare sample surfaces with a voltage sweep ranging between +5 and –5 V in an ambient atmosphere. As it has been previously reported, the surface of iridates is very sensitive to air exposure, and measurements of surface properties lose reliability a few days after deposition of the film.^{27,31} This intrinsic surface instability is very challenging for C-AFM measurements, especially for performing measurements with long exposure times as current maps. To perform C-AFM maps, a noncontinuous layer of platinum nanoparticles was deposited on top of the SIO film. More details on these measurements may be found later and in the [Supporting Information](#).

RESULTS

A high-resolution θ – 2θ scan corresponding to a 21 nm thick SIO film deposited on (001)-STO substrate is shown in [Figure 1a](#). The epitaxial nature of the SIO film is clearly evidenced by the figure. The (002) reflection peak corresponding to the perovskite structure of the ($n = \infty$) phase is shown. Apart from the (00 l) family, no additional peaks were found in the θ – 2θ scan, making evident the high purity of the $n = \infty$ phase in the

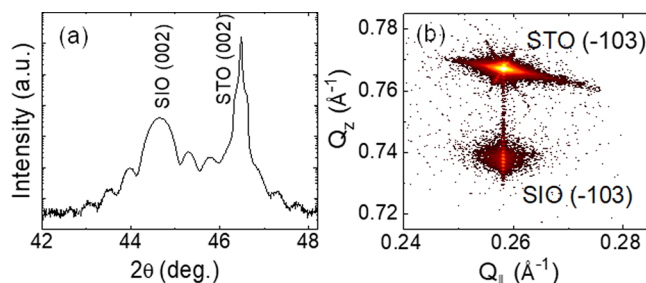


Figure 1. X-ray diffraction measurements of the SIO/STO thin films. (a) High-resolution θ – 2θ scan around (002) diffraction peaks. (b) Reciprocal space map of the (–103) peaks showing full strained state of the SIO films. For simplicity, all diffraction peaks are indexed in pseudocubic notation.

films. Moreover, satellite fringes can be clearly appreciated at both sides of the SIO Bragg peak. These oscillations, arising from the diffraction of the X-ray beam at film finite planes with coherent thickness, are indicative of the high crystalline quality of the films and of the parallel orientation respect to the substrate. The peak position corresponds to an out-of-plane lattice parameter of 4.056 Å; i.e., the SIO unit cell is slightly elongated with respect to the reported bulk value ($a_0 = 3.943$ Å).³² Such a value is in agreement with an elastic behavior governed by the in-plane compressive strain imposed by the smaller STO substrate ($a_{\text{STO}} = 3.905$ Å) as usually reported in the literature.^{14,23–25} Figure 1b displays a reciprocal space map around the (-103) reflection. It can be appreciated from the figure that both the substrate and the film peaks are aligned at the same in plane component (Q_{\parallel}), confirming the fully strained nature of the SIO film.

Surface morphology of SIO films, measured by AFM immediately after the deposition, corresponding to a 2 nm thick and a 26 nm thick samples are depicted in Figures 2a and

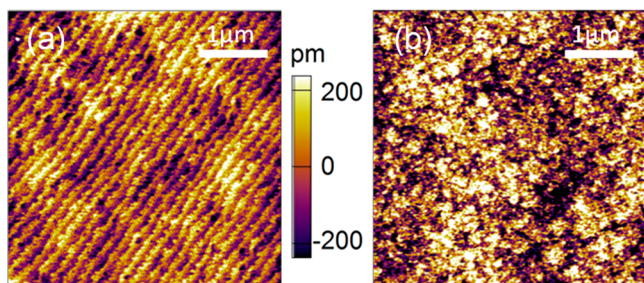


Figure 2. AFM topography images of two SIO thin films on STO with thicknesses of (a) 2 nm and (b) 26 nm. Both films exhibit flat surfaces with low roughness (rms below 0.2 nm). In the case of very thin film, the underlying terraced structure is still observed.

2b, respectively. Both samples show a flat topography with a surface roughness rms below 0.2 nm. In the case of extremely thin samples (rms typically below 0.12 nm) the underlying terrace and steps structure of the STO substrate is replicated on the SIO surface.

Electrical properties of SIO films are clearly thickness-dependent. Figure 3a depicts the temperature dependence of the sheet resistivity for a series of SIO films with thicknesses ranging between 2 and 26 nm. Metallic behavior is observed for film thickness down to ~ 3 nm, in agreement with previous results.^{23–27,33} However, as thickness decreases a progressive upturn of the resistivity at low temperatures is detected. The temperature at which the minimum in the resistivity is found shifts up in temperature as thickness decreases, and the system exhibits fully insulating behavior for the 2 nm thick sample, thus locating the MIT transition between 3 and 2 nm, in good agreement with previous reports.²⁴ Discrepancies regarding the actual thickness value at which the MIT takes place are usually attributed to differences in the microstructural quality of the samples.³⁴ For sample thickness above 10 nm the high-temperature behavior of the resistance is well described by the expression $\rho(T) = \rho_0 + CT^{4/5}$ (see Figure 3b). The value obtained for the residual resistivity, ρ_0 , is in all the samples below the so-called Mott–Ioffe–Regel (MIR) limit³⁵ ($h/e^2 \approx 26$ k Ω). In the low-temperature regime, the resistivity shows a T^2 dependence down to the lowest temperature measured (~ 10 K) indicative of a Fermi liquid behavior (see the inset of Figure 3b). This crossover from a non-Fermi liquid at high T

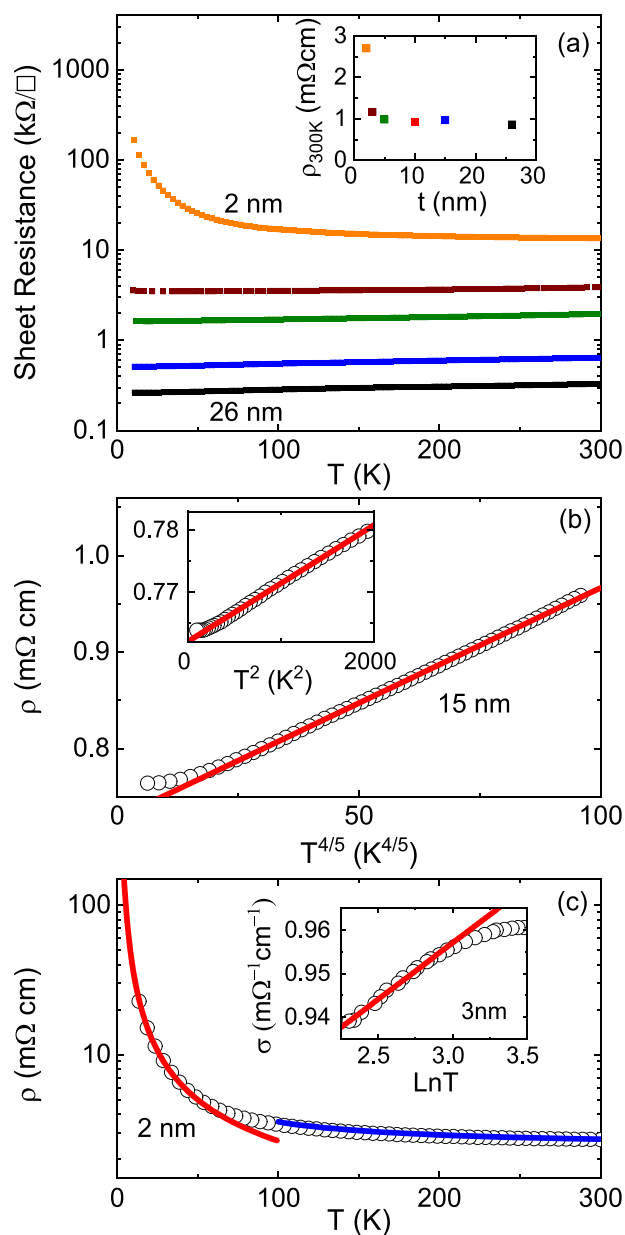


Figure 3. Electric properties of the SIO/STO films. (a) Temperature dependence of the sheet resistance in SIO films with thickness of 2 nm (orange), 3 nm (brown), 5 nm (green), 15 nm (blue), and 26 nm (black). Inset: resistivity of films at 300 K. A change of behavior from a semimetallic state to an insulating state when reducing thickness below 3 nm is clearly observed. (b) Temperature dependence of the resistivity of 15 nm thick SIO film vs $T^{4/5}$. Inset: details of the low-temperature regime to make evident the crossover to a Fermi liquid behavior at low T . (c) Temperature dependence of the resistivity of the 2 nm thick sample. The fittings using the Mott's variable range hopping (VRH) model, $\ln \sigma \propto 1/T^{1/(d+1)}$ (red line), at low T and the Arrhenius equation for thermal activation conduction, $\rho(T) = \rho_0 e^{(\Delta/k_B T)}$, at high T (blue line) are indicated. Inset: details of the low-temperature regime of the sheet conductivity of the 3 nm thick sample showing the $\ln T$ dependence indicative of two-dimensional weak localization.

to a Fermi liquid behavior at low T is typically associated with strongly correlated systems;³⁶ thus, we should conclude that thick SIO samples behave as a three-dimensional correlated metal.

As the critical thickness corresponding to the MIT transition is approached, the low-temperature upturn of the resistivity shifts up to higher temperature and becomes more abrupt, as typically observed when the MIT transition is approached from the metallic side. In the case of the 3 nm thick sample a notable upturn of the resistivity is observed below about 60 K, and the low-temperature regime is well described by a characteristic $\ln T$ dependence of the sheet conductance, indicative of two-dimensional weak localization (see the inset of Figure 3c).³⁷ Once the film thickness is reduced below 3 nm, the transport properties change abruptly. The resistance of the 2 nm thick film presents a typical insulating dependence with $d\rho/dT < 0$ in the whole temperature range. Clues of this transition can also be observed in the inset of Figure 3a, where the resistivity at 300 K is almost constant for the films with thickness between 3 and 26 nm but sharply increases for the 2 nm thick sample.

To clarify the nature of the MIT induced by reducing the film thickness, we have carefully analyzed the temperature dependence of the resistivity of the fully insulating 2 nm thick sample.³⁸ The low-temperature resistance upturn is well described by using the Mott's variable range hopping (VRH) model: $\ln \sigma \propto 1/T^{1/(d+1)}$, with σ being the conductivity and d the dimension.³⁹ As can be appreciated in Figure 3c, the VRH model with $d = 2$ fits experimental data almost perfectly up to about 40–45 K, while the high-temperature range is properly described by using the Arrhenius equation for thermal activation conduction $\rho(T) = \rho_0 e^{(\Delta/k_B T)}$, with Δ being an activation energy (a value of $\Delta \sim 6$ meV was obtained from the fit) and k_B the Boltzmann's constant (see Figure 3c). Therefore, from the analysis of the $R(T)$ curves we can conclude that the MIT induced in SIO films by reducing the thickness is of Anderson localization type due to disorder, in good agreement with previous reports.^{24,26}

The possibility of inducing an Anderson-type MIT by reducing film thickness suggests that resistivity of SIO thin films may be sensitive to different stimuli, especially for a thickness close to the critical one; therefore, it may be a good alternative for obtaining a strong RS response and thus of interest for the implementation of RS devices. For this purpose, we have approached the study of local I – V curves measured at room temperature by C-AFM of SIO thin films. To illustrate our findings, we present in Figure 4 details (below 100 nA) of the I – V curves on samples at both extremes of the thickness series (i.e., 2 and 26 nm). Results at intermediate thickness (5 nm) as well as the full IV curves may be found in the Supporting Information. In all cases hysteretic I – V curves are observed indicative of RS behavior. An anticlockwise behavior, where a positive sample voltage induces the low-resistance state (LRS) and a negative sample voltage induces the high-resistance state (HRS), is found. I – V curves were measured by applying a voltage sweep between +5 and –5 V with no current limitation. Figure 4a displays the I – V curves corresponding to the 2 nm thick film. As it can be seen, the current intensity remains constant and near zero until the threshold voltage value of about 2 V is reached, at which a sudden increase of the current takes place (indicated by arrow 1 in the figure). After reaching +5 V, the sample remains in the LRS returning to 0 V through the superior limit of the graph along the path denoted by arrow 2. In the negative voltage range, the I – V curve starts at the LRS, and the current is continuously increasing for voltages up to –5 V (trajectory marked by arrow 3). Upon reaching this voltage, the I – V curve

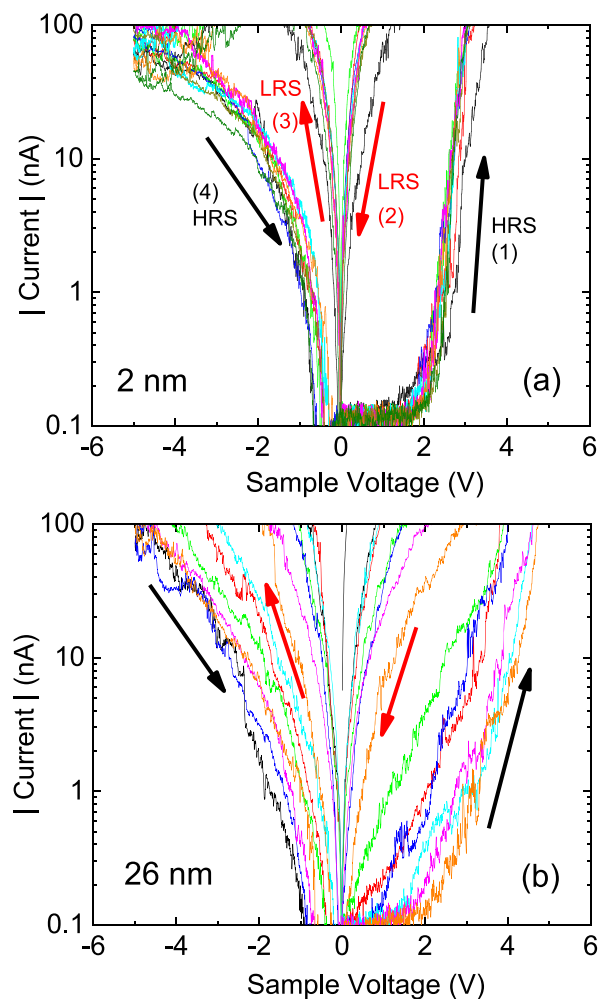


Figure 4. C-AFM I – V curve details in fresh SIO samples: (a) 2 nm thick film; (b) 26 nm thick film. The different colors of the curves represent the different consecutive voltage cycles between +5 and –5 V. The different arrows indicate the direction of the curves and their current resistance state (HRS: black; LRS: red).

returns to the HRS along the path indicated by arrow 4. Figure 4b depicts I – V curves corresponding to the 26 nm thick sample. In this latter case resistance changes in a continuous way, and no well-defined resistance states separated by a clear voltage threshold are observed. The similarity of the measured I – V curves in both samples suggests that the mechanism behind the observed variations of resistance is the same in both cases. However, the absence of a clear voltage threshold in the case of the thick sample suggests the absence of a well-defined energy transition separating the LRS and HRS.

A deeper insight into the RS process in SIO samples may be obtained by performing current maps over extended areas in both HRS and LRS states. Nevertheless, the significant statistical gain has the drawback that measurements are more aggressive and time-consuming than the local I – V curves. Performing a C-AFM map implies to move the AFM tip back and forth several times in the same area of the sample. The continuous scanning deteriorates the electrical tip–sample contact after a few cycles. This well-known drawback in C-AFM analysis of RS phenomena is usually attributed to tip contamination.⁴⁰ Experimentally, we have observed that capping of the SIO film surface with a noncontinuous layer of Pt nanoparticles (NPs) is useful to perform the C-AFM

maps. This beneficial effect of the Pt NPs avoids degradation of the tip–sample electrical contact either by reducing the degradation of film surface or by enhancing tip lifetime since brushing with Pt nanoparticles reduces tip contamination. Thus, current maps were performed in 26 nm films with their surface partially covered with platinum NPs (see further details in the Supporting Information). Figure 5a presents a 50×50

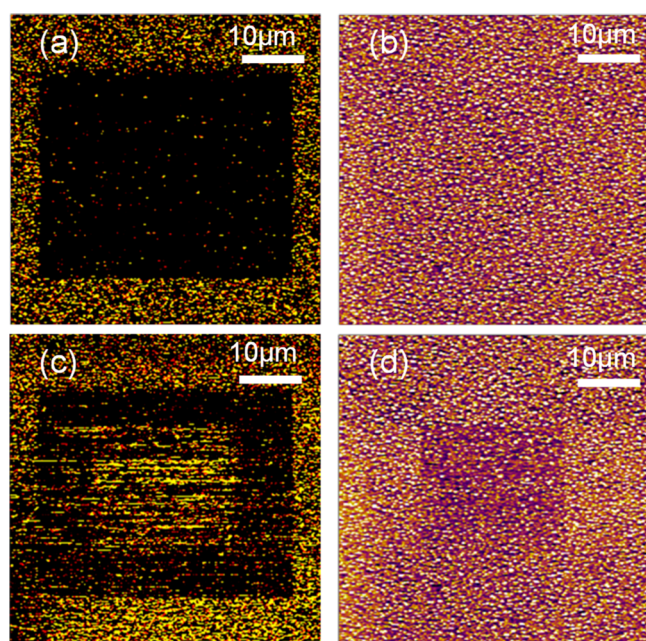


Figure 5. C-AFM current maps (a, c) and topography images (b, d) of a 26 nm SIO/STO sample with Pt NPs on the top obtained simultaneously. (a) Current map showing a $35 \times 35 \mu\text{m}^2$ zone set into the HRS. (b) Topography of the same zone showing no changes in the surface topography. (c) Current map of the same zone after resetting a $20 \times 20 \mu\text{m}^2$ zone to the LRS. (d) Topography image of the same zone, where minor changes in the topography can be noticed in the switched area.

μm^2 current map measured at low voltage (0.2 V) and 570 nN of normal load after the scanning of the central $35 \times 35 \mu\text{m}^2$ area at the negative bias voltage (-5 V) applied to the sample. A clear reduction of the conductivity can be observed in a central square (dark area) that corresponds to the established HRS. In contrast, the surrounded brighter area shows a higher current and corresponds to the pristine state. Figure 5b shows the topography image of the same zone measured simultaneously; no changes in the topography of the area switched into HRS are appreciated. Figure 5c shows a current map of the same zone measured after the scanning of the central $20 \times 20 \mu\text{m}^2$ area at $+3$ V applied to the sample. Now three different states can be observed: the pristine state at the outer parts of the current map, the HRS represented as a darker square ring, and finally the LRS depicted by a central bright square. Similar to the I – V curves in Figure 4, HRS was induced by negative sample voltage (-5 V), and it can be reversed to LRS by scanning at positive sample voltage ($+3$ V). The associated topography measurement is also shown in Figure 5d. Some minor topography changes are detected in the central area switched into LRS. They are represented by a slightly darker contrast, indicating a local decrease of the film height, which, in principle, could be caused by the removal of the Pt NPs or by a local compression of the film. Nevertheless, since accumu-

lations of NPs were not observed along outer rims of the scanning area, and the current intensity in this central zone even increases, NPs removal should be discarded as a possible explanation of the observed changes of the film's topography. On the other hand, because of the difficulties to reset the zone into LRS, a higher normal load (1140 nN) was applied during the scanning performed at $+3$ V. This increment in the normal load of the AFM tip may well be responsible for the observed local film compression.

Even with the increase of the normal load in the positive voltage scan, the switching into LRS was more difficult to achieve than the switching into HRS. One possible reason for this behavior is the occurrence of undesired reactions at the sample surface for high enough positive voltages due to local anodic oxidation,³⁸ decreasing the stability of the current measurements. To avoid these reactions, the sample voltage used to reset the surface into the LRS was decreased to a value of $+3$ V (instead of $+5$ V). This reduction in the reset voltage is probably the main reason for the less pronounced and stable switching into LRS displayed in Figure 5c.

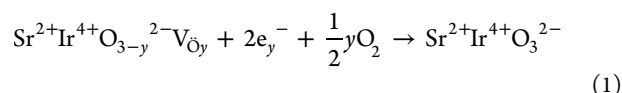
DISCUSSION

There is a large diversity of mechanisms proposed to explain RS phenomena.^{3–7} In the particular case of TMOs, redox-based mechanisms, driven by the motion of cations (coming from the electrodes) or defects such as oxygen vacancies, have attracted much attention.^{2,3,9} Two different categories can be distinguished: filamentary RS, consisting in the creation of filament of cations or vacancies in a TMO film sandwiched between two electrodes,¹ and interface RS, in which this process of ionic migration occurs at the interface between the metallic electrode and the active insulating oxide.⁸ Because of the in-plane geometry used in this study for the I – V measurements (the current path goes from AFM tip, through the sample surface, and finally to a metal contact placed on the sample surface), only interface RS should be considered.

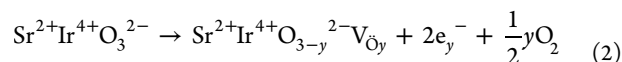
In correlated metals such as SIO, the variation on the concentration of oxygen vacancies can modify the valence of the surrounding metal cations. Because the oxygen vacancies substitute an oxygen position, the surrounding cations must adapt their valence to compensate for the charge variation. Therefore, new electrons would fill Ir orbitals changing the Fermi level and electric properties.¹¹ Depending on the type of majority charge carriers, this valence change will result in an increase (decrease) of the resistivity in the case of holes (electrons).² It is worth noting that the nature of the majority charge carriers in SIO thin films is not clearly established yet. As a semimetal, SIO is expected to have a conduction mechanism that involves both electrons and holes.^{19,27} Nevertheless, small differences in the charge carrier density could be critical for the RS mechanism. Recent results based on magnetotransport and thermoelectric measurements suggest that electrons and holes have similar densities and mobilities.²⁷ However, given the small unbalance between them²⁷ and the degree of disorder present in our films (considering the appearance of Anderson localization), it seems reasonable to consider that both electrons and holes could be the majority charge carriers in SIO films. Therefore, two similar mechanisms are proposed to explain the observed RS behavior in SIO films.

If electrons are considered the majority charge carriers, the change in the oxygen vacancies' concentration would be driven by their internal migration within a film induced by an

externally applied electric field.⁴¹ When a positive voltage is applied to the sample (negative voltage to AFM tip), oxygen vacancies would migrate toward the AFM tip, thus increasing the Fermi level. The subsequent rise of the electron concentration at the tip–sample interface would decrease the contact resistance and therefore transform the sample surface into the LRS. On the other hand, negative sample voltage (positive voltage at the AFM tip) would act reversely, expelling the vacancies from the tip–sample interface and thus decreasing the electron concentration and conductivity of the sample surface and leading it to HRS. Alternatively, if holes are considered the majority charge carriers, oxygen vacancies could be incorporated or removed from the interface by a redox reaction at the film surface triggered by an externally applied electric field.⁴² Contrary to the previous case, vacancies decrease the conductivity in hole-like systems since they are considered as acceptors scavengers. Positive voltage applied to sample would cause the reduction of the atmosphere's oxygen and the incorporation of oxygen anions into the oxide matrix, removing the vacancies from the interface according to eq 1.



Then, the Fermi level would decrease, while the hole density and the conductivity would increase and transform the sample surface beneath the AFM tip into the LRS. The system can be reversed into the HRS by applying negative voltage to the sample. In this case, the following oxidation reaction takes place:



With this reaction oxygen anions would be removed from the matrix, leaving vacancies behind. These vacancies would reduce drastically the number of holes and raise up the Fermi level, reducing this way the conductivity. Although both films seem to follow the same mechanism for the changes of resistance, the two set of I – V curves present notable differences. Figure 4b, corresponding to the 26 nm thick sample, shows smoothly rising I – V curves for the positive voltage range from 0 V to the saturation of the current detector. On the other hand, Figure 4a, corresponding to the 2 nm thick film, which has undergone MIT, shows an almost zero current up to a clear voltage threshold value of about 2 V, when an abrupt increase of the current intensity occurs. This different behavior is closely related to the differences in the band structures of the films that are induced by the MIT. On one hand, it is reported that thick SIO films (such as the employed 26 nm thick one) behave as a semimetal with electrons and holes having similar densities.^{18,19,27} On the other hand, even though the band structure of very thin films (such as the 2 nm thick one) has not been measured so far, thickness reduction may trigger the appearance of an Anderson-type MIT transition with strong carriers' localization.^{24,26} Furthermore, the aperture of a Mott gap in ultrathin SIO films has been recently documented.²⁸ With this picture in mind, the behavior of a thick SIO film (26 nm) reflects changes of resistance in a system with continuous energy levels having thus a smooth increase of the current. Moreover, the shift of the Fermi level would bring the system into a state with higher density of states, finally giving higher conductivity and setting it into the LRS. On the other hand, in

the case of the very thin film (2 nm), as long as the Fermi energy lies inside localized states, charge carrier's mobility is seriously hampered or even suppressed, and the current would be almost zero. Nevertheless, when the Fermi level crosses the mobility edge, an energy transition between localized and extended states takes place; for high enough positive voltage, an abrupt increase of the current would be observed, and obviously the system would be switched in the LRS with a higher conductivity.

CONCLUSIONS

The local transport properties of SrIrO₃ thin films prepared by RF sputtering on top of the (001)-SrTiO₃ substrates have been analyzed as a function of the film's thickness. Macroscopic measurements of the film's resistivity as a function of temperature allow demonstrating that an Anderson-type MIT transition can be induced, triggered by thickness reduction, below ~3 nm. On the other hand, SIO films exhibit hysteretic I – V curves indicative of RS behavior irrespective to their thickness. I – V curves show directional RS depending on the polarity of the applied voltage; thus, it can be classified as bipolar RS. Additionally, because of the particular experimental setup used, it is concluded that the observed RS is of interface type in which RS takes place at the interface between the metal electrode (AFM tip) and the SIO film. Electric field pulses promote oxygen vacancies migration through the interface; then, to maintain electrical neutrality, a valence change of the cations nearby takes place and therefore a modification of the charge carriers' density and of the position of the Fermi level. However, the features of the RS process are clearly different in the case of very thin samples (below 3 nm), where the appearance of the MIT, with the concomitant carriers' localization, is reflected in the existence of a well-defined voltage threshold value separating the low- and high-resistance states. In contrast, in thicker films with semimetallic behavior I – V curves present a continuous smooth variation of resistance, without a clear threshold voltage, making evident the absence of an energy sharp transition separating high- and low-resistance states. In this case, changes of resistance by applying voltage pulses are simply associated with the variation of charge carriers' density due to the migration of oxygen vacancies. In spite of the different behaviors, the same mechanisms involving oxygen vacancies are claimed to explain the observed results irrespective of the nature of the majority charge carriers, electrons or holes. Current maps performed with voltage values above the threshold value and of different polarity allow demonstrating the writing/erasing processes, making evident the feasibility of the system for the implementation of Re-RAMs.

ASSOCIATED CONTENT

Supporting Information

The Supporting Information is available free of charge on the ACS Publications website at DOI: 10.1021/acsaem.9b00519.

nonconformal capping of the SIO surface with Pt nanoparticles to improve C-AFM measurements; complete I – V curves of SIO thin films (2 and 26 nm); details of the I – V curve showing resistive switching for SIO film at intermediate thickness (5 nm) (PDF)

■ AUTHOR INFORMATION

Corresponding Author

*E-mail: apomar@icmab.es.

ORCID 

Benjamín Martínez: 0000-0001-9879-7748

Alberto Pomar: 0000-0002-5855-2356

Notes

The authors declare no competing financial interest.

■ ACKNOWLEDGMENTS

We acknowledge financial support from the Spanish Ministry of Science, Innovation and Universities through Severo Ochoa Program (SEV-2015-04969), MAT2015-71664-R (HETEROCS), and RTI2018-099960-B-I00 (SPINCURIOX) and funding from the European Union's Horizon 2020 research and innovation program under the Marie Skłodowska-Curie grant agreement no. 645658 (DAFNEOX Project) and FEDER Program. B.V. and Z.K. acknowledge the support of the Serbian Ministry of Education, Science and Technological Development (projects OI171005 and III45018).

■ ABBREVIATIONS

AFM, atomic force microscopy; C-AFM, conductive atomic force microscopy; MIT, metal–insulator transition; RS, resistive switching; LRS, low-resistance state; HRS, high-resistance state; Re-RAM, resistive random access memory; SIO, SrIrO₃; TMO, transition metal oxide; SOC, spin–orbit coupling; RSM, reciprocal space map; rms, root-mean-square; I–V, intensity–voltage; MIR, Mott–Ioffe–Regel; MIM, metal–insulator–metal.

■ REFERENCES

- (1) Waser, R.; Aono, M. Nanoionics-Based Resistive Switching Memories. *Nat. Mater.* **2007**, *6*, 833–840.
- (2) Sawa, A. Resistive Switching in Transition Metal Oxides. *Mater. Today* **2008**, *11*, 28–36.
- (3) Waser, R.; Dittmann, R.; Staikov, C.; Szot, K. Redox-Based Resistive Switching Memories Nanoionic Mechanisms, Prospects, and Challenges. *Adv. Mater.* **2009**, *21*, 2632–2663.
- (4) Lee, T.; Chen, Y. Organic Resistive Nonvolatile Memory Materials. *MRS Bull.* **2012**, *37*, 144–149.
- (5) Jeong, D. S.; Thomas, R.; Katiyar, R. S.; Scott, J. F.; Kohlstedt, H.; Petraru, A.; Hwang, C. S. Emerging Memories: Resistive Switching Mechanisms and Current Status. *Rep. Prog. Phys.* **2012**, *75*, No. 076502.
- (6) Yang, J. J.; Strukov, D. B.; Stewart, D. R. Memristive Devices for Computing. *Nat. Nanotechnol.* **2013**, *8*, 13–24.
- (7) Scott, J. C.; Bozano, L. D. Nonvolatile Memory Elements Based on Organic Materials. *Adv. Mater.* **2007**, *19*, 1452–1463.
- (8) Bagdzevicius, S.; Maas, K.; Boudard, M.; Burriel, M. Interface-Type Resistive Switching in Perovskite Materials. *J. Electroceram.* **2017**, *39*, 157–184.
- (9) Mehonic, A.; Kenyon, A. J. Resistive Switching in Oxides. In *Springer Series in Surface Sciences*; Jupille, J., Thornton, G., Eds.; Springer International Publishing: Cham, 2015; Vol. 58, pp 401–428.
- (10) Peña, L.; Garzón, L.; Galceran, R.; Pomar, A.; Bozzo, B.; Konstantinovic, Z.; Sandiumenge, F.; Balcells, L.; Ocal, C.; Martinez, B. Macroscopic Evidence of Nanoscale Resistive Switching in La_{2/3}Sr_{1/3}MnO₃ micro-Fabricated Bridges. *J. Phys.: Condens. Matter* **2014**, *26*, 395010.
- (11) Janod, E.; Tranchant, J.; Corraze, B.; Querré, M.; Stoliar, P.; Rozenberg, M.; Cren, T.; Roditchev, D.; Phuoc, V. T.; Besland, M. P.; Cario, L. Resistive Switching in Mott Insulators and Correlated Systems. *Adv. Funct. Mater.* **2015**, *25*, 6287–6305.

- (12) Zhang, L.; Pang, B.; Chen, Y. B.; Chen, Y. Review of Spin–Orbit Coupled Semimetal SrIrO₃ in Thin Film Form. *Crit. Rev. Solid State Mater. Sci.* **2018**, *43*, 367–391.

- (13) Cao, G.; Schlottmann, P. The Challenge of Spin-Orbit-Tuned Ground States in Iridates: A Key Issues Review. *Rep. Prog. Phys.* **2018**, *81*, No. 042502.

- (14) Biswas, A.; Jeong, Y. H. Growth and Engineering of Perovskite SrIrO₃ Thin Films. *Curr. Appl. Phys.* **2017**, *17*, 605–614.

- (15) Kim, J.; Casa, D.; Upton, M. H.; Gog, T.; Kim, Y. J.; Mitchell, J. F.; Van Veenendaal, M.; Daghofer, M.; Van Den Brink, J.; Khaliullin, G.; Kim, B. J. Magnetic Excitation Spectra of Sr₂IrO₄ Probed by Resonant Inelastic X-Ray Scattering: Establishing Links to Cuprate Superconductors. *Phys. Rev. Lett.* **2012**, *108*, 177003.

- (16) Wan, X.; Turner, A. M.; Vishwanath, A.; Savrasov, S. Y. Topological Semimetal and Fermi-Arc Surface States in the Electronic Structure of Pyrochlore Iridates. *Phys. Rev. B: Condens. Matter Mater. Phys.* **2011**, *83*, 205101.

- (17) Shitade, A.; Katsura, H.; Kuneš, J.; Qi, X. L.; Zhang, S. C.; Nagaosa, N. Quantum Spin Hall Effect in a Transition Metal Oxide Na₂IrO₃. *Phys. Rev. Lett.* **2009**, *102*, 256403.

- (18) Liu, Z. T.; Li, M. Y.; Li, Q. F.; Liu, J. S.; Li, W.; Yang, H. F.; Yao, Q.; Fan, C. C.; Wan, X. G.; Wang, Z.; Shen, D. W. Direct Observation of the Dirac Nodes Lifting in Semimetallic Perovskite SrIrO₃ Thin Films. *Sci. Rep.* **2016**, *6*, 30309.

- (19) Moon, S. J.; Jin, H.; Kim, K. W.; Choi, W. S.; Lee, Y. S.; Yu, J.; Cao, G.; Sumi, A.; Funakubo, H.; Bernhard, C.; Noh, T. W. Dimensionality-Controlled Insulator-Metal Transition and Correlated Metallic State in 5d Transition Metal Oxides Sr_{n+1}Ir_nO_{3n+1} (n = 1, 2, and ∞). *Phys. Rev. Lett.* **2008**, *101*, 226402.

- (20) Domingo, N.; Lopez-Mir, L.; Paradinas, M.; Holy, V.; Zelezny, J.; Yi, D.; Suresha, S. J.; Liu, J.; Rayan Serrao, C.; Ramesh, R.; Ocal, C.; Marti, X.; Catalan, G. Giant Reversible Nanoscale Piezoresistance at Room Temperature in Sr₂IrO₄ Thin Films. *Nanoscale* **2015**, *7*, 3453–3459.

- (21) Wang, C.; Seinige, H.; Cao, G.; Zhou, J. S.; Goodenough, J. B.; Tsoi, M. Electrically Tunable Transport in the Antiferromagnetic Mott Insulator Sr₂IrO₄. *Phys. Rev. B: Condens. Matter Mater. Phys.* **2015**, *92*, 115136.

- (22) Seinige, H.; Williamson, M.; Shen, S.; Wang, C.; Cao, G.; Zhou, J.; Goodenough, J. B.; Tsoi, M. Electrically Tunable Transport and High-Frequency Dynamics in Antiferromagnetic Sr₂IrO₇. *Phys. Rev. B: Condens. Matter Mater. Phys.* **2016**, *94*, 214434.

- (23) Zhang, L.; Liang, Q.; Xiong, Y.; Zhang, B.; Gao, L.; Li, H.; Chen, Y. B.; Zhou, J.; Zhang, S. T.; Gu, Z. Bin; Yao, S. H.; Wang, Z.; Lin, Y.; Chen, Y. F. Tunable Semimetallic State in Compressive-Strained SrIrO₃ Films Revealed by Transport Behavior. *Phys. Rev. B: Condens. Matter Mater. Phys.* **2015**, *91*, No. 035110.

- (24) Biswas, A.; Kim, K.-S.; Jeong, Y. H. Metal Insulator Transitions in Perovskite SrIrO₃ Thin Films. *J. Appl. Phys.* **2014**, *116*, 213704.

- (25) Gruenewald, J. H.; Nichols, J.; Terzic, J.; Cao, G.; Brill, J. W.; Seo, S. S. A. Compressive Strain-Induced Metal–Insulator Transition in Orthorhombic SrIrO₃ Thin Films. *J. Mater. Res.* **2014**, *29*, 2491–2496.

- (26) Wu, F.-X.; Zhou, J.; Zhang, L. Y.; Chen, Y. B.; Zhang, S.-T.; Gu, Z.-B.; Yao, S.-H.; Chen, Y.-F. Metal-Insulator Transition in SrIrO₃ with Strong Spin-Orbit Interaction. *J. Phys.: Condens. Matter* **2013**, *25*, 125604.

- (27) Manca, N.; Groenendijk, D. J.; Pallecchi, I.; Autieri, C.; Tang, L. M. K.; Telesio, F.; Mattoni, G.; McCollam, A.; Picozzi, S.; Caviglia, A. D. Balanced Electron-Hole Transport in Spin-Orbit Semimetal SrIrO₃ Heterostructures. *Phys. Rev. B: Condens. Matter Mater. Phys.* **2018**, *97*, No. 081105.

- (28) Groenendijk, D. J.; Autieri, C.; Girovsky, J.; Martinez-Velarte, M. C.; Manca, N.; Mattoni, G.; Monteiro, A. M. R. V. L.; Gauquelin, N.; Verbeeck, J.; Otte, A. F.; Gabay, M.; Picozzi, S.; Caviglia, A. D. Spin-Orbit Semimetal SrIrO₃ in the Two-Dimensional Limit. *Phys. Rev. Lett.* **2017**, *119*, 256403.

- (29) Schütz, P.; Di Sante, D.; Dudy, L.; Gabel, J.; Stübinger, M.; Kamp, M.; Huang, Y.; Capone, M.; Husanu, M. A.; Strocov, V. N.;

Sangiovanni, G.; Sing, M.; Claessen, R. Dimensionality-Driven Metal-Insulator Transition in Spin-Orbit-Coupled SrIrO₃. *Phys. Rev. Lett.* **2017**, *119*, 256404.

(30) Connell, J. G.; Isaac, B. J.; Ekanayake, G. B.; Strachan, D. R.; Seo, S. S. A. Preparation of Atomically Flat SrTiO₃ Surfaces Using a Deionized-Water Leaching and Thermal Annealing Procedure. *Appl. Phys. Lett.* **2012**, *101*, 98–101.

(31) Groenendijk, D. J.; Manca, N.; Mattoni, G.; Kootstra, L.; Gariglio, S.; Huang, Y.; Van Heumen, E.; Caviglia, A. D. Epitaxial Growth and Thermodynamic Stability of SrIrO₃/SrTiO₃ Heterostructures. *Appl. Phys. Lett.* **2016**, *109*, No. 041906.

(32) Zhao, J. G.; Yang, L. X.; Yu, Y.; Li, F. Y.; Yu, R. C.; Fang, Z.; Chen, L. C.; Jin, C. Q. High-Pressure Synthesis of Orthorhombic SrIrO₃ Perovskite and Its Positive Magnetoresistance. *J. Appl. Phys.* **2008**, *103*, 103706.

(33) Fruchter, L.; Schneegans, O.; Li, Z. Z. Anisotropy and Interaction Effects of Strongly Strained SrIrO₃ Thin Films. *J. Appl. Phys.* **2016**, *120*, No. 075307.

(34) Rondinelli, J. M.; Caffrey, N. M.; Sanvito, S.; Spaldin, N. A. Electronic Properties of Bulk and Thin Film SrRuO₃: Search for the Metal-Insulator Transition. *Phys. Rev. B: Condens. Matter Mater. Phys.* **2008**, *78*, 155107.

(35) Hussey, N. E.; Takenaka, K.; Takagi, H. Universality of the Mott-Ioffe-Regel Limit in Metals. *Philos. Mag.* **2004**, *84*, 2847–2864.

(36) Deng, X.; Mravlje, J.; Žitko, R.; Ferrero, M.; Kotliar, G.; Georges, A. How Bad Metals Turn Good: Spectroscopic Signatures of Resilient Quasiparticles. *Phys. Rev. Lett.* **2013**, *110*, No. 086401.

(37) Ramakrishnan, T. V.; Lee, P. A. Disordered Electronic Systems. *Rev. Mod. Phys.* **1985**, *57*, 287.

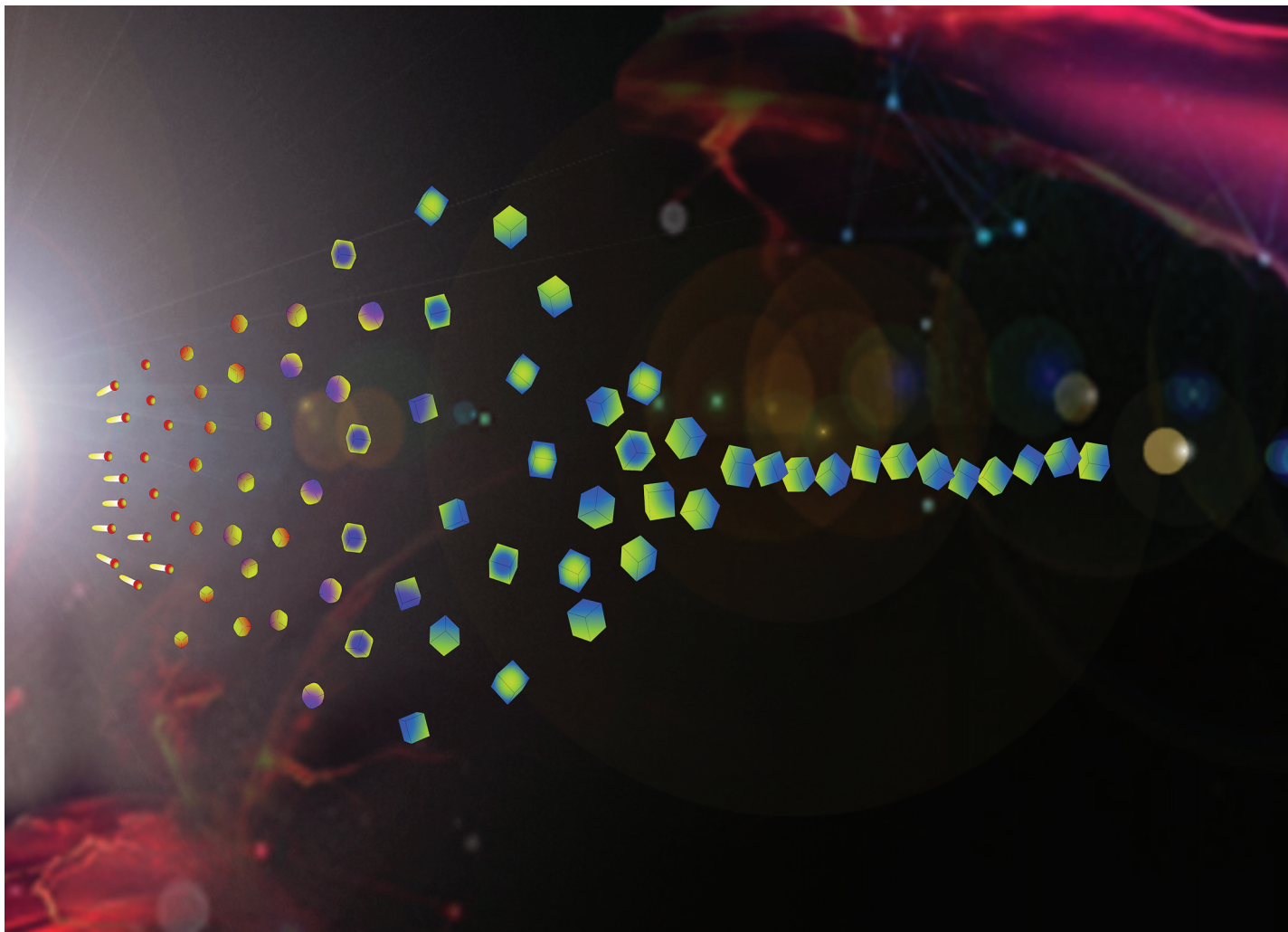
(38) Kim, K. W.; Lee, J. S.; Noh, T. W.; Lee, S. R.; Char, K. Metal-Insulator Transition in a Disordered and Correlated SrTi_{1-x}Ru_xO₃ System: Changes in Transport Properties, Optical Spectra, and Electronic Structure. *Phys. Rev. B: Condens. Matter Mater. Phys.* **2005**, *71*, 125104.

(39) Mott, N. *Metal-Insulator Transitions*, 2nd ed.; Taylor & Francis: London, 1998.

(40) Lanza, M.; Celano, U.; Miao, F. Nanoscale Characterization of Resistive Switching Using Advanced Conductive Atomic Force Microscopy Based Setups. *J. Electroceram.* **2017**, *39*, 94–108.

(41) Cui, Y.; Peng, H.; Wu, S.; Wang, R.; Wu, T. Complementary Charge Trapping and Ionic Migration in Resistive Switching of Rare-Earth Manganite TbMnO₃. *ACS Appl. Mater. Interfaces* **2013**, *5*, 1213–1217.

(42) Lee, H. S.; Choi, S. G.; Park, H. H.; Rozenberg, M. J. A New Route to the Mott-Hubbard Metal-Insulator Transition: Strong Correlations Effects in Pr_{0.7}Ca_{0.3}MnO₃. *Sci. Rep.* **2013**, *3*, 1704.

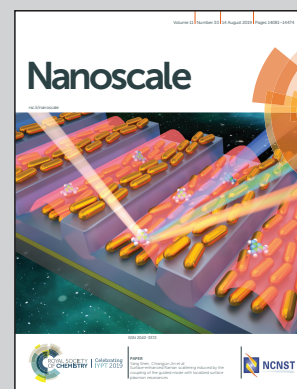


Showcasing research from the ACNM group, Instituto de Ciencia de Materiales de Barcelona – CSIC, Barcelona, Spain.

Spontaneous in-flight assembly of magnetic nanoparticles into macroscopic chains

This image illustrates the spontaneous self-assembly of magnetic nanoparticles into macroscopic chains by using a combination of magnetron sputtering and gas aggregation techniques. This research, a DAFNEOX collaboration, studies the behaviour of complex agglomerates at the nano- and mesoscales. The low-kinetic energy of the particles inside the magnetron vacuum chamber and strong dipolar magnetic interaction between individual nanoparticles are responsible for particles' agglomeration at very low volume fractions. These results prove that the cluster gun technique can go beyond single particle fabrication into controlled and reproducible self-assembly of nanoparticles.

As featured in:



See Igor Stanković *et al.*, *Nanoscale*, 2019, 11, 14194.



Cite this: *Nanoscale*, 2019, **11**, 14194

Spontaneous in-flight assembly of magnetic nanoparticles into macroscopic chains†

Lluís Balcells,  ^a Igor Stanković,  ^{*b} Zorica Konstantinović,  ^c Aanchal Alagh,  ^a Víctor Fuentes,  ^a Laura López-Mir,  ^a Judit Oró,  ^a Narcis Mestres,  ^a Carlos García,  ^d Alberto Pomar  ^a and Benjamin Martínez  ^a

Knowing the interactions controlling aggregation processes in magnetic nanoparticles is of strong interest in preventing or promoting nanoparticles' aggregation at wish for different applications. Dipolar magnetic interactions, proportional to the particle volume, are identified as the key driving force behind the formation of macroscopic aggregates for particle sizes above about 20 nm. However, aggregates' shape and size are also strongly influenced by topological ordering. 1-D macroscopic chains of several micrometer lengths are obtained with cube-shaped magnetic nanoparticles prepared by the gas-aggregation technique. Using an analytical model and molecular dynamics simulations, the energy landscape of interacting cube-shaped magnetic nanoparticles is analysed revealing unintuitive dependence of the force acting on particles with the displacement and explaining pathways leading to their assembly into long linear chains. The mechanical behaviour and magnetic structure of the chains are studied by a combination of atomic and magnetic force measurements, and computer simulation. The results demonstrate that [111] magnetic anisotropy of the cube-shaped nanoparticles strongly influences chain assembly features.

Received 17th March 2019,
Accepted 17th May 2019

DOI: 10.1039/c9nr02314c

rscl.li/nanoscale

1 Introduction

Magnetic nanoparticles (NPs), nanocomposites, and artificial array materials hold a special place in many areas of technology, not only because of their distinct properties, resulting from their discrete nature and high surface to volume ratios, but also because they can be used as functional building blocks for the design and development of new devices.^{1–4} Nowadays, different technological fields, such as catalysis,^{5,6} storage devices,^{7,8} or biomedicine,⁹ have gained strong industrial and economical relevance boosting research activities in these areas. Each of these applications has different requirements regarding shape, size and degree of particles' aggregation, and therefore, knowing the interactions controlling aggregation processes is of strong interest for preventing or promot-

ing nanoparticles' aggregation at wish for different applications. The growing activity in this field has also stimulated the development of methods for the production of NPs and clusters with precise control of size, shape, and composition. In this regard, gas aggregation sources,^{10–12} which allow obtaining core/shell structured nanoparticles^{6,10} easily, were recently modified to achieve also high production rates¹³ as in the case of wet chemistry synthesis techniques. Nevertheless, these latter methods have limitations in terms of the simplicity of the process, typically involving several processing steps, surface contamination and size distribution. In contrast, gas-phase techniques, operating in a controlled atmosphere, present a way for the fabrication and manipulation of magnetic particles with well-defined composition and a narrow size distribution. Fabrication of magnetic NPs with cuboidal geometry is of particular interest due to their higher surface to volume ratios, high packing density, and high surface adhesion due to atomically flat touching faces. These features are of high interest for applications in fields as diverse as catalysis,⁵ high-density magnetic storage devices,⁸ or tailored superlattices.^{14,15} In addition, single domain magnetic configurations are mandatory for applications requiring hard magnetic behaviour, such as hard disk drives⁷ or permanent magnets.¹⁶ The magnetic configuration of constitutive single domain elements in these applications is not determined solely by the magnetic material bulk properties (Fe, Co, *etc.*). Gatel *et al.*¹⁷ theoretically and experimentally analysed the

^aInstitut de Ciència de Materials de Barcelona, ICMAB-CSIC, Campus de la UAB, 08193 Bellaterra, Catalonia, Spain

^bScientific Computing Laboratory, Center for the Study of Complex Systems, Institute of Physics Belgrade, University of Belgrade, 11080 Belgrade, Serbia. E-mail: igor.stankovic@ipb.ac.rs

^cCenter for Solid State Physics and New Materials, Institute of Physics Belgrade, University of Belgrade, Pregrevice 118, 11080 Belgrade, Serbia

^dDepartamento de Física & Centro Científico Tecnológico de Valparaíso-CCTVal, Universidad Técnica Federico Santa María, Av. España 1680, Casilla 110-V, Valparaíso, Chile

†Electronic supplementary information (ESI) available. See DOI: 10.1039/C9NR02314C



magnetic configuration dependence on iron cube size. They showed a surprising transition between single-domain [001] and [111] (vortex) states with an increasing dimension of iron nanocubes from 25 to 27 nm. In turn, magnetic anisotropy changes the way particles assemble.^{18–22} In consequence, for sub-25 nm magnetic NPs in suspension, the dominant interaction changes from anisotropic, long-range, and oriented dipole–dipole coupling to the van der Waals short-range surface coupling.^{23,24} The potential of magnetic nanocubes to form mesoscopic structures with different geometries is enormous.²⁵ For example, at an air–liquid interface, large monolayers assembled by 9 nm magnetic cubes were created,^{14,26} whereas, in the same study, 13 nm NPs formed helices in the presence of a magnetic field.¹⁴

Here, we report on the spontaneous self-assembly of magnetic nanoparticles into macroscopic chains. We show that dipolar interactions, proportional to the particle volume, are the key driving force behind the formation of macroscopic aggregates for particle sizes above about 20 nm; however, aggregates' shape and size are strongly influenced by topological ordering. 1-D macroscopic chains of several μm lengths are obtained with 25 nm magnetic iron/iron-oxide cube-shaped magnetic nanoparticles fabricated by using a modified gas-aggregation technique, which allows particles to assemble in flight without the influence of the medium. Self-assembled chains represent an excellent paradigmatic system to explore the self-assembly process of individual particles and a unique model system to study the behaviour of complex agglomerates without dumping of the medium (*i.e.*, only conservative inter-particle forces are present) at the nano- and mesoscale ranges. Since magnetic cores and shells may have different magnetic anisotropies, a detailed characterisation of the NPs is required for understanding the magnetic structure of the nanocubes. We have used an exact analytical theory to predict the energetically favourable configurations. Our results reveal a complex energy landscape leading to non-intuitive force distance characteristics. Then, to validate the developed model, a series of magnetic and atomic force microscopy measurements and computer simulations were performed. Applying both techniques simultaneously, the processes governing self-assembly of magnetic cubes into single-stranded chains are unveiled.

2 Methods

2.1 Experiment

Arrays of core/shell NPs (see Fig. 1) were prepared in a home-built cluster source connected to a vacuum system with base pressure in the low 10^{-6} Torr. More details on the synthesis procedure are given in ESI.† A 1 inch diameter DC magnetron with a Fe target (99.95% purity) was operated typically at 50 W. During deposition, the flux of argon was fixed at 80 sccm, and the measured pressures were in the low 10^{-3} Torr. Si wafers were used as substrates, except for the samples aimed for transmission electron microscopy (TEM) imaging that were deposited on carbon-coated grids.

The particle-size characterisation was determined by scanning electron microscopy (SEM) using a QUANTA FEI 200 FEG-ESEM microscope. TEM, HRTEM and scanning TEM (STEM) in the high angle annular dark field (HAADF) mode were used to study the crystallinity, morphology, size, and dispersion of the samples. TEM images were obtained using a JEOL JEM 1210 transmission electron microscope operating at 120 kV. HRTEM and STEM images were acquired in a FEI Tecnai F20 microscope operating at 200 kV. Digital diffraction patterns (DDP) of power spectra were obtained from selected regions in the micrographs. No electron-beam-induced changes were observed in any of the analyzed particles.²⁷ Energy dispersive X-ray (EDS) spectra were acquired using an EDAX super ultrathin window (SUTW) X-ray detector.

Micro-Raman spectra were obtained by using a Jobin–Yvon T64000 monochromator with a liquid nitrogen cooled charge-coupled detector. The excitation light was a 514.5 nm line from an Ar-ion laser. The incident and scattered beams were focused by an Olympus microscope using a $\times 50$ objective to give a spot size of *ca.* 2 μm . Unpolarised Raman spectra were measured due to the polycrystalline nature of the samples.

MFM measurements were performed with an MFP-3D Asylum Research microscope using ASYMFM-HC probes with CoPt/FePt (30 nm) coating. In MFM the phase shift near the cantilever resonance was used to map stray fields by measuring in the amplitude modulation AFM (AM-AFM) mode and keeping the cantilever at a constant height (57 nm) from the surface. Variable field module (VFM2) from Asylum Research,

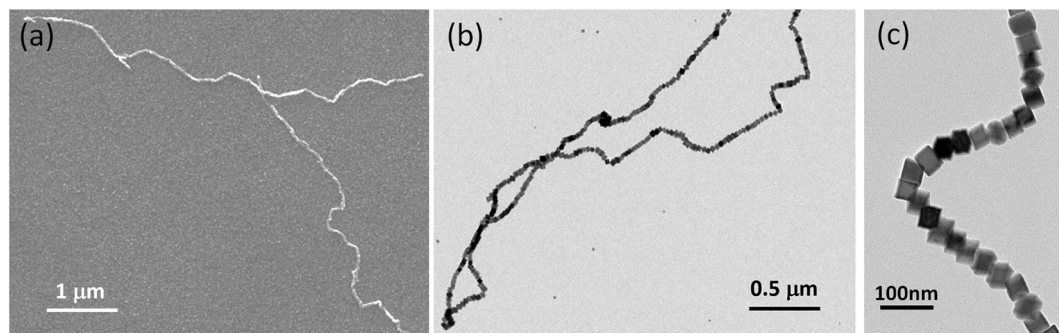


Fig. 1 Magnetic assembly of nanocubes in a single strand. (a) SEM and (b) TEM images of the micrometre long single-stranded core/shell iron NP chain. (c) TEM image of a chain segment.



which was a special holder with a rotating permanent magnet, was used to apply a magnetic field of up to 1 T in the in-plane direction.

2.2 Analytical theory and molecular dynamics simulations

We combine two modelling techniques to extract information on the mechanical response of a free-standing chain: (i) We utilise an exact analytical model to obtain a stray magnetic field from a single cubic magnetic domain and calculate the interaction energy of the two cubes,²⁸ as shown in Fig. 3. (ii) The mechanical properties of the magnetic chains are explored using cubes consisting of elements as suggested by John *et al.* (coarse-grained cube structure) and Zhang *et al.* (magnetic dipole approximation).^{24,29–31} Analytical calculations for uniformly magnetised cubes and simulations assumed monodisperse perfect cubes. Two systems were considered: one with magnetisation orientated in the [001] crystallographic direction, and the other with magnetisation along the [111] direction.

The John *et al.*²⁹ and Zhang *et al.*³⁰ models are modified in two ways: first, instead of only one central dipole, 9 were used (*cf.* illustration in Fig. S5†). In this way, we have reproduced the potential energy profile of the two cubes calculated analytically (see comparison in Fig. S6†). Also, additional dipoles take into account the interaction of the touching corners of the cubes, which is important for the stability of the chain under extension (see ESI Movies†). If we analyse a case of extreme extension, the magnetic energy of two [111] magnetised cubes with aligned magnetisation touching on the corner, which comes from the two adjacent corner cubes (radius $(2 - \sqrt{3})d/2 \approx 0.133d$), is two times larger than the energy stemming from the interaction between the central cubes (radius $d/2$), *i.e.*, $u_{\text{corner}}/u_{\text{central}} = 54 - 30\sqrt{3} \approx 2$. And second, an additional 24 spheres were placed inside of the cube edges in order to make a smooth surface and avoid pinning during mechanical manipulation. The geometrical contact between two cubes is simulated using the WCA potential for the spheres (truncated and shifted Lennard-Jones potential, elsewhere called also soft-sphere model) (see ESI)†.

We study the mechanical behaviour of the model system by means of molecular dynamics computer simulations: the cubes are represented by the WCA potential and carry nine-point dipoles as described in Fig. S5.† This model was the basis for zero temperature molecular dynamics simulation. The simulations of the breaking of the chains were performed by different forces exerted on the chain ends. Molecular dynamics was used to study mechanical manipulation of the free-standing chain composed of magnetic cubes. The total force was the conservative force of inter-particle interactions, *i.e.*, contact WCA potential of 33 (overlapping) spheres and 9 dipoles. The dipolar interactions were treated with cut-off at $r_{\text{cut}}/d = 8$ (*cf.* ref. 24), and a non-periodic simulation box was used. The constituent spheres within the cube were moved as rigid body data structures in every time step. The rotational degrees of freedom are also governed by the equations of motion for torque and angular velocity of the spheres. The

total force and torque on each cluster representing one cube are computed as the sum of the forces and torques on its constituent particles at each time step. The dipole orientation is accordingly rotated with the cube as a single entity. The rotation was implemented by creating internal data structures for each rigid body and performing time integration on these data structures.^{32,33} The mass of the cuboid corresponded to a 25 nm iron cube and was distributed over constitutive dipolar particles. MD step was $t = 4$ ps and the total length of the MD simulation 400 ns.

3 Arrays of core/shell iron nanocubes and their magnetic properties

3.1 One-step synthesis by gas-aggregation and magnetron sputtering

NPs used in this work were prepared by a combination of magnetron sputtering and gas-aggregation techniques.^{6,10} Sputtered Fe atoms are cooled down in the cluster source and then aggregate by collisions with flowing Ar gas at room temperature (see Fig. S1† for a schematic of the cluster gun setup in ESI†). Differential pumping drags the clusters through a small nozzle into the deposition chamber. The gas is flowing through the 3 mm slit at the rate of $80 \text{ cm}^3 \text{ min}^{-1}$, *i.e.*, with a speed 0.14 m s^{-1} . The kinetic energy of the particle due to the surrounding gas flow is around 10 meV. Clusters are therefore softly deposited onto a sample holder at room temperature, thus retaining their original shape.⁶ Mean NP size can be controlled by careful selection of the deposition conditions (sputtering power, travelling distances, chamber pressure, and Ar gas flow rates).¹⁰ The travel distance affects the size of the particles. Actually, the smaller travelling distance results in reduced particle size as observed in ESI.† The particles under 12 nm have a hollow magnetite shell structure (*cf.* Fig. 2a and ESI).† This appears as a consequence of the Kirkendall effect, *i.e.*, somewhat faster diffusion of iron towards the shell than oxygen atoms inwards. As a result, iron from the centre of the cluster diffuses towards the oxygen-rich shell leaving a void space inside the cube. We should note that in any case, natural oxidation makes it difficult to stabilise pure iron NPs after preparation.³⁴ Previous reports showed that an oxygen-rich atmosphere in the deposition chamber during processing leads to the formation of Fe/Fe oxide clusters.³⁵ In our case, the oxygen partial pressure (medium-vacuum conditions) in addition to the Ar atmosphere warrants reactive sputtering; thus, a chemical reaction occurs leading to the formation of iron oxide shells before clusters are deposited on the substrate.

In the present work, for a 5 cm travel distance, a large number of shell only particles were obtained with an average particle size of about 8 nm. Meanwhile, for an 8 cm travel distance, an increase of the average particle size to 15 nm is observed at the expense of the number of generated particles (see Fig. S2).† In addition, particles produced in the latter case were mainly of a core/shell structure (see Fig. 2a). Further



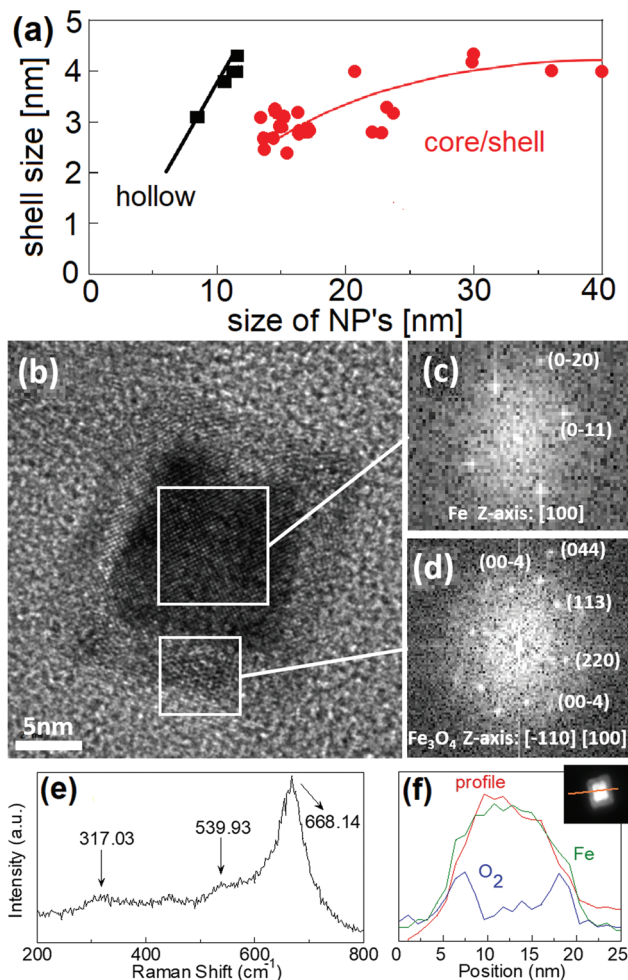


Fig. 2 Shell size as a function of the NP grain size obtained from different TEM images (a). Below 12 nm, the NPs show a hollow structure; above this size, they show a core/shell configuration. Lines are a guide to the eyes. High-resolution Z-contrast TEM image of a Fe/Fe oxide core/shell NP (b). The large areas marked by the full lines are used for the identification of (c) the Fe core and (d) the Fe oxide shell. (e) Raman spectrum confirming the presence of Fe₃O₄ in the shell. (f) EDX line profile analysis of one single NP making evident the core/shell structure.

increase of the travel distance resulted in a small increase in the particle size: for a 11 cm travel distance, the average size was 16 nm, while for 13 cm, the average size was 17 nm. When the oxidation process is dominated by the Cabrera–Mott-like mechanism, initial oxidation rapidly develops a 4 nm-thick oxide shell around the Fe core. A similar effect has been observed in the synthesis of iron core/shell cubes from solution,³⁶ where a partial oxidation promoted the formation of core/shell nanostructures with an iron core trapped inside the oxide shell. Following this procedure, single crystalline iron NPs covered by a crystalline Fe₃O₄ shell can be fabricated. For small enough NPs, *i.e.* below about 9–10 nm, the Cabrera–Mott like oxidation mechanism produces hollows. In contrast, for particles above 12 nm, a core/shell structure is obtained (see Fig. S3).[†] This evolution can be clearly observed in Fig. 2a. To promote spontaneous self-assembly, stronger interactions

between core/shell magnetic cubes are required, *i.e.*, a strongly magnetised iron core is necessary. Therefore, nanocube dimensions should be larger than 12 nm in order to have a core/shell structure with a strongly magnetised core.

3.2 Composition of magnetic cubes

A detailed characterization of the chemical composition of the NPs is required in order to understand the magnetic structure of the cubes, due to the different magnetic anisotropies of the core and shell parts. The synthesis of single crystalline iron NPs, ideally covered by a crystalline Fe₃O₄ (magnetite) shell, has been proposed as a promising way to improve chemical stability and preserve a substantial iron core.^{37,38} Pure iron NPs are unstable when brought to ambient conditions transforming into iron/iron-oxide core/shell structured NPs.

A high-resolution Z-contrast TEM image is shown in Fig. 2b. A well-defined square shape of the particle with a sharply defined 4 nm shell can be appreciated. The reflections of the power spectrum pattern (see Fig. 2c and d) obtained by TEM can be indexed using the corresponding reflections of cubic Fe for the core and the spinel structure for the shell. Since TEM and electron diffraction techniques cannot distinguish between the different oxide phases, Raman spectroscopy was used to identify them. Different bands in the Raman spectrum correspond to specific frequency vibration modes, allowing distinguishing different oxide phases. In particular, maghemite differs from magnetite because it contains no divalent iron species. Due to the fact that the ionic radius of Fe(II) is larger than that of Fe(III), Fe(II)–O bonds are longer and weaker than Fe(III)–O bonds; this shifts up the vibration frequency in the Raman spectrum, and hence, Raman analysis allows distinguishing between these two phases. In the Raman spectrum displayed in Fig. 2e, the main band centred at 668 cm⁻¹ and the weaker peaks at *ca.* 539 and 317 cm⁻¹ have been assigned to A_{1g}, T_{2g}, and E_g vibrational modes of magnetite, respectively.³⁹ EDX line profile analysis of one single particle shows the absence of oxygen at the core and the progressive increase at the surface (Fig. 2f), thus giving further support for the idea of core/shell nanostructures of Fe/Fe₃O₄.

3.3 Self-assembled chains of magnetic cubes

The NPs are synthesised with different sizes and directly deposited on various substrates in a controlled atmosphere. The presence of pure metallic iron is important since it promotes higher magnetisation value and, therefore, better functionality compared to iron–nickel alloys or iron-oxide particles. Far from “being weak”, dipolar magnetism plays a leading role in stabilising the structural order in the arrangements of NPs in one dimensional structures. During assembly into chains, the particles move and self-assemble in flight without the influence of the medium. Previously, dipolar chains were associated with ground states of [001] magnetic easy axis, whereas those with [111] oriented magnetic easy axis were expected to adopt square lattice structures, *i.e.*, to form clusters.^{14,19,26} Mehdizadeh Taheri *et al.*²⁶ reported magnetic chains of iron cubes with a core/shell structure featuring fully touching faces



of the cubes and synthesised at 0.02 vol% concentration. The chains reported here are created in a controllable way in an even more diluted system.

The magnetic dipolar attraction of particles above 25 nm is strong enough to form long single stranded chains, while for particles less than 25 nm, only individual particles and clusters are detected (see Fig. 1). Individual particles are not observed, which implies that the growth of chains is completed before being deposited on the substrate. Therefore, the substrate does not influence chain formation. The emergence of chains is actually driven by interplay of the geometrical contact between two cubes and the magnetic dipolar interaction. It is worth mentioning that both contact and dipolar interaction are anisotropic. The nanometer-sized iron cubes display a fixed and permanent magnetic dipole moment that is strong enough to form single strand chains.

The chain morphology provides an insight into the particle magnetic anisotropy. The magnetic moment of magnetically anisotropic materials tends to align with an easy axis, which is an energetically favourable direction of spontaneous magnetisation. Actually, the direction of the easy axis of the magnetic cube can be controlled by the core to shell ratio. There are indeed two possible magnetic easy axes: one governed by the magnetite shell lying in the [111] direction and the other governed by the iron core along the [001] direction.^{17,37,40} Since hollow, *i.e.*, magnetite shell-only, cubes have dimensions below 12 nm, dipolar interactions are small and therefore no chains are formed along the [111] orientation. It is evident that the direction of the net magnetic orientation relative to the cube geometry changes the structure of the observed chains (see Fig. 3a and b). For chains of nanocubes, the assembly mechanism drives the particles to adopt structures that create a head–tail configuration, very much like chains of magnetic beads. In the case of [001] direction, this leads to deep central minimum of magnetic potential energy with respect to the lateral movement of the magnetic particles and consequently to quite stiff configuration (*cf.*, ESI Movie 1†). On the contrary, when the magnetisation is along the principal axis, *i.e.*, [111] direction, the structure becomes more flexible (*cf.*, ESI Movie 2†). The configuration with minimal energy has a zig-zag dipole vector placement (*cf.*, the top left panel where particles are placed in face-to-face configuration in Fig. 3b) of the magnetic cubes, and the system can extend to a head–tail configuration by relative rotation of the cubes (*cf.*, also ref. 24). The relative rotation is taking place along the bottom of the circular valley shown in Fig. 3b. The valley is denoted as a white circle and is tilted towards the centre of mass (c.m.) of the bottom particle. The highest point of the valley is when the c.m. of the upper particle is above the edge corner of the particle below. This corresponds to head–tail placement of the dipoles. Head–tail configuration of dipoles shows about a 20% energy increase along the valley. At the minimum energy point (zig-zag configuration), the distance between their centres of mass Δr_2 is equal to the cube size $\Delta r_2 = d$. At the furthest point of the circular minimum valley (*i.e.*, when c.m. of one particle is above the corner of the other), the centres of mass

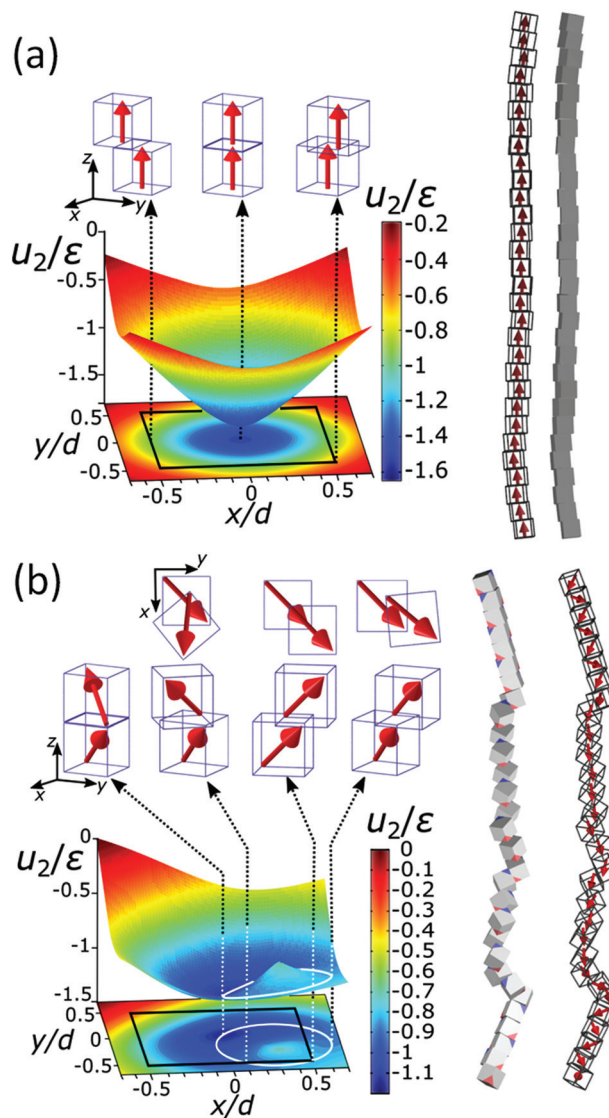


Fig. 3 The energy landscape obtained analytically and a schematic view of the chain of the particles for [001] (a) and [111] (b) easy magnetisation axis directions. Interaction energy per particle u_2 for pure iron particles is scaled with the reference interaction energy $\epsilon = 25$ eV (see also Fig. S4†). The contour of the bottom cube is shown with the black solid line in the energy diagrams. The white solid line circle in the energy diagram for the [111] magnetisation direction represents the bottom of the circular potential valley. Three representative configurations with [001] magnetisation directions are shown with side views in the upper panels of (a). From left to right: centre of mass (c.m.) of one particle in the middle of the edge of the other, one particle on top of the other, and c.m. of one particle on the corner of the other. Four representative configurations with [111] magnetisation are shown with top and side views. The configurations are shown in the upper panels of (b), from left to right: (i) zig-zag configuration, where the particles are above each other with the surfaces placed face-to-face (the zig-zag configuration is the most stable one), (ii) c.m. of the upper particle is at the edge of the contour of the lower particle, (iii) head–tail configuration when the upper particle's c.m. is at the edge of the bottom particle and (iv) the so-called unstable configuration, when c.m. of the upper particle is furthest from the contour of the bottom.



of the particles are 22% further apart than at global minimum (as shown in Fig. 4, $\Delta r_2/d = \sqrt{3}/2$, *i.e.*, $\Delta r_2 = 30.6$ nm for 25 nm particles).

Fig. 4a gives the calculated dependence of the magnetic restoring force on the distance between the centres of mass of the two particles. We see that there are two maximums of the force (roughly equal in size). The first peak, which is very narrow, locks particles in a zig-zag position while the second broad peak keeps the chain connected. The reason for the existence of the first narrow maximum is that particles have first to move laterally in order to come out of the zig-zag position (see also Fig. 2b). The shape of the magnetic potential energy valley further enhances the flexibility of the whole structure. The contour of the potential valley crosses the edge of the

bottom cube, and a large part of it lies outside of the contour of the bottom cube. In this area, the two-particle system becomes unstable. This means that one cube can flip over the edge of the other cube and change in the other equivalent position on the different side of the cube (see ESI Movie 3†). This is also a local minimum of the restoring force (*cf.*, $\Delta r_2 = 30$ nm) (Fig. 4a). Also, during extension, cubes can partially detach when they are in a head-tail configuration, *i.e.*, stay only attached by the corner-to-corner contact, *i.e.*, at $\Delta r_2 = \sqrt{3}d \approx 43$ nm. In the corner-to-corner configuration, the parts of the chain have a large rotational freedom. This is also a configuration from which we observe that the chain finally detaches (breaks). Still, the local maximum of the force is at roughly $\Delta r_2 \approx 39$ nm, and at this point, particles are still overlapping.

The response of the chain of magnetic cubes to strain is shown in Fig. 4b. We observe that the chain is extending and contracting quasi-elastically (see ESI Movie 4†). The energy u follows a parabolic curve, and the elastic force acting on the ends of the chain increases linearly with the extension of the chain. The estimated elastic coefficient of the chain is 0.21 ± 0.05 meV nm⁻². The elastic extension of the chain continues up to the point where the maximal force per particle approaches roughly 3 pN (see Fig. 4a) at roughly $\Delta r_2 = 40$ nm. It is also observed that there is a pinning of the parts of the chain in an energetically less favourable configuration, and as a result, the energy depends on the history of the mechanical manipulation.

3.4 Magnetic configuration of the chains

Our results demonstrate that dipole-dipole interactions, with the resulting magnetic moment pointing along the chain, are the origin of the chain formation. It is important to note,

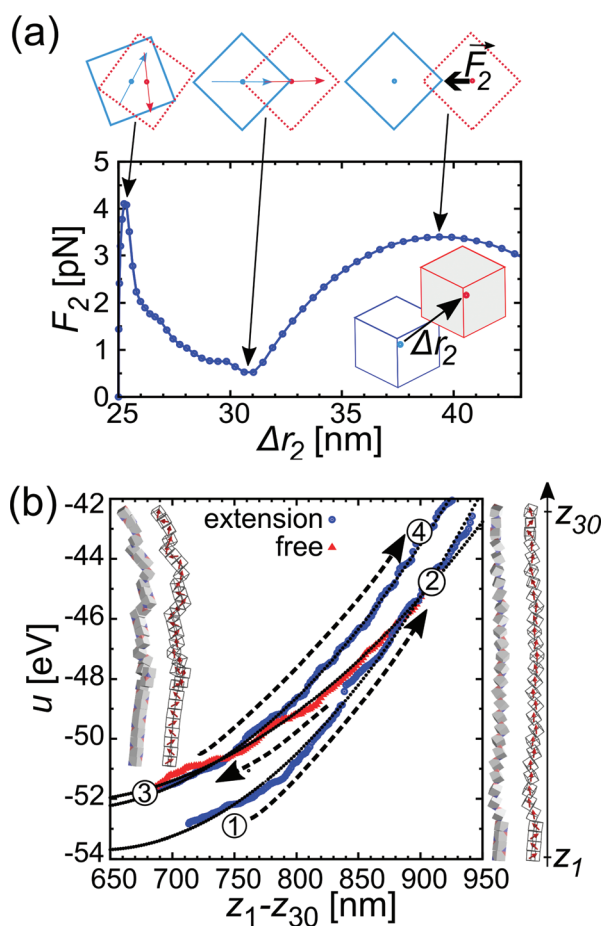


Fig. 4 Calculated magnetic force and energy evolution under extension. (a) Restoring force dependence on the centre of the mass distance between two 25 nm iron particles as one of the particles follows a minimal energy path and is obtained using an analytical model. (b) Energy per particle dependence on the length of the chain during repeated extension of the chain consisting of 30 iron cubes of 25 nm. Circles (blue) show energy evolution with the distance of its ends and triangles (red) evolution when the chain ends are free and the chain contracts. The extension/free chain retraction results are obtained from simulation. Dashed arrows show the direction of extension/contraction and numbers 1–4 sequence. Black lines are parabolas interpolated through the simulated data.

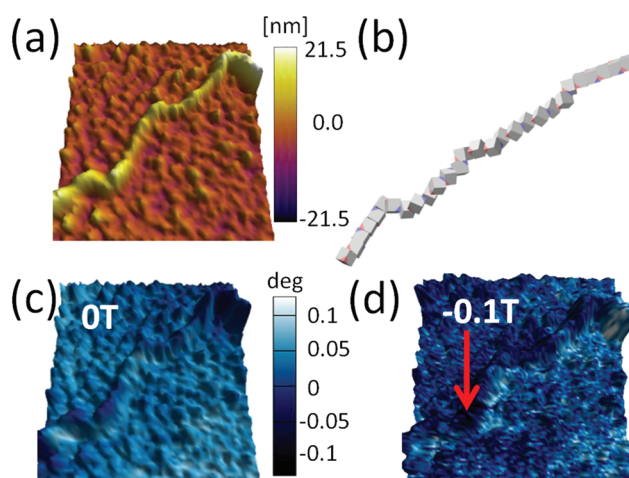


Fig. 5 (a) Topography image of part of the chain of iron/iron oxide core/shell magnetic cube. (b) Chain of magnetic cubes with [111] magnetisation obtained by computer simulation (see text). (c) MFM image of the chain before the magnetic field is applied, and (d) under 0.1 T in-plane magnetic field. The direction of the magnetic field is indicated by the red arrow.



however, that particles in the chain spontaneously turn their magnetisation in the presence of other magnetic particles to minimise their own energy. Still, the spontaneous magnetic moment of particles has to be along their easy magnetic axis, *i.e.*, [111] direction^{17,40} relative to cube geometry. When an externally applied magnetic field is stronger than the magnetic field of the particles itself, the magnetisation starts to align itself with the external field independent of easy axis direction. Therefore, an estimation of the dipole interaction can be obtained by applying the magnetic field perpendicular to the chain and measuring the field necessary to rotate their magnetic moment out of the chain direction.

In Fig. 5, we show the magnetisation dependence of individual cubes of a representative part of a chain on the external magnetic field. The stray magnetic field generated by the chain is small when no external magnetic field is initially applied (*cf.* AFM topography and MFM^{41,42} measurement in Fig. 5a and c, respectively). A computer generated configur-

ation with similar morphology as in the experiment is also shown in Fig. 5b. The magnetic field necessary to rotate the magnetisation direction of the cubes is larger than 0.1 T (*cf.*, no significant difference between Fig. 5c and d). The small differences in the two figures are a consequence of local reorientation of magnetisation due to the applied field. Still the field is not strong enough to determine magnetisation of all particles.

A sequence of MFM measurements at magnetic field -0.5 T, 0 T, 0.5 T, and 0 T is depicted in Fig. 6. In order to study magnetisation reversal in an external magnetic field, a field larger than that necessary to rotate the magnetisation direction of the cubes was applied. It is found that at -0.5 T, the magnetisation of the chain is completely aligned along the external field direction (see Fig. 6a). Therefore, we can conclude that the local magnetic field generated by cubes in the chain is less than 0.5 T. In fact, the analytical results for uniformly magnetised iron cubes give 0.35 T in the centre of the neighbouring cube placed face-to-face in a zig-zag configuration and 0.15 T in the head-tail configuration (see ESI†). Initially, a -0.5 T external magnetic field was applied to magnetise the chain in one direction and then the external magnetic field was turned off so that a spontaneous reordering of magnetisation can take place. No remanence is found when the external field is set back to zero, as observed in Fig. 6a and b. The magnetisation direction, after the external field is switched off, is along the chain backbone. The magnetisation orientation is determined by the previously applied external

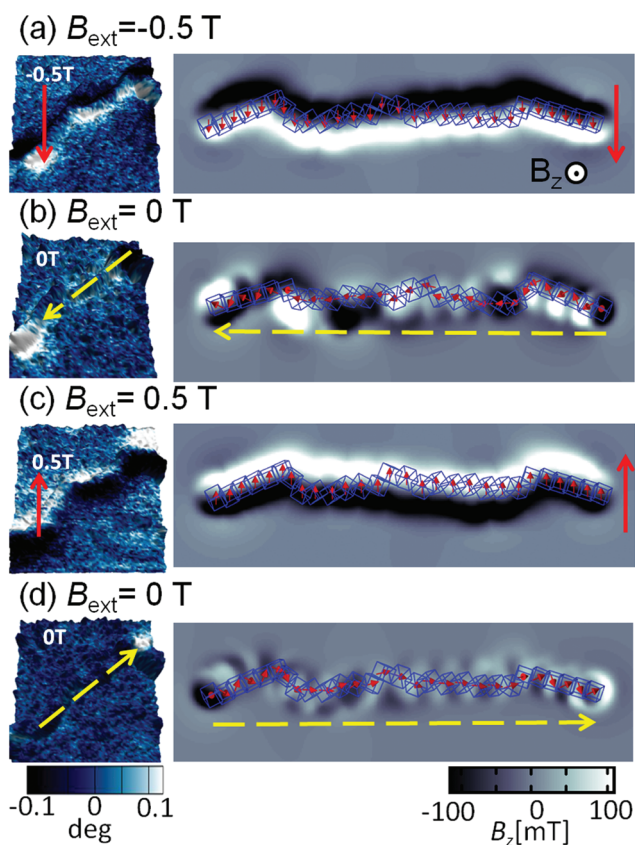


Fig. 6 Magnetic images of the chain of cubes. MFM images on left panels correspond to different magnetic fields applied in the following sequence (a) -0.5 T, (b) 0 T, (c) 0.5 T, and (d) 0 T. The direction of the applied magnetic field is indicated by a full line (red) and arrow, and magnetisation direction of the chain is indicated by dashed (yellow) arrow. The sequence of the changes of the magnetic field follows the order of the figures from the top (first) to the bottom (last). The visualisation of the magnetic field in the normal direction to the plane corresponding to the different magnetic configurations obtained from computer simulation is shown in the right panels.

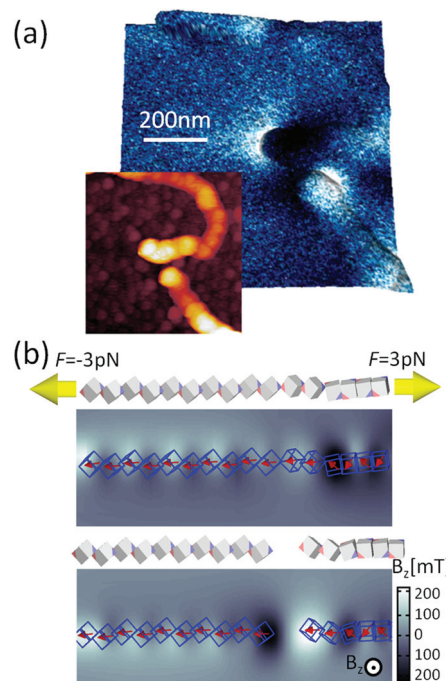


Fig. 7 Mechanical manipulation of the chain composed of magnetic nanocubes. (a) Topography and MFM image of a broken chain segment. (b) Force required to break the chain and the calculated magnetic field in the orthogonal direction of the plane.



magnetic field, as it can be observed at the corners in Fig. 6b. In the next step, a 0.5 T external field is applied in the opposite direction. As one would expect, after the magnetic field is switched off, the resulting configuration shows that the pole north and south of the individual cubes and the chain as whole have interchanged their positions. The visualisation of the sequence obtained from the computer simulation is shown in the right panels of Fig. 6.

The magnetic configuration of a broken chain is also shown in Fig. 7a. The MFM images illustrate that one end corresponds to the a north pole and other end to a south pole (the north and south poles are differentiated in the figure as light and dark contrasts), which is indicative of the magnetic moment aligned along the chain. This can be compared with the simulation results in Fig. 7e; the snapshots just before and after chain break-up are shown as well as the magnetic field perpendicular to the substrate plane. A constant force of 3 pN was applied on the terminal cubes. The initial configuration was a zig-zag magnetisation configuration where cubes are in face-by-face contact, seen on the right side of the panel in Fig. 7b. The transitions between these phases create the stray field. When the chain is finally broken, we observe at the two ends the stray field pointing up and down, similar to Fig. 7a.

4 Conclusions

We have shown that a combination of magnetron sputtering and gas aggregation techniques represents a powerful tool to generate complex structures of magnetic NPs in a single step fabrication process. Single-stranded micrometer-long chains made up of 25 nm magnetic nanocubes are obtained by spontaneous self-assembly. The morphology of these chains is remarkably different from those of spheres or fabricated in suspension, *i.e.*, they are long and single-stranded. It is found that dipolar magnetism is the driving force boosting chain formation and its structure reveals a tendency to keep connected under major degrees of structural strain in the process of formation and deposition. Using an exact analytical model and numerical simulations, we have estimated the magnetic energy scales governing the process. The low-kinetic energy of the particles inside the magnetron vacuum chamber and strong dipolar magnetic interaction between individual particles are responsible for agglomeration of the particles at very low volume fractions. The competition between anisotropic interactions and shape offers various pathways for self-assembly, each with exciting possibilities. Here, we have discussed self-assembly of 25 nm magnetic core/shell nanocubes with [111] magnetisation. Since anisotropies of iron and iron-oxide are different, *i.e.*, [001] and [111], respectively, the overall anisotropy of the cubes can be selected through different core/shell ratios controlled by gas-aggregation process parameters. As a general frame, the present results demonstrate that the cluster gun technique can go beyond fabrication of single particles into controlled and reproducible self-assembly of NPs as they form.

Conflicts of interest

There are no conflicts to declare.

Author contributions

L.I.B. and Z.K. designed the work. A.A. prepared the samples. V.F. and L.L-M. performed the SPM experiments, J.O. the TEM measurements, and N.M. the Raman experiments. I.S. developed the theory and performed the computations. C.G. verified the material parameters. I.S. and C.G. wrote the manuscript with the participation of L.I.B. and Z.K. A.P. and B.M. participated in the discussion of the results and the final version of the paper.

Acknowledgements

The authors acknowledge the financial support from European Commission H2020 project DAFNEOX (Grant No. 645658). I. S. and Z. K. acknowledge the support of Ministry of Education, Science, and Technological Development of Republic of Serbia – projects ON171017 and III45018. Financial support from Spanish Ministry of Economy and Competitiveness through the Severo Ochoa Programme for Centres of Excellence in R&D (SEV-2015-0496), RTI2018-099960-B-I00, and MAT2015-71664-R, co-financed by the European Regional Development Fund, is gratefully acknowledged. I.S. and C.G. acknowledge the financial support received from Proyecto CONICYT PIA/Basal FB 0821 and CONICYT MEC80170122. A.P., V.F. and Z.K. thank Sensor-INFIZ (Serbia) for the cooperation provided during their respective secondments. Numerical calculations were run on the PARADOX supercomputing facility at the Scientific Computing Laboratory of the Institute of Physics Belgrade.

References

- 1 A. Fernández-Pacheco, R. Streubel, O. Fruchart, R. Hertel, P. Fischer and R. P. Cowburn, *Nat. Commun.*, 2017, **8**, 15756.
- 2 R. Streubel, P. Fischer, F. Kronast, V. P. Kravchuk, D. D. Sheka, Y. Gaididei, O. G. Schmidt and D. Makarov, *J. Phys. D: Appl. Phys.*, 2016, **49**, 363001.
- 3 L. Wu, A. Mendoza-Garcia, Q. Li and S. Sun, *Chem. Rev.*, 2016, **116**, 10473–10512.
- 4 E. Bellido, N. Domingo, I. Ojea-Jiménez and D. Ruiz-Molina, *Small*, 2012, **8**, 1465–1491.
- 5 C. Dey, A. Chaudhuri, A. Ghosh and M. M. Goswami, *ChemCatChem*, 2017, **9**, 1953–1959.
- 6 L. Balcells, C. Martínez-Boubeta, J. Cisneros-Fernández, K. Simeonidis, B. Bozzo, J. Oró-Sole, N. Bagués, J. Arbiol, N. Mestres and B. Martínez, *ACS Appl. Mater. Interfaces*, 2016, **8**, 28599–28606.



- 7 N. Liakakos, T. Blon, C. Achkar, V. Vilar, B. Cormary, R. P. Tan, O. Benamara, G. Chaboussant, F. Ott, B. Warot-Fonrose, E. Snoeck, B. Chaudret, K. Soulantica and M. Respaud, *Nano Lett.*, 2014, **14**, 3481–3486.
- 8 L. Wu, P.-O. Jubert, D. Berman, W. Imaino, A. Nelson, H. Zhu, S. Zhang and S. Sun, *Nano Lett.*, 2014, **14**, 3395–3399.
- 9 E. Myrovali, N. Maniotis, A. Makridis, A. Terzopoulou, V. Ntomprougkidis, K. Simeonidis, D. Sakellari, O. Kalogirou, T. Samaras, R. Salikhov, M. Spasova, M. Farle, U. Wiedwald and M. Angelakeris, *Sci. Rep.*, 2016, **6**, 37934.
- 10 D. Llamosa, M. Ruano, L. Martinez, A. Mayoral, E. Roman, M. Garcia-Hernandez and Y. Huttel, *Nanoscale*, 2014, **6**, 13483–13486.
- 11 H. Haberland, M. Karrais and M. Mall, *Zeitschrift für Physik D Atoms, Molecules and Clusters*, 1991, vol. 20, pp. 413–415.
- 12 M. Mery, N. Orellana, C. A. Acevedo, S. Oyarzun, F. Araneda, G. Herrera, D. Aliaga, W. Creixell, T. Corrales and C. Romero, *Materials*, 2018, **11**, 2574.
- 13 L. Martínez, K. Lauwaet, G. Santoro, J. Sobrado, R. Peláez, V. J. Herrero, I. Tanarro, G. Ellis, J. Cernicharo, C. Joblin, Y. Huttel and J. Martin Gago, *Sci. Rep.*, 2018, **8**, 7250.
- 14 G. Singh, H. Chan, A. Baskin, E. Gelman, N. Repnin, P. Král and R. Klajn, *Science*, 2014, **345**, 1254132.
- 15 B. Bian, G. Chen, Q. Zheng, J. Du, H. Lu, J. P. Liu, Y. Hu and Z. Zhang, *Small*, 2018, **14**, 1801184.
- 16 K. Gandha, K. Elkins, N. Poudyal, X. Liu and J. P. Liu, *Sci. Rep.*, 2014, **4**, 5345.
- 17 C. Gatel, F. J. Bonilla, A. Meffre, E. Snoeck, B. Warot-Fonrose, B. Chaudret, L.-M. Lacroix and T. Blon, *Nano Lett.*, 2015, **15**, 6952–6957.
- 18 L. Rossi, J. G. Donaldson, J.-M. Meijer, A. V. Petukhov, D. Kleckner, S. S. Kantorovich, W. T. M. Irvine, A. P. Philipse and S. Sacanna, *Soft Matter*, 2018, **14**, 1080–1087.
- 19 J. G. Donaldson and S. S. Kantorovich, *Nanoscale*, 2015, **7**, 3217–3228.
- 20 R. Messina and I. Stanković, *Physica A: Statistical Mechanics and its Applications*, 2017, vol. 466, pp. 10–20.
- 21 R. Messina, L. A. Khalil and I. Stanković, *Phys. Rev. E: Stat., Nonlinear, Soft Matter Phys.*, 2014, **89**, 011202.
- 22 I. Stankovic, M. Dasic, J. A. Otalora and C. García, *Nanoscale*, 2019, **11**, 2521–2535.
- 23 A. Baskin, W.-Y. Lo and P. Král, *ACS Nano*, 2012, **6**, 6083–6090.
- 24 A. Satoh, *Modeling of magnetic particle suspensions for simulations*, CRC Press, 2017.
- 25 F. Mazuel, S. Mathieu, R. Di Corato, J.-C. Bacri, T. Meylheuc, T. Pellegrino, M. Reffay and C. Wilhelm, *Small*, 2017, **13**, 1701274.
- 26 S. Mehdizadeh Taheri, M. Michaelis, T. Friedrich, B. Förster, M. Drechsler, F. M. Römer, P. Bösecke, T. Narayanan, B. Weber, I. Rehberg, S. Rosenfeldt and S. Förster, *Proc. Natl. Acad. Sci. U. S. A.*, 2015, **112**, 14484–14489.
- 27 D. A. J. Herman, S. Cheong, M. J. Banholzer and R. D. Tilley, *Chem. Commun.*, 2013, **49**, 6203–6205.
- 28 R. Engel-Herbert and T. Hesjedal, *J. Appl. Phys.*, 2005, **97**, 074504.
- 29 B. S. John, A. Stroock and F. A. Escobedo, *J. Chem. Phys.*, 2004, **120**, 9383–9389.
- 30 X. Zhang, Z. Zhang and S. C. Glotzer, *J. Phys. Chem. C*, 2007, **111**, 4132–4137.
- 31 D. Luo, C. Yan and T. Wang, *Small*, 2015, **11**, 5984–6008.
- 32 S. Plimpton, *J. Comput. Phys.*, 1995, **117**, 1–19.
- 33 H. Kamberaj, R. J. Low and M. P. Neal, *J. Chem. Phys.*, 2005, **122**, 224114.
- 34 A. Pratt, L. Lari, O. Hovorka, A. Shah, C. Woffinden, S. P. Tear, C. Binns and R. Kröger, *Nat. Mater.*, 2014, **13**, 26.
- 35 Y. Qiang, J. Antony, A. Sharma, J. Nutting, D. Sikes and D. Meyer, *J. Nanopart. Res.*, 2006, **8**, 489–496.
- 36 A. Shavel, B. Rodríguez-González, M. Spasova, M. Farle and L. Liz-Marzán, *Adv. Funct. Mater.*, 2007, **17**, 3870–3876.
- 37 K. Leistner, M. Yang, C. Damm, S. Oswald, A. Petr, V. Kataev, K. Nielsch and K. L. Kavanagh, *Nanoscale*, 2017, **9**, 5315–5322.
- 38 S. Peng, C. Wang, J. Xie and S. Sun, *J. Am. Chem. Soc.*, 2006, **128**, 10676–10677.
- 39 O. N. Shebanova and P. Lazor, *J. Solid State Chem.*, 2003, **174**, 424–430.
- 40 C. Moya, A. M. Abdelgawad, N. Nambiar and S. A. Majetich, *J. Phys. D: Appl. Phys.*, 2017, **50**, 325003.
- 41 S. Schreiber, M. Savla, D. V. Pelekhov, D. F. Iscru, C. Marginean Selcu, P. Chris Hammel and G. Agarwal, *Small*, 2008, **4**, 270–278.
- 42 S. Sievers, K.-F. Braun, D. Eberbeck, S. Gustafsson, E. Olsson, H. W. Schumacher and U. Siegner, *Small*, 2012, **8**, 2675–2679.



Supplementary Information: Spontaneous in-flight assembly of magnetic particles into macroscopic chains

Lluís Balcells,[†] Igor Stanković,^{*,‡} Zorica Konstantinović,[¶] Aanchal Alagh,[†] Victor Fuentes,[†] Laura López-Mir,[†] Judit Oró,[†] Narcis Mestres,[†] Carlos García,[§] Alberto Pomar,[†] and Benjamin Martínez[†]

[†]*Institut de Ciència de Materials de Barcelona, ICMA-B-CSIC, Campus de la UAB, 08193 Bellaterra, Catalonia, Spain*

[‡]*Scientific Computing Laboratory, Center for the Study of Complex Systems, Institute of Physics Belgrade, University of Belgrade, 11080 Belgrade, Serbia.*

[¶]*Center for Solid State Physics and New Materials, Institute of Physics Belgrade, University of Belgrade, Pregrevica 118, 11080 Belgrade, Serbia*

[§]*Departamento de Física & Centro Científico Tecnológico de Valparaíso-CCTVal, Universidad Técnica Federico Santa María, Av. España 1680, Casilla 110-V, Valparaíso, Chile.*

E-mail: igor.stankovic@ipb.ac.rs

Synthesis procedure

Assembled iron nanocube chains are prepared in a gas phase cluster gun. The cluster source is quenching a hot iron vapor, steaming from magnetron head on the left side of Fig. S1, in a flowing stream of cool inert gas (argon) in aggregation chamber. The iron atoms condense

and crystallize during gradual cooling process, producing NPs with a low internal temperature. The NPs are then extracted into a high vacuum region through a slit nozzle at the end of an aggregation chamber. The distance from the magnetron sputtering head to the slit is the principal variable controlling NPs size. Another variable is the sputtering power that determines the rate at which NPs are produced. The inert gas and vapor mixture undergo supersonic expansion into a region maintained at a pressure below 10^3 Torr. The ionized beam leaves the aggregation chamber passes through a slit 3 mm to the high vacuum region differentially pumped with a flux of Ar of $80 \text{ cm}^3/\text{min}$.

The growth of the nanostructures by cluster gun technique depends on various parameters, such as Ar gas flow, cluster gun power, NPs traveling distance, etc. In present work, the size evolution of the core/shell iron/iron oxide NPs is studied at constant Ar flow. The first row in Fig. S2 shows the NP evolution with the growth distance. It is observed that a minimum distance of $d > 4 \text{ cm}$ is needed to collect NPs (see very scarce number of NPs for $d = 4 \text{ cm}$). In addition, for short growth distance ($d < 7 \text{ cm}$) the size variation is very fast, while at large distance ($d > 7 \text{ cm}$) no significant evolution is observed. At 5 cm travel distance average particle size is about 8 nm and at 8 cm distance an increase in particle size to 15 nm at the expense of the number of the generated particles was attained. The particles produced at 8 cm are dominantly of core/shell type. Further increase of the travel distance results in a small increase in the particle size: for 11 cm average size is 16 nm and for 13 cm average size is 17 nm. The lower row in Fig. S2 summarizes the evolution of the NP size with the gun power at fixed travel distance of 7 cm. In this case the size evolution is modest but the amount of NPs increase very fast. This work has been done without the use of a mass quadrupole that allows selecting the particle size.

Model

Magnetic NPs can have complex coupling involving both dipolar and exchange interactions. The atomic exchange interaction is relevant up to a length scale of 10 nm .¹ Thus, dipolar

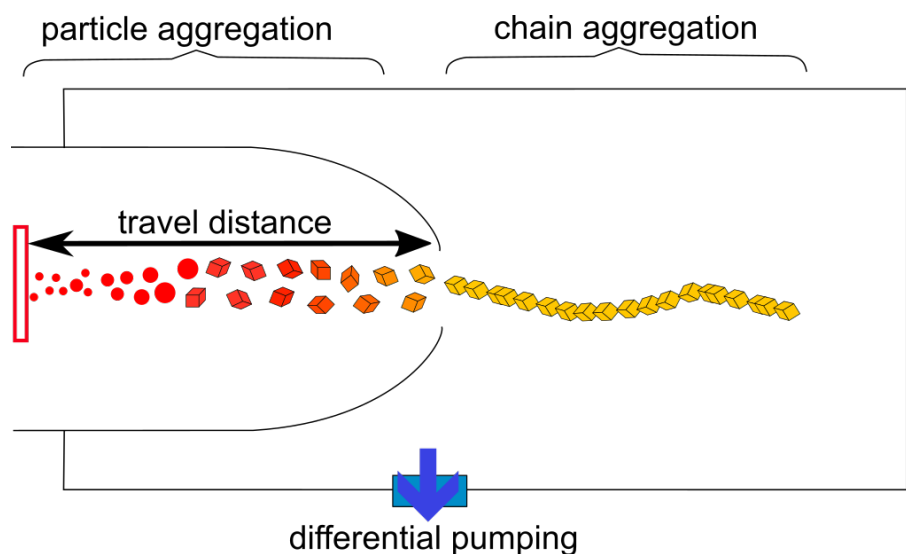


Figure S1: Scheme of the cluster gun, showing aggregation chamber, slit, and deposition chamber with differential pump exit.

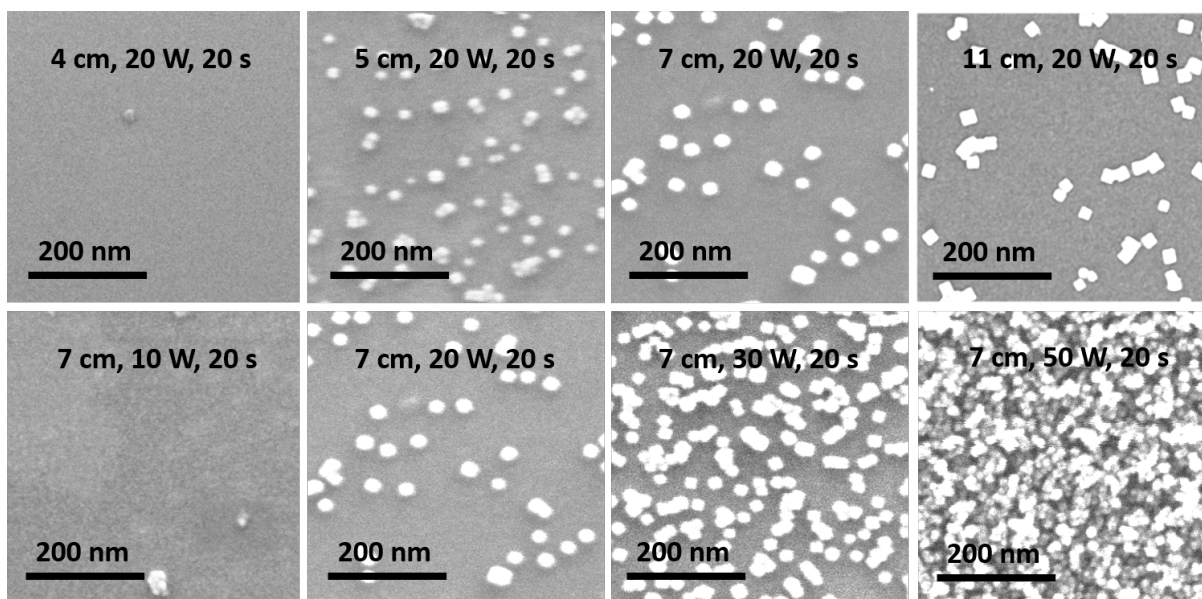


Figure S2: Field emission SEM images ($500 \times 500 \text{ nm}^2$) of core/shell iron NPs at constant Ar gas flow ($80 \text{ cm}^3/\text{min}$) and cluster gun power (20 W) as a function of NPs traveling distance (upper row). Lower row, SEM images of the obtained core/shell iron NPs as a function of cluster gun power at fixed ($80 \text{ cm}^3/\text{min}$) Ar gas flow and fixed traveling distance (7cm).

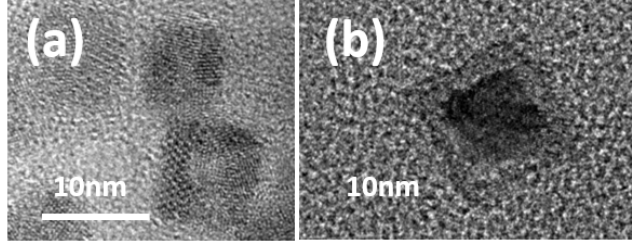


Figure S3: TEM images for NPs grown at different travel distance in the aggregation chamber (a) shell only particle are obtained for travel distance 5 cm and (b) core/shell particle for travel distances 11 cm.

coupling dominates in the formation of the structures on the length scales 10nm-100 μ m, with many potential applications.²⁻⁶ Due to shape anisotropy, small single domain magnets behave like uniaxial magnets. We characterize the system using dipole-dipole interaction potential: it is assumed that each particle carries identical dipolar (magnetic) moment with magnitude $M_0 = m_s d^3$ where m_s is the magnetization and d the size of the cube. In this work two magnetic easy axes are possible: the one governed by the magnetite shell lying in the [111], and the one induced by the iron core oriented along the [100] direction. The analytic expressions for the magnetic field, of a sphere or an infinite cylinder, are part of all classical magneto-static textbook. For complex geometries we need to employ numerical solvers. Still, solution for bar magnet, deduced from the Maxwell equations can be also obtained analytically. For a magnetic bar magnetized along the y -axis, i.e., [010]⁷ one finds:

$$B_x^{[010]}(x, y, z) = \frac{\mu_0}{4\pi} M_0 \sum_{k,l,m=1}^2 \log[z + (-1)^m z_b + A_{\text{sq}}^{klm}] \quad (1)$$

$$B_y^{[010]}(x, y, z) = -\frac{\mu_0}{4\pi} M_0 \sum_{k,l,m=1}^2 \frac{[y + (-1)^l y_b][x + (-1)^k x_b]}{|y + (-1)^l y_b||x + (-1)^k x_b|} \arctan\left\{ \frac{|x + (-1)^k x_b|[z + (-1)^m z_b]}{|y + (-1)^l y_b| A_{\text{sq}}^{klm}} \right\} \quad (2)$$

$$B_z^{[010]}(x, y, z) = \frac{\mu_0}{4\pi} M_0 \sum_{k,l,m=1}^2 \log[x + (-1)^k x_b + A_{\text{sq}}^{klm}] \quad (3)$$

where $A_{\text{sq}}^{klm} = \sqrt{[x + (-1)^k x_b]^2 + [y + (-1)^l y_b]^2 + [z + (-1)^m z_b]^2}$.

For a bar magnetized along the x -axis, it is sufficient to rotate the system in following

way: $B_x^{[100]}(x, y, z) = B_z^{[010]}(-y, x, z)$, $B_y^{[100]}(x, y, z) = -B_x^{[010]}(-y, x, z)$, and $B_z^{[100]}(x, y, z) = B_y^{[010]}(-y, x, z)$, and for a bar magnetized along the z -axis, $B_x^{[001]}(x, y, z) = B_x^{[010]}(x, z, -y)$, $B_y^{[001]}(x, y, z) = -B_z^{[010]}(x, z, -y)$, $B_z^{[001]}(x, y, z) = B_y^{[010]}(x, z, -y)$. Finally, for a magnetic field of a cube ($x_b = y_b = z_b$) magnetized along principal diagonal (i.e., [111]), magnetic field is the sum of the previous expressions, $\vec{B}^{[111]} = (\vec{B}^{[100]} + \vec{B}^{[010]} + \vec{B}^{[001]})/\sqrt{3}$. A significant uncertainty margin regarding magnetic moment of the magnetic particles exist. The hematite has small ($m_s \approx 2.2kAm^{-1}$), while magnetite and iron have a large spontaneous magnetization, i.e., $m_s \approx 480kAm^{-1}$ and $1600kAm^{-1}$, respectively.⁸

In case of pure iron particles, the reference magnetic interaction energy $\epsilon = \mu_0 M_0^2 / 4\pi d^3$, i.e., was estimated to be in the order of 25 eV, i.e., $10^3 k_B T$, where $T = 300K$ is the temperature and k_B is the Boltzmann's constant. The magnetic interaction energy ϵ decreases with increase of the iron oxide shell thickness, see Fig. S4. The magnetic field generated by one particle at the c.m. of the other particle (placed side by side) is $B_0 = \mu_0 M_0 / (2\pi d^3) = 160$ mT.

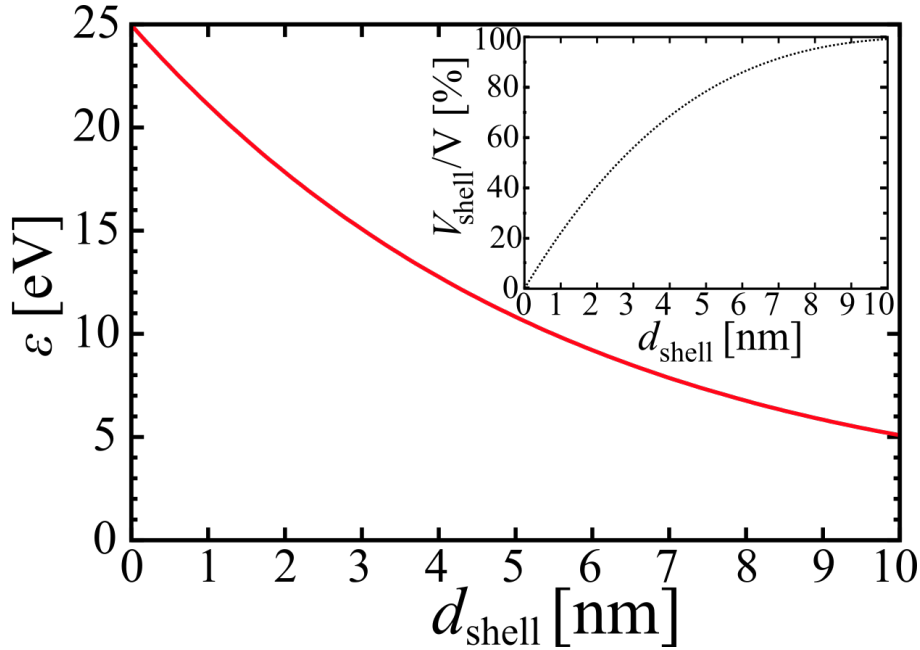


Figure S4: Dependence of reference magnetic interaction energy $\epsilon = \mu_0 M_0^2 / 4\pi d^3$ with thickness of magnetite shell d_{shell} for $d = 25$ nm core/shell iron/iron oxide cube. Inset shows ratio of shell to total volume of the cube.

The previous formula is applicable for the analytical analysis of dipolar interaction of

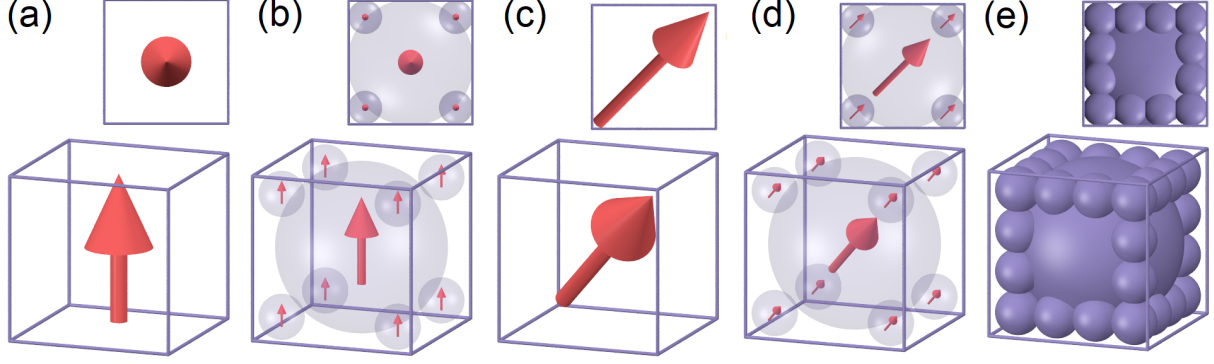


Figure S5: (a) Uniformly [001] magnetized magnetic cube, (b) nine dipole model for [001] magnetized cube, (c) uniformly [111] magnetized magnetic cube, (d) nine dipole model for [111] magnetized cube, and (e) mechanical contact model representation of the cube. Top (upper row) and side (lower row) view are given for comparison.

cubes but it is not practical for running a molecular dynamics simulations. We construct a model which combines numerical precision with computational efficiency.

The cubes are modeled as cluster of hard spheres filling a cubical frame. A magnetic cube with side d is represented with nine spheres a big sphere in the center with radius $d/2$ and eight smaller spheres touching the inner corners of the cube and the big central sphere with radii $(2 - \sqrt{3})d/2$. A cube is therefore represented using a potential energy of interaction $U(\vec{r}_{ij})$ between pairs of the point-like dipoles with the sphere centers located at \vec{r}_i and \vec{r}_j can be written as:

$$U_m(\vec{r}_{ij}) = \frac{\mu_0}{4\pi} \left[\frac{\vec{m}_i \cdot \vec{m}_j}{r_{ij}^3} - 3 \frac{(\vec{m}_i \cdot \vec{r}_{ij})(\vec{m}_j \cdot \vec{r}_{ij})}{r_{ij}^5} \right], \quad (4)$$

where $r_{ij} = |\vec{r}_{ij}| = |\vec{r}_j - \vec{r}_i|$, and $i, j = 1 \cdot 9$. The magnetic moments in this model carry a fraction of the of total magnetic moment. The magnetic moment m_i is expressed as $m_i = I^s v_i$, where v_i is the volume of the magnetic part of the particle. The volume of the central particle is $v_1 = \pi/6$ and the one of the smaller particles located at the corners is $v_{2...9} = \pi(2 - \sqrt{3})^3/6$. The magnetic density which insures same energy between uniformly magnetized cube placed on top of each other (minimal energy configuration) as in case of uniformly magnetized cubes is $I^s \approx 2.1 \cdot M_0/d^3$. This magnetic density is the same for both

investigated magnetization directions, i.e., [001] and [111].

Using nine dipoles, we take into account the interaction of the cube corners which was not taken into account in previously used models, Ref.⁹ The principle change is in the position of the second maximum when one c.m. of one particle is on the corner of the other, see Fig. S6. While in single dipole model⁹ the secondary (i.e., head-tail minimum) lies at $\Delta_{xy}^1/\sqrt{2}d \approx 0.39$, in our nine dipole model is at $\Delta_{xy}^9/\sqrt{2}d \approx 0.45$ significantly closer to the result for a uniformly magnetized cube $\Delta_{xy}^{\text{unif}}/\sqrt{2}d = 1/2$. The position of the secondary peak is important since it contributes to the flexible movement of the chain, i.e., particle at the corner can easily flip over the side to a similar energy state. Thereby, the total potential energy of magnetic interaction of two particles with indices α, β in a given structure U_m^{tot} is given by a sum over pairs of dipoles :

$$U_m^{\alpha\beta} = \sum_{\substack{i,j=1..9 \\ i>j}} U_m(\vec{r}_{ij}^{\alpha\beta}). \quad (5)$$

The contact potential of the cubes is represented by four overlapping spheres per edge with diameter radii $(2 - \sqrt{3})d/2$, having a total of 32 spheres, and the central sphere with radius $d/2$. These, in fact, cuboids are rigid bodies with fixed distances between spheres. This model is mainly chosen to account for cube overlaps while at the same time creating a smooth and incommensurate surfaces allowing smooth gliding of one cube over the other. The incommensurability is important since it prevents the system to mechanically lock in commensurable states and enables smooth gliding of one cube over the other. We describe the effect of isotropic contact interaction between the spherical particles using a minimal model, i.e., representing them by the soft-core beads. The spheres therefore interact isotropically by means of truncated at minima $r_{\text{cut}} = 2^{1/6}\sigma$ and shifted Lennard-Jones potential, also known as Weeks-Chandler-Andersen (WCA) potential. The interaction is defined as: $U_{\text{LJ}}^{\text{cut}}(r) = U_{\text{LJ}}(r) - U_{\text{LJ}}(r_{\text{cut}}), r < r_{\text{cut}}$ and $U_{\text{cut}} = 0, r \geq r_{\text{cut}}$, where r_{cut} is the distance at which the potential is truncated, and $U_{\text{LJ}}(r)$ is the conventional Lennard-Jones (LJ) potential, i.e.,

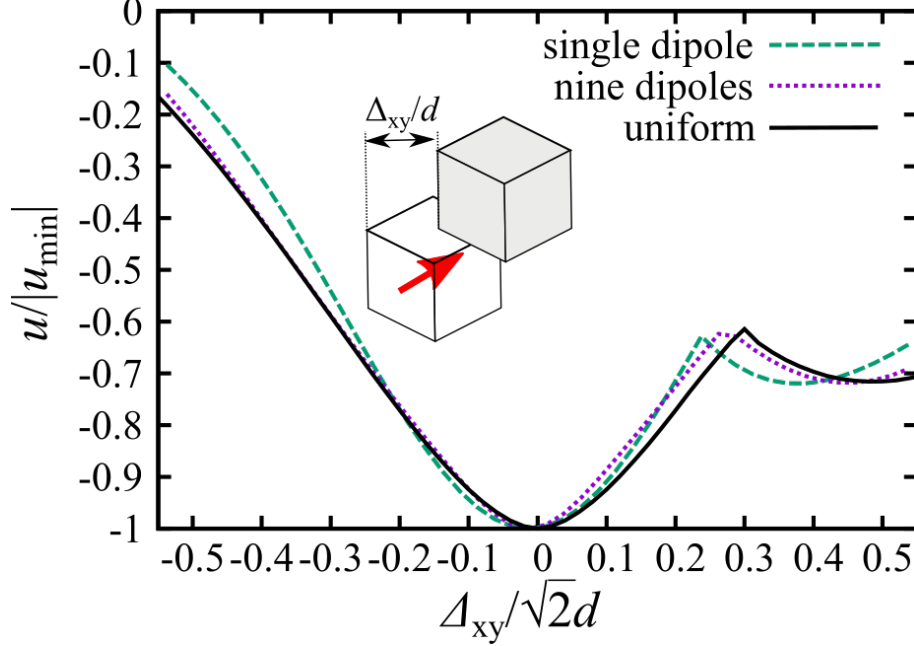


Figure S6: Comparison of the interaction energy of two uniformly magnetized cubes considering a nine dipole and a single dipole models.⁹ The minimal energy for different positions along the diagonal of the cube are shown.

$U_{LJ}(r) = -4\epsilon[(\sigma/r)^{12} - (\sigma/r)^6]$. The parameter ϵ corresponds to the energy scale of the interaction and σ is related to the characteristic diameter of the spheres δ . i.e., $\sigma = \delta/2^{1/6}$ and $\delta/d = 1$ and $(2 - \sqrt{3})d$ for large and small spheres respectively. The value of the sphere repulsive contact potential is taken $\epsilon_r = 7 \cdot 10^{-16} \text{J}$ for particles with the same $d = 25 \text{nm}$ size of the cube (i.e., $\epsilon_r = 800U_m^{\alpha\beta}$).

References

- (1) Lin, X.-M.; Samia, A. C. *Journal of Magnetism and Magnetic Materials* **2006**, *305*, 100 – 109.
- (2) Kuzyk, A.; Schreiber, R.; Fan, Z.; Pardatscher, G.; Roller, E.-M.; Hogele, A.; Simmel, F. C.; Govorov, A. O.; Liedl, T. *Nature* **2012**, *483*, 311–314.
- (3) Zhang, Y.; Lu, F.; Yager, K. G.; van der Lelie, D.; Gang, O. *Nat Nano* **2013**, *8*, 865–872.

- (4) Yan, J.; Bloom, M.; Bae, S. C.; Luijten, E.; Granick, S. *Nature* **2012**, *491*, 578–581.
- (5) Zhou, Y.; Shimizu, T. *Chemistry of Materials* **2008**, *20*, 625–633.
- (6) Liu, X.; Marangon, I.; Melinte, G.; Wilhelm, C.; Ménard-Moyon, C.; Pichon, B. P.; Ersen, O.; Aubertin, K.; Baaziz, W.; Pham-Huu, C.; Bégin-Colin, S.; Bianco, A.; Gazeau, F.; Bégin, D. *ACS Nano* **2014**, *8*, 11290–11304.
- (7) Engel-Herbert, R.; Hesjedal, T. *Journal of Applied Physics* **2005**, *97*, 074504.
- (8) Lowrie, W. *Fundamentals of geophysics*; Cambridge university press, 2007.
- (9) Rossi, L.; Donaldson, J. G.; Meijer, J.-M.; Petukhov, A. V.; Kleckner, D.; Kantorovich, S. S.; Irvine, W. T. M.; Philipse, A. P.; Sacanna, S. *Soft Matter* **2018**, *14*, 1080–1087.

Trapping and electrical characterization of single core/shell iron-based nanoparticles in self-aligned nanogaps

Cite as: Appl. Phys. Lett. **115**, 063104 (2019); doi: [10.1063/1.5094352](https://doi.org/10.1063/1.5094352)

Submitted: 28 February 2019 · Accepted: 12 July 2019 ·

Published Online: 7 August 2019



View Online



Export Citation



CrossMark

Jacqueline Labra-Muñoz,^{1,2}  Zorica Konstantinović,³  Lluís Balcells,⁴  Alberto Pomar,⁴ 
Herre S. J. van der Zant,¹  and Diana Dulic^{5,a)} 

AFFILIATIONS

¹Kavli Institute of Nanoscience, Delft University of Technology, Lorentzweg 1, 2628 CJ Delft, The Netherlands

²Electrical Engineering Department, Faculty of Physical and Mathematical Sciences, University of Chile, Av. Tupper 2007, Santiago, Chile

³Center for Solid State Physics and New Materials, Institute of Physics Belgrade, University of Belgrade, Pregrevica 118, 11080 Belgrade, Serbia

⁴Institut de Ciència de Materials de Barcelona, ICMA-B-CSIC, Campus de la UAB, 08193 Bellaterra, Spain

⁵Physics Department, Faculty of Physical and Mathematical Sciences, University of Chile, Av. Blanco Encalada 2800, Santiago, Chile

^{a)}Electronic mail: ddulic@ing.uchile.cl

ABSTRACT

We report on the fabrication and measurements of platinum-self-aligned nanogap devices containing cubed iron (core)/iron oxide (shell) nanoparticles (NPs) with two average different sizes (13 and 17 nm). The nanoparticles are deposited by means of a cluster gun technique. Their trapping across the nanogap is demonstrated by comparing the current vs voltage characteristics (I-Vs) before and after the deposition. At low temperature, the I-Vs can be well fitted to the Korotkov and Nazarov Coulomb blockade model, which captures the coexistence of single-electron tunneling and tunnel barrier suppression upon a bias voltage increase. The measurements thus show that Coulomb-blockaded devices can be made with a nanoparticle cluster source, which extends the existing possibilities to fabricate such devices to those in which it is very challenging to reduce the usual NP agglomeration given by a solution method.

Published under license by AIP Publishing. <https://doi.org/10.1063/1.5094352>

Due to the development of fabrication techniques in the last few decades, it is now possible to realize nanoelectronic devices with electrodes spacing down to the nanometer scale. In combination with their optical and magnetic properties, the unique size-dependent charge transport properties of nanoparticles (NPs) make them interesting candidates for exploring functionalities in such devices including those associated with biomedical applications.^{1–4} In this respect, iron oxide NPs represent intriguing examples. From a magnetic perspective, magnetite (Fe₃O₄) exhibits the strongest magnetism of any transition metal oxide.⁵ At room temperature, bulk magnetite is ferrimagnetic. However, at the same temperature, magnetite particles of a few nanometers in size are superparamagnetic. This aspect makes magnetite NPs suitable for use in magnetic resonance imaging (MRI) contrast agents for molecular and cell imaging.^{5,6} In addition, self-assembled iron-oxide NPs are proposed as data storage devices,^{7,8} being potential key components for a new generation of electronic materials.^{9,10}

Electrical characterization of NPs on a single-particle level implies two major challenges: (i) the fabrication of electrodes with a separation (gap) of a few nanometers, so that single NPs bridge the gap from the source to drain and (ii) the synthesis and deposition of reproducible NPs (in size and density) in the nanogaps. To decide which nanoelectrode fabrication technique to use depends on the NP shape, size, composition, and specific research aim. Thus far, the methods for trapping of NPs in nanogaps involve the deposition from a solution,^{11–16} and among them, the drop-casting technique is the most common.^{12,13} It can be used in combination with a subsequent drying process, such as exposure to high temperatures¹⁴ or vacuum exposure¹⁵ or in combination with applying an electric field (electrophoresis).¹⁶ The advantage of drop-casting is that it represents a very simple method;¹⁷ however, the usual NP agglomeration by the drop casting method can make a controlled deposition on the surface of the device challenging.¹⁸

In this work, we studied core/shell Fe/Fe₃O₄ nanoparticles that are deposited on self-aligned nanogaps by means of a nonsolution based cluster source.¹⁹ The method offers excellent control of the size distribution and stoichiometry of the NPs while minimizing NP agglomeration.²⁰ This constitutes the realization of devices in which single NPs are contacted in nanogaps using this deposition technique, which has not been reported before. We find that the devices are stable and allow for electrical characterization at room and low temperatures showing Coulomb blockade coexisting with barrier suppression as the main transport mechanism.

A schematic of the nanogap chip design is shown in Fig. 1. It consists of 36 devices, formed by a main electrode (in yellow) and 36 finger-like-auxiliary electrodes (in gray); each finger-like electrode has a length of 5 μm and a width of 1 μm. The gap between the main electrode and each auxiliary electrode (device) varies between 12 and 21 nm [see Fig. 1(b)]. The devices are enumerated from 1 to 36, as illustrated in Fig. 1(a). The self-aligned nanogaps are not defined by direct e-beam writing but instead are the result of a mask formed by chromium oxidation^{21–23} (see the end of the document for details). The nanoparticles have a cubic shape and consist of an iron core covered with an iron oxide shell (Fe₃O₄),²⁴ see the [supplementary material](#), Fig. S5. Specifically, we measured two chips with NPs that differ in size; the average sizes of the NPs are 13 nm (denoted chip *Small NPs*) and 17 nm (denoted chip *Big NPs*), respectively. Figure 1(d) shows a transmission electron microscopy (TEM) image of *Big NPs* from the same batch as used for the deposition. The particles are synthesized by a cluster source and *in situ* deposited on the devices with previously patterned electrode structures. After deposition, the

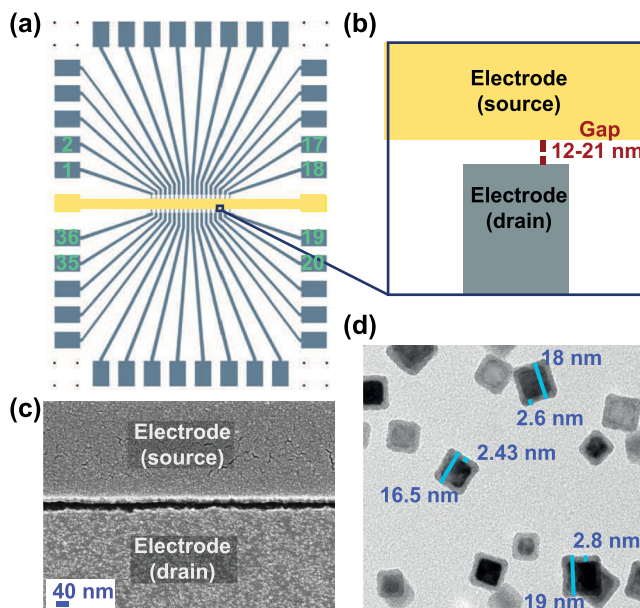


FIG. 1. (a) General design of the chip. In yellow, the main electrode is represented as the source. In gray, 36 auxiliary electrodes are shown, represented as the drain. (b) Schematic of the gap between a pair of source and drain electrodes (device). (c) Scanning electron microscopy image of an empty device. (d) Transmission electron microscopy image of the iron (core)/iron oxide (shell) nanoparticles (*Big NPs*) from the same batch as used for the deposition.

samples are taken out of the chamber and placed in a probe station for further electrical characterization.

Prior to NP deposition, the current vs voltage (*I-V*) characteristic of each electrode pair was recorded [Fig. 2(a)]. The noise level in our probe-station measurements was about 1 pA. We have chosen twice this value (i.e., 2 pA) as the threshold value to determine if NP trapping occurred in the gap. Thus, a device exhibiting an increase in current greater than 2 pA over the bias voltage range probed (± 1.5 V) was discarded, i.e., only open gaps (called “working devices”) were selected to characterize the NP device (100% of total electrode pairs of the chip *Big NPs* and 97% of the chip *Small NPs*). Once the NPs were deposited, we identified their presence within the gap [Fig. 2(b)] by comparing the *I-V* curve of the gap before and after deposition, measured in air and at room temperature. Figure 2(c) shows a typical *I-V* curve measured for device #6 (chip *Big NPs*), with the same appearance as the one presented in Fig. 1(c). After deposition, 92% of the working devices on the chip *Big NPs* showed an increase in the current without being short-circuited [Fig. S3(b)], indicating the trapping of NPs between the electrodes. Note that the *I-V*s show a superlinear behavior at high bias voltage; the current increases faster than the bias voltage does. The percentage of working devices on the chip *Small NPs* that trapped NPs after the deposition was 100% [Fig. S3(a)].

The NP working devices were stable to allow measurements at low temperature (20 K). At this temperature, 40% of the devices on the chip *Big NPs* showed symmetric *I-V*s and 58% of the devices showed asymmetric *I-V*s. For 2% of the devices, the current dropped below the noise level (2 pA) at this temperature over the bias voltage range probed (-1.5 V– 1.5 V). In the case of chip *Small NPs*, only 11% of the devices had symmetric *I-V*s, 49% showed asymmetric *I-V*s, and 40% of the devices showed currents below the threshold value of 2 pA. Figure 3 displays four typical symmetric *I-V* curves (in light blue) measured at 20 K, in vacuum, (#2 and #36 of chip *Big NPs* and #17 and #25 of chip *Small NPs*). For clarity, these *I-V* curves are the descendent curves of the *I-V* cycles, i.e., the current recorded from 1.5 V to -1.5 V. The *I-V*s were found to be free of hysteresis. The observed asymmetry in the other devices (see the [supplementary material](#), Fig. S4) may result from an asymmetry in the contact configuration on either side of the junction.

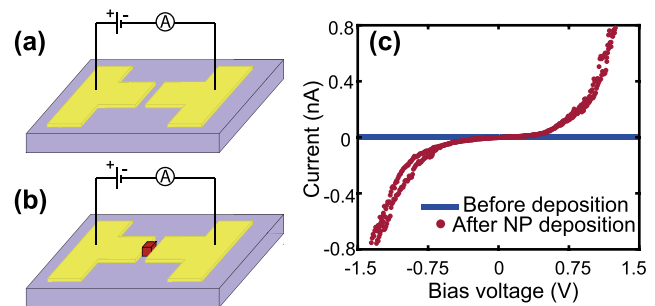


FIG. 2. Description of the measurement procedure. (a) Schematic circuit of a device before nanoparticle (NP) deposition (empty gap). (b) Schematic circuit of a device with an iron NP trapped between the electrodes. (c) Electrical characterization of device #6 (*Big NPs*) before and after NP deposition, measured at room temperature, in vacuum. The blue curve describes an open circuit, reflecting an empty device. The increase in current shown in the red curve indicates the capture of iron NPs. In both cases, the current is measured as follows: (I) voltage sweep from 0 V to 1.5 V. (II) Voltage sweep from 1.5 V to -1.5 V. (III) Voltage sweep from -1.5 V to 0 V.

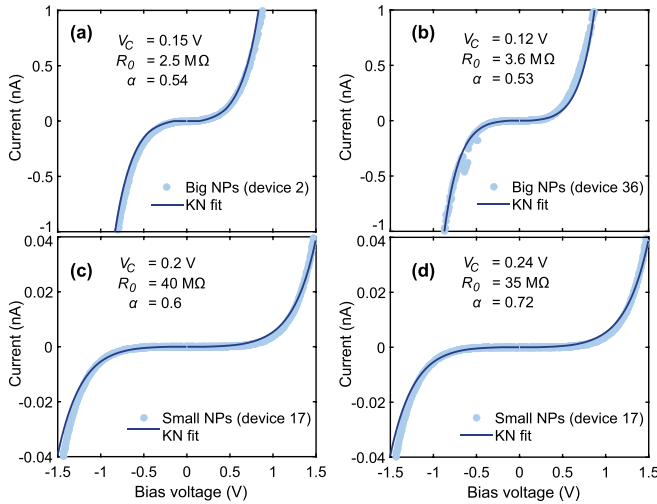


FIG. 3. Symmetric I - V characteristics (descendent part [defined in the caption of Fig. 2(c)] of the cycle) measured at 20 K, in vacuum. (a) Devices #2 and (b) #36 contain *Big NPs*. (c) Devices #17 and (d) #25 contain *Small NPs*. Fit parameters are listed in the inset. The associated charging energies (E_C) are 75 meV, 60 meV, 100 meV, and 120 meV, respectively.

Since the gap and nanoparticles are of the same size (12–21 nm) and the electrode width is 1 μm , the presence of more than one NP connected in parallel is plausible, although the dominant conductance pathway may well be through one particle connected with the lowest tunnel barriers to the two electrodes. With this picture in mind, we used the Korotkov and Nazarov (K-N)²⁵ model to describe the I - V characteristics. This model treats the coexistence of single-electron tunneling and effective tunnel barrier suppression (when increasing the voltage). Bezryadin *et al.*²⁶ applied this model to describe transport through palladium nanocrystals connected in between electrodes by electrostatic trapping.

According to the K-N model, the tunneling rates expressed in terms of the current at a given temperature T are approximated by the Stratton formula,²⁷

$$I(V) = (2\pi k_B T / eR_0) [\sinh(eV\tau/\hbar) / \sin(2\pi\tau k_B T/\hbar)], \quad (1)$$

where $\tau = L/\sqrt{(2U/m)}$ is the tunneling transversal time. L and U are the barrier width and height, respectively. R_0 is the resistance of the junction at zero bias and zero temperature, \hbar is the Planck's constant, and m is the electron mass. Unlike the classic Coulomb Blockade model,²⁸ the K-N model captures an essential part of the data, namely, the curvature of the I - V at higher bias, which is represented by the fitting parameter $\alpha = E_C \cdot \tau/\hbar$, defined as the ratio between the charging energy (E_C) and the energy scale for which the barrier suppression takes place. The charging energy is defined as $E_C = e^2/2C$, where C is the total capacitance. To limit the number of fit parameters, we assumed (i) the residual charge induced on the NP to be zero and (ii) the capacitances and resistance on the right and left sides to be equal ($C_1 = C_2, R_1 = R_2$), i.e., the condition for fitting symmetric I - V characteristics. Thus, the fitting parameters are α , $V_C = e/C$, and $R_0 = \tilde{R} \exp(2L\sqrt{2mU}/\hbar)$, where for *Big NPs*, \tilde{R} is approximated to be the ratio between the quantum resistance (13 k Ω) and the number of quantum channels, which is ~ 10 considering the NP size.

The symmetric I - V s fitted to this model were from 14 *Big NP* and 4 *Small NP* devices. The dark blue curves in Fig. 3 are the K-N fits to the data. The fitting parameters of all symmetric fitted curves are listed in Table S2. The average of the parameter α is 0.54 and 0.62 for *Big NPs* and for *Small NPs*, respectively, consistent with the presence of barrier suppression and the associated exponential-like shape of the I - V curves. The average values for V_C and R_0 are 0.15 V and 3.1 M Ω for the *Big NPs*, while they are 0.22 V and 40.3 M Ω for the *Small NPs*, respectively. From these fitting parameters, the height and the width of the tunnel barriers can be estimated, according to the expressions $U = eV_C \ln(R_0/\tilde{R})/8\alpha$ and $L = \hbar\sqrt{\alpha \ln(R_0/\tilde{R})/emV_C}$. The average value of U for the *Big NPs* and *Small NPs* is then found to be 0.3 eV assuming \tilde{R} to be 47 k Ω for the *Small NPs*, and the average of the estimated L for *Big NPs* and *Small NPs* is 1.5 nm and 1.2 nm, respectively. It can be noticed that L is of the same order of magnitude as the thickness of the iron-oxide shell.

Additionally, from the fits of *Big NPs*, the average total capacitance $C = e/V_C$ is found to be 1.1 aF with a corresponding charging energy of 75 meV. On the other hand, the fits of *Small NPs* devices yield an average C of 0.7 aF and a charging energy of 110 meV, corroborating the fact that the capacitances scale with the particle size. Furthermore, we can compare the estimated capacitances to the upper and lower bound estimates of the NP capacitance using two parallel plate capacitors located between the iron core of the NP and the two electrodes on either side, connected in series (see the supplementary material, Fig. S1). One can express those capacitances as $C_{shell1} = C_{shell2} = \epsilon_r \epsilon_0 A/d$, where ϵ_0 is the vacuum permittivity, ϵ_r is the relative permittivity of the Fe_3O_4 shell, which according to Hotta *et al.*²⁹ can be estimated to be around 8, and d is the distance between the plates, which corresponds to the iron-oxide-shell thickness (2.4 nm). The upper bound estimate considers the contact area to be maximized, i.e., the area of the parallel plate A is estimated to be $17 \times 17 \text{ nm}^2$ for *Big NPs* and $13 \times 13 \text{ nm}^2$ for *Small NPs*. Thus, the estimated capacitance of the nanoparticle is given by $C_{est} = (C_{shell1}^{-1} + C_{shell2}^{-1})^{-1}$, which results in 4.3 aF for *Big NPs* and 2.5 aF for *Small NPs*. Following an analogous reasoning, the lower limit case considers a minimized contact area (A) estimated to be $17 \times 2.6 \text{ nm}^2$ for *Big NPs* and $13 \times 2.6 \text{ nm}^2$ for *Small NPs*. The corresponding capacitances are 0.7 aF and 0.5 aF for *Big NPs* and *Small NPs*, respectively. The capacitance obtained from the K-N model lies in between the two estimated limiting values. See supplementary material Sec. I for a more elaborate discussion on the capacitances. Although the number of NPs present in the gaps cannot be established, the consistency between the measurements and the K-N model suggests that the dominant conduction pathway is through one particle. In some cases, like Fig. S2 device #17 (*Small NPs*), SEM images provide an additional indication for this. However, it was not possible to image all measured devices. In case that more particles would contribute, the estimates for the capacitance would not be affected, provided that the offset charge is similar for all of them.

In conclusion, we have demonstrated that individual NPs can be trapped in self-aligned nanogaps using a cluster gun technique to deposit the NPs. The NP devices are stable at low and room temperatures. Electrical characterization shows the I - V curves that are consistent with single electron tunneling in combination with barrier suppression to account for the exponential-like shape observed at high bias. The fabrication method can be extended to the study of other

types of NPs with the advantage that the direct deposition in vacuum conditions circumvents agglomeration of particles.

The devices are fabricated as follows. On top of a Si/SiO₂ substrate, the main electrode is defined by e-beam lithography (EBL) and evaporation of 5 nm of titanium (adhesive layer) and subsequently 30 nm of platinum. On top of the platinum layer, a 25 nm chromium layer is deposited. Upon exposure to ambient conditions, the chromium layer naturally oxidizes, expanding its size. In this manner, chromium oxide acts as a shadow mask of a few nanometers near the edge of the main electrode. The thickness of the chromium layer determines the size of the gap. A second EBL cycle defines the finger-like-auxiliary electrodes, by depositing 5 nm of titanium and 20 nm of platinum. In the final step, the chromium layer is etched away (wet-etch step) to reveal the underlying nanogaps. The recipe is depicted in Fig. S9.

The NPs are synthesized and deposited by means of a home-built combination of magnetron sputtering and gas-aggregation techniques.¹⁹ A DC magnetron with an Fe target (99.95% purity) was operated typically at 30 W. Deposition took place at a nozzle-substrate distance of 15 cm with a constant Ar flux of 90 sccm and pressures in the low 10⁻³ Torr range. To characterize the NPs (particle size and structure), test substrates are placed next to the chip. Si wafers were used for SEM inspection, and carbon-coated grids were used for TEM inspection. The characterization of devices was realized by scanning electron microscopy (SEM) using a QUANTA FEI 200 FEG-ESEM microscope. The core-shell structure of Fe/Fe₃O₄ nanoparticles (crystallinity, morphology, and size) was examined by transmission electron microscopy (TEM) using a JEOL, JEM 1210 transmission electron microscope operating at 120 kV. Diffraction patterns of power spectra were obtained from selected regions in the micrographs.

The electrical measurements were performed in a vacuum flow cryostat probe station with TU Delft home-built low-noise electronics. The minimum temperature is around 10–20 K.

See the [supplementary material](#) for more details of this study regarding device fabrication, nanoparticle deposition, and additional results.

This study was supported by the EU Horizon 2020 research and innovation program under the Marie-Sklodowska-Curie Grant Agreement No. 645658 (DAFNEOX Project), by two FONDECYT REGULAR Grant Nos. 1181080 and 1161775, and by two FONDEQUIP Grant Nos. EQM140055 and EQM180009. We thank the Spanish Ministry of Science, Innovation and Universities (Project Nos. MAT2015-71664-R and RTI2018-099960-B-I00) and the Serbian

Ministry of Education, Science and Technological Development (Project No. III45018) for their support. A.P. and Z.K. thank Sensor-INFIZ (Serbia) for the cooperation provided during their respective secondments.

REFERENCES

- ¹O. V. Salata, *J. Nanobiotechnol.* **2**, 3 (2004).
- ²C. Mah, I. Zolotukhin, T. J. Fraitess, J. Dobson, C. Batich, and B. J. Byrne, *Mol. Ther.* **1**, S239 (2000).
- ³J. Ma, H. Wong, L. B. Kong, and K. W. Peng, *Nanotechnology* **14**, 619 (2003).
- ⁴R. S. Molday and D. MacKenzie, *J. Immunol. Methods* **52**, 353 (1982).
- ⁵A. S. Teja and P. Koh, *Prog. Cryst. Growth Charact. Mater.* **55**, 22 (2009).
- ⁶N. Leeand and T. Hyeon, *Chem. Soc. Rev.* **41**, 2575 (2012).
- ⁷Z. Nie, A. Petukhova, and E. Kumacheva, *Nat. Nanotechnol.* **5**, 15 (2010).
- ⁸W. Wu, X. Xiao, S. Zhang, T. Peng, J. Zhou, F. Ren, and C. Jiang, *Nanoscale Res. Lett.* **5**, 1474 (2010).
- ⁹M. Shaalan, M. Saleh, M. El-Mahdy, and M. El-Matbouli, *Nanomedicine* **12**, 701 (2016).
- ¹⁰M. Holzinger, A. L. Goff, and S. Cosnier, *Front. Chem.* **2**, 63 (2014).
- ¹¹R. W. Murray, *Chem. Rev.* **108**, 2688 (2008).
- ¹²F. Chávez, G. Pérez-Sánchez, O. Goiz, P. Zaca-Morán, R. Peña-Sierra, A. Morales-Acevedo, C. Felipe, and M. Soledad-Priego, *Appl. Surf. Sci.* **275**, 28 (2013).
- ¹³T. Wang, L. Liu, Z. Zhu, P. Papakonstantinou, J. Hu, and H. L. M. Li, *Energy Environ. Sci.* **6**, 625 (2013).
- ¹⁴B. K. Kuila, A. Garai, and A. K. Nandi, *Chem. Mater.* **19**, 5443 (2007).
- ¹⁵Y. Sun, X. Li, J. Cao, W. Zhang, and H. P. Wang, *Adv. Colloid Interface Sci.* **120**, 47 (2006).
- ¹⁶T. Teranishi, M. Hosoe, T. Tanaka, and M. Miyake, *J. Phys. Chem.* **103**, 3818 (1999).
- ¹⁷A. Shavel, B. Rodríguez-González, M. Spasova, M. Farle, and L. M. Liz-Marzán, *Adv. Funct. Mater.* **17**, 3870 (2007).
- ¹⁸S. Roth, G. Herzog, V. Körtgens, A. Buffet, M. Schwartzkopf, J. Perlich, M. Abul, R. Döhrmann, R. Gehrke, and A. Rothkirch, *J. Phys.: Condens. Matter* **23**, 254208 (2011).
- ¹⁹L. Balcells, C. Martínez-Boubeta, J. Cisneros-Fernández, K. Simeonidis, B. Bozzo, J. Or-Sole, N. Bagus, J. Arbiol, N. Mestres, and B. Martínez, *ACS Appl. Mater. Interfaces* **8**, 28599 (2016).
- ²⁰B. Ramalingam, S. Mukherjee, C. J. Matha, K. Gangopadhyay, and S. Gangopadhyay, *Nanotechnology* **24**, 205602 (2013).
- ²¹A. Fursina, S. Lee, R. G. S. Sofin, I. V. Shvets, and D. Natelson, *Appl. Phys. Lett.* **92**, 113102 (2008).
- ²²J. Houtman, M.S. thesis, Delft University of Technology, 2018.
- ²³J. Labra-Muñoz, M.S. thesis, University of Chile, 2018.
- ²⁴L. Balcells, I. Stanković, Z. Konstantinović, A. Alagh, V. Fuentes, L. López-Mir, J. Oró, N. Mestres, C. García, A. Pomar, and B. Martínez, "Spontaneous in-flight assembly of magnetic nanoparticles into macroscopic chains," *Nanoscale* (published online).
- ²⁵A. N. Korotkov and Y. V. Nazarov, *Physica B* **173**, 217 (1991).
- ²⁶A. Bezryadin, C. Dekker, and G. Schmid, *Appl. Phys. Lett.* **71**, 1273 (1997).
- ²⁷R. Stratton, *J. Phys. Chem. Solids* **23**, 1177 (1962).
- ²⁸D. V. Averin and K. K. Likharev, *J. Low Temp. Phys.* **62**, 345 (1986).
- ²⁹M. Hotta, M. Hayashi, A. Nishikata, and K. Nagata, *ISIJ Int.* **49**, 1443 (2009).

Trapping and Electrical Characterization of Single Core/Shell Iron-Based Nanoparticles in Self-Aligned Nanogaps.

Jacqueline Labra-Muñoz,^{1,2} Zorica Konstantinovic,³ Lluís Balcells,⁴ Alberto Pomar,⁴ Herre S. J. van der Zant,¹ and Diana Dulic^{5, a)}

¹⁾*Kavli Institute of Nanoscience, Delft University of Technology, Lorentzweg 1, 2628 CJ Delft, The Netherlands.*

²⁾*Electrical Engineering Department, Faculty of Physical and Mathematical Sciences, University of Chile, Av. Tupper 2007, Santiago, Chile.*

³⁾*Center for Solid State Physics and New Materials, Institute of Physics Belgrade, University of Belgrade, Pregrevica 118, 11080 Belgrade, Serbia.*

⁴⁾*Institut de Ciència de Materials de Barcelona, ICMAB-CSIC, Campus de la UAB, 08193 Bellaterra, Spain.*

⁵⁾*Physics Department, Faculty of Physical and Mathematical Sciences, University of Chile, Av. Blanco Encalada 2800, Santiago, Chile.*

(Dated: 15 July 2019)

I. CAPACITANCE ESTIMATES

From our measurements, we cannot establish the number of nanoparticles (NPs) present in our gaps. However, the very good single-particle fits to the data strongly suggest that the dominant conduction pathway is through one particle. With respect to the comment on the capacitance, in case more particles would contribute, this would not change the estimates for the capacitance, provided that the offset charge is the same for all of them.

From the K-N model, we obtained average capacitances of 1.1 aF for *Big* and 0.7 aF, for *Small NPs*. Using a two parallel plate capacitor model located between the iron core of the NP and the two electrodes on either side, connected in series (see Figure S1a), the capacitance of each side of the NP is obtained by the expression $C_{shell1} = C_{shell2} = \epsilon_r \epsilon_0 A/d$, where ϵ_0 is the vacuum permittivity, $\epsilon_r \sim 8$ is the relative permittivity of the Fe_3O_4 NPs¹, A is the area of each parallel plate, and d is the distance between a pair of plates, which corresponds to the Fe_3O_4 shell (~ 2.4 nm). Thus, the total estimated NP capacitance is given by $C_{est} = (C_{shell1}^{-1} + C_{shell2}^{-1})^{-1}$,

We can now estimate two limiting cases: First, the upper limit case (Figure S1a), in which the contact area is maximized (as discussed in the main text). In this case the estimated area (A) is 17×17 nm² for *Big NPs* and 13×13 nm² for *Small NPs*, resulting in estimated capacitances of 4.3 aF for *Big NPs* and 2.5 aF for *Small NPs*. Second, one can consider the lower limiting case (Figure S1b), in which the contact area is minimized. The height of the plates is reduced, but it must be sufficiently high to assure that the core of the NP is electri-

cally accessible, i.e., not only the shell. A reasonable estimate is 2.6 nm. So, the estimated area (A) is now 17×2.6 nm² for *Big NPs* and 13×2.6 nm² for *Small NPs*. The corresponding NP capacitances are 0.7 aF and 0.5 aF for *Big* and *Small NPs*, respectively. The capacitance obtained from the K-N model lies in between the two estimated limiting values.

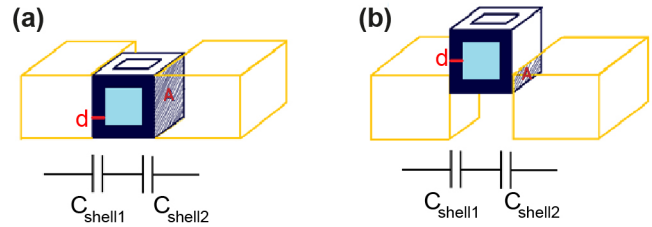


FIG. S1. Schematic of the limit cases of the NP parallel plate capacitors estimate (C_{est}). (a) Upper bound estimate case. (b) Lower bound estimate case.

TABLE S1. Comparison of the capacitance determined from the K-N model (C_{KN}) with the values estimated theoretically (C_{est}), by assuming a two parallel capacitor model.

NP size	K-N	Upper bound	Lower bound
	model estimate	estimate case	estimate case
	C_{KN} [aF]	C_{est} [aF]	C_{est} [aF]
Big	1.1	4.3	0.7
Small	0.7	2.5	0.5

¹⁾M. Hotta, M. Hayashi, A. Nishikata, and K. Nagata, ISIJ Int. **49**, 1443 (2009).

^{a)}Electronic mail: ddulic@ing.uchile.cl

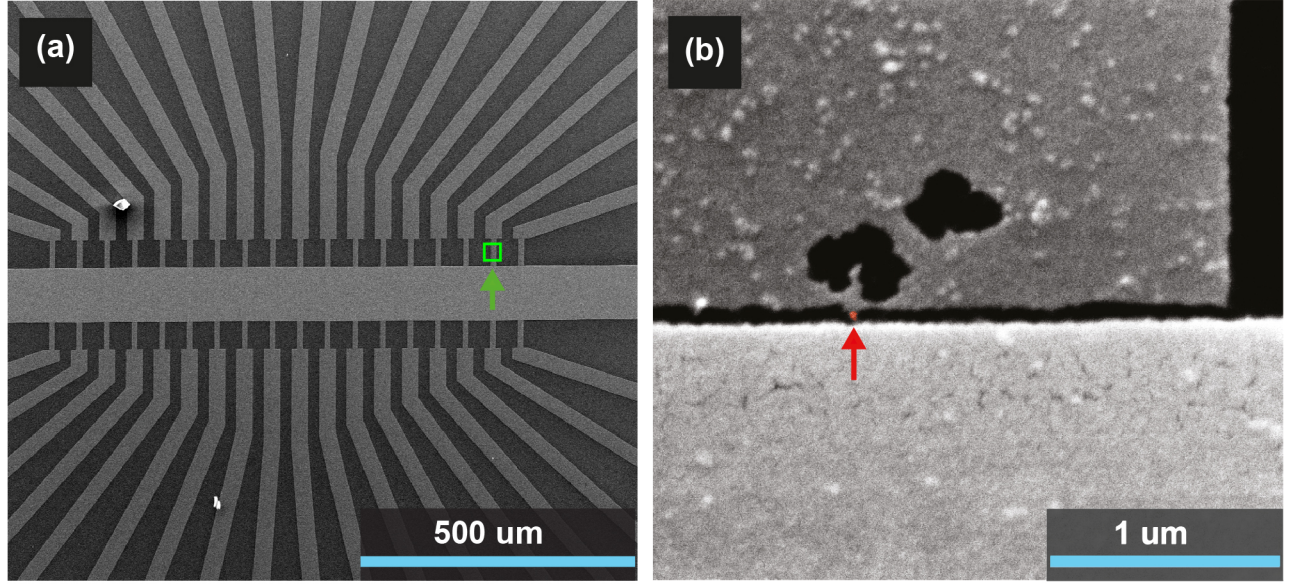


FIG. S2. SEM images taken after the measurements are finished. (a) Central zone of chip *Small NPs*; the green arrow indicates device # 17. (b) Close-up of device # 17; one NP was found to bridge the gap in this device. It is artificially colored in red and marked by the red arrow.

TABLE S2. Fitting parameters of symmetric curves measured at low temperature (20 K), in vacuum, for chips with *Big* and *Small NPs*.

<i>Big NPs</i>				<i>Small NPs</i>			
Device number	V_C [V]	R_0 [M Ω]	α	Device number	V_C [V]	R_0 [M Ω]	α
2	0.15	2.5	0.54	17	0.20	40.0	0.60
5	0.13	1.5	0.43	22	0.22	46.0	0.62
8	0.12	2.9	0.37	25	0.24	0.35	0.72
13	0.20	3.1	0.55	35	0.23	40.0	0.54
14	0.20	5.2	0.55	Average	0.22	40.3	0.62
15	0.18	3.3	0.55				
16	0.19	2.8	0.59				
19	0.14	2.8	0.60				
23	0.19	3.1	0.61				
30	0.10	1.4	0.31				
32	0.13	4.2	0.72				
33	0.13	3.2	0.64				
35	0.15	3.5	0.52				
36	0.12	3.6	0.53				
Average	0.15	3.1	0.54				

TABLE S3. Capacitance (C), charging energy (E_C), barrier height (U), barrier width (L) and tunneling transversal time (τ), for chips with *Big* and *Small NPs*. \tilde{R} is estimated to be 1.3 k Ω for the *Big NPs*. In order to keep U and L about the same, \tilde{R} has to be chosen to be 47 k Ω for the *Small NPs*.

	Average	<i>Big NPs</i>	<i>Small NPs</i>
C [aF]		1.1	0.7
E_C [meV]		75	110
U [eV]		0.3	0.3
L [nm]		1.5	1.2
τ [fs]		4.8	3.7

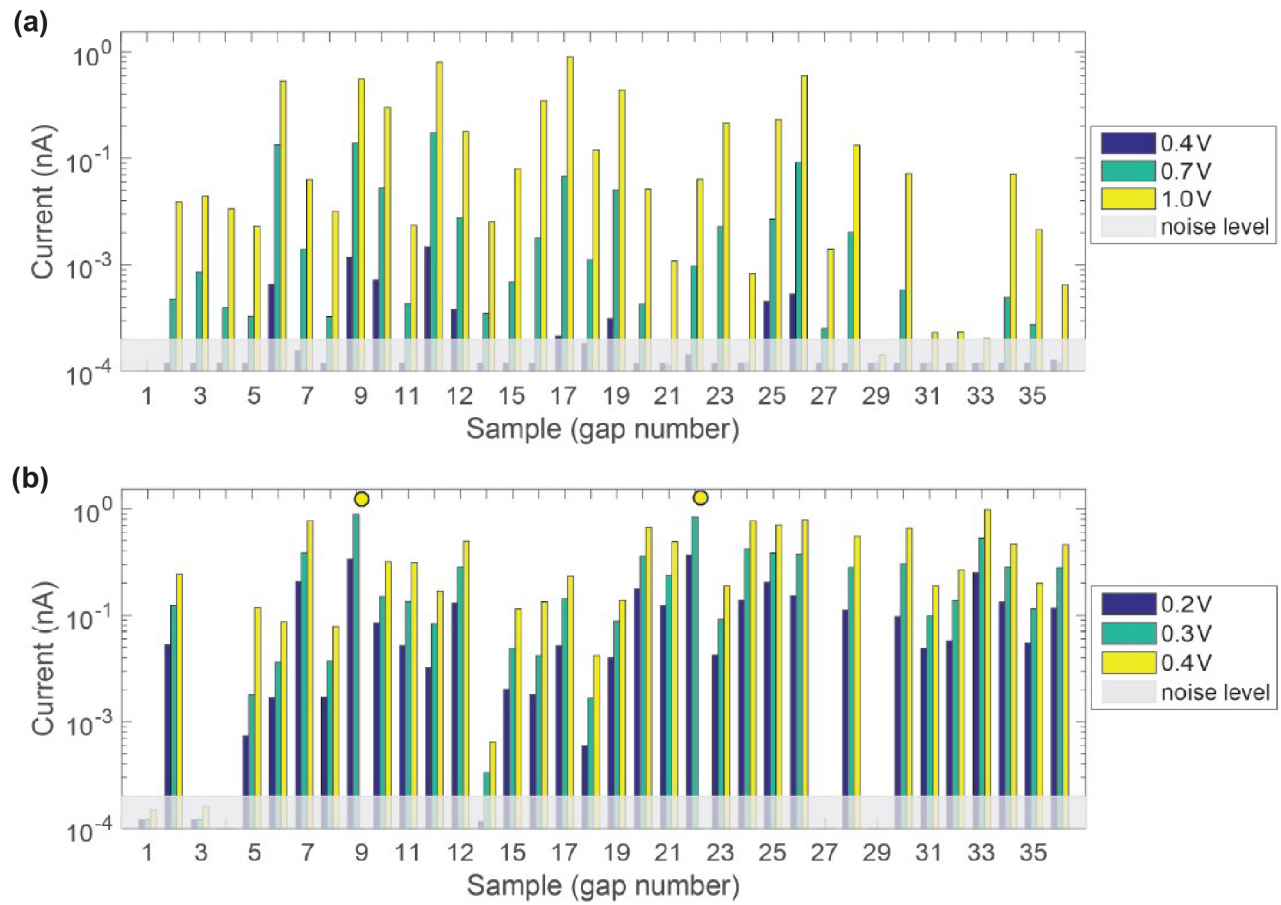


FIG. S3. Comparison of the current values taken at three different voltages as indicated in the inset next to figures. (a) Chip with *Small NPs*. (b) Chip with *Big NPs*. The circles located at the top of the bottom graph represent devices in which the current is larger than the maximum value of 1.2 nA. Devices that became short-circuited after deposition are not included.

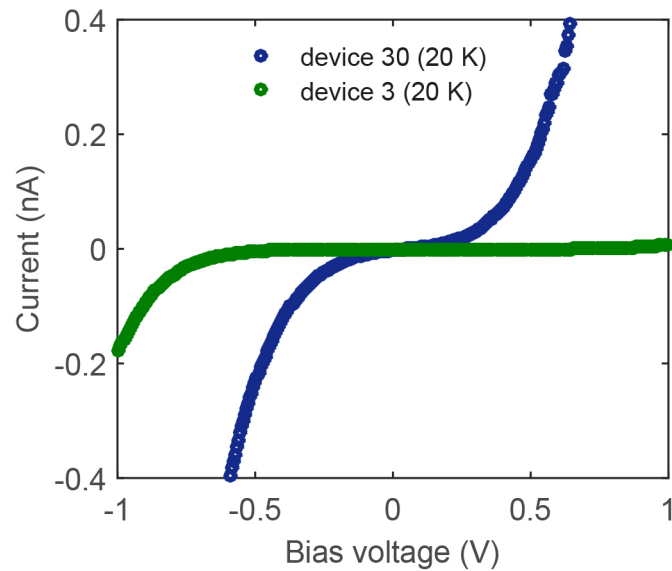


FIG. S4. Symmetric and asymmetric I - V characteristics (descendent part of the cycle) at 20 K. The I - V s correspond to devices from the chip with *Big NPs*.

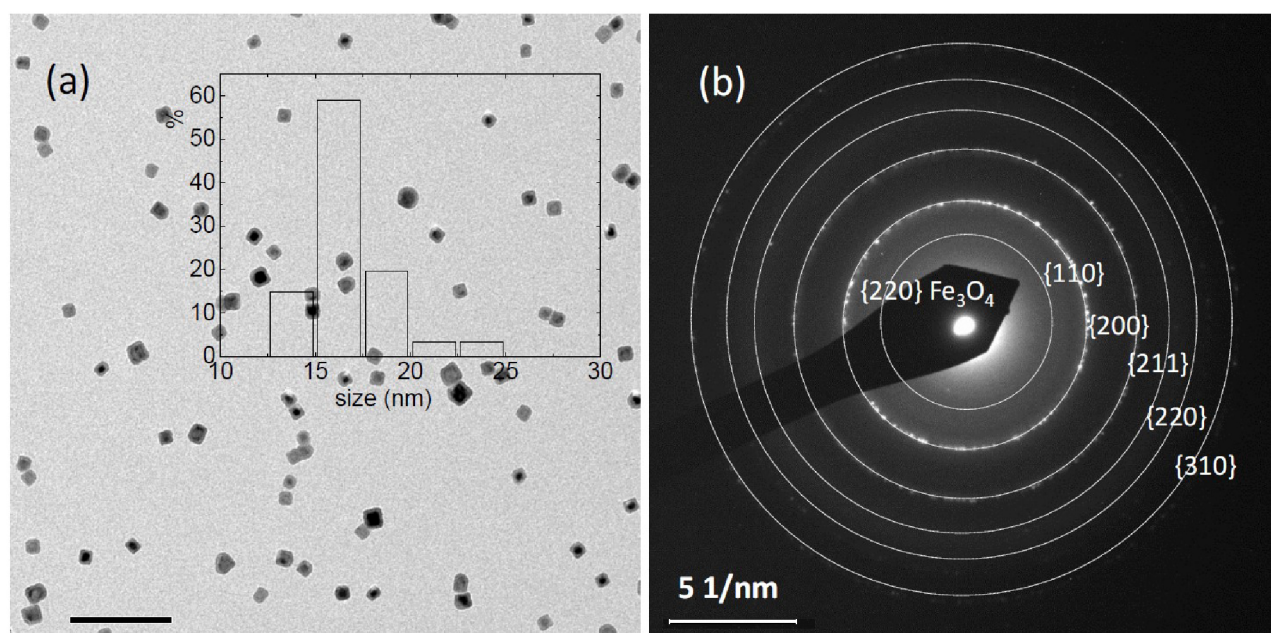


FIG. S5. (a) Transmission electron microscopy image of the iron-based nanoparticles with the nanoparticle size distribution as an inset. (b) Corresponding reflections of the power spectrum indexed using the iron cubic structure (space group $Im\text{-}3m$) from core and the cubic spinel structure of Fe_3O_4 (space group $Fd\text{-}3m$) from shell structure. The spinel structure was confirmed by RAMAN spectroscopy, not shown^b.

^b L. Balcells, C. Martnez-Boubeta, J. Cisneros-Fernndez, K. Simeonidis, B. Bozzo, J. Or-Sole, N. Bagus, J. Arbiol, N. Mestres, and B. Martnez, ACS Appl. Mater. Interfaces **8**, 28599 (2016).

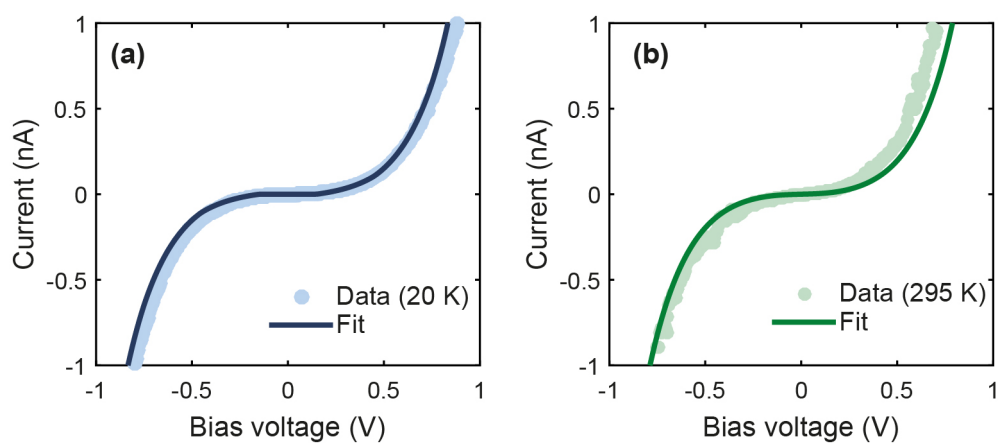


FIG. S6. Descending current-voltage curve measured on device #2 of chip *Big NPs*; (a) at 20 K (light dots) and (b) at 295 K (light green dots). The thin dark blue and dark green curves denote the fits of the KN model. The fitting parameters for both curves are $V_C = 0.15 \text{ V}$, $R_0 = R_1 = R_2 = 2.48 \text{ M}\Omega$, $\alpha = 0.54$, $T = 20 \text{ K}$ or $T = 295 \text{ K}$, respectively.

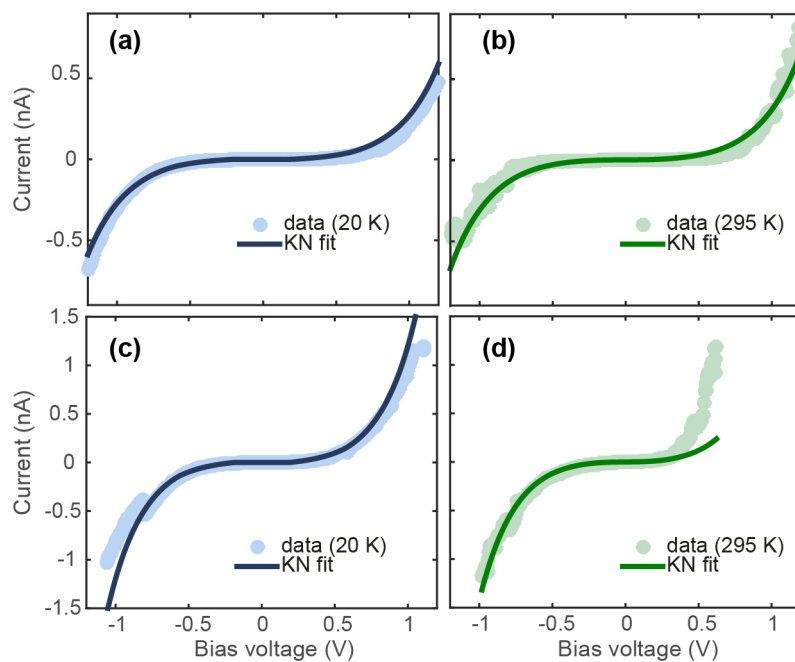


FIG. S7. Descending current-voltage characteristics of four devices from the chip with *Big NPs*. (a) Symmetric curve measured on device #14 at 20 K, in light blue, and (b) at 295 K (light green). (c) Asymmetric curve measured in device #16 at 20 K, in light blue, and (d) at 295 K, in light green. The thin dark blue and dark green curves denote the respective fits of the KN model (parameters are shown in Table S1).

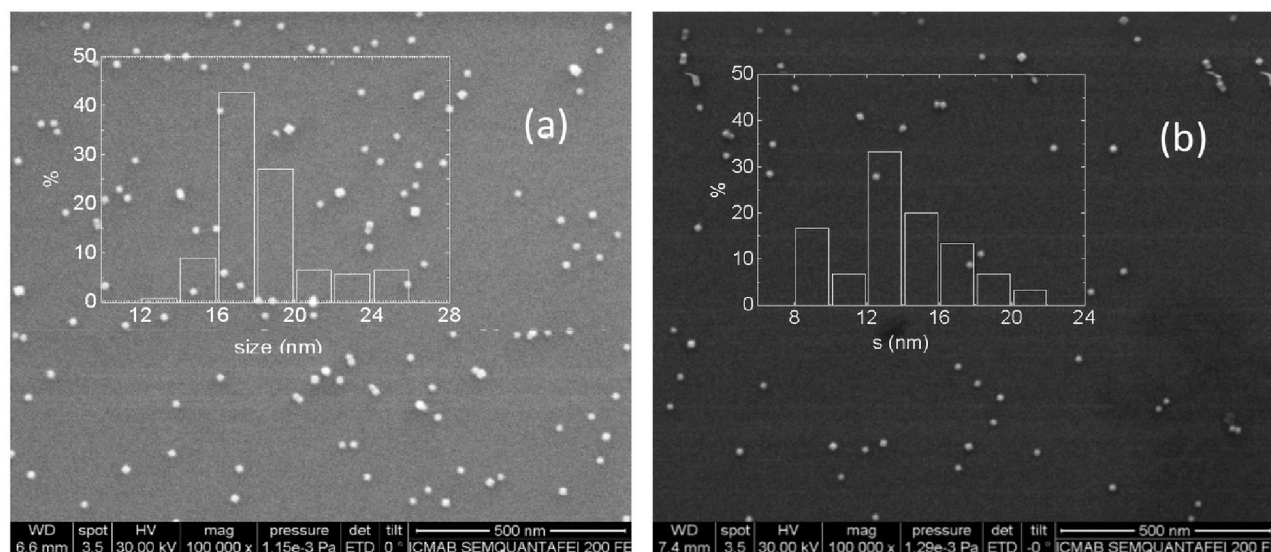


FIG. S8. SEM images and corresponding size-particle distribution of (a) *Big NPs* and (b) *Small NPs*.

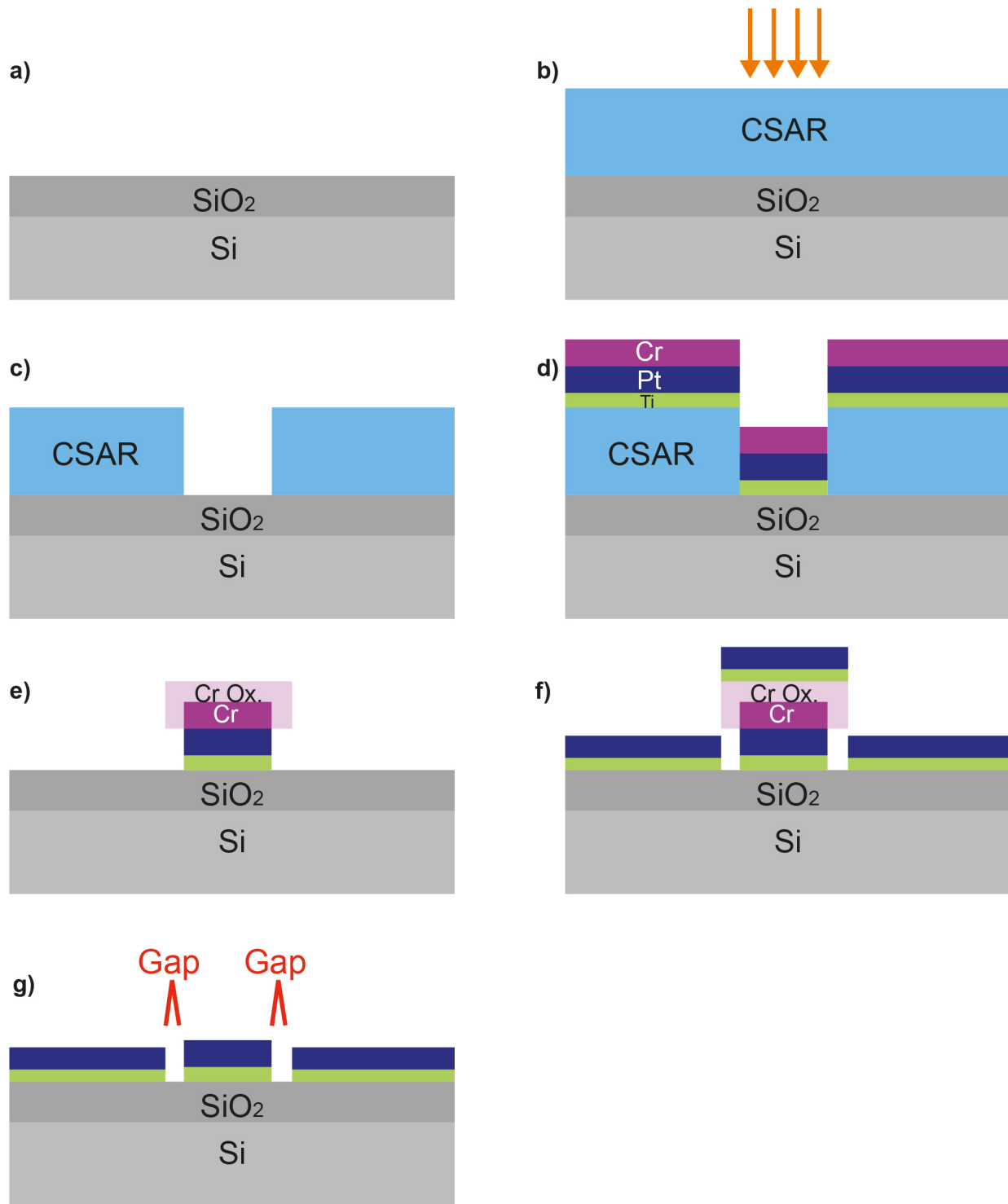


FIG. S9. Schematic depiction of the fabrication process. (a) A 19 by 19 mm^2 piece of a silicon wafer with a silicon oxide layer of 290 nm on top (the substrate), is the starting point of the process. The first step is chemical cleaning of this substrate. (b) A layer of CSAR AR6200 positive resist is spin-coated and baked. Then, it is exposed to an e-beam to define the main electrode. (c) The sample is developed so that the pattern becomes visible and the descumming process takes place. (d) A thin layer of titanium (5 nm) is evaporated to adhere two consecutive layers of platinum (30 nm) and chromium (25 nm) on top of the titanium layer. (e) Lift-off removes the unexposed resist including the metal on top. Now the platinum main electrode (source) is visible. (f) Second e-beam lithography cycle to define the drain electrodes (spincoating & baking, exposure, evaporation, developing, lift-off). (g) After, Chromium wet-etching; nanogaps are now ready to be used in the electrical characterization measurements. Now the gaps are defined.

Cite this: *Nanoscale Adv.*, 2019, 1, 1763

Nanoscale mechanical control of surface electrical properties of manganite films with magnetic nanoparticles†

Borislav Vasić,^{a*} Zorica Konstantinović,^b Elisa Pannunzio-Miner,^{‡c}
Sergio Valencia,^d Radu Abrudan,^e Radoš Gajić^a and Alberto Pomar^c

Mechanical control of electrical properties in complex heterostructures, consisting of magnetic FeO_x nanoparticles on top of manganite films, is achieved using atomic force microscope (AFM) based methods. Under applied pressure of the AFM tip, drop of the electrical conductivity is observed inducing an electrically insulating state upon a critical normal load. Current and surface potential maps suggest that the switching process is mainly governed by the flexoelectric field induced at the sample surface. The relaxation process of the electrical surface potential indicates that the diffusion of oxygen vacancies from the bulk of the manganite films towards the sample surface is the dominant relaxation mechanism. The magnetic FeO_x nanoparticles, staying attached to the sample surface after the rubbing, protect the underlying manganite films and provide stability of the observed resistive switching effect. The employed mechanical control gives a new freedom in the design of resistive switching devices since it does not depend on the film thickness, and biasing is not needed.

Received 22nd October 2018

Accepted 18th February 2019

DOI: 10.1039/c8na00301g

rsc.li/nanoscale-advances

1 Introduction

Further improvement of nanoelectronic devices such as switches and memories, requires development of novel materials as well as advanced mechanisms for the dynamic control of their electrical

properties. In this context, one of the most studied mechanisms is resistive switching – an electrically induced change of the resistance of various thin metal-oxide films.^{1–7} This research is mainly driven by possible applications in new data storage devices such as resistive random access memories.^{4–7}

In order to fully understand complex physicochemical processes during resistive switching, investigations at the nanoscale are of particular relevance, where methods based on atomic force microscopy (AFM) are prerequisite.^{8–11} At the same time, AFM could provide novel methods for the manipulation of resistive switching. Namely, in addition to the electrical control, strain engineering is a simple approach to tailor the electrical properties of metal oxide films.^{12–17} The significant coupling between the strain and the electrical properties is based on flexoelectricity (an internal electric field resulting from a strain gradient) and the inverse Vegard effect (changes of ion concentrations due to a stress).¹⁸ The flexoelectricity is typically small. However, it has recently been shown that stress and stress gradients at the nanoscale can lead to sizable effects.^{19–21}

A large nanoscale gradient of stress can be obtained by using the tip of an AFM which has been employed for mechanically induced resistive switching^{22–29} and switching of ferroelectric polarization.^{30–36} Since purely mechanical control is independent of film thickness and biasing is not needed, it could provide new prospects for the resistive switching. While recent studies^{22–29} have been focused on the mechanically induced switching of homogeneous metal-oxide films, it is interesting to investigate the phenomena in the presence of nano-objects on the film surface. In this respect, nanoparticles (NPs) constitute a model system as

^aGraphene Laboratory of Center for Solid State Physics and New Materials, Institute of Physics Belgrade, University of Belgrade, Pregrevačka 118, 11080 Belgrade, Serbia. E-mail: bvasic@ipb.ac.rs

^bCenter for Solid State Physics and New Materials, Institute of Physics Belgrade, University of Belgrade, Pregrevačka 118, 11080 Belgrade, Serbia

^cInstitut de Ciència de Materials de Barcelona, ICMA-B-CSIC, Campus de la UAB, 08193 Bellaterra, Spain

^dHelmholtz-Zentrum Berlin für Materialien und Energie, Albert-Einstein-Str. 15, 12489 Berlin, Germany

^eInstitut für Experimentalphysik/Festkörperphysik, Ruhr-Universität Bochum, 44780 Bochum, Germany

† Electronic supplementary information (ESI) available: ESI contains the reciprocal space maps of (103) reflections and in-plane magnetization curves of the LSMO film (Fig. S1), the results of XAS measurements and the resulting XMCD for the LSMO film (Fig. S2), the reciprocal space maps of (103) reflections and in-plane magnetization curves of the LSFMO film (Fig. S3), AFM images of the LSFMO film (Fig. S5), the electrical current (C-AFM images in Fig. S5) and surface potential (KPFM images in Fig. S6) distributions after the rubbing of the LSFMO film, and the maps of the electrical surface potential of the LSFMO film after combined rubbing with grounded and biased probe (KPFM images in Fig. S7). See DOI: 10.1039/c8na00301g

‡ Present address: Centro de Investigaciones en Ciencias de la Tierra (CICTERRA-CONICET-UNC), Facultad de Ciencias Exactas, Físicas y Naturales, Av. Velez Sarsfield 1611, X5016GCA, Ciudad Universitaria, Córdoba, Argentina.

§ Present address: Helmholtz-Zentrum Berlin für Materialien und Energie, Albert-Einstein-Str. 15, 12489 Berlin, Germany.



they not only improve mechanical properties,³⁷ but also may provide enhanced functionalities such as novel magnetotransport phenomena³⁸ or optoelectronic capabilities,^{39,40} and they could serve as novel magnetic tunnel junctions^{41,42} or memory devices.⁴³

Here we investigate the local mechanical control of the surface electrical properties of a heterostructure consisting of a manganite film with magnetic FeO_x NPs. The AFM tip is used to generate a local stress by rubbing the sample surface, and the resulting changes in local conductivity and electrical surface potential are subsequently measured by conductive AFM (C-AFM) and Kelvin probe force microscopy (KPFM), respectively. It is shown that for a high enough normal load, the manganite surface can be switched to an insulating state. At the same time, the sample exhibits weak room-temperature magnetism due to the presence of FeO_x NPs which stay well attached to the sample surface even after the rubbing at a high normal load.

2 Experimental

2.1 Sample preparation

Samples consisting of iron oxide FeO_x NPs assembled onto manganite films, were grown by radio frequency (RF) magnetron sputtering on the top of (001)-oriented SrTiO₃ (STO) substrates. Two manganite families were considered with very different properties, fully spin polarized La_{0.67}Sr_{0.33}MnO₃ (LSMO) on one side and insulating La_{0.5}Sr_{0.5}Fe_{0.5}Mn_{0.5}O₃ (LSFMO) thin film on the other side. Nanostructured thin films were deposited under a pure oxygen partial pressure (0.19 mbar) at a high temperature (850–900 °C) with a wide range of nominal thickness (between 20 nm and 100 nm),⁴⁴ while the detailed microstructure of LSMO films can be also found in ref. 44. Iron oxide NPs have been deposited under a pure oxygen pressure of 0.06 mbar at 700 °C.

2.2 Structural and magnetic characterization

The surface morphology of nanostructured thin films was characterized by field emission scanning electron microscopy (SEM) (QUANTA FEI 200 FEG-ESEM). The crystal structure of manganite films was characterized by X-ray diffraction based reciprocal space mapping using a Bruker AXS GADDS system equipped with a 2D X-ray detector.

Magnetic properties were measured with a superconducting quantum interference device magnetometer (SQUID) (Quantum Design). The structural and magnetic nature of iron oxide NPs was studied by X-ray absorption spectroscopy (XAS) and X-ray magnetic circular dichroism (XMCD). The synchrotron experiments were performed at room temperature by using the ALICE chamber⁴⁵ at the PM3 beamline of the electron storage ring BESSY II of the Helmholtz-Zentrum Berlin. The radiation impinged on samples at a grazing angle of 30°. The polarization of the incoming radiation was set to circular ($P_c = 0.92(3)$). Data were acquired across the Fe L_{3,2} edges by means of total electron yield. The XMCD spectrum was obtained for a fixed helicity of the incoming polarization by reversing the magnetization direction at every data point from positive to negative by means of an external magnetic field (± 0.1 T). Data were obtained in magnetic remanence. XMCD was defined as the difference in

the absorption for the curves obtained after applying the external magnetic field +0.1 T (β^+) and -0.1 T (β^-), respectively.

2.3 AFM measurements

AFM measurements were performed using an NTEGRA Prima AFM system from NT-MDT under ambient conditions. Tapping AFM mode was used for the topographic imaging. Simultaneously, phase imaging was performed by recording the phase lag of the employed AFM cantilevers.

Electrical measurements were done using C-AFM and KPFM. In C-AFM, local electrical currents were measured in contact mode, while DC voltage was applied between the sample and the AFM tip. KPFM was employed to measure the contact potential difference (CPD) between the AFM tip and the sample surface. The CPD is equal to the difference in the work functions of the tip and sample. KPFM measurements were done using a standard two-pass technique. In the first pass, sample topography was measured in tapping mode. In the second pass, the AFM cantilever was lifted by 30 nm and the sum of AC and variable DC voltage was applied between the cantilever and the sample. In the second pass, the lifted probe, only electrically excited and with a switched-off mechanical feedback loop, followed the topography measured in the first pass. Then, the CPD in every point of a two-dimensional AFM image was the value of the variable DC voltage which canceled the electrically excited oscillations of the AFM cantilever in the second pass.

The procedure for the mechanical control of the surface electrical properties was the following: first, the local electrical current or CPD was measured on an area of $2 \times 2 \mu\text{m}^2$, and then we switched to contact AFM mode and only the inner and central part of $1 \times 1 \mu\text{m}^2$ was rubbed at an increased normal force (in the order of $1 \mu\text{N}$), whereas after the rubbing, we switched back to C-AFM or KPFM mode, and measured either local electrical currents or electrical surface potentials, respectively, on the initial area of $2 \times 2 \mu\text{m}^2$. Hereafter, the rubbing will stand for controllable scanning at increased normal load in order to induce local changes of the electrical properties.

Both AFM imaging, rubbing and electrical measurements were done using diamond coated and nitrogen doped DCP20 probes from NT-MDT. They have triangular cantilevers with the typical force constant of 48 N m^{-1} and a resonant frequency of 420 kHz. Diamond coatings make these probes wear resistive, while a high doping with nitrogen provides excellent conductivity. Therefore, these robust and conductive probes are suitable for the rubbing in contact AFM mode at high normal loads (in the order of μN) and subsequent AFM imaging as well as electrical measurements many times. Since C-AFM measurements were done in contact mode as well, in order to avoid any influence of the applied normal force from the AFM tip during the C-AFM scanning, these measurements were done at low normal load from 50–100 nN.

3 Results and discussion

Manganites are an important class of metal oxides, especially in the context of resistive switching, because of both



magnetoresistive^{46,47} and electroresistive properties.^{48–50} Strain engineering is an additional and simple approach to tailor their properties.^{25,51–54} Epitaxial manganite films are usually elastically strained due to a lattice mismatch between the films and underlying substrates (STO in the considered case). This strain facilitates growth of various self-organized morphologies such as pit arrays^{55–57} which can serve as templates for subsequent self-assembly of NPs.⁴⁴ The strain state in our films is analyzed by the asymmetric reciprocal space mapping of the reflection (103) for the nanostructured 100 nm thick LSMO film grown on top of the STO substrate (Fig. S1(a) of the ESI†). As observed previously,⁵⁵ the LSMO film seems to be fully strained with the in-plane lattice constant close to $a_{\parallel, \text{STO}} = 3.905 \text{ \AA}$. On the other hand, the estimated out-of-plane lattice constant $a_{\perp, \text{LSMO}} = 3.882(6) \text{ \AA}$ is slightly smaller than the corresponding bulk value of 3.889 \AA , as expected due to presence of a tensile strain.^{44,55} Nevertheless, the higher value of the out-of-plane parameter $3.882(6) \text{ \AA}$ compared with the one of the fully strained films of 3.868 \AA (ref. 58) indicates the presence of a small quantity of oxygen vacancies, as previously discussed.⁵⁵

The AFM topographic and the corresponding phase image of the LSMO film with FeO_x NPs are given in Fig. 1(a) and (b), respectively. In the topographic image, NPs are visible as bright domains. They are better resolved in the phase image, where they are dark and with a pronounced contrast compared to the underlying LSMO film. The phase images recorded in forward and backward directions were the same, implying that the observed phase difference was due to the material contrast (not

just a topographic artifact) between NPs and the LSMO substrate. As a reference, an array of three NPs is marked by dashed lines in both topographic and phase images. The SEM image of the sample is depicted in Fig. 1(c). According to the SEM images, the surface coverage of the film by NPs was around 50%, while the NP size distribution is presented in Fig. 1(d) showing that the average NP size is around 60 nm.

The magnetic characterization reveals that iron-oxide NPs provide weak room-temperature magnetism as shown in Fig. S1(b) of the ESI.† At 300 K, the magnetization disappears in bare manganite films and remains principally only in the structures with FeO_x NPs as depicted in Fig. S4 of the ESI.† According to the results of XAS and XMCD measurements, the NPs are mostly $\gamma\text{-Fe}_2\text{O}_3$ (the results of XAS and the fit of the XMCD curve are presented in Fig. S2 of the ESI†).

The influence of the local pressure from the AFM tip on the electrical properties of the manganite film decorated with iron-oxide NPs is presented in Fig. 2(a). The current maps were measured by C-AFM on six different $2 \times 2 \mu\text{m}^2$ areas, after the rubbing of inner $1 \times 1 \mu\text{m}^2$ domains with the AFM tip at increasing normal force, starting from $0.32 \mu\text{N}$ to $1.6 \mu\text{N}$. As can be seen, after the rubbing, the electrical current of inner square domains is decreased. At a normal load of $1.6 \mu\text{N}$, the inner

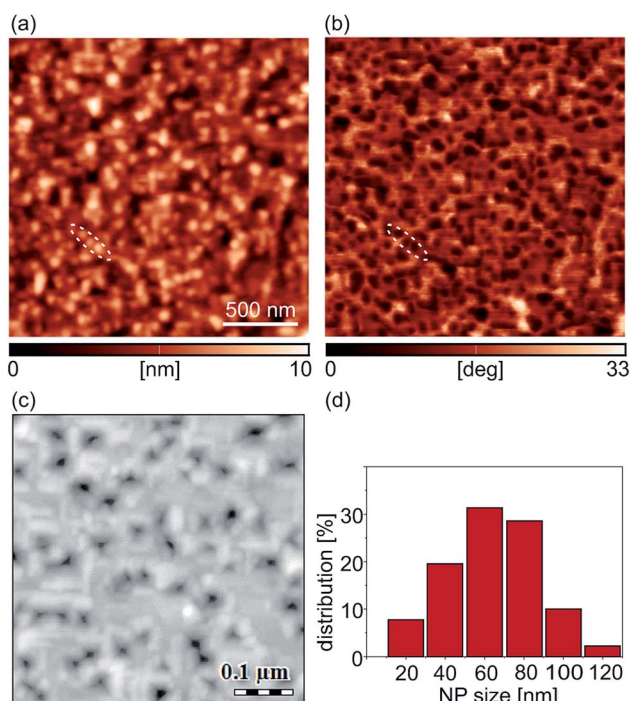


Fig. 1 Sample morphology: (a) AFM topographic image (z -scale is 10 nm), and (b) AFM phase image acquired during the imaging in tapping mode. As an example, an array of three NPs is encircled in both the topographic and phase images. (c) SEM image and (d) the size distribution of iron-oxide NPs.

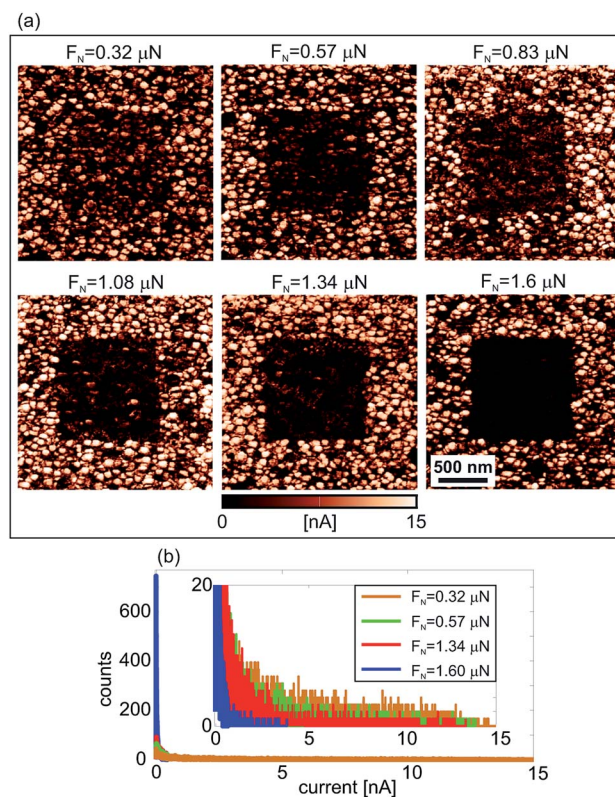


Fig. 2 (a) $2 \times 2 \mu\text{m}^2$ current maps measured by C-AFM (at the sample bias voltage $U_s = 2 \text{ V}$) after the rubbing of inner $1 \times 1 \mu\text{m}^2$ domains at specified normal force (from $0.32 \mu\text{N}$ to $1.6 \mu\text{N}$). The results were obtained on six different sample regions. The current scale is 15 nA. (b) Histograms of the current distribution on rubbed domains in (a) for the selected normal forces. In the inset, the histograms are saturated at 20 counts for a better visibility.



square is switched to a practically insulating state (with almost zero electrical current). The histograms of the current distribution measured only on rubbed domains are given in Fig. 2(b). All current peaks are located around zero, but they become much more pronounced with increasing normal load. For the highest load, almost all points in the histogram are located around zero (just few of them with non-zero current) showing that the sample surface is really switched to an insulating state.

Fig. 3(a) presents the CPD maps measured by KPFM on $2 \times 2 \mu\text{m}^2$ areas after the rubbing of inner $1 \times 1 \mu\text{m}^2$ regions with the AFM tip at an increasing normal force from $0.62 \mu\text{N}$ to $2.4 \mu\text{N}$. As in the previous case, the CPD maps were measured on different sample locations. As can be seen, CPD increases on the rubbed domains. Since the CPD stands for the difference between the work functions of the AFM tip and the sample, an increase in the CPD implies a lower work function of the sample. Therefore, the KPFM results indicate the existence of an electric field originating from negative charges on the sample surface.

The typical histogram of the CPD distribution is depicted in Fig. 3(b) for a normal load of $2.4 \mu\text{N}$. There are two clearly resolved peaks corresponding to the rubbed (the peak at a higher CPD) and non-rubbed (the peak at a lower CPD)

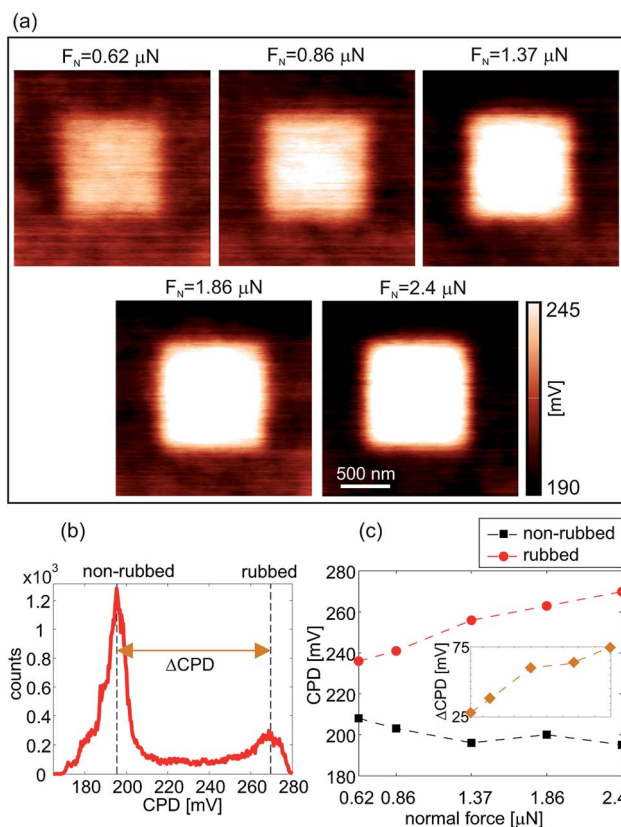


Fig. 3 (a) $2 \times 2 \mu\text{m}^2$ CPD maps measured by KPFM after the rubbing of inner $1 \times 1 \mu\text{m}^2$ domain at specified normal force (from $0.62 \mu\text{N}$ to $2.4 \mu\text{N}$). The CPD scale is 190–245 mV. (b) Histogram of the CPD distribution for a normal load of $2.4 \mu\text{N}$. (c) Changes in the CPD and ΔCPD on rubbed and non-rubbed regions in (a) as a function of the normal force.

domains. Histograms were calculated for all CPD maps in this manner, whereas the histogram peaks were selected as CPD representatives as a function of a normal load. The corresponding results, together with a difference in the CPD between rubbed and non-rubbed domains (ΔCPD), are given in Fig. 3(c). As can be seen, ΔCPD continuously increases with the normal load from around 25 mV to 75 mV.

The topographic images of the sample surface before and after the rubbing (at a high normal force of $1.6 \mu\text{N}$) are given in Fig. 4(a) and (b), respectively. The $1 \times 1 \mu\text{m}^2$ rubbed domain is marked by a dashed square. The rubbed region is only slightly darker than the surrounding, non-rubbed part. The histograms and corresponding fits of the height distribution within the square domains before and after the rubbing are given in Fig. 4(c). As can be seen, the mean height is decreased by around 0.3 nm after the rubbing, meaning that the sample surface is locally compressed along the perpendicular direction. Similar results were obtained for the sample with the LSFMO film as depicted in the topographic images in Fig. S6(b) ESI,† again for the cases recorded before and after the rubbing (at a high normal force of $1.34 \mu\text{N}$). These topographic images illustrate that NPs were not pushed away by the AFM tip during the rubbing even at very high normal loads. This was confirmed by the absence of accumulated NPs along the rims of the inner $1 \times 1 \mu\text{m}^2$ rubbed domains. Still, in addition to the small local compression of the sample surface within the rubbed domains, the topographic images after the rubbing show that the height

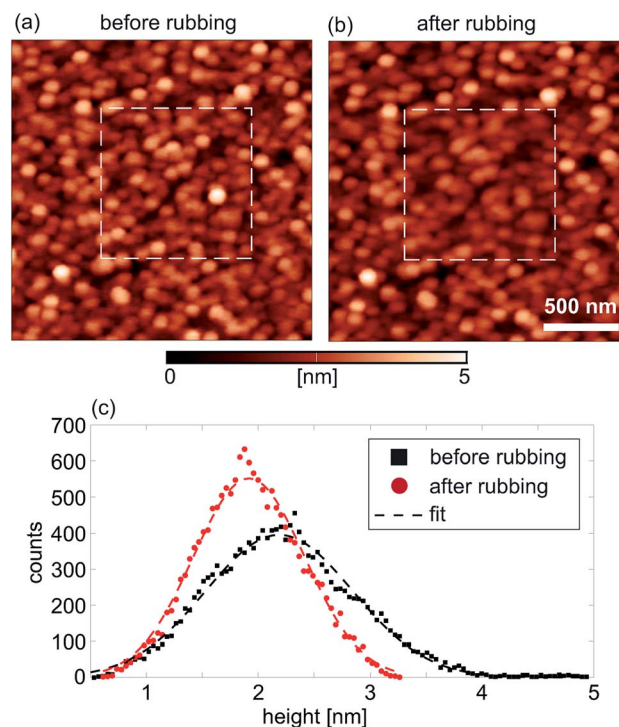


Fig. 4 AFM topographic images of the sample surface acquired (a) before and (b) after the rubbing of the inner $1 \times 1 \mu\text{m}^2$ domain (marked by dashed lines) at a normal force of $1.6 \mu\text{N}$. z-scale is 5 nm. (c) Histogram of the height distribution within the square domains marked in parts (a) and (b).



of some NPs is slightly decreased. This can be seen by lower brightness and clarity of these NPs. Therefore, NPs stay stable on the film surface and they are not removed, but some of them can be worn since their height is decreased due to local scratching. Still, the most important finding is that the NPs are tightly attached to the underlying film which stays protected.

The protection by NPs is two-fold. They mechanically protect the underlying manganite film from normal load applied by the AFM probe preventing any morphological damage of the film and facilitating a stable and reliable switching process. At the same time, NPs prevent aging of manganite films due to their exposure to the environment. Namely, it is well known that environmental factors deteriorate electrical properties (conductivity for example) of thin metal-oxides, usually due to detrimental reactions with various species from the atmosphere. This is the reason why higher conductivity was usually observed on areas of the manganite film covered by NPs, as can be seen in Fig. 2(a).

In order to further explain the observed effects, the rubbing with a grounded probe at increased normal load was combined with the scanning in contact mode using a biased AFM tip, but at a low normal force. CPD maps after such manipulations are depicted in Fig. 5(a) and (b). In Fig. 5(a), the $2 \times 2 \mu\text{m}^2$ square domain was firstly rubbed with the grounded tip, and then the inner $1 \times 1 \mu\text{m}^2$ domain was scanned in contact mode with a bias voltage of $U_t = -1 \text{ V}$ applied to the AFM tip. In Fig. 5(b), the order was the opposite, the larger square domain was scanned in contact mode at $U_t = -1 \text{ V}$, while the inner one was rubbed with the grounded tip. In both cases, the rubbing with the grounded tip and increased normal load leads to an increased CPD. This is exactly the opposite to the case with the applied negative voltage (in this case, the CPD was lowered). Therefore, the local pressure from the AFM probe has a similar

effect as the rubbing with a positive bias voltage applied to the AFM tip.

According to the type of conducting path, there are two resistive switching mechanisms: with a filamentary and an interface-type conducting path.⁴ The switching mechanism of LSMO films belongs to the second type and it is based on oxygen vacancy migrations.⁵⁹ This mechanism is usually characterized by the formation of a Schottky barrier at the interface between a metal electrode and a semiconducting metal-oxide film.^{4,60} The width and height of the barrier can be tuned by applying a bias voltage which controls the oxygen vacancy concentration within the charge depletion layer at the metal-semiconductor interface.

In the considered case of mechanically induced resistive switching, instead of an externally applied bias voltage, the width and height of the Schottky barrier between the AFM tip (DCP20 probes are highly conductive, so they can be considered as metallic ones) and sample surface are controlled by the inverse Vegard effect and flexoelectric field. According to the Vegard law of a chemical expansion, the local stress and strains are proportional to the mobile ion concentration.¹⁸ Generally, the unit cell volume increases with the oxygen vacancy concentration.²⁶ In the considered case, the sample surface rubbed with the AFM tip is locally compressed along the surface normal, so the oxygen vacancy concentration is decreased. As a result, an excess of negative charges on the sample surface appears. This is in accordance with the results of KPFM measurements, where an increased CPD was observed on rubbed parts, meaning that the Fermi level was locally raised. The electrical transport in LSMO is based on the hopping of electrons between adjacent Mn^{3+} and Mn^{4+} ions across oxygen ions.⁶¹ During the rubbing, the oxygen ion concentration beneath the tip is increased (since the oxygen vacancy concentration is decreased), so this effect does not seem to be a mechanism for the observed decrease of the electrical conductivity.

At the same time, a local and non-uniform compression of a sample surface leads to a strain gradient and a local flexoelectric field. This field is oriented from the sample surface toward the bulk.³¹ This pushes oxygen vacancies away from the sample surface, while attracting negative charges toward the sample surface, again in accordance with the KPFM results. Since the C-AFM maps in Fig. 2(a) were measured with a positive bias voltage applied to the sample, the induced flexoelectric field is an obstacle for the electron transport from the AFM tip to the sample. Therefore, the induced flexoelectric field makes an additional potential barrier for the electron transport resulting in lower currents as observed in the C-AFM maps.

The inverse Vegard effect and flexoelectric field can be coupled as well. The LSMO films grown on the STO substrate are under in-plane tensile strain due to a lattice mismatch as can be seen from the asymmetric reciprocal space map given in Fig. S1(a) of the ESI.† This tensile strain can induce an in-built flexoelectric field.²¹ The strain can be relaxed by increasing the oxygen vacancy concentration.²¹ However, in a sample rubbed with the AFM tip, the oxygen vacancy concentration is further decreased due to the inverse Vegard effect. The strain is then

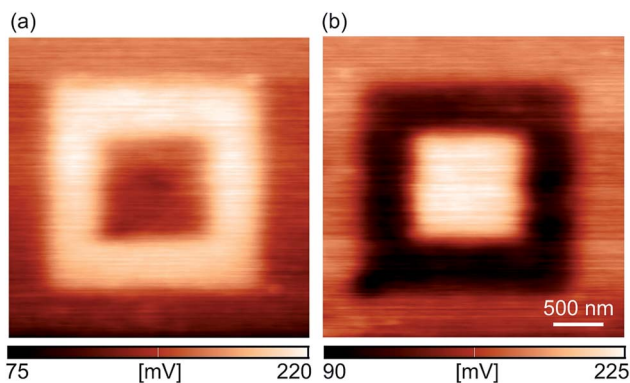


Fig. 5 $3 \times 3 \mu\text{m}^2$ CPD maps of the sample rubbed with both grounded (at high normal load) and biased (low normal load and negative bias voltage) tips: (a) first, the inner $2 \times 2 \mu\text{m}^2$ domain was rubbed with the grounded AFM probe and at a normal force $0.48 \mu\text{N}$, and then, the smaller inner $1 \times 1 \mu\text{m}^2$ domain was scanned in the contact mode at a low normal force $0.16 \mu\text{N}$ and with a tip bias voltage of -1 V , and (b) first, the inner $2 \times 2 \mu\text{m}^2$ domain was scanned in the contact mode at a low normal force of $0.16 \mu\text{N}$ and with a tip bias voltage of -1 V , and then the smaller inner $1 \times 1 \mu\text{m}^2$ domain was rubbed with the grounded AFM probe and at a normal force of $0.48 \mu\text{N}$. The CPD scale is (a) 75–220 mV and (b) 90–225 mV.



even more enhanced, potentially leading to an additional increase of the flexoelectric field. As a result, both the inverse Vegard effect and flexoelectric field could raise the potential barrier supporting the observed changes of the electrical properties.

The efficiency and robustness of the resistive switching process were tested also in the case of an insulating LSFMO thin film with FeO_x NPs on top. At the same time, besides different conductivities of the underlying film (here the measured current on non-rubbed areas was up to 50 pA, that is, three order of magnitude lower than on the LSMO film with NPs), the surface coverage of the LSFMO film by NPs was increased in order to check its influence on the switching process. The asymmetric reciprocal space map and the in-plane magnetization curves for this sample are given in Figs. S3(a) and (b) of the ESI,[†] respectively. The morphology of the investigated sample is depicted in Fig. S5 of the ESI.[†] The surface coverage of the LSFMO substrate by FeO_x NPs is more than 80%. As a result, the AFM tip is practically in direct contact only with the NPs (on the other hand, due to a lower surface coverage of the LSMO film, there are parts with a bare LSMO substrate which can be directly probed with the AFM tip). The influence of a local pressure on the surface electrical properties is displayed in Fig. S6 (C-AFM analysis) and S7 (KPFM analysis) of the ESI.[†] They illustrate that the local electrical current drops, while the local CPD grows with the normal force applied during a rubbing. The CPD maps measured after the combined rubbing with a grounded tip at an increased normal load and a negatively biased tip are given in Fig. S8 of the ESI.[†] The observed changes in the CPD indicate that the rubbing with the grounded tip is equivalent to the applying a positive bias voltage by the AFM tip.

According to the presented results, the electrical properties were changed in the same way for both samples despite a different surface coverage by NPs. We hence conclude that the observed changes are dominantly related to manganite films since the surface coverage by NPs does not have a significant influence. Therefore, during the rubbing with the AFM tip, the applied mechanical load is transferred across NPs to the underlying manganite films, so the AFM tip does not need to be in direct contact with the films. Since FeO_x NPs are not laterally connected, electrical currents go from the AFM tip across NPs to manganite films, or directly from the tip to the films. After that, charge carriers are transported laterally through the manganite films to an external electrical contact.

The results of KPFM measurements indicate that the rubbing with a grounded AFM tip and increased normal load induce localized charges on a sample surface. In metal-oxides generally, localized charges appear due to local changes in the oxygen vacancy concentration. In order to measure the time evolution of the localized charges, the CPD was measured as a function of a time. The resulting CPD maps after the rubbing of the inner 1 × 1 μm² square domain are given in Fig. 6(a) (immediately after the rubbing, after 2 h and after 3 h) and Fig. 6(b) (immediately after the rubbing, after 3 h and after 6 h) for LSMO and LSFMO films, respectively.

The results for the time-dependent measurements are summarized in Fig. 7(a1) and (b1) for the samples with LSMO

and LSFMO films, respectively, displaying the CPD for both rubbed and non-rubbed regions. The representative values of the CPD were calculated from the corresponding histograms, as in the previous analysis. The CPD on the rubbed regions was decreasing rather slowly. After around 4 h and 6 h for the LSMO and LSFMO films, respectively, the CPD was almost equal on both rubbed and non-rubbed domains. The difference in the CPD between two domains, ΔCPD as a function of time is depicted in Fig. 7(a2) and (b2) for the LSMO and LSFMO films, respectively. The experimental results were fitted with the following curve: ΔCPD(*t*) = ΔCPD(0)exp(−*t*/τ) (given by the dashed line), where *t* is time in hours, while τ is the time constant of the relaxation process. For the sample with the LSMO film, τ = 1.75 h, while for that with the LSFMO film, the relaxation was much slower, with the time constant τ = 3.5 h.

The rate constant of the relaxation of oxygen vacancies can be calculated according to the measured CPD in the following way:⁶²

$$\gamma(t) = \frac{\Delta\text{CPD}(t) - \Delta\text{CPD}(0)}{\Delta\text{CPD}(\infty) - \Delta\text{CPD}(0)}, \quad (1)$$

where ΔCPD(*t*) is the change in the CPD between rubbed and non-rubbed domains, while ΔCPD(0) and ΔCPD(∞) stand for ΔCPD at the initial moment and at the end of the relaxation, respectively. Generally, oxygen incorporation into a metal-oxide film can be divided into two processes, the surface reaction and diffusion in the sample bulk,^{62–64} so the rate constant can be deduced in the following way:

$$\gamma(t) = \gamma_{\text{surf}}(t) + \gamma_{\text{diff}}(t), \quad (2)$$

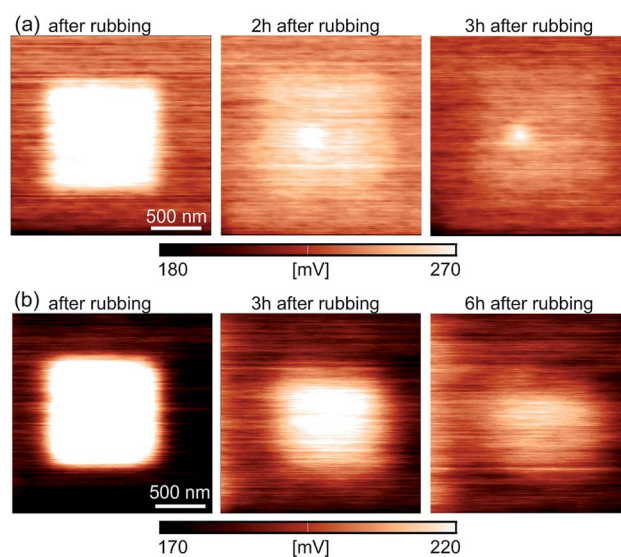


Fig. 6 Evolution of CPD maps after the rubbing (at a normal force of 0.55 μN) of the inner 1 × 1 μm² domain as a function of time: (a) CPD maps of the sample with a LSMO substrate measured immediately after the rubbing, after 2 h, and after 3 h, (b) CPD maps of the sample with a LSFMO substrate measured immediately after the rubbing, after 3 h, and after 6 h. The CPD scale is (a) 180–270 mV and (b) 170–220 mV.



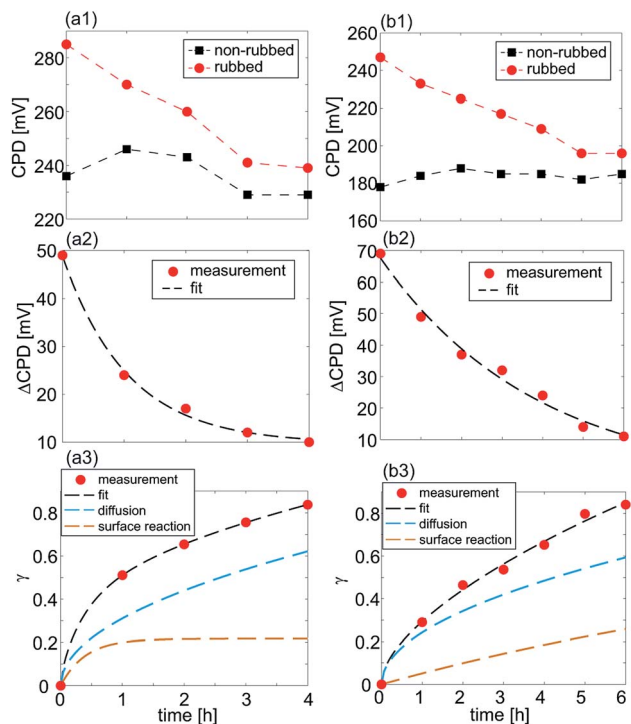


Fig. 7 Evolution of CPD, Δ CPD, and γ as a function of time for the (a) LSMO and (b) LSFMO samples. Top row (a1) and (b1): CPD on rubbed and non-rubbed areas. Middle row (a2) and (b2): CPD difference, Δ CPD, calculated as the difference between CPDs on rubbed and non-rubbed areas. Dashed lines stand for the fit to experimentally obtained points. Bottom row (a3) and (b3): factor γ obtained from the experimental results (points) and the corresponding fit (dashed lines) with the individual contribution of $\gamma_{\text{surf}}(t)$ and $\gamma_{\text{diff}}(t)$.

where γ_{surf} and γ_{diff} stand for the rate constants of the surface reaction and diffusion, respectively. The surface reaction part can be approximated with an exponential law $\gamma_{\text{surf}}(t) \sim 1 - \exp(-k_s t/L)$, where k_s is the surface reaction constant and L is the film thickness. The diffusion part is proportional to $\gamma_{\text{diff}}(t) \sim \sqrt{t}$. The overall rate constant $\gamma(t)$ together with the contributions of $\gamma_{\text{surf}}(t)$ and $\gamma_{\text{diff}}(t)$ are given in Fig. 7(a3) and (b3) for both samples, LSMO and LSFMO films, respectively. As can be seen, the diffusion has larger contribution in the overall relaxation of oxygen vacancies. Accordingly, the relaxation process can be described in the following way. The rubbing with the AFM tip leads to a local sample compression and a decrease of the oxygen vacancy concentration at the sample surface. When the AFM tip is removed, the sample surface relaxes slowly, with a time constant in the order of hours. During that time, oxygen vacancies diffuse from the sample bulk toward the surface in order to reach the initial concentration.

KPFM maps measured after the rubbing suggest that the mechanical interaction AFM tip-sample could induce trapped charges in the sample surface due to either contact charging (local pressure in a single point) or triboelectrification (during AFM tip motion in contact with the sample). However, our measurements were done under ambient conditions at a high humidity around 50%. At such high humidity, it was not

possible to observe any trapped charges induced by either contact charging or triboelectrification. Due to the conductive water layer at a sample surface, the time scale of the relaxation process of the trapped charges is very small (smaller than the time needed to switch to C-AFM (KPFM) mode and make a full scan). At the same time, the relaxation of trapped charges is generally followed by lateral charge spreading. On the other hand, in our case, we didn't observe any spreading of domains with modified surface potential as can be seen in the KPFM images in Fig. 6. In addition, tribocharges generally improve conductivity due to resulting, discharge induced currents, while we observed exactly the opposite behaviour. Therefore, decreased conductivity, the time constant of the relaxation process and clear spatial confinement of domains with the modified electrical surface potential imply that we really induced an internal flexoelectric field, while trapped charges due to triboelectrification can be excluded.

4 Conclusions

In summary, we have demonstrated mechanically induced switching of the electrical conductivity of thin manganite films covered by iron-oxide NPs. The sample surface is switched to an insulating state for a high enough local pressure applied by the AFM tip. The pressure induces the flexoelectric field while the corresponding potential barrier prevents further flow of charge carriers from the AFM tip to the sample. After removing the AFM tip, the sample surface is relaxed slowly, with the time constant in the order of hours. During this time, oxygen vacancies diffuse from the bulk of manganite films towards the surface until the equilibrium electrical surface potential is not reached. Top iron-oxide NPs provide weak room-temperature magnetism, protect the surface of manganite films from aging caused by environmental factors, and assure wear resistance and a reliable switching process of manganite films since the NPs are mechanically stable and tightly attached to the underlying manganite films even after the rubbing at high normal loads. The considered heterostructures are potential candidates for novel multifunctional devices with switchable both electric and magnetic properties. In that sense, in order to reach their full potential, the next step would be to explore the switching of their magnetic properties.

Conflicts of interest

There are no conflicts to declare.

Acknowledgements

B. V. and Z. K. acknowledge the support of the Serbian Ministry of Education, Science and Technological Development (Projects No. OI171005 and III45018). E. P.-M. and A. P. acknowledge financial support from the Spanish Ministry of Economy and Competitiveness through the "Severo Ochoa" Programme for Centres of Excellence in R&D (SEV-2015-0496), and project MAT2015-71664 R. This work has received funding from the European Union's Horizon 2020 research and innovation



programme under the Marie Skłodowska-Curie grant agreement No. 645658 (DAFNEOX Project). B. V. thanks Dimitrije Stepanenko for fruitful discussions.

References

- 1 D. B. Strukov, G. S. Snider, D. R. Stewart and R. S. Williams, *Nature*, 2008, **453**, 80–83.
- 2 J. J. Yang, M. D. Pickett, X. Li, D. A. A. Ohlberg, D. R. Stewart and R. S. Williams, *Nat. Nanotechnol.*, 2008, **3**, 429–433.
- 3 R. Waser and M. Aono, *Nat. Mater.*, 2007, **6**, 833–840.
- 4 A. Sawa, *Mater. Today*, 2008, **11**, 28–36.
- 5 D. S. Jeong, R. Thomas, R. S. Katiyar, J. F. Scott, H. Kohlstedt, A. Petraru and C. S. Hwang, *Rep. Prog. Phys.*, 2012, **75**, 076502.
- 6 D. B. Strukov and H. Kohlstedt, *MRS Bull.*, 2012, **37**, 108–114.
- 7 D. Ielmini, *Semicond. Sci. Technol.*, 2016, **31**, 063002.
- 8 B. J. Choi, D. S. Jeong, S. K. Kim, C. Rohde, S. Choi, J. H. Oh, H. J. Kim, C. S. Hwang, K. Szot, R. Waser, B. Reichenberg and S. Tiedke, *J. Appl. Phys.*, 2005, **98**, 033715.
- 9 K. Szot, W. Speier, G. Bihlmayer and R. Waser, *Nat. Mater.*, 2006, **5**, 312–320.
- 10 M. Lanza, U. Celano and F. Miao, *J. Electroceram.*, 2017, **39**, 94–108.
- 11 Y. Yang, X. Zhang, L. Qin, Q. Zeng, X. Qiu and R. Huang, *Nat. Commun.*, 2017, **8**, 15173.
- 12 I. Bozovic, G. Logvenov, I. Belca, B. Narimbetov and I. Sveklo, *Phys. Rev. Lett.*, 2002, **89**, 107001.
- 13 J. H. Haeni, P. Irvin, W. Chang, R. Uecker, P. Reiche, Y. L. Li, S. Choudhury, W. Tian, M. E. Hawley, B. Craigo, A. K. Tagantsev, X. Q. Pan, S. K. Streiffer, L. Q. Chen, S. W. Kirchoefer, J. Levy and D. G. Schlom, *Nature*, 2004, **430**, 758.
- 14 L. Abad, V. Laukhin, S. Valencia, A. Gaup, W. Gudat, L. Balcells and B. Martínez, *Adv. Funct. Mater.*, 2007, **17**, 3918–3925.
- 15 A. Tebano, C. Aruta, S. Sanna, P. G. Medaglia, G. Balestrino, A. A. Sidorenko, R. De Renzi, G. Ghiringhelli, L. Braicovich, V. Bisogni and N. B. Brookes, *Phys. Rev. Lett.*, 2008, **100**, 137401.
- 16 S. Lee, A. Pirogov, M. Kang, K.-H. Jang, M. Yonemura, T. Kamiyama, S.-W. Cheong, F. Gozzo, N. Shin, H. Kimura, Y. Noda and J.-G. Park, *Nature*, 2008, **451**, 805.
- 17 A. Herklotz, D. Lee, E.-J. Guo, T. L. Meyer, J. R. Petrie and H. N. Lee, *J. Phys.: Condens. Matter*, 2017, **29**, 493001.
- 18 A. N. Morozovska, E. A. Eliseev, A. K. Tagantsev, S. L. Bravina, L.-Q. Chen and S. V. Kalinin, *Phys. Rev. B*, 2011, **83**, 195313.
- 19 P. Zubko, G. Catalan and A. K. Tagantsev, *Annu. Rev. Mater. Res.*, 2013, **43**, 387–421.
- 20 P. Zubko, G. Catalan, A. Buckley, P. R. L. Welche and J. F. Scott, *Phys. Rev. Lett.*, 2007, **99**, 167601.
- 21 D. Lee, A. Yoon, S. Y. Jang, J.-G. Yoon, J.-S. Chung, M. Kim, J. F. Scott and T. W. Noh, *Phys. Rev. Lett.*, 2011, **107**, 057602.
- 22 H. Lu, D. J. Kim, C.-W. Bark, S. Ryu, C. B. Eom, E. Y. Tsybmal and A. Gruverman, *Nano Lett.*, 2012, **12**, 6289–6292.
- 23 D. Lee, S. M. Yang, J.-G. Yoon and T. W. Noh, *Nano Lett.*, 2012, **12**, 6436–6440.
- 24 Y. Kim, S. J. Kelly, A. Morozovska, E. K. Rahani, E. Strelcov, E. Eliseev, S. Jesse, M. D. Biegalski, N. Balke, N. Benedek, D. Strukov, J. Aarts, I. Hwang, S. Oh, J. S. Choi, T. Choi, B. H. Park, V. B. Shenoy, P. Maksymovych and S. V. Kalinin, *Nano Lett.*, 2013, **13**, 4068–4074.
- 25 S. J. Kelly, Y. Kim, E. Eliseev, A. Morozovska, S. Jesse, M. D. Biegalski, J. F. Mitchell, H. Zheng, J. Aarts, I. Hwang, S. Oh, J. S. Choi, T. Choi, B. H. Park, S. V. Kalinin and P. Maksymovych, *Nanotechnology*, 2014, **25**, 475302.
- 26 P. Sharma, S. Ryu, J. D. Burton, T. R. Paudel, C. W. Bark, Z. Huang, Ariando, E. Y. Tsybmal, G. Catalan, C. B. Eom and A. Gruverman, *Nano Lett.*, 2015, **15**, 3547–3551.
- 27 Y. Wang, K. Zhao, X. Shi, G. Li, G. Xie, X. Lai, J. Ni and L. Zhang, *Sci. Rep.*, 2015, **5**, 10841.
- 28 S. Das, B. Wang, Y. Cao, M. Rae Cho, Y. Jae Shin, S. Mo Yang, L. Wang, M. Kim, S. V. Kalinin, L.-Q. Chen and T. W. Noh, *Nat. Commun.*, 2017, **8**, 615.
- 29 A. Gómez, J. M. Vila-Fungueiriño, R. Moalla, G. Saint-Girons, J. Gázquez, M. Varela, R. Bachelet, M. Gich, F. Rivadulla and A. Carretero-Genevriero, *Small*, 2017, **13**, 1701614.
- 30 G. Catalan, A. Lubk, A. H. G. Vlooswijk, E. Snoeck, C. Magen, A. Janssens, G. Rispens, G. Rijnders, D. H. A. Blank and B. Noheda, *Nat. Mater.*, 2011, **10**, 963–967.
- 31 H. Lu, C.-W. Bark, D. Esque de los Ojos, J. Alcala, C. B. Eom, G. Catalan and A. Gruverman, *Science*, 2012, **336**, 59–61.
- 32 Y.-J. Li, J.-J. Wang, J.-C. Ye, X.-X. Ke, G.-Y. Gou, Y. Wei, F. Xue, J. Wang, C.-S. Wang, R.-C. Peng, X.-L. Deng, Y. Yang, X.-B. Ren, L.-Q. Chen, C.-W. Nan and J.-X. Zhang, *Adv. Funct. Mater.*, 2015, **25**, 3405–3413.
- 33 Y. Gu, Z. Hong, J. Britson and L.-Q. Chen, *Appl. Phys. Lett.*, 2015, **106**, 022904.
- 34 L. Chen, Z. Cheng, W. Xu, X. Meng, G. Yuan, J. Liu and Z. Liu, *Sci. Rep.*, 2016, **6**, 19092.
- 35 T. Jia, H. Kimura, Z. Cheng and H. Zhao, *Sci. Rep.*, 2016, **6**, 31867.
- 36 Z. Lu, Z. Fan, P. Li, H. Fan, G. Tian, X. Song, Z. Li, L. Zhao, K. Huang, F. Zhang, Z. Zhang, M. Zeng, X. Gao, J. Feng, J. Wan and J. Liu, *ACS Appl. Mater. Interfaces*, 2016, **8**, 23963–23968.
- 37 D. Guo, G. Xie and J. Luo, *J. Phys. D: Appl. Phys.*, 2014, **47**, 013001.
- 38 K. Yakushiji, F. Ernult, H. Imamura, K. Yamane, S. Mitani, K. Takanashi, S. Takahashi, S. Maekawa and H. Fujimori, *Nat. Mater.*, 2005, **4**, 57–61.
- 39 H. A. Atwater and A. Polman, *Nat. Mater.*, 2010, **9**, 205–213.
- 40 X. Yu, T. J. Marks and A. Facchetti, *Nat. Mater.*, 2016, **15**, 383.
- 41 J.-G. J. Zhu and C. Park, *Mater. Today*, 2006, **9**, 36–45.
- 42 S. Yuasa, T. Nagahama, A. Fukushima, Y. Suzuki and K. Ando, *Nat. Mater.*, 2004, **3**, 868.
- 43 Z. Xu, M. Gao, L. Yu, L. Lu, X. Xu and Y. Jiang, *ACS Appl. Mater. Interfaces*, 2014, **6**, 17823–17830.
- 44 Z. Konstantinović, F. Sandiumenge, J. Santiso, L. Balcells and B. Martínez, *Nanoscale*, 2013, **5**, 1001–1008.
- 45 R. Abrudan, F. Brüßing, R. Salikhov, J. Meermann, I. Radu, H. Ryll, F. Radu and H. Zabel, *Rev. Sci. Instrum.*, 2015, **86**, 063902.



- 46 E. Dagotto, T. Hotta and A. Moreo, *Phys. Rep.*, 2001, **344**, 1–153.
- 47 A.-M. Haghiri-Gosnet and J.-P. Renard, *J. Phys. D: Appl. Phys.*, 2003, **36**, R127.
- 48 T. Wu, S. B. Ogale, J. E. Garrison, B. Nagaraj, A. Biswas, Z. Chen, R. L. Greene, R. Ramesh, T. Venkatesan and A. J. Millis, *Phys. Rev. Lett.*, 2001, **86**, 5998–6001.
- 49 C. Moreno, C. Munuera, S. Valencia, F. Kronast, X. Obradors and C. Ocal, *Nano Lett.*, 2010, **10**, 3828–3835.
- 50 L. Balcells, L. Peña, R. Galceran, A. Pomar, B. Bozzo, Z. Konstantinović, F. Sandiumenge and B. Martínez, *J. Appl. Phys.*, 2013, **113**, 073703.
- 51 A. Tebano, C. Aruta, P. G. Medaglia, F. Tozzi, G. Balestrino, A. A. Sidorenko, G. Allodi, R. De Renzi, G. Ghiringhelli, C. Dallera, L. Braicovich and N. B. Brookes, *Phys. Rev. B: Condens. Matter Mater. Phys.*, 2006, **74**, 245116.
- 52 L. Marín, L. A. Rodríguez, C. Magén, E. Snoeck, R. Arras, I. Lucas, L. Morellón, P. A. Algarabel, J. M. De Teresa and M. R. Ibarra, *Nano Lett.*, 2015, **15**, 492–497.
- 53 J. Ma, Y. Zhang, L. Wu, C. Song, Q. Zhang, J. Zhang, J. Ma and C.-W. Nan, *MRS Commun.*, 2016, **6**, 354–359.
- 54 R. U. Chandrasena, W. Yang, Q. Lei, M. U. Delgado-Jaime, K. D. Wijesekara, M. Golalikhani, B. A. Davidson, E. Arenholz, K. Kobayashi, M. Kobata, F. M. F. de Groot, U. Aschauer, N. A. Spaldin, X. Xi and A. X. Gray, *Nano Lett.*, 2017, **17**, 794–799.
- 55 Z. Konstantinović, J. Santiso, L. Balcells and B. Martínez, *Small*, 2009, **5**, 265–271.
- 56 Z. Konstantinović, J. Santiso, D. Colson, A. Forget, L. Balcells and B. Martínez, *J. Appl. Phys.*, 2009, **105**, 063919.
- 57 Z. Konstantinović, L. Balcells and B. Martínez, *J. Magn. Mater.*, 2010, **322**, 1205–1208.
- 58 A. Tebano, C. Aruta, P. G. Medaglia, F. Tozzi, G. Balestrino, A. A. Sidorenko, G. Allodi, R. De Renzi, G. Ghiringhelli, C. Dallera, L. Braicovich and N. B. Brookes, *Phys. Rev. B: Condens. Matter Mater. Phys.*, 2006, **74**, 245116.
- 59 L. Yao, S. Inkinen and S. van Dijken, *Nat. Commun.*, 2017, **8**, 14544.
- 60 Y.-L. Chung, P. Y. Lai, Y.-C. Chen and J.-S. Chen, *ACS Appl. Mater. Interfaces*, 2011, **3**, 1918–1924.
- 61 J. M. D. Coey, M. Viret and S. von Molnár, *Adv. Phys.*, 2009, **58**, 571–697.
- 62 M. Andra, F. Gunkel, C. Baumer, C. Xu, R. Dittmann and R. Waser, *Nanoscale*, 2015, **7**, 14351–14357.
- 63 T. Bieger, J. Maier and R. Waser, *Sens. Actuators, B*, 1992, **7**, 763–768.
- 64 R. Merkle and J. Maier, *Angew. Chem., Int. Ed.*, 2008, **47**, 3874–3894.



Nanoscale mechanical control of surface electrical properties of manganite films with magnetic nanoparticles – Electronic Supplementary Information (ESI)

Borislav Vasić,^{*a} Zorica Konstantinović,^b Elisa Pannunzio-Miner,^{‡c} Sergio Valencia,^d
Radu Abrudan,^{¶e} Radoš Gajić,^a and Alberto Pomar^c

^a *Graphene Laboratory of Center for Solid State Physics and New Materials, Institute of Physics Belgrade, University of Belgrade, Pregrevica 118, 11080 Belgrade, Serbia; E-mail: bvasic@ipb.ac.rs*

^b *Center for Solid State Physics and New Materials, Institute of Physics Belgrade, University of Belgrade, Pregrevica 118, 11080 Belgrade, Serbia*

^c *Institut de Ciència de Materials de Barcelona, ICMA-B-CSIC, Campus de la UAB, 08193 Bellaterra, Spain*

^d *Helmholtz-Zentrum Berlin für Materialien und Energie, Albert-Einstein-Str.15, 12489 Berlin, Germany*

^e *Institut für Experimentalphysik/Festkörperphysik, Ruhr-Universität Bochum, 44780 Bochum, Germany*

[‡] *Present address: Centro de Investigaciones en Ciencias de la Tierra (CICTERRA-CONICET-UNC), Facultad de Ciencias Exactas, Físicas y Naturales, Av. Velez Sarfield 1611, X5016GCA Ciudad Universitaria, Cordoba, Argentina*

[¶] *Present address: Helmholtz-Zentrum Berlin für Materialien und Energie, Albert-Einstein-Str.15, 12489 Berlin, Germany*

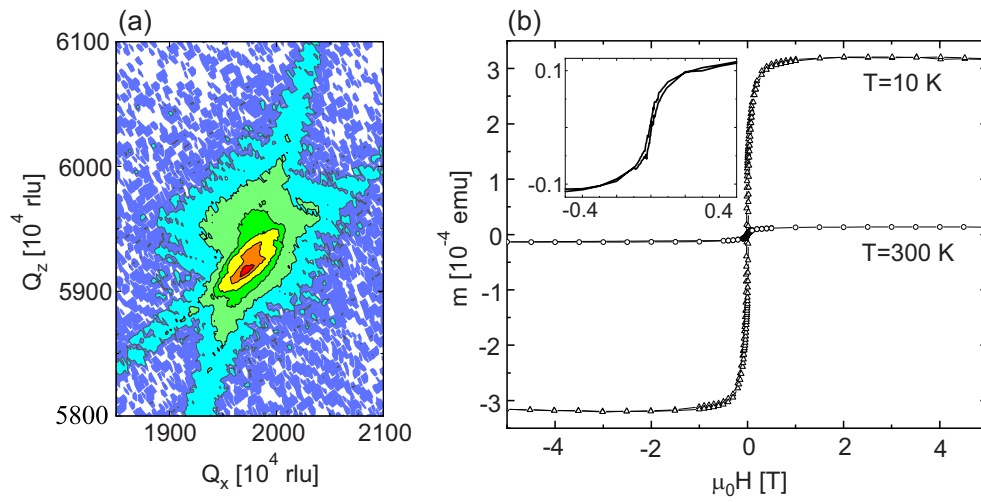


Figure S1: (a) Reciprocal space maps of (103) reflections of the LSMO film. (b) In-plane magnetization curves of the LSMO thin film with self-assembled FeO_x nanoparticles measured at 10 K and 300 K. The inset in (b): detail of the room temperature hysteresis loop. Low temperature magnetization curve ($T = 10$ K) is dominated by the signal from 100 nm thick LSMO film. On the other hand, the high temperature magnetization is very weak and the hysteresis is almost closed ($H_c = 50$ Oe). Taking into account the depressed value of the ferromagnetic transition ($T_c = 270$ K) in nanostructured manganite thin films [1], the magnetization curve at room temperature ($T = 300$ K) should arise from iron-based nanoparticles (notice that, at $T = 300$ K, the magnetization disappears in bare LSMO films and remains principally only in the film with FeO_x NPs as shown in Fig. S4(b)).

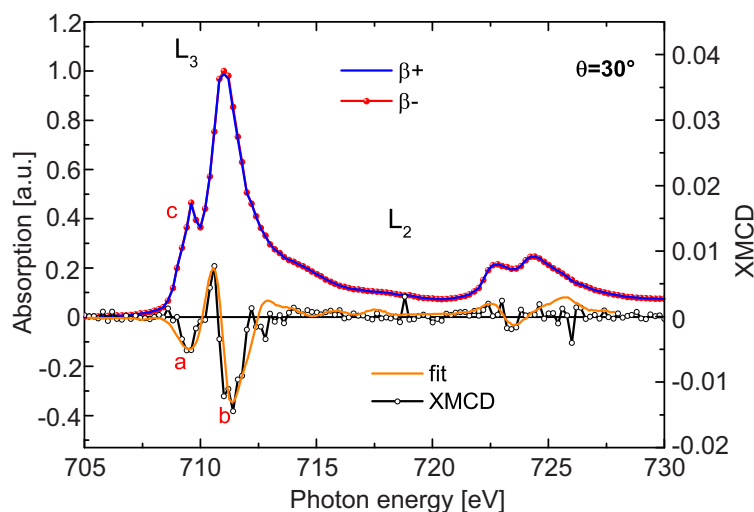


Figure S2: The results of XAS measurements ($\beta+$ and $\beta-$ curves) as well as the resulting XMCD. The XAS spectrum can be considered to be alike to the individual $\beta+$ and $\beta-$ curves due to the small dichroic effect (max ca. 1.5%). The Fe $L_{3,2}$ -edge absorption curve is representative of a Fe^{3+} oxidation state [2]. More information can be obtained from the XMCD shape. More concretely, the strength of spectroscopic features a, b and c appearing at the L_3 edge of the XMCD of magnetic iron oxide compounds are known to depend on the Fe oxidation state and coordination of the Fe magnetic species, i.e. Fe^{2+} in octahedral coordination and Fe^{3+} in octahedral and tetrahedral coordination [3]. We have fit the experimental XMCD curve with reported XMCD curves for the individual contributions [3]. The best fit is in agreement with the XAS data pointing to a major Fe^{3+} contribution (92%), although a minute amount of Fe^{2+} needs to be considered in order to reproduce the intensity of the feature. The fit shows that 65% of Fe is in octahedral coordination (52.5% Fe^{3+} and 8.0% Fe^{2+}) while 39.5% in tetrahedral one. The XAS, the size of the effect as well as the fit results of the XMCD curve seem to indicate that we have a $\gamma\text{-Fe}_2\text{O}_3$ phase [4, 5, 6, 7].

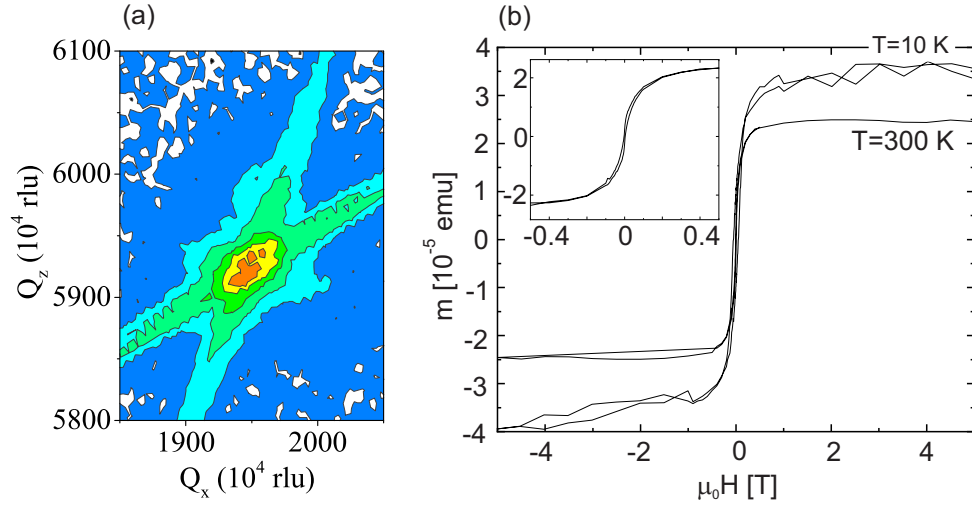


Figure S3: (a) The asymmetric reciprocal space map of (103) reflections of the 20 nm thick LSFMO film grown on top of the STO substrate. Although, the reflection from LSFMO (103) is low, the LSFMO film seems to be fully strained with in-plane lattice constant close to $a_{\parallel, \text{STO}} = 3.905 \text{ \AA}$. Due to presence of tensile strain in the thin film, the out-of-plane parameter is reduced than the corresponding bulk value $a_{\text{LSFMO}} = 3.873 \text{ \AA}$ [8] and estimated to $a_{\perp, \text{LSFMO}} = 3.862(8) \text{ \AA}$. (b) In-plane magnetization curves of the 20 nm thick LSFMO film with self-assembled FeO_x NPs measured at 10 K and 300 K. The inset in (b): detail of the room temperature hysteresis loop typically found in disordered manganite thin films. On the other hand, the high temperature magnetization is very weak and the hysteresis is almost closed ($H_c = 50 \text{ Oe}$). Taking into account that the ferromagnetic transition of LSFMO lies below the room temperature ($T_c = 270 \text{ K}$), the magnetization curve at room temperature should arise, as in the previous case, from iron-based NPs (notice that, at $T = 300 \text{ K}$, the magnetization disappears in bare LSFMO films and remains principally only in the film with FeO_x NPs as shown in Fig. S4(c)).

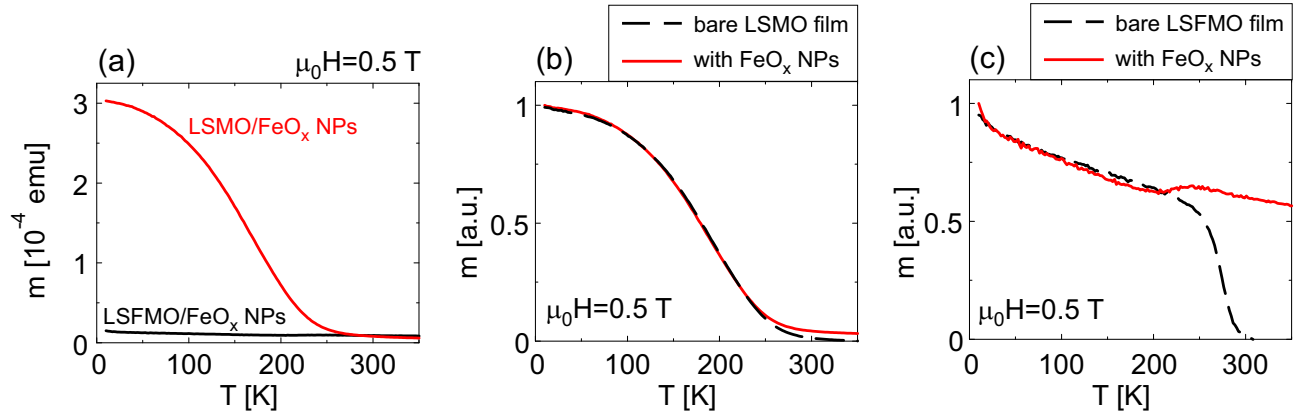


Figure S4: (a) In-plane magnetization curves of LSMO and LSFMO film with FeO_x NPs measured under $H = 0.5 \text{ T}$. Comparison of the normalized magnetization of bare manganite films (dashed line) and the one with FeO_x NPs (solid line) for (b) LSMO (100 nm thick film) and (c) LSFMO (20 nm thick film). At 300 K, the magnetization disappears in bare manganite films and remains principally only in the structures with FeO_x NPs.

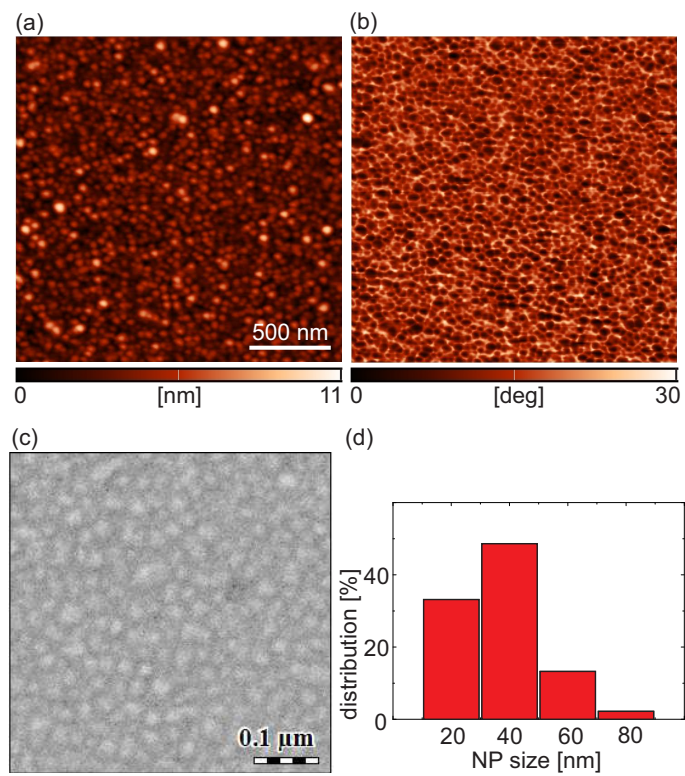


Figure S5: Morphology of the sample consisting of LSFMO film with iron-oxide NPs: (a) AFM topographic image and (b) the corresponding phase image of the sample acquired during the imaging in tapping mode, (c) SEM image and (d) the size distribution of iron-oxide NPs.

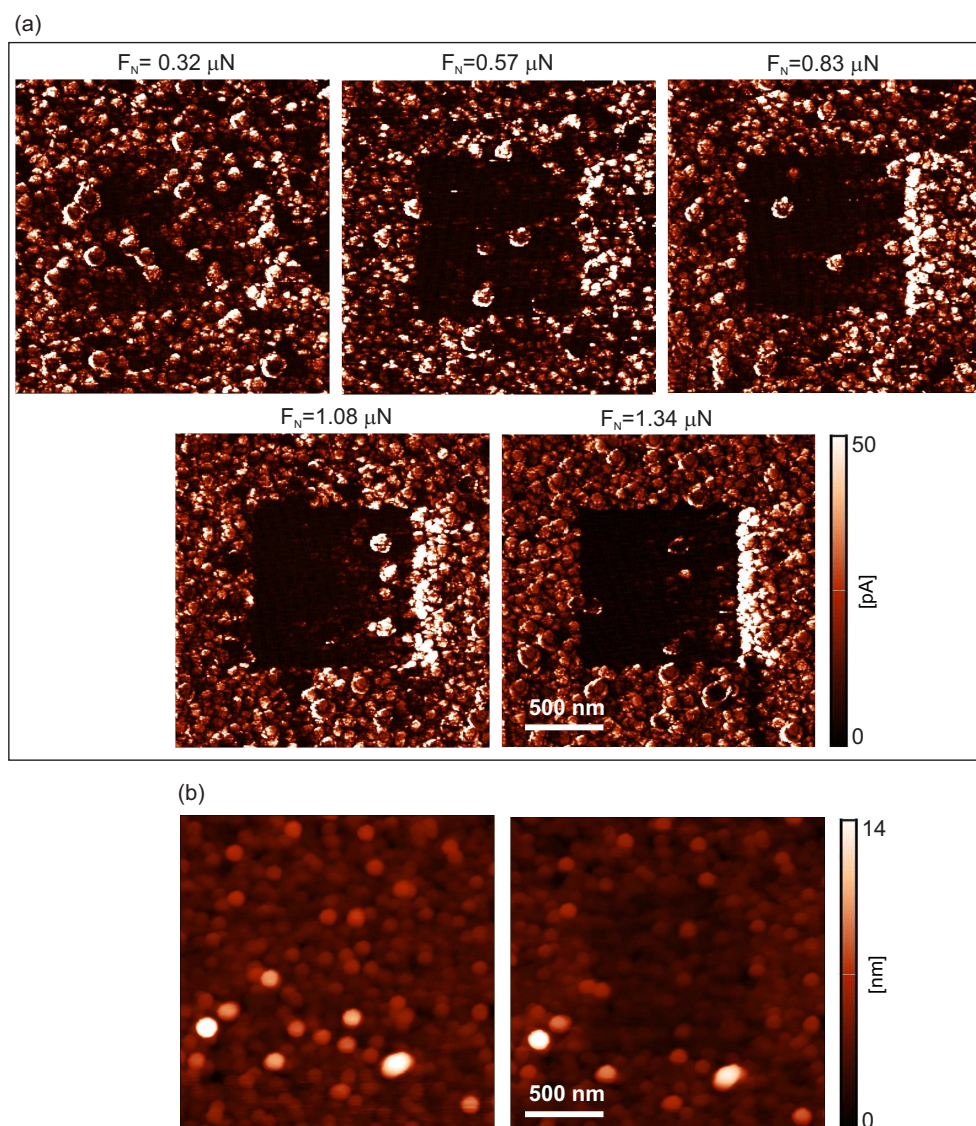


Figure S6: Conductivity of the sample consisting of LSFMO film with iron-oxide NPs: (a) $2 \times 2 \mu\text{m}^2$ current maps measured by C-AFM after the rubbing of inner $1 \times 1 \mu\text{m}^2$ domain at specified normal force, (b) Sample morphology before (the left image) and after (the right image) the rubbing of the inner square $1 \times 1 \mu\text{m}^2$ domain at the highest normal load of $1.34 \mu\text{N}$.

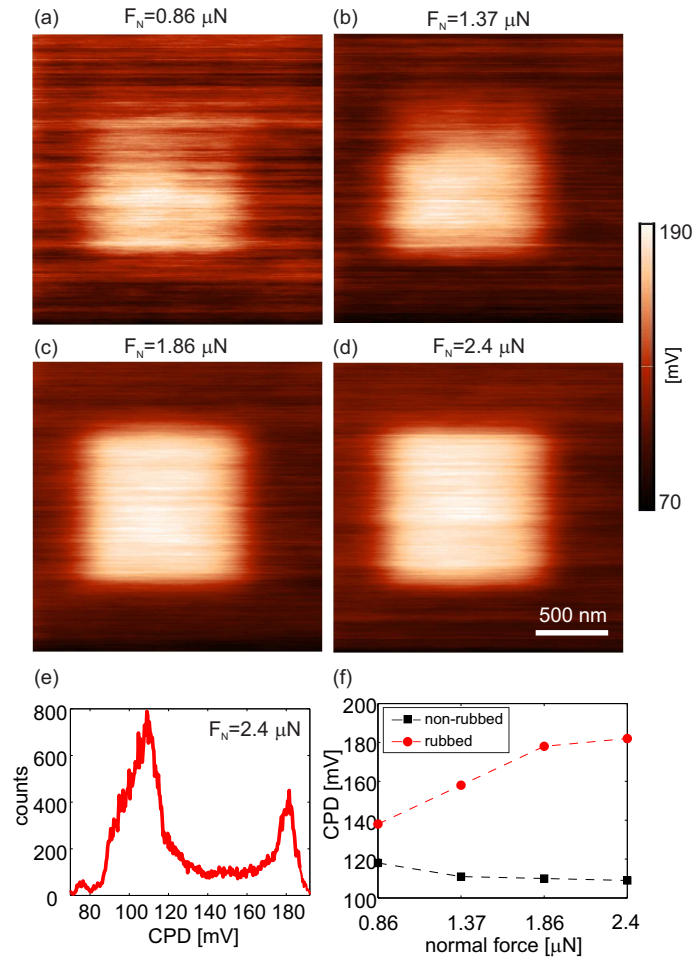


Figure S7: Electrical surface potential of the sample consisting of LSFMO film with iron-oxide NPs: (a-d) $2 \times 2 \mu\text{m}^2$ CPD maps measured by KPFM after the rubbing of inner $1 \times 1 \mu\text{m}^2$ domain at specified normal force, and (f) CPD change on rubbed and non-rubbed regions as a function of normal force.

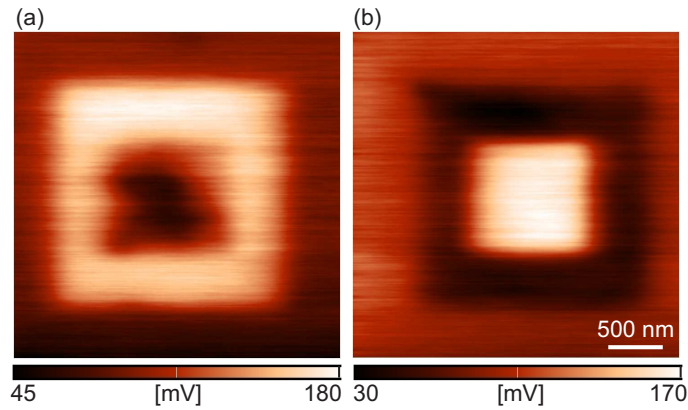


Figure S8: $3 \times 3 \mu\text{m}^2$ CPD maps of the sample consisting of LSFMO film with iron-oxide NPs, rubbed with both grounded (at high normal load) and biased (low normal load and negative bias voltage) tip: (a) first, the inner $2 \times 2 \mu\text{m}^2$ domain was rubbed by grounded AFM probe and at the normal force $0.48 \mu\text{N}$, and then, the smaller inner $1 \times 1 \mu\text{m}^2$ domain was scanned in the contact mode at low normal force $0.16 \mu\text{N}$ and with tip bias voltage -1 V , and (b) first, the inner $2 \times 2 \mu\text{m}^2$ domain was scanned in the contact mode at low normal force $0.16 \mu\text{N}$ and with tip bias voltage -1 V , and then the smaller inner $1 \times 1 \mu\text{m}^2$ domain was rubbed by grounded AFM probe and at the normal force $0.48 \mu\text{N}$.

References

- [1] Z. Konstantinović, J. Santiso, Ll. Balcells, and B. Martínez. Strain-Driven Self-Assembled Network of Antidots in Complex Oxide Thin Films. *Small*, 5:265–271, 2009.
- [2] T. J. Regan, H. Ohldag, C. Stamm, F. Nolting, J. Lüning, J. Stöhr, and R. L. White. Chemical effects at metal/oxide interfaces studied by x-ray-absorption spectroscopy. *Phys. Rev. B*, 64:214422, 2001.
- [3] R. A. D. Pattrick, G. Van Der Laan, C. M. B. Henderson, P. Kuiper, E. Dudzik, and D. J. Vaughan. Cation site occupancy in spinel ferrites studied by X-ray magnetic circular dichroism: developing a method for mineralogists. *Eur. J. Mineral.*, 14:1095–1102, 2002.
- [4] S. Brice-Profeta, M.-A. Arrio, E. Tronc, N. Menguy, I. Letard, C. Cartier dit Moulin, M. Noguès, C. Chanéac, J.-P. Jolivet, and Ph. Sainctavit. Magnetic order in $\gamma - \text{Fe}_2\text{O}_3$ nanoparticles: a XMCD study. *J. Magn. Magn. Mater.*, 288:354 – 365, 2005.
- [5] E. Pellegrain, M. Hagelstein, S. Doyle, H. O. Moser, J. Fuchs, D. Vollath, S. Schuppler, M. A. James, S. S. Saxena, L. Niesen, O. Rogojanu, G. A. Sawatzky, C. Ferrero, M. Borowski, O. Tjernberg, and N. B. Brookes. Characterization of Nanocrystalline $\gamma - \text{Fe}_2\text{O}_3$ with Synchrotron Radiation Techniques. *Phys. Status Solidi B*, 215(1):797–801, 1999.
- [6] D. H. Kim, H. J. Lee, G. Kim, Y. S. Koo, J. H. Jung, H. J. Shin, J.-Y. Kim, and J.-S. Kang. Interface electronic structures of $\text{BaTiO}_3@X$ nanoparticles ($X=\gamma - \text{Fe}_2\text{O}_3$, Fe_3O_4 , $\alpha - \text{Fe}_2\text{O}_3$, and Fe) investigated by XAS and XMCD. *Phys. Rev. B*, 79:033402, 2009.
- [7] L. Cao, Z.-X. Jiang, Y.-H. Du, X.-M. Yin, S.-B. Xi, W. Wen, A. P. Roberts, A. T. S. Wee, Y.-M. Xiong, Q.-S. Liu, and X.-Y. Gao. Origin of Magnetism in Hydrothermally Aged 2-Line Ferrihydrite Suspensions. *Environ. Sci. Technol.*, 51:2643–2651, 2017.
- [8] G. Zhang and J. Lin. Synthesis, electronic and magnetic properties of the double B mixed perovskite series $\text{La}_{0.5}\text{Sr}_{0.5}\text{Mn}_{1-x}\text{Fe}_x\text{O}_3$. *J. Alloys Compd.*, 507:47 – 52, 2010.

Nonstoichiometry Driven Ferromagnetism in Double Perovskite $\text{La}_2\text{Ni}_{1-x}\text{Mn}_{1+x}\text{O}_6$ Insulating Thin Films

Monica Bernal-Salamanca,^{*,†} Zorica Konstantinović,^{†,‡} Lluís Balcells,[†] Elisa Pannunzio-Miner,^{†,§} Felip Sandiumenge,[†] Laura Lopez-Mir,[†] Bernat Bozzo,[†] Javier Herrero-Martín,[⊥] Alberto Pomar,[†] Carlos Frontera,^{†,||} and Benjamín Martínez^{†,||}

[†]Institut de Ciència de Materials de Barcelona, ICMA-B-CSIC, Campus UAB, 08193 Bellaterra, Spain

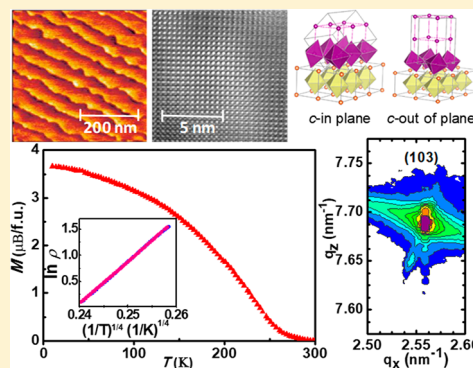
[‡]Center for Solid State Physics and New Materials, Institute of Physics Belgrade, University of Belgrade, Pregrevica 118, 11080 Belgrade, Serbia

[§]Facultad de Ciencias Exactas, Físicas y Naturales, Centro de Investigaciones en Ciencias de la Tierra (CICTERRA-CONICET-UNC), Av. Velez Sarfield 1611, X5016GCA Ciudad Universitaria, Cordoba, Argentina

[⊥]ALBA Synchrotron Light Source, C. de la Llum 2-26, E 08920 Cerdanyola del Vallès, Spain

Supporting Information

ABSTRACT: In this work we report on the epitaxial growth of $\text{La}_2\text{NiMnO}_6$ double perovskite thin films on top of (001) oriented SrTiO_3 substrates by RF magnetron sputtering. The influence of oxygen pressure (P_{O_2}) and growth temperature on the microstructure, stoichiometry of the films, and magnetic and transport properties is thoroughly investigated. It is found that high oxygen pressure promotes the growth of stoichiometric films, with a Ni/Mn ratio almost equal to 1. However, these films exhibit poor ferromagnetic properties with respect to the expected optimum values corresponding to ferromagnetic ordering mediated by superexchange interaction between Mn^{4+} and Ni^{2+} according to the Goodenough-Kanamori rules. Most interestingly, films grown at low P_{O_2} exhibit Ni/Mn ratios below 1, but ferromagnetic properties close to the optimal ones. The valence balance between Ni and Mn ions in nonstoichiometric sample has been elucidated by X-ray absorption spectroscopy. The results indicate that Ni deficiency plays a crucial role in the puzzling insulating ferromagnetic behavior observed in nonstoichiometric samples.



INTRODUCTION

The urgent need to solve the problems of energetic efficiency and data storage and processing speed of current micro-electronic devices has boosted the search for new materials and paradigms capable of circumventing those problems. Spintronics has been signaled as a potential alternative technology to develop multifunctional electronics that combines logic operations, data storage and transmission with an improved energetic efficiency. The development of spintronic devices requires the generation and control of highly spin-polarized currents¹ or pure spin currents.² A way of obtaining a highly spin polarized current is by using a spin filtering effect through ferromagnetic-insulator-ferromagnetic tunnel barriers.^{3,4} The same effect can be obtained simply by using a ferromagnetic insulating barrier.^{5,6} However, ferromagnetic insulators (FMI) are very scarce; among the few FMI known double perovskite (DP) oxides, like $\text{La}_2\text{NiMnO}_6$ (LNMO) and $\text{La}_2\text{CoMnO}_6$, have attracted considerable attention due to their high Curie temperature, T_C , and magnetodielectric properties.^{7–9} In both cases, the ferromagnetic (FM) ordering is explained by superexchange interaction between Mn^{4+} and Ni^{2+} or Co^{2+}

according to the Goodenough-Kanamori rules,¹⁰ and it is very sensitive to the ordered distribution of cations in the B-sublattice of the DP structure.¹¹ In the case of LNMO, cationic order gives rise to 180° ferromagnetic interactions between Ni^{2+} (d^8 , $t_{2g}^6 e_g^2$, $S = 1$) and Mn^{4+} (d^3 , $t_{2g}^3 e_g^0$, $S = 3/2$) ions¹² and results in a T_C very close to RT ($T_C \approx 280$ K). Disorder of Ni and Mn ions, and oxygen vacancies may strongly suppress FM superexchange interaction.¹³ In fact, cationic disorder reduces the saturation magnetization from $5 \mu\text{B}/\text{f.u.}$ (the maximum expected for the FM contribution of Ni^{2+} and Mn^{4+}) since, according to the Goodenough-Kanamori rules, disorder introduces antiferromagnetic (AF) $\text{Mn}^{4+}-\text{O}-\text{Mn}^{4+}$ and $\text{Ni}^{2+}-\text{O}-\text{Ni}^{2+}$ interactions.^{8,15}

In this work we report on the growth and characterization of $\text{La}_2\text{Ni}_{1-x}\text{Mn}_{1+x}\text{O}_6$ thin films prepared by RF magnetron sputtering on top (001)-oriented SrTiO_3 (STO) substrates. Substrates have been cleaned in an ultrasonic bath with Milli-Q

Received: December 21, 2018

Revised: March 4, 2019

Published: March 15, 2019

Table 1. Chemical Composition and Stoichiometry Ratio of LNMO- δ D (140 mTorr) and LNMO- δ G (300 mTorr) Samples

P_{O_2} (mTorr)	La (atom %)	Ni (atom %)	Mn (atom %)	O (atom %)	La/Ni + Mn	Ni/Mn	x
140	19.2 \pm 0.2	6.0 \pm 0.1	14.0 \pm 0.1	60.0 \pm 0.5	0.96	0.4	0.43
300	20.0 \pm 0.1	9.0 \pm 0.1	9.0 \pm 0.1	60.0 \pm 0.2	1.11	1.0	0.0

water and then annealed at 1000 °C in air for 2 h to obtain a clean and smooth surface typical for single TiO₂ termination.¹⁶ Growth conditions, such as temperature, annealing, and oxygen partial pressure, have been optimized to obtain LNMO thin films with M_S and T_C close to the optimum values. However, it is found that Ni/Mn stoichiometric samples always exhibit values of T_C and M_S far from the optimum ones. In contrast, samples with a remarkable Ni deficiency show excellent magnetic properties. We report a detailed study of structural, magnetic, and transport properties of these two characteristic types of samples.

EXPERIMENTAL DETAILS

A series of LNMO samples were grown with oxygen partial pressures ranging from 70 to 300 mTorr and temperatures between 500 and 900 °C. As-grown samples were annealed in-situ at the same temperature for 1 h under high oxygen pressure (420 Torr, see Supporting Information SI1c). The surface quality of samples was characterized by atomic force microscopy (AFM), using a MFP-3D AFM (Asylum Research) in tapping mode. Structural characterization was made by means of X-ray diffraction and reflectivity techniques using a X'Pert MRD-Panalytical and a Siemens D5000 diffractometers. The chemical composition and stoichiometry ratio of LNMO thin films were determined by wavelength dispersive spectrometer (WDS) electron probe microanalysis (EPMA) using a CAMECA SX-50 electron microprobe equipped with four wavelength-dispersive X-ray spectrometers. High-resolution transmission electron microscopy (HRTEM) was used to study the microstructure of cross section specimens of LNMO thin films on a FEITecni G2F20 S-TWIN HR(S)TEM operated at 200 kV. Cross section specimens were prepared by focus ion beam (FIB). The transport properties were measured in a Physical Properties Measurement System (PPMS, Quantum Design) by a four-probe technique. Magnetization measurements were done using a superconducting quantum interferometer device (SQUID, Quantum Design). X-ray absorption spectroscopy (XAS) and X-ray magnetic circular dichroism (XMCD) were investigated at the Ni and Mn $L_{2,3}$ edges in BL29-BOREAS beamline at ALBA Synchrotron Light Source (Barcelona, Spain). The spectra were measured in both the total electron yield (TEY) and total fluorescence yield (TFY) modes, under ultrahigh vacuum conditions (2×10^{-10} mbar). The applied magnetic field (parallel to the X-ray beam) was 4 T.

RESULTS AND DISCUSSION

Previous results corresponding to LNMO/STO thin films prepared by pulsed laser deposition (PLD)^{13,17–20} make evident that magnetic properties depend on film thickness and growth conditions. Similarly, samples prepared by RF sputtering, in a broad range of temperatures ($500 \text{ °C} \leq T \leq 900 \text{ °C}$) and oxygen pressure ($70 \text{ mTorr} \leq P_{O_2} \leq 300 \text{ mTorr}$), exhibit strong dependence on the growth conditions. Samples grown/annealed at high temperature and oxygen pressures above ~ 200 mTorr show very deficient magnetic properties with T_C below 150 K. On lowering oxygen pressure (maintaining the same annealing temperature), T_C rises up to ~ 225 K and then decreases again (see Supporting Information SI1a). We have also found a non-monotonous dependence of T_C on the deposition temperature (see Supporting Information SI1b). On lowering the growth

temperature from 900 to 850 °C, at a partial oxygen pressure of 140 mTorr, T_C increases from $T_C \sim 160$ K to ~ 240 K (estimated from inflection point). As a result, the optimal Curie temperature, $T_C \approx 240$ K, has been obtained for samples grown/annealed at 850 °C and at an oxygen partial pressure of 140 mTorr. This sample was labeled as LNMO- δ D.

According to previous results reported for LNMO samples prepared by PLD, good FM properties (i.e., $T_C \approx 260$ K and $M_S \approx 5 \mu_B/\text{f.u.}$ at low T) are obtained in samples prepared at higher oxygen pressures, i.e., 300 mTorr,¹⁷ or even 800 mTorr, and temperatures around 750–800 °C,^{13,14} with in situ annealing (in 760 Torr of O₂) to promote B site cationic ordering and minimize the oxygen deficiency.²¹ In general, for lower oxygen pressures, samples present a low saturation magnetization,¹³ with the exception of ref 17 where films prepared under $p_{O_2} > 180$ mTorr are reported to have $M_S \approx 5 \mu_B/\text{f.u.}$

These results are in contrast with our own observations, so to clarify the origin of those discrepancies we have carefully analyzed the stoichiometry (using EPMA) of our samples. Results are shown in Supporting Information SI2a. It is found that all the samples present a La:(Ni + Mn) atomic ratio near 1, but the Ni/Mn ratio strongly depends on p_{O_2} used in the growth process. Thus, the actual composition of the samples should be expressed as La₂Ni_{1-x}Mn_{1+x}O₆. Samples grown at high pressure present a Ni/Mn ratio close to 1 (and thus good stoichiometry), but at lower pressures samples become Ni-deficient, reaching values of a Ni/Mn ratio of about 0.3 ($x \approx 0.54$, La₂Ni_{0.46}Mn_{1.54}O₆). In spite of this remarkable Ni deficiency, samples exhibit excellent FM properties (see Supporting Information SI1a). It must be remarked that Blasco et al. report, for bulk LaNi_{0.25}Mn_{0.75}O₃, a FM behavior with $T_C = 200$ K and $M_S = 2.75 \mu_B/\text{f.u.}$ (equivalent to $5.5 \mu_B/\text{f.u.}$ in double perovskite notation). It is also worth to remark that the same work reports stoichiometric oxygen content when samples were sintered in O-poor atmosphere (Ar). On another hand, a very detailed local study of LNMO films grown by molecular beam epitaxy (at very low oxygen pressure) has shown a spontaneous segregation of the stoichiometric La₂NiMnO₆ into a La₂Ni_{1-x}Mn_{1+x}O₆ ($x \approx 0.2$) matrix and NiO inclusions.²²

Lowering the growth/annealing temperature to 850 °C has little effect on the stoichiometry of the films (see Supporting Information SI2b) which are still Ni deficient. Actually, sample LNMO- δ D has a Ni/Mn ratio of 0.40 ($x = 0.43$) as shown in Table 1. Next, we will focus on two samples prepared by using the same conditions: growth temperature 850 °C and annealing at 850 °C for 60 min, one under 140 mTorr of O₂ pressure (LNMO- δ D), and the second under 300 mTorr (LNMO- δ G). This second sample has nearly the nominal Ni/Mn = 1 stoichiometry but poor ferromagnetic properties.

XRR curves of nonstoichiometric (LNMO- δ D) and stoichiometric (LNMO- δ G) samples are depicted in Figure 1a,b, which correspond to the highest and lowest T_C obtained, the fitting to these data (black lines) has been done using XRay utilities library.²³ Thickness values found for both samples are

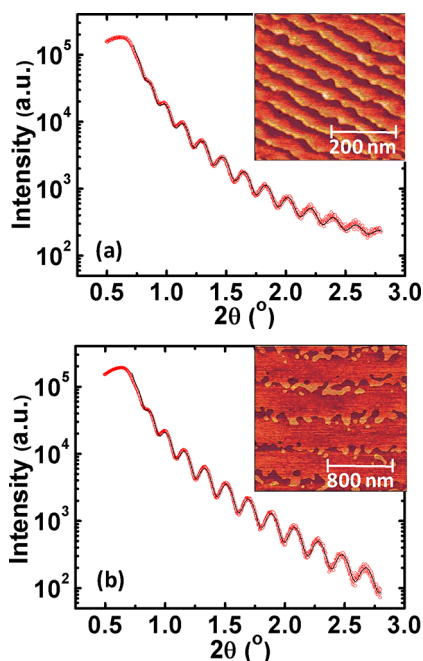


Figure 1. XRR data of (a) LNMO- δ D (140 mTorr O₂) and (b) LNMO- δ G (300 mTorr O₂) thin films grown on STO(001) substrate, with thickness values of 42 and 44 nm; insets show AFM topography images of a small area of the samples.

very similar (42 and 44 nm). Inset in **Figure 1** shows AFM topography images in tapping mode of both films, topography shows a high quality flat surface with a terrace-steps type morphology. The root-mean-square (rms) value of surface roughness is found to be very small about of 0.2 nm and steps height of about 0.4 nm, corresponding to the perovskite unit cell. Annealing at high oxygen pressures (420 Torr) favors the formation of well-defined terraces mimicking the STO substrate.

In addition, structural properties have been investigated by high resolution $\theta/2\theta$ X-ray diffraction (XRD), **Figure 2a,c** shows scans around (002)_{STO} reflection using Cu-K α_1 monochromatic radiation of LNMO- δ D and LNMO- δ G samples, respectively. From these $\theta/2\theta$ XRD scans the corresponding out-of-plane lattice parameters are determined: $c = 3.895$ Å for LNMO- δ D and $c = 3.908$ Å LNMO- δ G, which are slightly higher than the pseudocubic perovskite lattice parameter of bulk LNMO, namely, 3.879 Å,²⁴ and this difference may be caused by the presence of Mn³⁺. It is also worth mentioning here that Laue fringes can only be seen in LNMO- δ G sample but not in LNMO- δ D one. Reciprocal space maps, around (103)_{STO} reflection of the same samples, are shown in **Figure 2b,d**. Measures evidence that films grow fully strained. In fact, for LNMO- δ D sample, a small peak coming from the LNMO film can be seen just above the substrate peak. For LNMO- δ G sample, both peaks are fully overlapped due to the high similarity between the out-of-plane lattice parameters.

A deeper insight into the microstructural features can be obtained by using high resolution transmission electron microscopy (HRTEM) (see **Figure 3a,b**. For HRTEM observations in **Figure 3a** sample LNMO- δ D was cut along the (100) direction of STO. HRTEM images show the coexistence of domains with different orientations as can be appreciated in the Fourier transform (FT) of the image. The

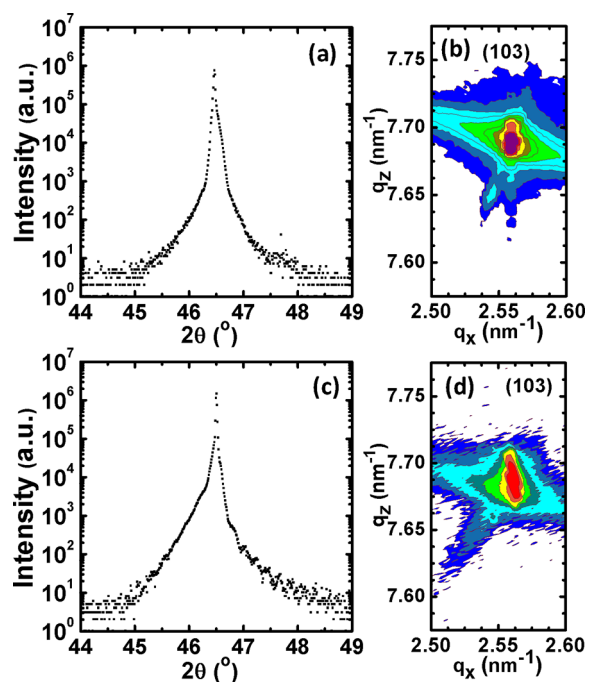


Figure 2. High-resolution $\theta/2\theta$ XRD scans of the (002) reflections for (a) LNMO- δ D and (c) LNMO- δ G films. Panels (b) and (d) show RSM around (103) reflections for the same samples.

FT of a large area shows different spots corresponding to the enlargement of the LNMO lattice with respect to STO (LNMO cell parameters are of the type $a \approx b \approx \sqrt{2}a_p$, $c \approx 2a_p$ where a_p is the primitive perovskite cell parameter). These spots can be indexed as (0 $k/2$ 1) (k odd), (0 k 1/2) (1 odd), and (0 $k/2$ 1/2) (k and 1 odd) and indicate different orientations of the LNMO cell in the film. This is better illustrated by FT of small regions. For some regions only spots corresponding to (0 $k/2$ 1) (k odd) are found thus in those regions c_{LNMO} is parallel to (010)-STO substrate direction; in other zones only spots of the type (0 k 1/2) (1 odd) can be seen, which correspond to c_{LNMO} parallel to (001)-STO; and finally a third type of regions where spots of the type (0 $k/2$ 1/2) (k and 1 odd) are present corresponds to c_{LNMO} parallel to (100)-STO. On the other hand, in **Figure 3b** sample LNMO- δ G was cut along the (110)-STO direction. In this case, the sample is more homogeneous, only one type of spot corresponding to the larger cell of LNMO is observed, and superstructure spots are indexed as ($h/2$ $-h/2$ 1/2) (h and 1 odd). This indicates that the orientation of c_{LNMO} axis is parallel to (100) or (010) (in the plane of the film). Therefore, HRTEM observations confirm that domains with in-plane and out-of-plane orientations of c_{LNMO} coexist in LNMO- δ D sample, while only in-plane orientation of c_{LNMO} is stabilized for LNMO- δ G sample. This multiple orientations of c -axis in LNMO- δ D must be related to the absence of Laue fringes in the $\theta/2\theta$ scans.

Zero field cooling-field cooling (ZFC-FC) magnetization curves of both, LNMO- δ D and LNMO- δ G, samples measured using a field of $H \approx 0.1$ T, are depicted in **Figure 4a**. This figure evidences the strong dependence of the magnetic behavior on the oxygen pressure during the growth process. $M(T)$ curves of LNMO- δ G sample do not show evidence of ferromagnetic ordering. On the other hand, $M(T)$ curves of LNMO- δ D display the expected temperature dependence of

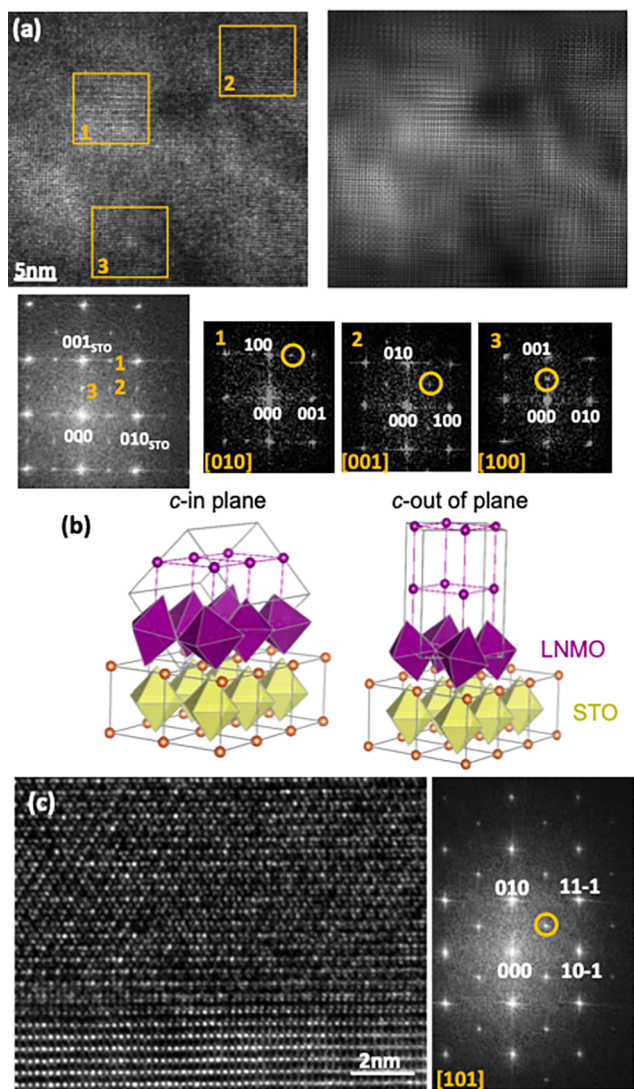


Figure 3. (a) Cross-section HRTEM image of the LNMO- δ D (140 mTorr) film viewed along the STO [100] zone axis and corresponding Fourier filtered image emphasizing the strain state of the film and the coexistence of nanodomains with different orientations. Bottom panels show, from left to right, an FFT of the whole image exhibiting superlattice spots at $(0\ 0\ 1/2)$, $(0\ k/2\ 1/2)$, and $(0\ k/2\ 0)$ (indexed according to STO orientation), and FFT patterns obtained from windows 1, 2 and 3, respectively, revealing the orientations of different nanodomains: In 1 the c -axis of the film is in-plane and parallel to the image, in 2 the c -axis is in-plane and perpendicular to the image, and in 3 it is oriented out-of-plane. In 1, 2, and 3, peaks and zone axes are referred to the pseudocubic unit cell of LNMO. (b) Schematic models for the observed epitaxial relationships. (c) Cross-section HRTEM image and corresponding FFT pattern of the LNMO- δ G (300 mTorr) film viewed along the [110] zone axis, exhibiting high crystalline quality and an in-plane orientation of the monoclinic c_{LNMO} axis. The encircled spot corresponds to the $(h/2\ h/2\ -1/2)$ superlattice. Indices are referred to the pseudocubic unit cell of LNMO.

an FM with no signal of double transition, and a Curie temperature of about 240 K. The field dependence of the magnetization, $M(H)$, after correcting the diamagnetic contribution from substrate and other instrumental contributions,²⁵ is shown in Figure 4b. $M(H)$ loops corresponding to sample LNMO- δ D at $T = 10$ K exhibit the expected hysteretic behavior with a coercive field of about 1.4 kOe and 1.2 kOe for

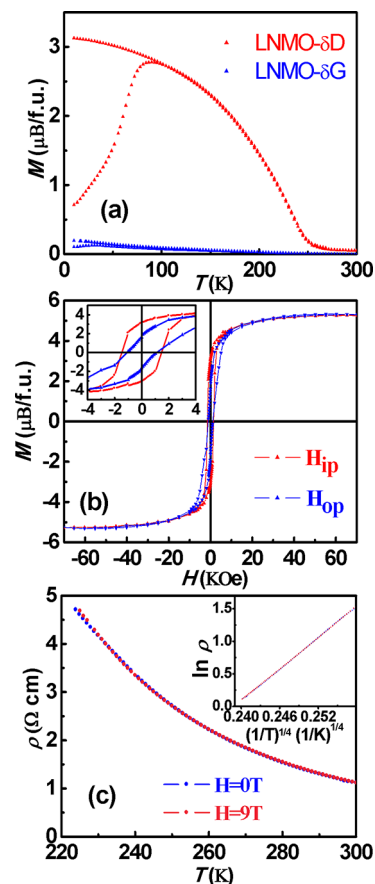


Figure 4. (a) Magnetization measured after ZFC and FC as a function of temperature under an applied field of 1 kOe (in the plane of the film) of LNMO- δ D (140 mTorr O₂, red curve) and LNMO- δ G (300 mTorr O₂, blue curve). (b) $M(H)$ hysteresis loops of LNMO- δ D at 10 K for H applied in-plane and out-of-plane, the inset shows in detail the low field region. (c) Temperature dependent resistivity of LNMO- δ D under zero and 9 T magnetic field. Inset, $\ln \rho$ vs $(1/T)^{1/4}$.

the field applied in-plane and out-of-plane configurations, respectively. Accordingly, magnetization remanence for the in-plane configuration ($M_r \approx 3.1\ \mu_B/\text{f.u.}$) is larger than that found for the out-of-plane ($M_r \approx 1.7\ \mu_B/\text{f.u.}$). A saturation magnetization of $M_s \approx 5.3\ \mu_B/\text{f.u.}$ is found, i.e., somewhat larger than the expected theoretical value ($\sim 5\ \mu_B/\text{f.u.}$) for perfectly ordered stoichiometric $\text{La}_2\text{Ni}^{2+}\text{Mn}^{4+}\text{O}_6$,²⁶ and also larger than the experimental bulk value ($\sim 4.96\ \mu_B/\text{f.u.}$). At this point it is worth mentioning that nonstoichiometry enhances the maximum value achievable for the magnetization for full FM ordering. For the stoichiometry (Ni/Mn ratio) found in our case M_s should be around $5.9\ \mu_B/\text{f.u.}$, as $2\ \mu_B/\text{Ni}$ ($\times 0.57\ \text{Ni}/\text{f.u.}$) are attributed to Ni^{2+} and $3.34\ \mu_B/\text{Mn}$ ($\times 1.43\ \text{Mn}/\text{f.u.}$) to $\text{Mn}^{3.66+}$ (as a fraction of Mn^{4+} must reduce to Mn^{3+} to compensate Ni deficiency).

On the other hand, according to Figure 4b the easy magnetization direction lies in the film plane. Although this is the usual behavior in thin films since shape anisotropy tends to place magnetization in plane, the large remanence coercive field of the out-of-plane magnetization curve cannot be understood by considering only shape anisotropy and indicates that magnetocrystalline anisotropy also plays an important role. Furthermore, HRTEM characterization has shown that domains with different crystallographic orientations coexist. Consequently, magnetocrystalline anisotropy would contribute

to both in-plane and out-of-plane directions, in accordance with the observed behavior.

Figure 4c shows the temperature and field-dependence of the resistivity of the LNMO- δ D film. The measurements show that the resistivity values increase when cooling, thus exhibiting insulating behavior in the whole temperature range. Almost no magnetic field dependence of the resistivity is detected even when crossing T_C (~ 240 K). The temperature dependence can be well described by using a three-dimensional (3D) variable-range hopping (VRH) model: $\rho(T) = \rho_0 \exp(T_0/T)^{1/4}$, where ρ_0 is the prefactor and T_0 is the characteristic hopping temperature, related to the electron hopping probability, P , of the material.²⁷ The slope of the curve corresponds to $T_0^{1/4}$, and in this case, we have obtained a value of $T_0 \approx 0.4 \times 10^8$ K, which is similar to the values reported for other transition metal oxides.^{28,29}

As mentioned in the introduction, the FM character of $\text{La}_2\text{NiMnO}_6$ is understood in terms of the superexchange interactions between Ni^{2+} and Mn^{4+} according to the Goodenough-Kanamori rules. However, the large Ni deficiency found in LNMO- δ D sample puts a question mark over this interpretation. To determine the valence states of Ni and Mn ions in Ni-deficient samples, X-ray absorption spectroscopy (XAS) experiments have been carried out in LNMO- δ D ($x \approx 0.43$) sample (at two different temperatures: 20 and 300 K). The $L_{2,3}$ ($2p \rightarrow 3d$ transition) XAS spectra, measured by using the TEY technique, corresponding to Mn and Ni are shown in Figure 5a,b. The Ni L_3 edge (see Figure 5b) is overlapped with the La M ($3d_{3/2} \rightarrow 4f$) absorption peak and is hard to analyze. In contrast, the Ni L_2 edge ($\hbar\nu \approx 865\text{--}875$ eV) absorption peak (shown in the inset) can be easily compared with that of NiO (Ni^{2+}) also shown in the inset. All three edges present a double peak feature that is quite similar to all Ni-divalent compounds and is well understood in terms of a covalent ground state of mainly Ni^{2+} ($3d^8$) character plus an anion-dependent fraction of the $3d^9 \underline{L}$ and $3d^{10} \underline{L}$ configurations, where \underline{L} stands for an anion (ligand) hole.^{30,32} This double peak is also displayed by L_2 edge of a stoichiometric (and with almost full cationic ordering) sample of $\text{La}_2\text{NiMnO}_6$, and very different from the L_2 peak of PrNiO_3 and NdNiO_3 corresponding to (Ni^{3+}).^{31,32} Therefore, we can conclude that the oxidation states of Ni ions in our Ni-deficient sample is 2+. It is worth mentioning that a XANES study in bulk samples of $\text{LaNi}_{1-x}\text{Mn}_x\text{O}_3$ has concluded that for $x \geq 0.5$ the valence of Ni stabilizes to 2+.³³

In order to determine the valence of Mn, we have also measured the $L_{2,3}$ edges of reference samples LaMnO_3 (Mn^{3+}), $\text{La}_{0.7}\text{Sr}_{0.3}\text{MnO}_3$ ($\text{Mn}^{3.3+}$), and CaMnO_3 (Mn^{4+}). Spectra measured in both TEY and TFY detection modes at room temperature are compared in Figure 5e. A shift of the Mn L_3 peak toward higher energies for all XAS spectra in the series of samples is detected. By comparing L_3 absorption peaks of LaMnO_3 at 642.5 eV (Mn^{3+}) and CaMnO_3 located at 644.1 eV (Mn^{4+}), with that of LNMO- δ D centered between both compounds at 643.5 eV, the valence of the latter can be estimated to be around +3.6. Therefore, assuming a 2+ valence for Ni, and recovering sample stoichiometry values determined by EPMA, a mixed valence of 3.64+ is obtained for Mn. Thus, XAS measurements lead us to conclude that Ni-deficient samples (LNMO- δ D) contain a certain quantity of Mn^{3+} , and therefore, Mn must be in a mixed-valence $\text{Mn}^{3+}/\text{Mn}^{4+}$ oxidation state. For that reason, since Mn^{3+} ions have a larger magnetic moment than Mn^{4+} ones, larger values of the

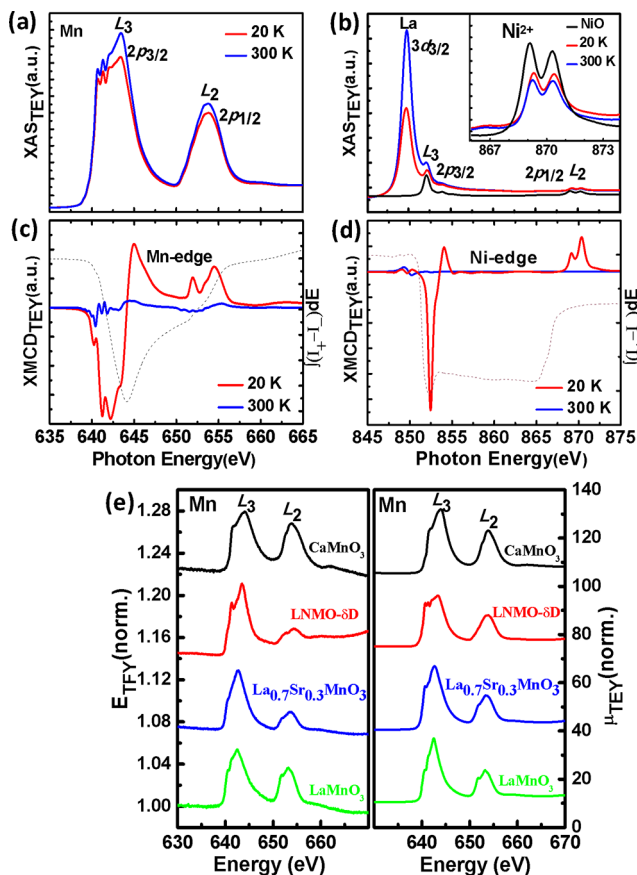


Figure 5. XAS spectra for an epitaxial LNMO- δ D thin film. (a) Mn $L_{2,3}$ and (b) Ni $L_{2,3}$, the inset shows the Ni $2p_{1/2}$ absorption spectrum, absorption spectrum of NiO is also plotted for comparison (black curve). XMCD of (c) Mn $L_{2,3}$ and (d) Ni $L_{2,3}$, measured at 20 K (red curves) and room temperature (RT) (blue curves); the dashed line shows the corresponding integral at 20 K (right axis, note that dashed lines start at zero value). (e) Absorption-corrected FY (left) and TEY (right) Mn $L_{2,3}$ XAS edge of LNMO- δ D film compared with reference spectra such as LaMnO_3 , LSMO, and CaMnO_3 at 300 K respectively.

saturation magnetization might be observed in Ni-deficient samples.

X-ray magnetic circular dichroism (XMCD) has been used to investigate the specific magnetic properties of Mn and Ni ions in the LNMO- δ D sample. All the XMCD spectra (see Figure 5c,d) have been normalized to the integrated area of the corresponding XAS spectra.³³ These spectra were measured by the TEY method at 20 K and 300 K. It is found that L_3 absorption peak shows a strong negative XMCD signal at both Ni and the Mn edges, which indicates that the Ni^{2+} and Mn^{4+} ions are aligned ferromagnetically. The XMCD signal nearly disappears at room temperature (above T_C).

In order to extract quantitative information about orbital magnetic moment μ_{orb} and spin magnetic moment μ_{spin} contributions to the magnetic moment of Mn 3d and Ni 3d states, we made use of the so-called sum-rules in the XMCD spectra.^{34–36}

$$\mu_L = -\frac{4\left(\int_{L_3} \Delta I(E) dE + \int_{L_2} \Delta I(E) dE\right)}{3\left(\int_{L_3} I(E) dE + \int_{L_2} I(E) dE\right)}(10 - N_{3d}) \quad (1)$$

$$\mu_S + 7\mu_T = -\frac{2 \int_{L_3} \Delta I(E) dE - 4 \int_{L_2} \Delta I(E) dE}{\int_{L_3} I(E) dE + \int_{L_2} I(E) dE} (10 - N_{3d}) \quad (2)$$

where $\Delta I = I^+ - I^-$; $I = I^+ + I^-$; N_{3d} is the 3d electron occupation number and μ_T is the magnetic-dipole moment (usually negligible for transition metals in octahedral environment). The corresponding integral of the XMCD signal is also depicted in (Figure 5c,d). In the case of Mn ions from the integral of XMCD signal it is found that $\mu_L^{\text{Mn}} \approx 0$. In contrast we obtained $\mu_L^{\text{Ni}}/\mu_S^{\text{Ni}} = 0.32$ at 20 K for Ni. Thus, XMCD study reveals that orbital moment of Ni is not quenched. It is worth mentioning that this orbital contribution is necessary for spin-orbit interactions giving rise to magnetocrystalline anisotropy and reinforces the interpretation that this must be the origin of the magnetic anisotropy evidenced in Figure 4b.

CONCLUSIONS

In summary, we have shown that high-quality epitaxial thin films of the double perovskite LNMO, with Curie temperatures of $T_c = 240$ K and saturation magnetization of $5.3 \mu_B/\text{f.u.}$, can be prepared by using the RF sputtering technique. However, magnetic properties turn out to be strongly dependent on the preparation conditions, particularly on the oxygen partial pressure, p_{O_2} , used during the growth process. Samples prepared at low p_{O_2} (≤ 140 mTorr) are Ni-deficient with a Ni/Mn ratio of about 0.43, while those prepared at high p_{O_2} (≥ 300 mTorr) show the expected Ni/Mn ≈ 1 ratio. However, stoichiometric samples show poor ferromagnetic properties, i.e., low T_c and low saturation magnetization. In contrast, nonstoichiometric samples exhibit high $T_c \approx 240$ K and high saturation magnetization of $M_s \approx 5.3 \mu_B/\text{f.u.}$ Assuming that FM ordering in the double perovskite structure comes from superexchange interactions between Ni^{2+} and Mn^{4+} , according to the Goodenough-Kanamori rules, the values of T_c and M_s obtained for stoichiometric samples clearly indicate that Ni/Mn cationic ordering in the B-sublattice is absent. On the other hand, XAS measurements allow concluding that Ni ions are stabilized as Ni^{2+} even in nonstoichiometric samples. Additionally, XAS measurements in nonstoichiometric samples also demonstrate that Mn ions are in a mixed-valence $\text{Mn}^{3+/4+}$ state with an effective valence of +3.6. However, samples exhibit insulating behavior, and therefore double-exchange interaction cannot be invoked to explain the observed FM ordering. So, to explain the excellent magnetic properties found in Ni-deficient samples some kind of cationic ordering between Ni^{2+} , Mn^{3+} , and Mn^{4+} in the B sublattice has to be assumed, and thus, the question of whether a Ni deficiency can favor Ni/Mn ordering arises. On the other hand, our XMCD measurements show that the contribution of the orbital moment to the magnetic moment of Mn ions is negligible, but for Ni ions it is quite important, $\mu_L^{\text{Ni}}/\mu_S^{\text{Ni}} = 0.32$, thus allowing us to conclude that magnetic anisotropy observed in the magnetic measurements ($M(H)$ loops) is of magnetocrystalline origin.

ASSOCIATED CONTENT

Supporting Information

The Supporting Information is available free of charge on the ACS Publications website at DOI: 10.1021/acs.cgd.8b01897.

Additional $M(T)$ curves and stoichiometry of the LNMO films (PDF)

AUTHOR INFORMATION

Corresponding Author

*E-mail: mbernal@icmab.es. Telephone: +34 935 801 853.

ORCID

Carlos Frontera: 0000-0002-0091-4756

Benjamín Martínez: 0000-0001-9879-7748

Notes

The authors declare no competing financial interest.

ACKNOWLEDGMENTS

M.B.-S., LL.B., F.S., B.B., C.F., B.M., and A.P. acknowledge financial support from the Spanish Ministry of Economy and Competitiveness through the “Severo Ochoa” Programme for Centres of Excellence in R&D (SEV-2015-0496), and Project MAT2015-71664-R. This work has received funding from the European Union’s Horizon 2020 Research and Innovation Programme under the Marie Skłodowska-Curie Grant Agreement No. 645658 (DAFNEOX Project). Z.K. acknowledge the support of the Serbian Ministry of Education, Science and Technological Development (III45018). Authors thank ALBA synchrotron (Spain) for the provision of beamtime.

REFERENCES

- (1) Bibes, M.; Villegas, J. E.; Barthélémy, A. Ultrathin oxide films and interfaces for electronics and spintronics. *Adv. Phys.* **2011**, *60*, 5.
- (2) Žutić, I.; Fabian, J.; Das Sarma, S. Spintronics: Fundamentals and applications. *Rev. Mod. Phys.* **2004**, *76*, 323.
- (3) Moodera, J. S.; Gallagher, E. F.; Robinson, K.; Nowak, J. Optimum tunnel barrier in ferromagnetic–insulator–ferromagnetic tunneling structures. *Appl. Phys. Lett.* **1997**, *70*, 3050.
- (4) Itoh, H.; Ozeki, J.; Inoue, J. Electronic structure and spin-filter effect of ferromagnetic insulators with double perovskite structure. *J. Magn. Magn. Mater.* **2007**, *310*, 1994–1996.
- (5) Li, P.; Xia, C.; Zhu, Z.; Wen, Y.; Zhang, Q.; Alshareef, H. N.; Zhang, X.-X. Ultrathin Epitaxial Ferromagnetic $\gamma\text{-Fe}_2\text{O}_3$ Layer as High Efficiency Spin Filtering Materials for Spintronics Device Based on Semiconductors. *Adv. Funct. Mater.* **2016**, *26*, 5679.
- (6) López-Mir, L.; Frontera, C.; Aramberri, H.; Bouzehouane, K.; Cisneros-Fernández, J.; Bozzo, B.; Balcells, L.; Martínez, B. Anisotropic sensor and memory device with a ferromagnetic tunnel barrier as the only magnetic element. *Sci. Rep.* **2018**, *8*, 861.
- (7) Dass, R. I.; Goodenough, J. B. Multiple magnetic phases of $\text{La}_2\text{CoMnO}_{6-\delta}$ ($0 \leq \delta \leq 0.05$). *Phys. Rev. B: Condens. Matter Mater. Phys.* **2003**, *67*, 014401.
- (8) Dass, R. I.; Yan, J.-Q.; Goodenough, J. B. Oxygen stoichiometry, ferromagnetism, and transport properties of $\text{La}_{2-x}\text{NiMnO}_{6+\delta}$. *Phys. Rev. B: Condens. Matter Mater. Phys.* **2003**, *68*, 064415.
- (9) Devi Chandrasekhar, K.; Das, A. K.; Mitra, C.; Venimadhav, A. The extrinsic origin of the magnetodielectric effect in the double perovskite $\text{La}_2\text{NiMnO}_6$. *J. Phys.: Condens. Matter* **2012**, *24*, 495901.
- (10) Goodenough, J. B. An interpretation of the magnetic properties of the perovskite-type mixed crystals $\text{La}_{1-x}\text{Sr}_x\text{CoO}_{3-\lambda}$. *J. Phys. Chem. Solids* **1958**, *6*, 287.
- (11) Goodenough, J. B.; Wold, A.; Arnott, R. J.; Menyuk, N. Relationship Between Crystal Symmetry and Magnetic Properties of Ionic Compounds Containing. *Phys. Rev.* **1961**, *124*, 373.
- (12) Hashisaka, M.; Kan, D.; Masuno, A.; Takano, M.; Shimakawa, Y.; Terashima, T.; Mibu, K. Epitaxial growth of ferromagnetic with ordered double-perovskite structure. *Appl. Phys. Lett.* **2006**, *89*, 032504.
- (13) Guo, H. Z.; Burgess, J.; Ada, E.; Street, S.; Gupta, A.; Iliev, M. N.; Kellock, A. J.; Magen, C.; Varela, M.; Pennycook, S. J. Influence of

defects on structural and magnetic properties of multifunctional $\text{La}_2\text{NiMnO}_6$ thin films. *Phys. Rev. B: Condens. Matter Mater. Phys.* **2008**, *77*, 174423.

(14) Truong, K. D.; Singh, M. P.; Jandl, S.; Fournier, P. Influence of Ni/Mn cation order on the spin-phonon coupling in multifunctional $\text{La}_2\text{NiMnO}_6$ epitaxial films by polarized Raman spectroscopy. *Phys. Rev. B: Condens. Matter Mater. Phys.* **2009**, *80*, 134424.

(15) Zhao, S.; Shi, L.; Zhou, S.; Zhao, J.; Yang, H.; Guo, Y. Size-dependent magnetic properties and Raman spectra of $\text{La}_2\text{NiMnO}_6$ nanoparticles. *J. Appl. Phys.* **2009**, *106*, 123901.

(16) Konstantinović, Z.; Santiso, J.; Colson, D.; Forget, A.; Balcells, L.; Martínez, B. Self-organization processes in highly epitaxial $\text{La}_2/3\text{Sr}1/3\text{MnO}_3$ thin films grown on SrTiO_3 (001) substrates. *J. Appl. Phys.* **2009**, *105*, 063919.

(17) Hashisaka, M.; Kan, D.; Masuno, A.; Takano, M.; Shimakawa, Y.; Terashima, T.; Mibu, K. Epitaxial growth of ferromagnetic $\text{La}_2\text{NiMnO}_6$ with ordered double-perovskite structure. *Appl. Phys. Lett.* **2006**, *89*, 032504.

(18) Guo, H.; Burgess, J.; Street, S.; Gupta, A.; Calvarese, T. G.; Subramanian, M. A. Growth of epitaxial thin films of the ordered double perovskite $\text{La}_2\text{NiMnO}_6$ on different substrates. *Appl. Phys. Lett.* **2006**, *89*, 022509.

(19) Iliev, M. N.; Guo, H.; Gupta, A. Raman spectroscopy evidence of strong spin-phonon coupling in epitaxial thin films of the double perovskite $\text{La}_2\text{NiMnO}_6$. *Appl. Phys. Lett.* **2007**, *90*, 151914.

(20) Sakurai, Y.; Ohkubo, I.; Matsumoto, Y.; Koinuma, H.; Oshima, M. Influence of substrates on epitaxial growth of B-site-ordered perovskite $\text{La}_2\text{NiMnO}_6$ thin films. *J. Appl. Phys.* **2011**, *110*, 063913.

(21) Guo, H.; Burgess, J.; Street, S.; Gupta, A.; Calvarese, T. G.; Subramanian, M. A. Growth of epitaxial thin films of the ordered double perovskite $\text{La}_2\text{NiMnO}_6$ on different substrates. *Appl. Phys. Lett.* **2006**, *89*, 022509.

(22) Spurgeon, S. R.; Du, Y.; Droubay, T.; Devaraj, A.; Sang, X.; Longo, P.; Yan, P.; Kotula, P. G.; Shutthanandan, V.; Bowden, M. E.; LeBeau, J. M.; Wang, C.; Sushko, P. V.; Chambers, S. A. Competing pathways for nucleation of the double perovskite structure in the epitaxial synthesis of $\text{La}_2\text{MnNiO}_6$. *Chem. Mater.* **2016**, *28*, 3814–3822.

(23) Kriegner, D.; Wintersberger, E.; Stangl, J. X-ray utilities: a versatile tool for reciprocal space conversion of scattering data recorded with linear and area detectors. *J. Appl. Crystallogr.* **2013**, *46*, 1162–1170.

(24) Guo, H.; Burgess, J.; Street, S.; Gupta, A.; Calvarese, T. G.; Subramanian, M. A. Growth of epitaxial thin films of the ordered double perovskite $\text{La}_2\text{NiMnO}_6$ on different substrates. *Appl. Phys. Lett.* **2006**, *89*, 022509.

(25) Stamenov, P.; Coey, J. M. D. Sample size, position, and structure effects on magnetization measurements using second-order gradiometer pickup coils. *Rev. Sci. Instrum.* **2006**, *77*, 015106.

(26) Rogado, N. S.; Li, J.; Sleight, A. W.; Subramanian, M. A. Magnetocapacitance and Magnetoresistance Near Room Temperature in a Ferromagnetic Semiconductor: $\text{La}_2\text{NiMnO}_6$. *Adv. Mater.* **2005**, *17*, 2225–2227.

(27) Guo, Y.; Shi, L.; Zhou, S.; Zhao, J.; Liu, W. Near room-temperature magnetoresistance effect in double perovskite $\text{La}_2\text{NiMnO}_6$. *Appl. Phys. Lett.* **2013**, *102*, 222401.

(28) Renner, B.; Lunkenheimer, P.; Schetter, M.; Loidl, A.; Reller, A.; Ebbinghaus, S. G. Dielectric behavior of copper tantalum oxide. *J. Appl. Phys.* **2004**, *96*, 4400.

(29) Lin, Y. Q.; Chen, X. M.; Liu, X. Q. Relaxor-like dielectric behavior in $\text{La}_2\text{NiMnO}_6$ double perovskite ceramics. *Solid State Commun.* **2009**, *149*, 784–787.

(30) Medarde, M.; Fontaine, A.; Garcia-Munoz, J. L.; Rodriguez-Carvajal, J.; De Santis, M.; Sacchi, M.; Rossi, G.; Lacorre, P. RNiO₃ perovskites (R = Pr, Nd): Nickel valence and the metal-insulator transition investigated by x-ray-absorption spectroscopy. *Phys. Rev. B: Condens. Matter Mater. Phys.* **1992**, *46*, 14975.

(31) Guo, H.; Gupta, A.; Varela, M.; Pennycook, S.; Zhang, J. Local valence and magnetic characteristics of $\text{La}_2\text{NiMnO}_6$. *Phys. Rev. B: Condens. Matter Mater. Phys.* **2009**, *79*, 172402.

(32) Sánchez, M. C.; García, J.; Blasco, J.; Subías, G.; Perez-Cacho, J. Local electronic and geometrical structure of $\text{LaNi}_{1-x}\text{Mn}_x\text{O}_{3+\delta}$ perovskites determined by x-ray-absorption spectroscopy. *Phys. Rev. B: Condens. Matter Mater. Phys.* **2002**, *65*, 144409.

(33) Kang, J.-S.; Lee, S. M.; Kim, D. H.; Kolesnik, S.; Dabrowski, B.; Park, B.-G.; Kim, J.-Y.; Lee, J.; Kim, B.; Min, B. I. Temperature-dependent magnetic circular dichroism study of ferromagnetic double perovskite $\text{La}_2\text{MnNiO}_6$. *J. Appl. Phys.* **2010**, *107*, 09D721.

(34) Guo, H.; Gupta, A.; Varela, M.; Pennycook, S.; Zhang, J. Local valence and magnetic characteristics of $\text{La}_2\text{NiMnO}_6$. *Phys. Rev. B: Condens. Matter Mater. Phys.* **2009**, *79*, 172402.

(35) Carra, P.; Thole, B. T.; Altarelli, M.; Wang, X. X-Ray Circular Dichroism and Local Magnetic Fields. *Phys. Rev. Lett.* **1993**, *70*, 694.

(36) Thole, B. T.; Carra, P.; Sette, F.; van der Laan, G. X-Ray Circular Dichroism as a Probe of Orbital Magnetization. *Phys. Rev. Lett.* **1992**, *68*, 1943.

SUPPORTING INFORMATION

Non-Stoichiometry driven ferromagnetism in double perovskite $\text{La}_2\text{Ni}_{1-x}\text{Mn}_{1+x}\text{O}_6$ insulating thin films

Monica Bernal-Salamanca^{†,*}, Zorica Konstantinović^{†,‡}, Lluís Balcells[†], Elisa Pannunzio-Miner[‡], Felip Sandiumenge[†], Laura Lopez-Mir[†], Bernat Bozzo[†], Javier Herrero-Martín[§], Alberto Pomar[†], Carlos Frontera[†], Benjamín Martínez[†]

[†] *Institut de Ciència de Materials de Barcelona, ICMAB-CSIC, Campus UAB, 08193 Bellaterra, Spain*

[‡] *Center for Solid State Physics and New Materials, Institute of Physics Belgrade, University of Belgrade, Pregrevica 118, 11080 Belgrade, Serbia*

[‡] *Centro de Investigaciones en Ciencias de la Tierra (CICTERRA-CONICET-UNC), Facultad de Ciencias Exactas, Físicas y Naturales, Av. Velez Sarfield 1611, X5016GCA Ciudad Universitaria, Cordoba, Argentina*

[§] *ALBA Synchrotron Light Source, C. de la Llum 2-26, E 08920 Cerdanyola del Vallès, Spain*

1. $M(T)$ curves of LNMO samples grown under different oxygen pressures and growth temperatures.

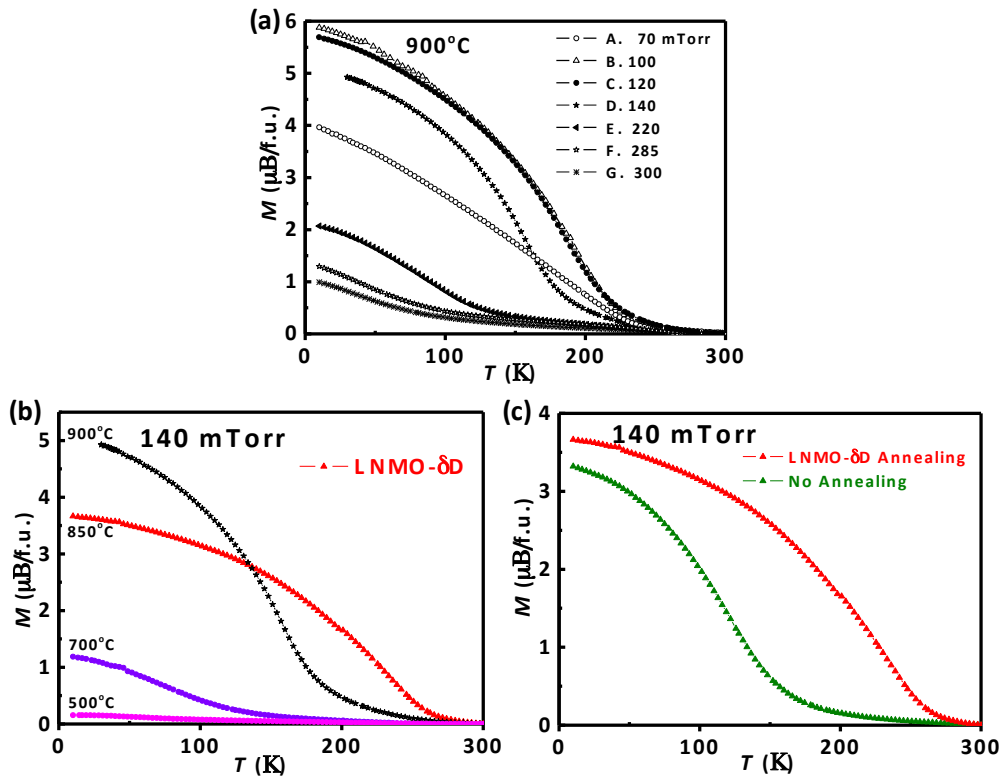


FIG. S11. In-plane magnetization of LNMO samples as a function of temperature under $H=5\text{ KOe}$ grown (a) under oxygen pressure ranging from 70 to 300 mTorr at 900°C , with annealing at the same temperature for 1h at 420 Torr O_2 . (b) at different growth temperatures. (c) Comparison of a LNMO- δD (growth at 850°C under 140 mTorr O_2) with 1h of annealing at 420 Torr O_2 (red curve) and a LNMO film (growth at 850°C under 140 mTorr O_2) without annealing (green curve).

2. Stoichiometry of the LNMO films

We have performed electron probe micro-analysis (EPMA) to determine the composition of LNMO films. Representative data about the composition of several samples are shown as a function of oxygen pressure and temperature.

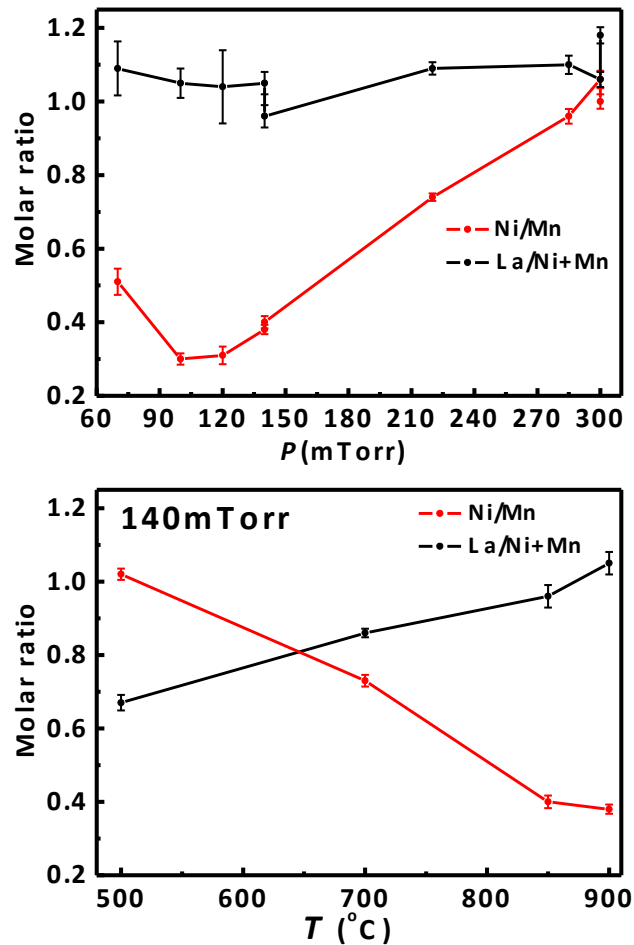


FIG. S12. Stoichiometry ratio of LNMO thin films grown on STO (001) substrates (a) under oxygen pressures ranging from 70 to 300 mTorr (b) at different growth temperatures under 140 mTorr O_2 for 1h (obtained by EPMA). Error bars have been estimated from the dispersion of the EPMA results at different points of the samples.



Hydrothermal synthesis of Mn²⁺ doped titanate nanotubes: Investigation of their structure and room temperature ferromagnetic behavior

M. Vranješ^{a,*}, J. Kuljanin Jakovljević^a, M. Milošević^a, G. Ćirić-Marjanović^b, M. Stoiljković^a, Z. Konstantinović^{c,d}, V. Pavlović^e, D. Milivojević^a, Z. Šaponjić^a

^a Vinča Institute of Nuclear Sciences, University of Belgrade, P.O. Box 522, 11001 Belgrade, Serbia

^b Faculty of Physical Chemistry, University of Belgrade, Studentski Trg 12-16, 11158 Belgrade, Serbia

^c Center for Solid State Physics and New Materials, Institute of Physics Belgrade, University of Belgrade, Pregrevica 118, 11080 Belgrade, Serbia

^d Institut de Ciència de Materials de Barcelona, CSIC, Campus UAB, 08193 Bellaterra, Spain

^e Faculty of Agriculture, University of Belgrade, Nemanjina 6, 11080 Belgrade, Serbia

ARTICLE INFO

Keywords:

Titanate nanotubes
Mn²⁺ doped nanotubes
Hydrothermal synthesis
EPR spectroscopy
Ferromagnetic properties

ABSTRACT

Hydrothermal synthesis of Mn²⁺ doped titanate nanotubes (TNTs), which exhibited room temperature ferromagnetism (RTFM), is reported. Dispersions of 1 and 5 at.% Mn²⁺ doped anatase TiO₂ nanocrystals were used as precursors. Size and shape of Mn²⁺ doped TNTs and precursor nanocrystals were studied by transmission electron microscopy (TEM). The relatively uniform size distribution of transverse dimension of nanotubes of about 10 nm was observed while their lengths varied up to few hundred nanometers. The X-Ray Diffraction (XRD) analysis and Raman spectroscopy of resultant powder confirmed the hydrogen dititanate (H₂Ti₂O₅ x H₂O) crystal phase of Mn²⁺ doped TNTs with the presence of small amount of sodium titanates. Electron paramagnetic resonance (EPR) experiments were performed to probe the local atomic and electronic structure of Mn in the nanotubes. Room temperature ferromagnetic ordering with saturation magnetic moment (*M_s*) in the range of 0.6–1.5 μ_B per Mn atom was observed.

1. Introduction

The size, shape and crystal structure of nanoparticles are important parameters that control their chemical, optical, electrical and even magnetic properties and affect their catalytic activity [1,2]. Low dimensional (1D) titania/titanate nanostructures such as nanotubes, nanowires, and nanobelts have attracted a great attention in recent years because they have potential applications in electronics, magneto-electronics, optics, catalysts, sensors, and energy conversion [1–8]. These nanotubes are characterized by high aspect ratio, large specific surface area and structure that open up possibilities for enhanced electron transfer and charge separation, thereby helping to increase the efficiencies for solar cells, electrolysis, and photocatalysis [9].

Titania/titanate nanotubes of various dimensions have been synthesized by different methods such as anodization, sol–gel, molecular assembly and hydrothermally. It was proposed that the formation of nanotubes was a result of the condensation of hydroxyl groups that terminated layers/sheets of TiO₂ obtained in the alkaline treatment of the nanocrystalline anatase TiO₂ precursor. According to the literature,

the crystalline structure of the scrolled nanotubes obtained by this method varies from pure anatase, mixed phase of anatase and rutile, to titanate [3,6,10–12]. The formation mechanism of the scrolled nanotubes has not yet been clarified.

As mentioned above, 1D nanostructured titania/titanate materials have potential application in magneto-electronic devices. The ability to control the spin of electrons in 1D titania/titanate nanostructures, and not only the charge of electrons in diluted magnetic semiconductors, would expand applications of these nanomaterials in conventional spintronic devices. The term diluted magnetic semiconductor (DMS) refers to a non-magnetic semiconductor material where the host cations are replaced with magnetic impurities up to a few atomic percent. DMSs were mostly based on II-VI or III-V compounds, but these materials were unattractive for practical electronic applications since ferromagnetism has been achievable far below room temperature [13]. Recently it was theoretically predicted that transition metal ions doped metal oxides (TiO₂, SnO₂, In₂O₃, ZnO) are suitable materials for DMSs with ferromagnetic behavior at room temperature [14–16].

In this paper we reported for the first time, to the best of our

* Corresponding author. Laboratory for Radiation Chemistry and Physics, Vinča Institute of Nuclear Sciences, University of Belgrade, P.O. Box 522, 11001 Belgrade, Serbia.

E-mail address: mila@vinca.rs (M. Vranješ).

<https://doi.org/10.1016/j.solidstatesciences.2019.06.008>

Received 16 November 2018; Received in revised form 12 February 2019; Accepted 17 June 2019

Available online 20 June 2019

1293-2558/ © 2019 Elsevier Masson SAS. All rights reserved.

knowledge, structural, optical and magnetic characterizations of Mn^{2+} doped titanate nanotubes (TNTs) synthesized by hydrothermal method using dispersions of Mn^{2+} doped anatase TiO_2 nanoparticles as precursors. Size and shape of the precursor nanoparticles and resulted Mn^{2+} doped TNTs were studied by transmission electron microscopy (TEM), while their crystalline structures were studied by the X-ray Diffraction (XRD) analysis and Raman spectroscopy. The ICP Emission Spectrometry was applied for determination of the concentrations of Mn^{2+} dopant ions incorporated within the host. The optical characterization of powdered samples of the Mn^{2+} doped TNTs was carried out by UV-Vis spectroscopy in reflection mode. Oxidation state of Mn ions and their coordination environment was determined using electron paramagnetic resonance (EPR) spectroscopy. The superconducting quantum interference device (SQUID) magnetometer was used to study the magnetic properties of films made of Mn^{2+} doped TNTs.

2. Experimental procedure

All chemicals were reagent-grade from Aldrich and used as received. Mn^{2+} doped TNTs were synthesized according to modified (different autoclaving time and temperature and post-synthetic rinsing treatment) procedure of Kasuga et al., using dispersions of 1 and 5 at.% Mn^{2+} doped anatase TiO_2 nanoparticles as precursors [12]. The 250 mg of precursor powder was dispersed in 10 ml 10 M NaOH and hydrothermally treated 20 h in a Teflon vessel (total volume 25 ml) under saturated vapor pressure of water at 150 °C. After autoclaving, the ensuing powder was washed with distilled water until pH of water achieved 7. The powder was then air dried at 70 °C.

Mn^{2+} doped anatase TiO_2 precursor powder was synthesized according to the slightly modified procedure of Carević et al. [17]. In brief, 1 and 5 at.% of MnCl_2 was dissolved in 500 ml of solvent mixture (water: isopropanol = 1:1, pH \approx 2 adjusted by HNO_3) at 0 °C. Then, a solution of 4 ml titanium (IV) isopropoxide in 20 ml isopropanol was added drop-wise under vigorous stirring. After 15 min at T = 0 °C, the ice bath was removed and the reaction mixture was continuously stirred at room temperature for 48 h. The resulting white dispersion was dialyzed against water until pH = 6 was reached, then centrifuged (4000 rpm, 30 min) and dried until a constant weight at 75 °C. In the case of the non-doped sample, the synthesis was performed in the same way but without addition of MnCl_2 .

The percentage ratio of Mn^{2+} to Ti^{4+} ions in doped TNTs was determined using ICP Emission Spectrometer: ICAP 6000 series (Thermo Electron Corporation). Prior to the ICP measurements, the powdered sample was dispersed in 3 ml of concentrated sulfuric acid and hydrothermally treated for 60 min at 250 °C in Teflon vessel (Parr acid digestion bomb, total volume 25 ml). The final concentrations of Mn^{2+} ions in samples of doped TNTs were 0.01 and 0.017 at.% of the amount of Ti^{4+} ions.

The shape and size of Mn^{2+} doped nanotubes and precursor Mn^{2+} doped anatase TiO_2 powder were characterized using JEM 1400 transmission electron microscope operating at 120 kV.

The X-ray powder diffraction (XRD) patterns were obtained using a Philips PW-1050 automated diffractometer using Cu K-alpha radiation (operated at 40 kV and 30 mA). Diffraction data for crystallographic analysis were collected in the 2θ range 10–120°, with scanning steps of 0.02 and exposition time of 12 s. Samples for XRD measurements were prepared using standard protocol [18].

Raman spectra were recorded with a DXR Raman microscope (Thermo Scientific, USA), equipped with a research optical microscope and a CCD detector. A diode-pumped solid-state laser with the excitation wavelength (λ_{exc}) of 532 nm was used for all measurements. The powder sample was placed on X-Y motorized sample stage and the laser beam was focused on the sample at objective magnification of 10 ×. The scattered light was analyzed by the spectrograph with a 900 lines per mm grating. The laser power on the sample was kept at 10.0 mW. For all Raman spectra an automated fluorescence correction was

performed, using the OMNIC software (Thermo Scientific). The exposure time was 10 s and 10 exposures per spectrum were applied.

Reflectance spectra of powders of undoped and Mn^{2+} doped TNTs were recorded at room temperature using Thermo Scientific Evolution 600 UV/Vis spectrophotometer.

X-band electron paramagnetic resonance (EPR) experiments were conducted at room temperature and T = 77 K on a Magnetech MiniScope MS300 spectrometer.

The field dependence magnetic moment was measured with a superconducting quantum interference device magnetometer (Quantum Design). The magnetic field was applied parallel to the film surface. The measured magnetization at 300 K was corrected for the diamagnetic background of the glass substrate (derived from high-field dependence magnetization data). Films for magnetic characterization were prepared by drop casting of dispersions of Mn^{2+} doped TNTs onto pre-cleaned glass substrate. The films were annealed in air for 2 min at 100 °C after each drop. Weight of each film, on the basis of which is determined the amount of the dopant ions for magnetic moment calculation, was measured.

3. Results and discussion

In this study, Mn^{2+} doped TNTs were synthesized by hydrothermal processing of dispersions of various concentrations (1 and 5 at.%) of Mn^{2+} doped anatase TiO_2 nanoparticles, in proton deficient aqueous solutions. TEM image of the 5 at.% Mn^{2+} doped TiO_2 nanoparticles, revealed their faceted shape with highly uniform size distribution, ranged between 8 and 10 nm (Fig. 1).

Crystalline structures of the precursor Mn^{2+} doped TiO_2 nanoparticles were studied by X-Ray powder Diffraction (XRD) analysis. The XRD spectra of 1 and 5 at.% Mn^{2+} doped TiO_2 nanoparticles are shown in Fig. 2. Peaks appearing in XRD patterns of both samples at $2\theta = 25.31^\circ, 37.81^\circ, 48.10^\circ, 53.91^\circ, 55.11^\circ, 62.71^\circ$ and 68.81° can be undoubtedly assigned to (101), (004), (200), (105), (211), (204) and (116) planes, respectively, of the tetragonal anatase crystal form of TiO_2 [JCPDS 89-4921]. The appearance of diffraction peaks at $2\theta = 30.65^\circ$, in both diffractograms, indicated the presence of small content (amount) of brookite TiO_2 crystalline phase, as could be expected for samples synthesized without thermal treatment [JCPDS 29-1360, 17, 19]. Within detection limit of the instrument, no diffraction peaks of other metal oxides impurities were observed, implying successful incorporation of Mn^{2+} ions into TiO_2 crystal lattices.

Hydrothermal processing is a very simple and efficient method for the synthesis of scrolled titania/titanate nanotubes using most often as a precursor highly alkaline dispersion of commercial TiO_2 powders, at elevated temperatures (120 C–200 C) [20]. The convenience of this

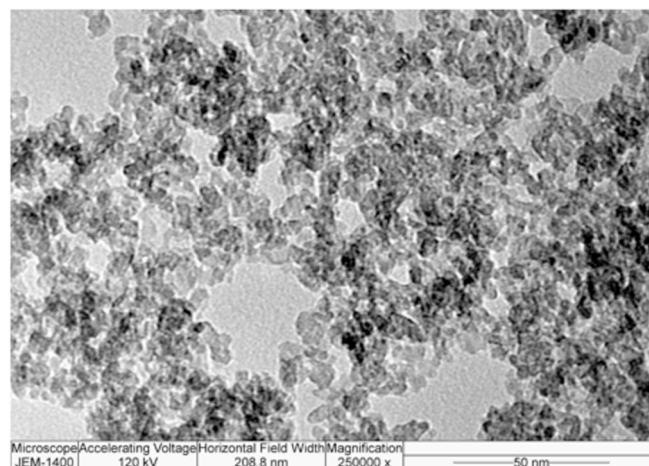


Fig. 1. TEM image of 5 at.% Mn^{2+} doped TiO_2 nanoparticles.

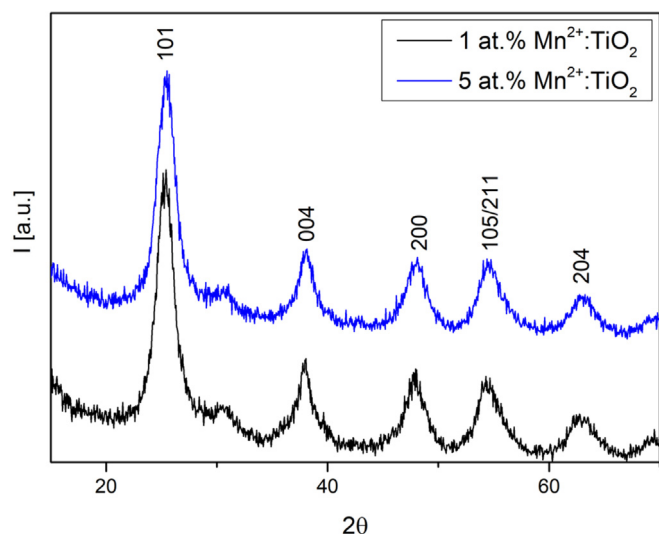


Fig. 2. XRD patterns of 1 and 5 at.% Mn^{2+} doped TiO_2 nanoparticles.

method for the synthesis of TNTs is also reflected in the possibility of utilizing other precursor materials, such as colloidal TiO_2 nanoparticles and molecular Ti based compounds [21].

We exploited previous facts for the synthesis of Mn^{2+} doped TNTs applying dispersions of 1 and 5 at.% Mn^{2+} doped anatase TiO_2 nanoparticles as precursors. The reason for such synthetic approach lies in harsh experimental conditions (extreme alkalinity, 10 M NaOH) and high temperature (up to 200 °C) attained during 20 h long hydrothermal treatment. These conditions exclude the possibility of use molecular precursors of dopant ions and their successful incorporation in crystalline structures due to appearance of their undesired oxidation state and/or formation of hydroxide forms before incorporation. Oxidized form of dopant ions such as manganese, in general, strongly influence overall magnetic properties of doped metal oxides, while on the other hand presence of manganese-hydroxide prevents incorporation in TNT crystal lattice.

Taking into account that formation of TNTs, during the hydrothermal treatment of nanoparticles dispersions and post-synthetic rinsing procedures, was induced by rearrangement of nanoparticles structural units (face-sharing and edge-sharing TiO_6 octahedra) forming lamellar sheets which subsequently scrolled into nanotubes, one can expect successful synthesis of doped nanotubes from doped nanoparticles [20,22]. Using Mn^{2+} doped TiO_2 anatase nanoparticles as precursor material, in the manner described, problems related to the nucleation stage in synthesis of Mn^{2+} doped tubular nanocrystals which could lead to ineffective doping, were avoided.

The conventional TEM image of the 0.017 at.% Mn^{2+} doped TNTs with open-ended multiwall structure is shown in Fig. 3. Relatively uniform size distribution of Mn^{2+} doped TNTs with average diameters of $d \sim 10$ nm was observed. The length of the nanotubes varied in the range up to hundreds of nanometers. There is no significant difference in TNTs morphologies between samples with different dopant concentrations (not shown).

Despite the considerable efforts to defining the formation mechanism and crystalline structure of hydrothermally synthesized TNTs, the debate on this issue is still ongoing. Hydrothermal synthesis of crystalline TNTs requires optimization of the following parameters: the temperature, the applied volume of dispersion (filling fraction), and the concentration of the hydrochloric acid used for the post-synthetic rinsing.

Upon NaOH treatment, some of the Ti-O-Ti bonds are broken, forming an intermediate containing Ti-O-Na and Ti-OH which rearrange to form sheets of edge-sharing TiO_6 octahedra with Na^+ and OH^- intercalated between the sheets. The formed structure is sodium

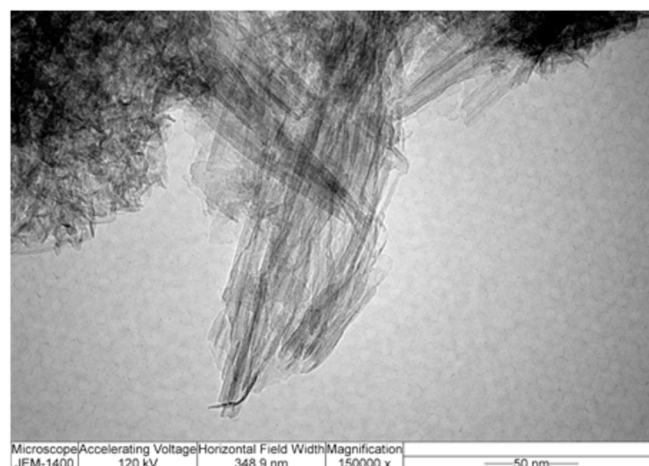


Fig. 3. TEM image of 0.017 at.% Mn^{2+} doped TNTs.

titanate with layers composed of the TiO_6 octahedra edge-shared in a zigzag configuration that can be correlated with the principal unit layer of the anatase TiO_2 projected along (101) crystal plane [3,12,20]. Experimental data show that both anatase and rutile can be transformed into titanate nanotubes via the NaOH treatment [8,23,24]. The rearrangement of the TiO_6 octahedra in rutile would be more vigorous in order to form the titanate because the principal structures of anatase and the titanate are more similar. The formed sodium titanate layers would undergo Na^+ exchange with H^+ in the post-synthetic washing treatment. The exchange would result in variation of the surface charge, leading to a peeling-off of the individual layers of the titanate and subsequent scrolling of the layers into nanotubes [3,12,20].

The XRD data of powdered samples of 0.01 and 0.017 at.% Mn^{2+} doped TNTs are given in Fig. 4. The XRD pattern confirms the presence of mixed titanate phases in the samples, with the orthorhombic $\text{H}_2\text{Ti}_2\text{O}_5 \times \text{H}_2\text{O}$ phase as the dominant phase for both samples independently of the Mn^{2+} concentrations. Orthorhombic hydrogen titanate ($\text{H}_2\text{Ti}_2\text{O}_5 \times \text{H}_2\text{O}$) usually appears as a main crystalline phase of hydrothermally synthesized nanotubes rinsed with water only. Diffraction peaks at $2\theta = 24.2^\circ, 28.4^\circ, 34.5^\circ, 38.6^\circ, 48.4^\circ,$ and 49.1° can be assigned to (110), (310), (301), (501), (020) and (220) crystalline planes, respectively, of orthorhombic $\text{H}_2\text{Ti}_2\text{O}_5 \times \text{H}_2\text{O}$ compound. Furthermore, the unstructured wide band at $2\theta \sim 61^\circ$ can be assigned to (002), (202) and

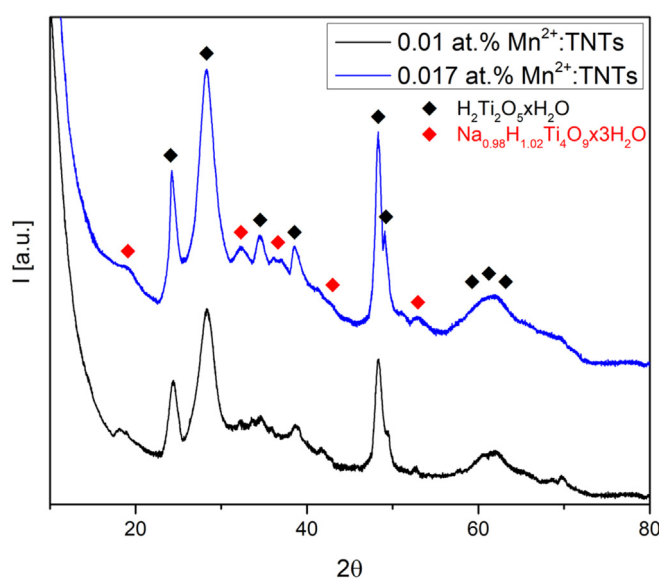


Fig. 4. XRD patterns of 0.01 and 0.017 at.% Mn^{2+} doped TNTs.

(521) planes of $\text{H}_2\text{Ti}_2\text{O}_5 \cdot x \text{H}_2\text{O}$ (Fig. 4) [25]. Appearance of peaks at $2\theta = 18.9^\circ, 32.3^\circ, 36.1^\circ, 37^\circ, 41.7^\circ$ and 52.9° in diffractograms of all studied samples indicated the presence of the second crystalline phase, sodium titanium hydrogen oxide hydrate ($\text{Na}_{0.98}\text{H}_{1.02}\text{Ti}_4\text{O}_9 \cdot x \text{H}_2\text{O}$). The presence of this compound can be predictable taking into the account expectations that certain content of sodium ions is left behind after rinsing, which allowed the formation of titanium salt [JCPDS 38-0221, 26, 27, 28, 29]. The intensity ratio of diffraction peaks at $2\theta = 24.2^\circ$ and 28.4° can be used as a measure of sodium content. The peak at $2\theta = 24.2^\circ$ is less intensive than the one at $2\theta = 28.4^\circ$ which suggests the incomplete replacement of Na^+ ions by H^+ during washing procedure [28].

While some authors found that the peak at 28° confirms the presence of hydrogen titanate, it could be also assigned to the distance between the layers in the tube walls [21,30].

Brunatova et al. investigated the crystal structure of hydrothermally synthesized TNTs using computer simulation of XRD pattern utilizing the Debye formula for the structure verification [25]. Their XRD pattern of TNTs was similar to ours. The best match was achieved for the $\text{H}_2\text{Ti}_2\text{O}_5 \cdot x \text{H}_2\text{O}$ phase with an orthorhombic structure and the unit cell parameters: $a = 1.803 \text{ nm}$; $b = 0.378 \text{ nm}$; $c = 0.2998 \text{ nm}$.

Poulet et al. studied the effect of filling fraction of the autoclave as well as the concentration of the acid solution applied in post-synthetic treatment, on controlling the purity and crystallinity of the resulting nanotubes [27]. They found that highly crystalline nanotubes could be obtained only if the filling fraction of the autoclave is 80% or more. Also, acid treatment was necessary for achieving a good crystallinity of nanotubes and identified an optimal concentration between 0.5 and 1.5 M HCl for high yield of pure nanotubes. Concentrations above 2 M destroyed the nanotubes while concentrations below 0.5 M failed to remove the sodium impurities. However, even at these optimal concentrations the sodium impurities could be removed only when the autoclave step was performed close to the optimal volume fraction. So, apparently, the nanotube crystallinity is controlled primarily by the autoclave step, while the impurities are controlled primarily by the acid treatment. In our synthetic procedure filling fraction was 40%, while in the post-synthetic washing step we used only 4D H_2O . This, as well as the presence of dopant ions in precursor material (Mn^{2+} doped anatase nanoparticles), could account for the poor crystallinity of the synthesized TNTs, as well as the presence of mixed titanate crystal phases in the samples.

To further investigate the crystal structure of the samples, as well as the electronic interaction between the Ti and Mn, Raman spectroscopy was conducted. Raman spectra of Mn^{2+} doped TNTs samples are given in Fig. 5.

As can be seen from Fig. 5, Raman spectra of Mn^{2+} doped TNTs are composed of the bands at wavenumbers 123 cm^{-1} (w), 276 cm^{-1} (vs), 383 cm^{-1} (m), 445 cm^{-1} (s), 669 cm^{-1} (s), 708 cm^{-1} (s), 820 cm^{-1} (s) and 906 cm^{-1} (s). Characteristic bands of TiO_2 anatase crystal form at c.a. 144 cm^{-1} (E_g), 399 cm^{-1} (B_{1g}), 513 cm^{-1} (A_{1g}), and 640 cm^{-1} (E_g), as well as bands characteristic of TiO_2 rutile crystal form at around 244 cm^{-1} (second order mode $B_{1u} + E_u$) and 612 cm^{-1} (A_{1g}) were not detected, with the exception of the bands at 445 cm^{-1} and 820 cm^{-1} that are at close positions to the rutile modes at c.a. 450 cm^{-1} (E_g) and 826 cm^{-1} (B_{2g}) [31–34]. These findings are in agreement with XRD characterization, since no TiO_2 -specific peaks (for anatase and rutile phases) in XRD patterns were observed. On the other hand, the Raman spectra of our samples, Fig. 5, are very similar to the spectra reported for titanate crystal forms of nanotubes [28,29,31,35,36]. However, the exact assignment of the bands in the Raman spectra of TNTs is still a matter of debate.

Recent studies reported that Raman bands appearing at $276, 445$ and 669 cm^{-1} to be characteristic for titanate crystal phase [35,37–39]. The Raman band at about 276 cm^{-1} has been related in the literature as an intrinsic mode related to the sodium titanates, i.e. to the Ti–O vibration affected by the sodium ion in the near vicinity [29,31]. The

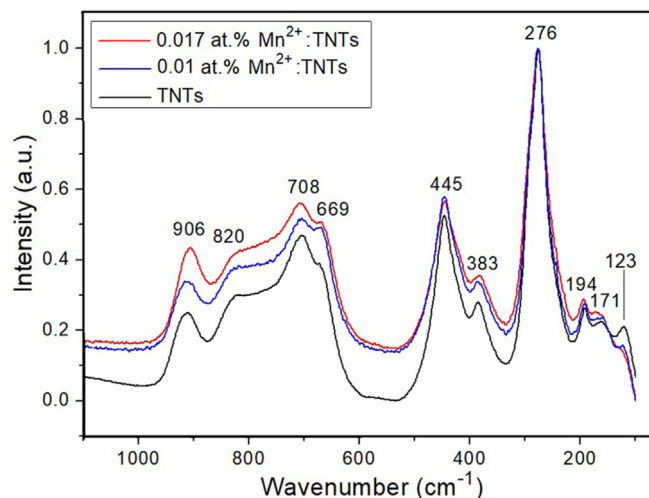


Fig. 5. Raman spectra of 0.01 and 0.017 at.% Mn^{2+} doped TNTs ($\lambda_{\text{exc}} = 532 \text{ nm}$).

band at 445 cm^{-1} could be assigned to the Ti–O–Ti vibration in titanate nanotubes, although rutile E_g mode appears at similar position [31,33,35,36]. Taking into consideration that no diffraction peaks of rutile were observed in XRD patterns, Fig. 4, it could be supposed that the discussed band is associated with titanate nanotubes. Band appearing at 669 cm^{-1} is related to the Ti–O–Ti or Ti–O–Na vibrations in nanotubes [28,35,36]. Another band that could be related to the sodium titanate structure is a band located at 906 cm^{-1} , which is assigned to the symmetric stretching mode of a short Ti–O bond of sodium titanate in layer structure [31]. Bavykin et al. assigned the band at 917 cm^{-1} in the spectra of titanate nanotubes to Ti–O–Na stretching vibration in the interlayer regions of the nanotube walls [35,36]. Cortes-Jacome et al. compared the Raman spectra of the nanotubes before and after neutralization with HCl and noticed that peaks appearing at 665 and 903 cm^{-1} were more evident before neutralization suggesting that both are related to the vibration of Ti–O–Na. Weak band at 123 cm^{-1} has been attributed to Na–O bonds in sodium titanate, while the band at 820 cm^{-1} is correlated to covalent Ti–O–H bonds in nanotubes [31]. Qian et al. studied the effect of acid washing treatment on the nanotubes and demonstrated that Ti–O–Na bonds in the alkali-treated specimen would be replaced by Ti–O–H bonds through proton-exchanged reaction which resulted in appearance of a broad weak band around 830 cm^{-1} in their Raman spectrum (covalent Ti–O–H bonding) [31].

It is interesting that the bands of Mn^{2+} doped TNTs at c.a. $669, 708, 820$ and 906 cm^{-1} are affected by the presence of Mn^{2+} in the samples, and their intensity increases with the increase of Mn concentration in the samples (Fig. 5). This feature indicates that Mn^{2+} participates in the bonds included in the vibrations associated to these bands, most probably in the formation of Ti–O–Mn bonds, and/or that these vibrations are influenced by the presence of Mn^{2+} ions.

It should be noted that the Raman spectra of synthesized samples, Fig. 5, generally differ from the spectra of pure phase manganese titanate MnTiO_3 (pyrophanite) reported in the literature [40,41]. However, the band at near 700 cm^{-1} , which is the most intense band in the spectra of MnTiO_3 pyrophanite (in the region $200\text{--}800 \text{ cm}^{-1}$), is also present in the spectra of our samples, at 708 cm^{-1} . Other bands characteristic for MnTiO_3 pyrophanite are not seen in the spectra of Mn^{2+} doped TNTs [40]. The most typical Raman band of pure phase MnTiO_3 near 700 cm^{-1} has been attributed to the highest frequency vibrational mode of MnO_6 octahedra i.e., to the symmetric stretching mode (A_{1g} symmetry for regular O_h octahedral) [41]. Thus, the presence of the band at 708 cm^{-1} in the spectra of Mn^{2+} doped TNTs indicates formation of MnO_6 octahedra in the structure of synthesized materials.

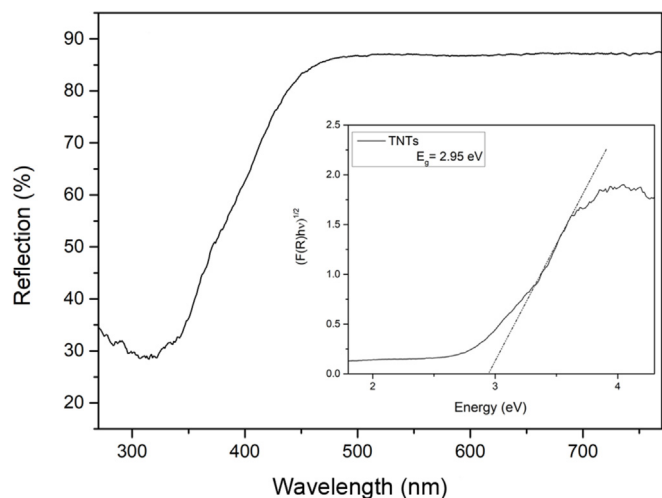


Fig. 6. Reflection spectra of non-doped TNTs; Inset: band gap determinations.

Considering all the above said, we can conclude that the results of Raman study are in a good agreement with the XRD data, confirming the presence of mixed hydrogen/sodium titanate crystal phases in our samples, as well as the efficient incorporation of Mn^{2+} ions in the crystal lattice of nanotubes.

The optical characterization of the samples was carried out by measuring their diffuse reflectance at room temperature. The optical spectra of undoped TNTs (Fig. 6) manifest strong absorption extended to 400 nm. Presence of dopant ions did not affect significantly the optical properties of TNTs (data not shown). This absorption corresponds to the intrinsic electron excitation from the valence (VB) to the conduction band (CB) of semiconductor.

For the analysis of reflectance spectra Kubelka–Munk relation was used, which allows the optical absorbance of a sample to be approximated from its reflectance (R) (Inset Fig. 6.). The function for alkali titanates with indirect transition is expressed as:

$$F(R) = (1 - R)^2/2R \quad (1)$$

Using this equation semiconducting materials can be analyzed with a Tauc plot, whereby the absorption coefficient, α , in the Tauc equation is substituted with $F(R)$ [42–44]. The estimated band gap, E_g , value for the undoped TNTs is 2.95 eV (Inset Fig. 6). This value is smaller than those reported for titanates which ranges from 3.4 to 3.7 eV [42,45]. Considering that the titanates have electronic structures very similar to the TiO_2 (all energy band structures exhibit indirect band gaps, and that most O 2p and Ti 3d states are located in the top of the VB and the bottom of the CB), the results here reported seem to support that comparable effects may occur when comparing to TiO_2 materials [42,46]. The existence of oxygen vacancies in the crystal lattice leads to formation of the defect states in the forbidden zone of the energy band gap of TNTs [47]. Because of the tubular morphology TNTs contain a large fraction of structural defects which consequently is responsible for the observed red shift of absorption in our sample.

Manganese ions do not create aggregates in TNTs structure as a consequence of suppressed diffusion during transformation. Considering that XRD measurements are limited to identifying minority phases at sub-percent concentration of dopant, as applied in these samples, we employed EPR spectroscopy as dopant-specific technique which provides highly detailed microscopic information about the oxidation state and the local environment of the substituent paramagnetic ions in the crystal lattice of the host. Furthermore, EPR is sensitive to the interactions between the paramagnetic ions.

The EPR spectra of the Mn^{2+} doped TNTs recorded at $T = 77$ K are shown in Fig. 7. The EPR spectra measured at lower temperatures, $T = 77$ K, do not differ in shape from the spectra recorded at room

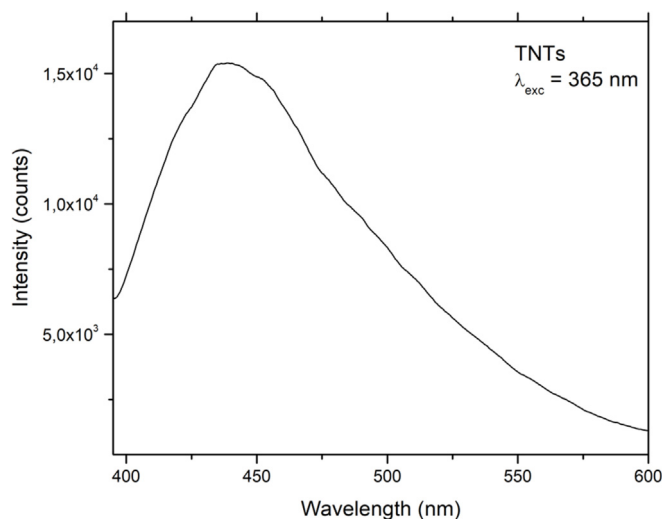


Fig. 7. Experimental (a) and simulated (a and b) EPR spectra of 0.017 at.% Mn doped TNTs recorded at $T = 77$ K and different field range, Inset: EPR spectra of 0.01 and 0.017 at.% Mn doped TNTs recorded at $T = 77$ K.

temperature (RT), data not shown), except that intensity at RT is about 3 times lower. The spectrum consists of a group of six narrow lines with the pairs of lines between each of these six lines (Fig. 7a and b). The spectrum is due to hyperfine interaction between the electron and nuclear spin ($I = 5/2$) of Mn^{2+} ions with six allowed, $\Delta m_I = 0$, and five pairs of $\Delta m_I = \pm 1$ forbidden transitions. The main contribution to the EPR spectra of materials with random orientation of the Mn^{2+} ions comes from central transitions ($M_S = +1/2 \leftrightarrow M_S = -1/2$) with hyperfine splitting into six lines, while the outer fine structure transitions ($M_S = \pm 5/2 \leftrightarrow M_S = \pm 3/2$) and ($M_S = \pm 3/2 \leftrightarrow M_S = \pm 1/2$) are smeared out due to strong angular dependence and random orientation, and can be observed as a broad line of about 50 mT width (Fig. 7a) [48]. This broad line in the EPR spectra superimposed to the narrow hyperfine sextet is characteristic of Mn^{2+} ions located in strongly distorted octahedral sites [49]. Counio et al. suggested that this signal would correspond to the Mn^{2+} ions located inside the nanocrystals, but in strongly distorted sites [50].

Szirmai et al. found that the Mn^{2+} ions occupy two positions in titanate nanotubes: the first having an almost perfect cubic symmetry while the other is in a strongly distorted octahedral site [49]. The fact that we have observed fine structure (Fig. 7b) is a strong indication of the relative ordering between Mn^{2+} dopants. The sextet signal in EPR spectra, as well as the calculated value of hyperfine structure parameter, $A = 9.0$ mT, is characteristic for Mn^{2+} ions in octahedral crystal fields, but, since the forbidden transitions are observable as well, Mn^{2+} ions do not occupy strictly cubic sites, as strictly cubic centers have zero probability of forbidden transitions. This is the indication that the distortion relative to the cubic symmetry is small [49]. The intense forbidden transitions reflect distortion of the crystal lattice surrounding Mn^{2+} ions. It shows that Mn^{2+} ions occupy lattice sites with lower symmetry. Near the surface of the nanoparticle the crystal field symmetry is distorted leading to the relaxation of the $\Delta m_I = 0$ selection rule. Also, the axial fine structure parameter D becomes relevant. Unfortunately, we could not obtain good fit of the spectrum, and the value of D , using the theoretical calculation of positions of allowed and forbidden lines made by Wijn and Balderen [48]. The spectrum distinctive features, associated with D , were hidden by forbidden lines, and the fitting procedure is not reliable.

The sextet comes from isolated Mn^{2+} ions since Mn–Mn pairs or Mn–O–Mn do not produce the six-line spectrum that we observed.

Since the hyperfine interactions strongly depend on the local environment of Mn^{2+} ions, the EPR spectrum can be used to provide more information on the specific location of the ions in the lattice. The

spectrum that shows hyperfine structure with larger A , may be a result of increase in ionic character of the bonding of Mn, which occurs when Mn is close to the surface [51]. In powdered polycrystalline systems noncentral transitions ($m_S \neq 1/2$) are always broadened and unresolved. This is due to the strong angular dependence of the lines and a parameter distribution in both hyperfine- and fine coupling parameters. As previously determined, dipole–dipole interaction between Mn^{2+} ions broaden the sextuplet lines corresponding to the central $\Delta m_I = 1$ transition [49]. Considering that the concentrations of Mn^{2+} ions in our samples are relatively low, we can exclude the dipolar interactions. Counio et al. demonstrated that a distribution of hyperfine interaction which could arise from isolated Mn^{2+} ions located inside the nanocrystals, but near the surface would be responsible for broadening of EPR signal. Electronic density of Mn^{2+} ions close to the surface will undergo a drastic change and fluctuations in the Mn-O bond will give rise a distribution of the hyperfine interaction [50].

The value of hyperfine structure parameter, $A = 9.0$ mT, shape of the spectra and the line width resemble the spectra of the $TiO_2:Mn^{2+}$ that we have already showed to comes from Mn atoms incorporated in TiO_2 lattice, occupying two different sites having different binding energies: undercoordinated surface sites and core octahedral sites of TiO_2 nanoparticles [52].

The magnetic response for films made of 0.01 and 0.017 at.% Mn^{2+} doped TNTs as a function of magnetic field strength (H) was followed at room temperature. The diamagnetic contribution determined from the room temperature magnetic field dependence of magnetization at high field (for $H > 10$ kOe) was subtracted in all samples. As can be seen from Fig. 8. RTFM behavior of Mn^{2+} doped TNTs was observed, with coercive field of $H_c \sim 200$ Oe and relatively high values of saturation magnetization moments in the range of $M_S = 0.6$ – $1.5 \mu_B/Mn$.

Based on the results of experimental and the theoretical models it was determined that oxygen vacancies (F^+ centers in precisely-electron associated at oxygen vacancy) seem to have an important role in mediating the magnetic ordering in oxide based DMS materials [53,54]. Ferromagnetic ordering in transition metal doped titania/titanate materials could be explained in terms of the non-carrier mediated bound magnetic polaron (BMP) model. According to this theory, electrons associated at oxygen vacancy defects mediate the ferromagnetic coupling between dopant ions located within their orbits and BMPs are formed. If the BMPs overlap, the ferromagnetic state occurs [55,56]. In order for ferromagnetic ordering to occur, the polaron concentration must exceed its percolation threshold, δ_p , while the concentration of the dopant ion must be far below its percolation threshold, x_p [56].

As confirmed by some authors, RTFM of Mn^{2+} doped TiO_2 is sensitively dependent on structural defects [53,57]. Only the bulk oxygen vacancy mediates the FM ordering. Santara et al. also demonstrated that concentration of oxygen vacancies per se does not affect the magnitude of magnetic moment, but they also suggested that the defect environment and the surface morphology of the nanoparticles could be of crucial importance for achieving of measurable ferromagnetic interaction [58]. The greater density of the oxygen vacancy helps to produce more BMP which yields a greater overall volume occupied by BMP, leading to an overlap of BMPs and enhancing ferromagnetic behavior.

In a titania based semiconductor materials, it is often energetically favorable for native donor defects such as oxygen vacancies and titanium interstitials to aggregate in the vicinity of grain boundaries [59]. That means that BMPs also aggregate near such grain boundaries. However, aggregation depends on differing electrostatic interactions with the defects, strain effects, or other factors. Defect aggregation could favor the RTFM once the polaron concentration exceeds a minimum threshold. That means that the RTFM would depend on the availability of the favorable grain boundaries rather than a total internal surface area [60].

In our previous work, we investigated the structure of multilayered titania nanotubes [21]. Nanotubes contain a large fraction of structural

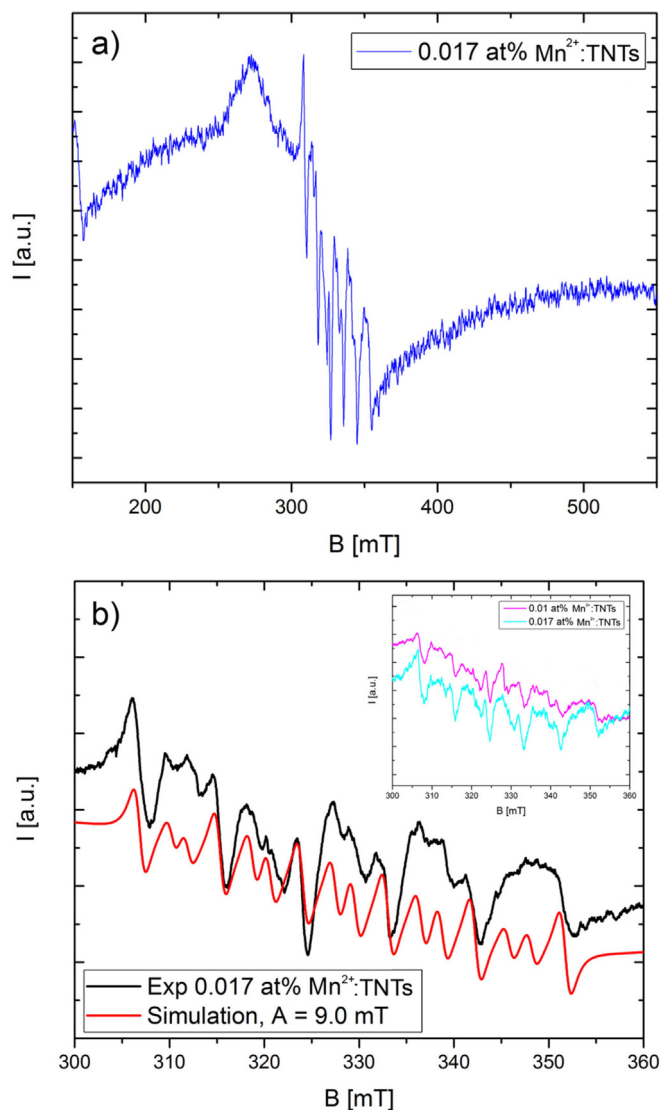


Fig. 8. RTFM of films made of 0.01 and 0.017 at.% Mn^{2+} doped TNTs.

defects and majority of them is located on the interior walls of the nanotubes. Namely, 40% of Ti atom in scrolled titania are undercoordinated. Also, substitution of Mn^{2+} into the lattice for Ti^{4+} induces the formation of oxygen vacancies to maintain charge neutrality. Nanotubes are composed of multiple layers separated by a gap of ~ 0.3 nm, while layer to layer distance is 0.9 nm. Coey et al. predicted in their calculations the radius of the BMP in anatase TiO_2 to be 0.48 nm [56]. Percolation of the polarons occurs when they fill roughly 16% of space [61]. Considering the fact that the layer thickness of TNTs is comparable to the polaron radius, as well as the high content of defects (40%) in TNTs we could imply that the high value of M_S in our sample despite low concentration of Mn is caused by combined effect of shape and structure of TNTs. Namely, all mentioned above suggests that a relatively high fraction of BMPs, as well as Mn^{2+} ions in our samples are overlapped and ferromagnetically coupled.

Different studies confirmed that lower Mn doping content (< 1 at. %) favors the ferromagnetic interaction and that higher concentrations of Mn lead to formation of antiferromagnetic Mn clusters [53,60]. According to BMP model, ferromagnetism appears at concentrations of $3d$ dopants that lie far below the percolation threshold, x_p associated with nearest-neighbor cation coupling. The average moment per dopant cation approaches (or even exceeds) the spin-only moment at low dopant concentrations, x and it falls progressively as x increases towards

x_p [56]. High value of M_s in our sample indicates a high content of bulk oxygen vacancy in TNTs and that a very high fraction of Mn^{2+} ions are involved in FM ordering though their concentration is relatively low.

4. Conclusion

The Mn^{2+} doped titanate nanotubes were synthesized applying hydrothermal treatment on dispersion of 1 and 5 at.% Mn^{2+} doped anatase TiO_2 nanopowder in proton deficient aqueous solution. XRPD and Raman study confirmed that the nanotubes had a mixed phase (sodium and hydrogen titanate) crystal structure. $H_2Ti_2O_5 \cdot xH_2O$ phase prevails. The ferromagnetic ordering at room temperature with closed loop ($H_c \sim 200$ Oe) and M_s in the range of 0.6–1.5 μ_B /Mn atom were observed in film made of Mn^{2+} TNTs. The reason for observed ferromagnetism and relatively high value of M_s could be found in the high content of bulk oxygen vacancies (F^+ centers) and their interaction with the substitutional Mn^{2+} impurity. Therefore, we can suggest that both oxygen vacancies and an optimum level of Mn^{2+} are necessary for getting ferromagnetism in Mn^{2+} doped TNTs.

Acknowledgments

The financial support for this work was provided by the Ministry of Education, Science and Technological Development of Republic of Serbia (Project 172056).

References

- [1] E.C. Scher, L. Manna, A.P. Alivisatos, *Philos. Trans. R. Soc. London, Ser. A* 361 (2003) 421.
- [2] S. Link, M.A. El-Sayed, *Annu. Rev. Phys. Chem.* 54 (2003) 331.
- [3] T. Kasuga, M. Hiramatsu, A. Hoson, T. Sekino, K. Nihara, *Langmuir* 14 (1998) 3160.
- [4] W. Wang, O. Varghese, M. Paulose, C.A. Grimes, *J. Mater. Res.* 19 (2004) 417.
- [5] W. Wang, C.A. Grimes, O. Varghese, M. Paulose, Unpublished, (2003).
- [6] Y. Lei, L.D. Zhang, G.W. Meng, G.H. Li, X.Y. Zhang, C.H. Liang, W. Chen, S.X. Wang, *Appl. Phys. Lett.* 78 (2001) 1125.
- [7] G.K. Mor, M.A. Carvalho, O.K. Varghese, M.V. Pishko, C.A. Grimes, *J. Mater. Res.* 19 (2004) 628.
- [8] Z.R. Tian, J.A. Voigt, J. Liu, B. Mc Kenzie, H. Xu, *J. Am. Chem. Soc.* 125 (2003) 12384.
- [9] H.J. Yun, H. Lee, J.B. Joo, W. Kim, J. Yi, *J. Phys. Chem. C* 113 (2009) 3050.
- [10] M. Adachi, Y. Murata, I. Okada, S. Yoshikawa, *J. Electrochem. Soc.* 150 (2003) G488.
- [11] K. Varghese, D. Gong, M. Paulose, C.A. Grimes, E.C. Dickey, *J. Mater. Res.* 18 (2003) 156.
- [12] T. Kasuga, M. Hiramatsu, A. Hoson, T. Sekino, K. Nihara, *Adv. Mater.* 11 (1999) 1307.
- [13] R. Janisch, P. Gopal, N.A. Spaldin, *J. Phys. Condens. Matter* 17 (2005) 657.
- [14] J.Y. Kim, J.H. Park, B.G. Park, H.J. Noh, S.J. Oh, J.S. Yang, D.H. Kim, S.D. Bu, T.W. Noh, H.J. Lin, H.H. Hsieh, C.T. Chen, *Phys. Rev. Lett.* 90 (2003) 017401.
- [15] M. Venkatesan, C.B. Fitzgerald, J.G. Lunney, J.M.D. Coey, *Phys. Rev. Lett.* 93 (2004) 177206.
- [16] A. Gupta, H. Cao, K. Parekh, K.V. Rao, A.R. Raju, U.V. Waghmare, *J. Appl. Phys.* 101 (2007) 09N513.
- [17] M. Carević, N.D. Abazović, T. Savić, T.B. Novaković, M.D. Mojović, M.I. Čomor, *Ceram. Int.* 42 (2016) 1521.
- [18] V.K. Pecharsky, P.Y. Zavalij, *Fundamentals of Powder Diffraction and Structural Characterization of Materials*, Springer, 2005.
- [19] J. Xu, Y. Ao, D. Fu, C. Yuan, *Colloids Surf* 334 (2009) 107.
- [20] N. Liu, X. Chen, J. Zhang, J.W. Schwank, *Catal. Today* 225 (2014) 34.
- [21] Z.V. Šaponjić, N.M. Dimitrijević, D.M. Tiede, A.J. Goshe, X. Zuo, L.X. Chen, A.S. Barnard, P. Zapol, L. Curtiss, T. Rajh, *Adv. Mater.* 17 (2005) 965.
- [22] J.N. Nian, H. Teng, *J. Phys. Chem. B* 110 (2006) 4193.
- [23] M. Zhang, Z. Jin, J. Zhang, X. Guo, J. Yang, W. Li, X. Wang, Z. Zhang, *J. Mol. Catal. A Chem.* 217 (2004) 203.
- [24] A. Thorne, A. Kruth, D. Tunstall, J.T.S. Irvine, W. Zhou, *J. Phys. Chem. B* 109 (2005) 5439.
- [25] T. Brunatova, D. Popelkova, W. Wan, P. Oleynikov, S. Danis, X. Zou, R. Kuzel, *Mater. Char.* 87 (2014) 166.
- [26] V. Štengl, Bakardjieva, J. Šubr, E. Večerníková, L. Szatmary, M. Klementova, V. Balek, *Appl. Catal. B Environ.* 63 (2005) 20.
- [27] B.Poudel W.Z. Wang, C. Dames, J.Y. Huang, S. Kunwar, D.Z. Wang, D. Banerjee, G. Chen, Z.F. Ren, *Nanotechnology* 16 (2005) 1935.
- [28] S. Mozia, E. Borowiak-Palen, J. Przepiorski, B. Grzmil, T. Tsumura, M. Toyoda, J. Grzechulska-Damszel, A.W. Morawski, *J. Phys. Chem. Solids* 71 (2010) 263.
- [29] D.J. Jovanović, I.M. Dugandžić, G. Čirić-Marjanović, T. Radetić, S.P. Ahrenkiel, O.B. Milošević, J.M. Nedeljković, Z.V. Šaponjić, L.T. Mancic, *Ceram. Int.* 41 (2015) 14754.
- [30] Y.Q. Wang, G.Q. Hu, F. Duan, H.L. Sun, Q.K. Xue, *Cem. Phys. Lett.* 365 (2002) 427.
- [31] L. Qian, Z.L. Du, S.Y. Yang, Z.S. Jin, *J. Mol. Struct.* 749 (2005) 103.
- [32] T. Gao, H. Fjellvåg, P. Norby, *Inorg. Chem.* 48 (2009) 142.
- [33] D. Regonini, A. Jaroenworarluck, R. Stevens, C.R. Bowen, *Surf. Interface Anal.* 42 (2010) 139.
- [34] O. Frank, M. Zúkalova, B. Laskova, J. Kürti, J. Koltai, L. Kavan, *Phys. Chem. Chem. Phys.* 14 (2012) 14567.
- [35] D.V. Bavykin, J.M. Friedrich, A.A. Lapkin, F.C. Walsh, *Chem. Mater.* 18 (2006) 1124.
- [36] M.A. Cortes-Jacome, G.F. Torres, L.F.F. Ortiz, C. Angeles-Chavez, E.L. Salinas, J. Escobar, M.L. Mosqueira, J.A. Toledo-Antonio, *Catal. Today* 126 (2007) 248.
- [37] Y.V. Kolenko, K.A. Kovnir, A.I. Gavrilov, A.V. Garshev, J. Frantti, O.I. Lebedev, B.R. Churagulov, G.V. Tendeloo, M. Yoshimura, *J. Phys. Chem. B* 110 (2006) 4030.
- [38] M. Hodos, E. Horvath, H. Haspel, A. Kukovecz, Z. Konya, I. Kiricsi, *Chem. Phys. Lett.* 399 (2004) 512.
- [39] A. Kukovecz, M. Hodos, Z. Konya, I. Kiricsi, *Chem. Phys. Lett.* 411 (2005) 445.
- [40] Z.Q. Song, S.B. Wang, W. Yang, M. Li, H. Wang, H. Yan, *Mater. Sci. Eng., B* 113 (2004) 121.
- [41] G.W. Zhou, K.Y. Soo, *Mater. Sci. Eng. C* 24 (2004) 71.
- [42] Y. An, Z. Li, J. Shen, *Physica B* 429 (2013) 127.
- [43] J. Tauc, R. Grigorovici, A. Vancu, *Phys. Status Solidi* 15 (1966) 627.
- [44] M. Pal, U. Pal, J.M.G.Y. Jimenez, F. Perez-Rodriguez, *Nanoscale Res. Lett.* 7 (2012) 1.
- [45] S. Rahut, R. Panda, J.K. Basu, *J. Photochem. Photobiol. A Chem.* 341 (2017) 12.
- [46] V.C. Ferreira, M.R. Nunes, A.J. Silvestre, O.C. Monteiro, *Mater. Chem. Phys.* 142 (2013) 355.
- [47] A.V. Emeline, V.N. Kuznetsov, V.K. Rybchuk, N. Serpone, *Int. J. Photoenergy* (2008) 2583942008.
- [48] H.W. Wijn, R.F. van Balderen, *J. Chem. Phys.* 46 (1967) 1381.
- [49] P. Szirmai, E. Horvath, B. Nafrádi, Z. Mickovic, R. Smajda, D.M. Djokic, K. Schenk, L. Forro, A. Magrez, *J. Phys. Chem. C* 117 (2013) 697.
- [50] G. Counio, S. Esmouf, T. Gacoin, J. Boilot, *J. Phys. Chem.* 100 (1996) 20021.
- [51] E. Simanek, K.A. Müller, *J. Phys. Chem. Solids* 31 (1970) 1027.
- [52] Z.V. Šaponjić, N.M. Dimitrijević, O.G. Poluektov, L.X. Chen, E. Wasinger, U. Welp, D.M. Tiede, Xi Zuo, T. Rajh, *J. Phys. Chem. B* 110 (2006) 25441.
- [53] S.A. Ahmed, *J. Magn. Magn. Mater.* 402 (2016) 178.
- [54] S.V. Chong, J. Xia, N. Suresh, K. Yamaki, K. Kadowaki, *Solid State Commun.* 148 (2008) 345.
- [55] S.K.S. Patel, N.S. Gajbhiye, *Mater. Chem. Phys.* 132 (2012) 175.
- [56] J.M.D. Coey, M. Venkatesan, C.B. Fitzgerald, *Nature* 4 (2005) 173.
- [57] S.A. Ahmed, *J. Mater. Sci. Mater. Electron.* 27 (2016) 7589.
- [58] B. Santara, P.K. Giri, K. Imakita, M. Fujii, *Nanoscale* 5 (2013) 5476.
- [59] M.K. Nowotny, L.R. Sheppard, T. Bak, J. Nowotny, *J. Phys. Chem. C* 112 (2008) 5275.
- [60] B. Choudhury, A. Choudhury, *Curr. Appl. Phys.* 13 (2013) 1025.
- [61] R.M. Zallen, *Physics of Amorphous Solids*, Wiley, New York, 1983.